Organic materials for solar fuel generation

Charlotte Smith

Dr A. Cowan and Prof. A. I. Cooper

Thesis submitted to the University of Liverpool in partial fulfilment of the degree of Doctor in Philosophy.

August 2019

Stephenson Institute for Renewable Energy

Abstract

In this work, organic materials have been studied for their application in photoelectrochemical water oxidation and the electrochemical reduction of CO_2 in water, using porous and linear conjugated polymers and hydrogels. The use of such organic materials for solar fuel generation is highly attractive as they are cheap, relatively easy to synthesise and their structure-properties can be fine-tuned for selective gas uptake, changes in optical and physical properties such as band gap, pore size, surface area and solubility.

The use of a conjugated microporous polymer containing a bipyridine (CMP-$(bpy)_{20}$) unit allowed for the incorporation of a well-known CO_2 molecular electrocatalyst, $[Mn(bpy)(CO)_3Br]$, in order to prevent the undesirable process of dimerisation of Mn centres prior to the formation of the catalytically active reduced species. Engineering of the electrode was explored *via* drop casting a suspension of CMP-$(bpy)_{20}$-Mn in a polymer/acetonitrile solution, such as Nafion or PANI to aid adhesion to the electrode surface and exploit secondary functionalities such as proton and electrical conduction respectively. Although dimerisation of Mn catalyst was prevented, CO Faradaic Efficiencies and the electroactive content were low. This is likely due to only a small fraction of catalytic centres becoming electroactive due to structural distortions across the polymer backbone resulting in insulated regions, and only Mn that is in direct contact with the electrode surface is electroactive. We also explored growing CMP-$(bpy)_{20}$ onto the surface of a GCE to produce thin film electrodes in an attempt to increase the planarity of CMP-$(bpy)_{20}$ and diffusion through the porous structure.

Two soluble linear polymers, P8s and P56, known to be good photocatalysts for hydrogen evolution were spectroscopically studied *via* transient absorption spectroscopy to gain insight into their photocatalytic mechanism and the role of solvents present. Due to the ease of processability and superior hydrogen evolution rate of P8s, we then went on to explore P8s as a photoanode for water oxidation purposes. XPS measurements showed P8s to be a suitable material for overall water splitting as it straddles the band gap for both hydrogen and oxygen evolution. Improved photocurrents were achieved by the fabrication of a heterojunction using TiO_2 by a factor of 30 reaching photocurrents up to 20.97 $\mu A.cm^{-2}$. Photoactivity was further enhanced by increasing the amount of absorbed photons by using high surface area mesoporous TiO_2. Transient absorption spectroelectrochemistry gave insight into the excited state dynamics of the photoanode and their lifetimes, which showed a long-lived hole in the material. Utilisation of the hole was demonstrated by the addition of a hole scavenger into the electrolyte, followed by the incorporation of a co-catalyst for water oxidation.

An amino acid functionalised perylene bisimide (PBI-A) hydrogel was studied in various hydrated states using UV-Visible absorption spectroscopy and neutron scattering to explore how drying affects changes in structure. Although the overall networks were similar, drying of a PBI-A hydrogel to form a xerogel resulted in an irreversible change in packing on the molecular scale between PBI-A units within a fibre. Spectroscopic studies showed a long-lived charge separated state under visible light illumination unlike previous reports of dominant UV activity for this class of materials. Therefore we tested the materials as photoanodes for water oxidation and explored how the difference in water content within a gel affects photoactivity and their excited state dynamics. Utilisation of the photogenerated hole was determined from oxygen evolution experiments in the addition of an IrO_x water oxidation co-catalyst.

List of Publications

D. J. Woods, R. S. Sprick, C. L. Smith, A. J. Cowan and A. I. Cooper, *Adv. Energy Mater.*, 2017, 7, 1700479.

J. J. Walsh, M. Forster, C. L. Smith, G. Neri, R. J. Potter and A. J. Cowan, *Phys. Chem. Chem. Phys.*, 2018, 20, 6811–6816.

J. J. Walsh, G. Neri, C. L. Smith and A. J. Cowan, *Organometallics*, 2019, 38, 1224–1229.

Vogel, A., Forster, M., Wilbraham, L., Smith, C. L., Cowan, A. J., Zwijnenburg, M. A., Cooper, A. I. (2019). Photocatalytically active ladder polymers. *Faraday Discuss.*, 2019,215, 84-97

C. L. Smith, R. Clowes, R. S. Sprick, A. I. Cooper and A. J. Cowan Sustainable Energy Fuels, 2019,3, 2990-2994

C. L. Smith, L. M. Mears, B. Greeves, E. R. Draper, J. Doutch, D. J. Adams and A. J. Cowan Physical Chemistry Chemical Physics, 2019 (accepted for publication)

List of Awards

19-03-2018: 6th UK Solar Fuels Symposium, University of York, poster prize, "Hydrogel photoanodes for energy conversion."

26-01-2017: 5th UK solar fuel symposium and postgraduate afternoon, flash presentation prize, "Conjugated microporous polymers for electrochemical CO_2 reduction in water."

15-06-2016: ECS north-west symposium, poster prize, "Conjugated microporous polymers for electrochemical CO_2 reduction."

Acknowledgements

This work is by no means a sole achievement, and there are many people of whom I would like to thank.

Firstly, I would like to thank my supervisor Dr. Alex Cowan for all of your invaluable help, support and guidance over the last 5 years which has made me the more confident scientist/person I am today. You are a fountain of knowledge and should be so proud of the group you have built. Thank you for also allowing us to take some time out of research to build and present our Solar Powered Dolls House at outreach events. Thank you for listening to me over the years and allowing me to have a little cry in your office every now and again… not that you had much choice in the matter! Finally, thank you for being the best supervisor one could ask for.

I would like to thank Prof. Andy Cooper and Dr. Seb Sprick for all of their support and guidance over the years. Thank you to Dr. Michael Briggs and the rest of Cooper group for all of your support, and for all the karaoke and Chinese wine nights out.

Dr. Gaia Neri, where do I start! You helped welcome me into the group when I started as a master's student, and have become such an amazing friend over the years. I truly look up to you. Thank you for helping me become not only the scientist but the person I am today, and for always being there for me. Thank you to Dr. Jamie Walsh for all your words of wisdom and guidance, and for also being subjected to beauty and fashion conversations in the lab. Thank you to Dr. Chloe Pugh, my twin! Thanks for becoming such an amazing and supportive friend, and for making so many memories from the rat of Rome to Rocket Man. Thank you to Dr. Ben Alston for always being a supportive friend. Thank you Dr. Laura Mears for all your support and advice it is truly appreciated, and also for introducing me to the world of neutrons which I thoroughly enjoyed…even through the lack of sleep!! I would like to thank Verity Piercy for always listening to me and trying to hold back the laughter at my stories when I was trying to be serious, and for being my personal CSD service desk. Thank you to Dave Muskett for always putting a smile on my face. Thank you to Dr. Silvia Mariotti for always being a ray of sunshine, and to Claudia Gatti for all the arts and craft fun.

I gratefully acknowledge all of my collaborators and colleagues who I have had the pleasure to work with during my PhD. I would like to thank the Chemistry department, Stephenson Institute for Renewable Energy and the Material Innovation Factory for allowing me to use their facilities. I would like to thank the Chemistry department's analytical services team and the materials innovation factory support team. Thanks goes to Dr. K. Arnold and Dr. M. Forster for their help with SEM experiments. Thanks goes to Dr. E. Draper for synthesising

PBI-A, and to R. Clowes for gas sorption measurements. I would like to thank Jose Coca-Clemente for XPS measurements. I would like to thank Dr. D. Adams for all of his advice and guidance during my time working on PBI.

I would like to thank everyone in the SIRE for being so friendly and a pleasure to work with, you all made coming into work every day a real pleasure. Special thanks goes to all members, past and present, of the Cowan group, for your endless support and advice which is very much appreciated. You all made me feel so welcome when I started, and all kept me sane during the stressful times! Thank you for being a group of wonderful and friendly people who have never failed in making me laugh, you all truly made my time here the best it could possibly be.

I would like to thank all of my family and friends for your constant encouragement and support. Thank you to my mum and dad for listening when I would explain, in detail, my stresses about my lab work, and just in general for putting up with me! Thanks goes to Luke for always providing Chester with treats and for always letting me in the house in the early hours when I forgot my house keys again!! Thank you, Monty, for the loud and lengthy squawking sessions at the most inconvenient of times, and thank you Chester for being the fluffiest of furballs and the friendliest rabbit who came home with me a couple of weeks before I started the PhD. Thank you to my Nanny Dot who always told me how proud she was and that she will be waiting with balloons and banners at the end of my PhD. Thank you to my Grandad George who I know would have been an enthusiast for the research I have done. Thank you to my Nanny Elsie and Grandad Gerry for their good luck prayers and love and support. Thank you to the Mensa family for making sure we never go hungry. Bekah, Andrew and Skye, I don't even know where I would be without you three, thank you for spurring me on whilst writing the thesis, generally keeping me sane and always making me laugh.

Finally, I would like to thank Stefano. Thank you for making me laugh every day, loving me and feeding me! I could not ask for a better partner and best friend, life would be a lot duller without you. We have learnt and done so much together, I cannot wait to see what the future holds! Grazie mille amore mio.

List of Abbreviations

Commonly abbreviated terms used commonly throughout this thesis are listed below. Each term will be explained at their first use in the main text.

A	Alanine
AQA	Apparent Quantum Yield
AWA	Amplitude Weighted Averages
BET	Brunauer-Emmett-Teller
bpy	2,2′-bipyridine
CMP	Conjugated Microporous Polymer
CMP-$(bpy)_{20}$	Conjugated Microporous Polymer containing 2,2′-bipyridine sites
CMP-$(bpy)_{20}$-Mn	Conjugated Microporous Polymer containing $[Mn(CO)_3Br]$ bound to 2,2′-bipyridine sites
CO	Carbon Monoxide
COF	Covalent Organic Framework
CPE	Controlled Potential Electrolysis
CV	Cyclic Voltammetry
dcbpy	2,2′-bipyridine-5,5′-dicarboxylic acid
DCVA	Differential Cyclic Voltabsorptometry
DEA	Diethylamine
DPP	Diketopyrrolopyrrole
DPV	Differential Pulse Voltammetry
FE	Faradaic Efficiency
FTO	Fluorine Doped Tin Oxide
GC	Gas Chromatography
g-C_3N_4	Graphitic Carbon Nitride
GCE	Glassy Carbon Electrode
GdL	Glucono-δ-lactone
HCl	Hydrochloric Acid
HCOOH	Formic Acid
HER	Hydrogen Evolution Reaction
HOMO	Highest Occupied Molecular Orbital
IC	Ion Chromatography
IPCE	Incident Photon Conversion Efficiency
ITO	Indium Tin Oxide

LED	Light Emitting Diode
LMWG	Low Molecular Weight Gelator
LSV	Linear Sweep Voltammogram
LUMO	Lowest Unoccupied Molecular Orbital
MeCN	Acetonitrile
mesbpy	6,6′-dimesityl-2,2′-bipyridine
MOF	Metal Organic Framework
NT	Multi-Walled Carbon Nanotubes
n-TiO_2	Nanoporous Titanium Dioxide
PANI	Polyaniline
PBI	Perylene Bisimide
PBI-A	Alanine Functionalised Perylene Bisimide
PEC	Photoelectrochemical
PIA	Photo-induced Absorption
PIM	Polymers of Intrinsic Microporosity
PMI	Perylene Monoimide
PMPDI	N,N′-bis(phosphonomethyl)-3,4,9,10-perylenediimide
PXRD	Powder X-Ray Diffraction
SANS	Small Angle Neutron Scattering
SEC	Spectroelectrochemistry
SEM	Scanning Electron Microscopy
SLD	Scattering Length Density
SWV	Square Wave Voltammogram
$t_{50\%}$	Half-life
TA	Transient Absorption
TBAP	Tetrabutylammonium perchlorate
TEA	Triethylamine
TEOA	Triethanolamine
TFE	Tetrafluoroethanol
TGA	Thermogravimetric Analysis
TiO_2	Titanium Oxide
TOF	Turn Over Frequency
TON	Turn-Over Number
UiO-67	$Zr_6O_4(OH)_4(bpdc)_6$
WOC	Water Oxidation Catalyst
XPS	X-ray Photoelectron Spectroscopy

XRD	X-ray Diffraction

Table of Contents

"Start by doing what's necessary;
then do what is possible; and suddenly
you are doing the impossible."

– Francis of Assisi

Chapter 1

Introduction

1.1 Scope of this thesis

In this thesis, we focus on the engineering of a variety of organic materials for their application in overall water splitting and CO_2 reduction *via* photoelectrochemical (PEC) and electrochemical techniques. In chapter 2 we incorporate a well-known CO_2 reduction molecular catalyst into a conjugated microporous polymer (CMP), and carried out electrochemical characterisation using various electrochemical techniques. Engineering of the electrode to gain stability and increased activity was the primary focus of this chapter. In chapter 3 we use transient absorption (TA) spectroscopy to rationalise the mechanism by which photocatalytic hydrogen evolution occurs in two organic linear polymers in the presence of a sacrificial donor. We then used the most active hydrogen evolution catalyst for the fabrication of a photoanode for water oxidation using a bulk heterojunction to gain insight into the possibility of complete overall water splitting with P8s. Finally, chapter 4 focuses on the use of an amino acid functionalised perylene bisimide (PBI) gel for water oxidation. The gels used in this chapter contain *ca.* 95% water, and we use both photoelectrochemical and spectroscopic techniques to gain meaningful insight into how structure-activity is affected in various hydrated states. We then go on to test the most active hydrated gel for water oxidation. As this thesis covers a variety of organic materials and techniques, for ease and clarity each chapter will be accompanied by its own detailed introduction providing insight into the current state-of-the-art and relevant background.

1.2 Solar fuels for renewable energy

The cheap extraction methods and high energy densities obtained from the burning of fossil fuels have resulted in them becoming the favored global energy resource for > 200 years.[1] In recent years the negative impact of global warming to our climate and ecosystems has been a hot topic worldwide.[2] The depletion of fossil fuels renders the heavy reliance we have on them as an energy source limited, and so finding new ways in which energy can be sustainably generated, stored and transported is therefore of great interest. Solar energy is the most abundant source of renewable energy available, and provides a promising method for the generation of carbon-neutral energy which is scalable, inexpensive and inexhaustible.[3,4] Nature exploits the use of solar energy every day to produce oxygen and carbon based sugars, and so the ability to mimic nature *via* artificial photosynthesis is highly attractive for the capturing and storing of energy in the form of chemical bonds which can be used when desired, for example during the night time when solar energy is not present. For example the production of synthesis gas (syngas, H_2 and CO) yields a sustainable route to the production of numerous carbon based products.[5,6] Ways in which artificial synthesis can be achieved is *via* PV electronic technologies,[7] photocatalytic[8] or electrocatalytic[9] routes and are shown in Figure 1.1. To reach commercial applications CO_2 reduction and water splitting catalysts must exhibit

high Faradaic Efficiencies at low overpotentials and good selectivity with long operating stabilities, ideally in an aqueous environment. The use of organic materials for such applications is of interest to achieve low-cost and sustainable routes to solar fuel generation.

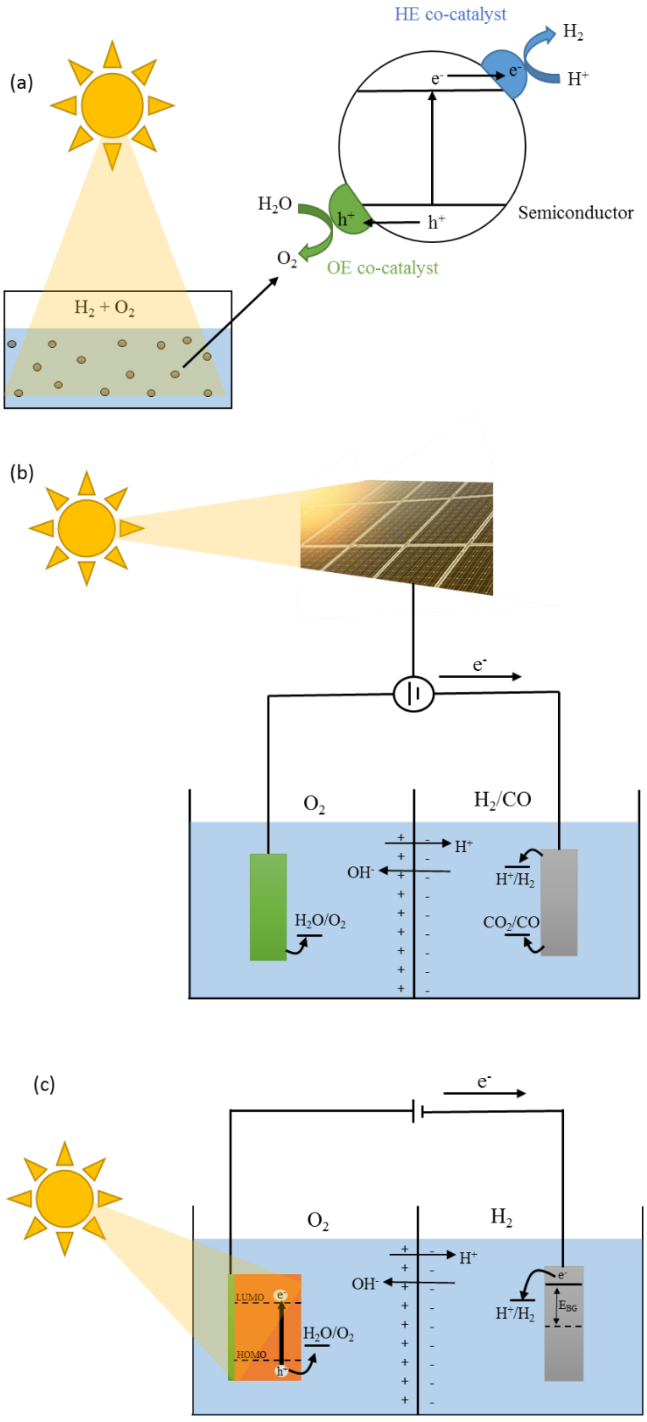

Figure 1.1 Various solar fuel generation routes are shown: photocatalysis using a light absorbing material and suitable co-catalysts to achieve oxygen evolution (OE) and hydrogen evolution (HE) reactions (a), electrochemical cells which are powered by PV cells are used to produce electrical energy from sunlight (b) and PEC systems using an organic light absorbing photoanode to carry out water oxidation and HE at the counter electrode (c). Figure adapted from Issues in Environmental Science and Technology, 2018, vol. 2019–Jan, pp. 184–209.[3]

1.2.1 CO_2 reduction

A promising way for the generation of carbon-based fuels is the reduction of CO_2 coupled with water oxidation. The direct electrochemical reduction of CO_2 *via* a single electron transfer, in the absence of a proton-coupled step, is thermodynamically unfavourable, and occurs at very negative potentials in aprotic solvents (-1.9 V_{NHE} at pH 7) Eq. 1.1.[10] In the presence of a proton source, lower energy CO_2 reduction pathways exist (e.g. $CO_2 + 2H^+ + 2e^- \rightarrow CO + H_2O$, -0.53 V_{NHE} at pH 7), however these are in competition with direct proton reduction ($2H^+ + 2e^- \rightarrow H_2$, -0.41 V_{NHE} at pH 7) which increases the difficulty of efficient CO_2 reduction as selectivity towards carbon-based products decreases. The use of molecular complexes of transition metals and noble metal electrodes as electrocatalysts has been extensively explored in the literature,[11,12] because they offer a route to lowering the required overpotential for CO_2 reduction, and increase selectivity to achieve high CO_2 conversion efficiencies. CO_2 reduction can go *via* 2, 4, 6 or 8 electron reduction pathways,[13] where although the generation of methanol and methane are thermodynamically favourable, it is a challenging goal as it is kinetically less favourable. Therefore, the reduction of CO_2 to CO is of particular interest as it can be used in syngas to produce carbon-based products *via* the well-known Fischer-Tropsch process. To reach commercialisation the development of cheap electrocatalysts that exhibit high Faradaic Efficiencies at low overpotentials in aqueous environments is highly desirable.

Equations 1.1 – 1.7 show the standard thermodynamic potentials for CO_2 reduction and H_2 evolution at pH 7 vs NHE in aqueous electrolyte.

$CO_2 + \bar{e} \longrightarrow CO_2^{\bullet -}$	E^o= -1.9V	Eq. 1.1
$CO_2 + 2H^+ + 2\bar{e} \longrightarrow CO + H_2O$	E^o= -0.53V	Eq. 1.2
$CO_2 + 2H^+ + 2\bar{e} \longrightarrow HCO_2H$	E^o= -0.61V	Eq. 1.3
$CO_2 + 4H^+ + 4\bar{e} \longrightarrow H_2CO + H_2O$	E^o= -0.48V	Eq. 1.4
$CO_2 + 6H^+ + 6\bar{e} \longrightarrow CH_3OH + H_2O$	E^o= -0.38V	Eq. 1.5
$CO_2 + 8H^+ + 8\bar{e} \longrightarrow CH_4 + 2H_2O$	E^o= -0.24V	Eq. 1.6
$2H^+ + 2e \longrightarrow H_2$	E^o= -0.41V	Eq. 1.7

1.2.2 Water splitting

The splitting of water into oxygen and hydrogen is an endothermic reaction requiring a large amount of energy (standard Gibbs free energy change of 237 $kJmol^{-1}$, or 1.23 eV) to drive the half reactions for water splitting as shown in Eq. 1.8 – 1.10.[14] In particular, it is thermodynamically challenging to oxidise water, due to the requirement of 4 electrons, which is often coupled with slow surface kinetics.[15] The use of semiconductors for water splitting

applications is of particular interest due to their narrow band gaps,[16] allowing for efficient photoexcitation using the visible region of the spectrum which accounts for *ca.* 46% of the solar spectrum.[17] A semiconductor is defined as a material that has conductivity between that of an insulator and a metal,[18] i.e. a filled valence band and an empty conduction band. Upon photoexcitation with photons that have an energy greater than or equal to its band gap, an electron from the valence band is photoexcited to the conduction band, creating holes in the valence band. They become highly conductive upon oxidation or reduction, which can be achieved *via* chemical, electrochemical,[19] photochemical[20] or chemical[21] doping *via* the insertion or removal of electrons or holes respectively.

Equations 1.8 – 1.10 showing the standard thermodynamic potentials for water splitting at pH 0 vs NHE.

$$2H_2O \longrightarrow O_2 + 4H^+ + 4e^- \qquad E^o = 1.23\ V \qquad \text{Eq. 1.8}$$

$$4H^+ + 4e^- \longrightarrow 2H_2 \qquad E^o = 0.00\ V \qquad \text{Eq. 1.9}$$

$$2H_2O \longrightarrow O_2 + 2H_2 \qquad E^o_{cell} = 1.23\ V \qquad \text{Eq. 1.10}$$

Therefore, ideal semiconducting materials for water splitting must possess a band gap large enough that the valence and conducting band edges straddle those of H_2O/O_2 and H^+/H_2 couples at +1.23 and 0.00 V_{NHE} at pH 0 respectively (Eq. 1.7 - 1.9). As it is desirable to utilise visible light (> 400 nm) the band gap should therefore be < 3 eV,[17] and some examples of semiconductors which exhibit such narrow band gaps are shown in Figure 1.2.[22,23]

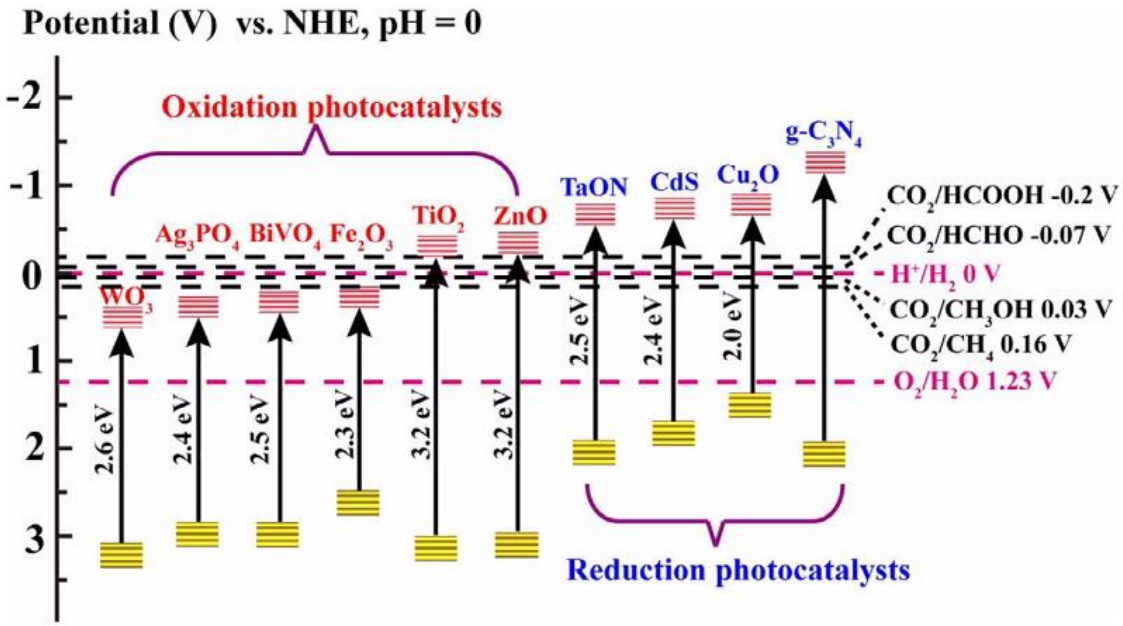

*Figure 1.2 Band positions of semiconductors with different valence (yellow) and conduction (red) band energies and their band gaps. The energies reported are vs NHE at pH 0. Figure taken from Mater. Today, 2018, **21**, 1042–1063.*[23]

Photocatalytic water splitting using a single semiconductor material is theoretically possible, however these materials suffer from a lack of high charge separation rates and so need the use of a sacrificial donor or hole scavenger to prevent charge recombination.[24] One way in which this can be overcome is by the use of a Z-scheme approach which resembles nature's photosynthetic system.[23,25,26] The Z-scheme approach was first reported by Bard in 1979, where two semiconductors (PCI and PCII) work together *via* a coupled electron transfer process using a redox shuttle, such as Fe^{3+}/Fe^{2+} and IO_3^-/I^-, to perform water oxidation at one semiconductor and hydrogen evolution at the other as shown in Figure 1.3a.[23,26] However, back reactions of the redox shuttle are thermodynamically favoured along with diffusion limitations hindering charge transfer, pH sensitivity and instability which all result in decreased activity of the Z-scheme system.[16,27] To overcome such limitations, solid state Z-schemes and direct Z-schemes have been explored, Figure 1.3b and c, although they can be costly to synthesise and far from fulfilling practical requirements.[27]

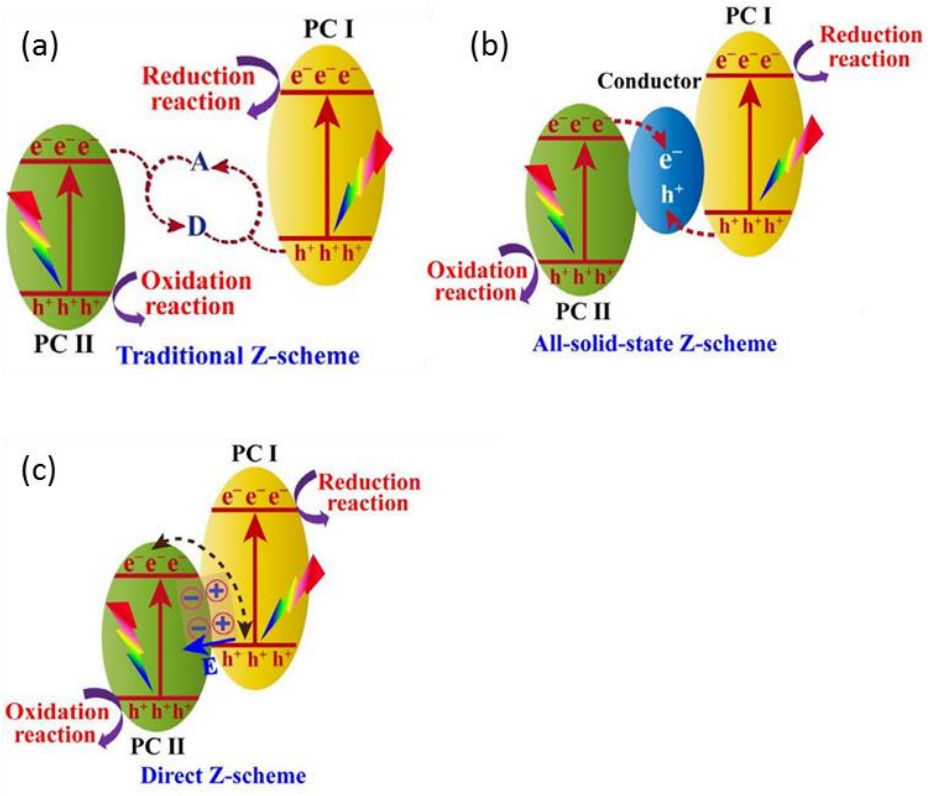

*Figure 1.3 Schematic diagram showing the traditional Z-scheme where donor (D) and acceptor (A) redox shuttles are used for electron and hole consumptions (a), an all-solid-state Z-scheme (b) and a direct Z-scheme (c). PC stands for photocatalyst. Figure taken from Mater. Today, 2018, **21**, 1042–1063.*[23]

Alternatively, water splitting can be achieved *via* PEC routes, where ideally no bias is required to the semiconductor in aqueous electrolyte. The addition of this extra energy into the system allows the use of narrow band gap materials, Figure 1.1c.[9,26] Upon the application of a bias, for example a positive bias, an electric field is created where electrons diffuse into the bulk of the material towards the electrode and holes migrate towards the surface/electrolyte

interface to participate in water oxidation reactions.[26] When semiconducting materials are used, their ability to absorb light generates an electron-hole pair in the HOMO/LUMO which can go on to carry out water splitting with a lower amount of electrical energy input compared with a purely electrochemical system.

1.3 Organic materials for solar fuel generation

The use of carbon-based materials for solar fuels generation is highly desirable as unlike inorganic materials for solar fuel generation they are cheap and relatively easy to synthesise, and are comprised of earth abundant elements. Additionally, organic materials can be easily tailored to meet desired requirements, such as changing the optical properties,[28–31] physical properties,[32–34] and selective gas uptake,[35–37] by modification of the structure.[38] Graphitic carbon nitride (g-C_3N_4) is one of the most studied organic materials for solar fuel generation due to its high selectivity and activity in the visible region.[39–41] However, lack of control over the structure during synthesis makes it difficult to finely tune the structural properties, and its insolubility makes electrode fabrication difficult.[42] Fullerenes are one of the most widely used electron acceptors in organic photovoltaics due to a large delocalised LUMO across the molecules surface, that promotes high electron mobility and transport.[43] However, these are costly to synthesise, have instability, limited tunability and weak absorption in the visible region.[43] Therefore, the fabrication of alternative organic materials that are cheap, active in the visible region, processable and easy to tune physical properties is highly desirable. The use of organic polymers offers a route from which this can be achieved, and to date organic polymers have been widely studied for their application in overall water splitting,[44,45] CO_2 reduction,[46,47] photocatalysis[48] and electrochemistry.[49]

1.3.1 Conjugated organic materials

Conjugated organic materials are comprised of sp^2 hybridised carbon atoms where the non-hybridised p orbitals overlap between adjacent sp^2 hybridised carbon atoms to form π-bonds. The formation of these π-conjugated states results in electron delocalisation across the polymer network lowering the energy of the system giving semiconducting properties to the polymer.[50] The HOMO is defined from the π bonding orbitals, and the LUMO from the π antibonding orbitals that make up the sp^2 hybridised bonds. The band gap is therefore the energy gap between the HOMO and LUMO. The optical and conductive properties associated with π-conjugated polymers are dependent on many factors such as shape, size, planarity and isomerisation of monomer units used. An oligomer consists of few repeating units within its structure such as dimers and trimers, whereas a polymer consists of an infinite number of repeating units. Therefore, the electronic behaviour of oligomers can give meaningful insights

in order to rationalise the electronic structure of π-conjugated polymers both experimentally and computationally.[50,51]

1.3.2 Organic semiconductors

Unlike inorganic semiconductors, organic semiconductors have narrow band gaps (typically *ca.* 1.5 eV),[31] which allow for more efficient photoexcitation in the visible region of the spectra. Upon photoexcitation, with a photon with energy equal to or greater than the band gap, electrons are promoted from the valence to the conduction band, increasing conductivity of the organic semiconductor by the generation of excitons or longer-lived polarons.[52] In materials that exhibit small dielectric constants, such as organic semiconductors, these excitons are known as Frenkel excitons, and are photo-generated electrons and holes that are tightly bound *via* Coulombic interactions.[53] The photo-generation of Frenkel excitons occurs across the polymer chain following the direction of electron delocalisation. Upon aggregation of polymer chains *via* intermolecular forces such as Van der Waals forces and π-π stacking between aromatic units, overlap of the π-orbitals occurs yielding electron delocalisation also in directions perpendicular to the polymer chain which is fundamental for high charge carrier mobility.[54] Whereas, a polaron is generated when an electron or hole is localises within the lattice inducing a structural change within the surrounding lattice; the polaron is then able to migrate through the material *via* thermally-activated hopping.[55] The formation of an electron or hole polaron is favourable for photocatalytic applications as recombination is disfavoured, resulting in a long-lived charge which can migrate off the organic semiconductor to a substrate to carry out oxidation/reduction reactions.

Organic semiconductors such as polymers have structural or chemical defect sites. Chemical defect sites occur from the presence of impurities in the material from its synthesis or from film preparation,[56] whereas structural defect sites arise due to grain boundaries, chain ends and other structural parameters such as torsional disorder.[56] As organic semiconductors have a large distribution of molecular environments, they are therefore expected to have higher amounts of defect sites present. Defect sites can result in charge trapping such as the formation, for example, of a hole polaron which can then migrate to the surface to form a single catalytic sites that can carry out oxidation reactions at the surface. However, charge localisation also may lead to charge recombination if the localised charge is not extracted faster than recombination rates with delocalised electrons. As organic semiconductors are considered as 1D inorganic semiconductors, increased conjugation is expected to reduce the rate of electron-hole pair recombination. Planarization to form linear π-conjugated polymers is one route to overcome such limitations to enhance electron-hole pair concentrations,[57] and

linear π-conjugated polymers have been reported to exhibit higher photocatalytic hydrogen evolution rates than porous π-conjugated polymers.[30,58–61]

1.3.3 Porous organic materials

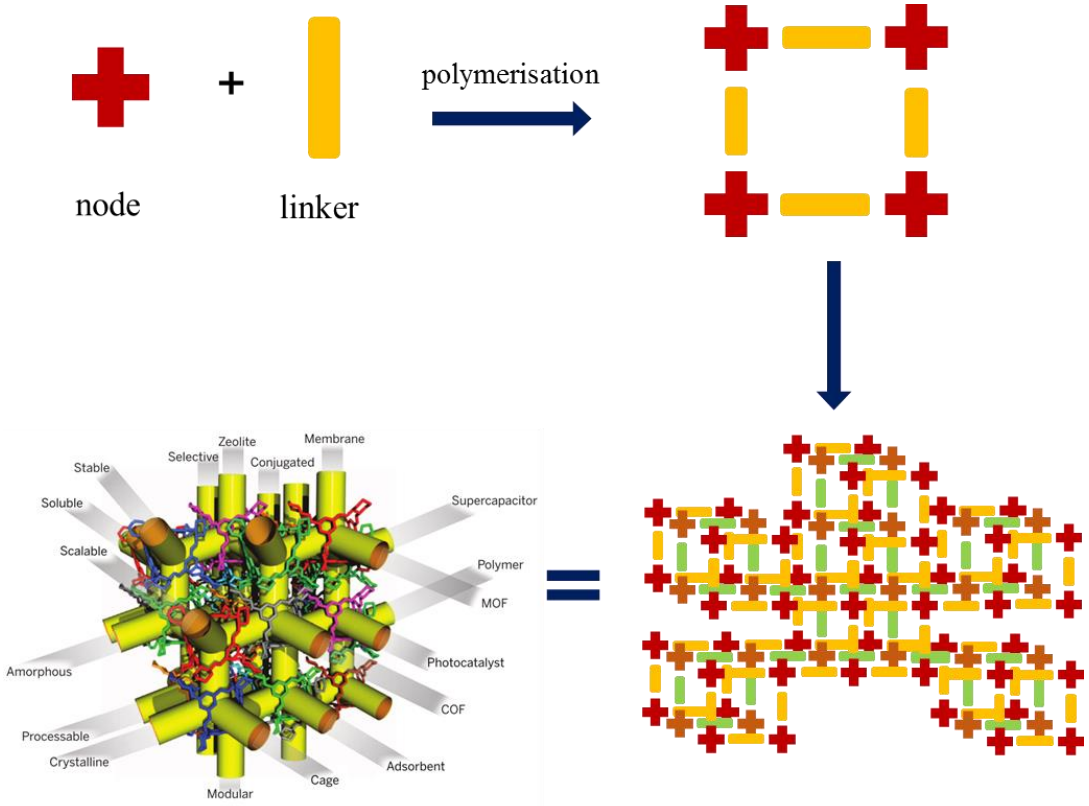

Figure 1.4 Schematic diagram showing the polymerisation of monomer units, and how the symmetry of node units and the length and functionality of strut units control the dimensionality and the properties of the polymer synthesised. Figure taken from Science, 2015, 348, 8075–8075.[34]

Polymer materials can be synthesised from click type reactions, acid or base catalysed condensation reactions, oxidative couplings, trimerisations or Friedel-Crafts type couplings which can result in the formation of 1D, 2D or 3D structures.[62,63] The type of structure formed is controlled by the use of monomer units (building blocks) used, Figure 1.4. There are two types of building blocks that allow for fine control over the structure properties which are nodes and struts.[38] Nodes establish the dimension of the network achieved from the polymerisation reaction, i.e. 1D, 2D or 3D, and are defined by their symmetry. Properties such as rigidity, pore size and selective gas uptake are controlled by the length, conjugation and functional groups of the strut.[64] Therefore, by careful consideration over the building blocks used fine control over the structure and its properties can be achieved, and this has resulted in the synthesis of a wide variety of polymers that can exhibit high surface areas, tuneable band gaps, selective gas uptake, high thermal and chemical stabilities and (in)solubility.[64,65] Many sub-classes of porous polymers have been developed and are summarised in Table 1.1.

Sub-classes of porous materials are inorganic materials (zeolites), metal organic (metal organic frameworks (MOFs)) and organic materials (covalent organic frameworks (COFs), porous organic polymers, polymers of intrinsic microporosity (PIMs) and porous molecular solids.[34] In all cases the dimensionality is determined from the node which can be an organic building block in the case of organic materials, or alternatively for inorganic and metal organic materials the co-ordination number of the metal ion or cluster.

Porous materials have been used in applications such as catalysis,[66] sensing,[67] optoelectronics,[68] selective gas soprtion and energy storage.[69–71] The most commonly reported porous materials used for solar fuel generation applications are MOFs and COFs and have been reviewed elsewhere,[46,48,62,72–75] which are highly to moderately crystalline porous materials, giving rise to good conduction and diffusion pathways and gas adsorption properties which are advantageous for catalysis applications.[34] The use of MOFs as a photocatalysts was first reported in 2009 using a sacrificial donor and $Ru(bpy)_3^{2+}$ photosensitizer under visible light irradiation for hydrogen evolution,[76] and since have been used in hydrogen[77] and CO_2 reduction photocatalysis.[78–80] Due to the poor solubility in aqueous conditions, typically MOFs were explored as a suspension in photocatalysis.[77] Since, the fabrication of MOF thin films and composites has been achieved *via* (i) direct growth/deposition from solvothermal solutions, (ii) assembly of nanocrystals, (iii) layer-by-layer growth onto a substrate, (iv) electrochemical deposition and (v) a gel-layer approach, which is reviewed elsewhere.[81] COFs are comprised of organic elements only such as carbon, nitrogen, hydrogen, oxygen and boron, and to date many different sub-classes of COFs are known such as imine-, hydrazone- and keto-enol- linked COFs.[82–84] Similarly to MOFs, COFs are limited by their insolubility and unprocessable properties, but thin film fabrication has been achieved by bottom-up or top-down approaches such as solvothermal growth and exfoliation, which have recently been reviewed.[85] Conjugated microporous polymers (CMPs) are a sub-class of porous organic polymers, and are comprised of aromatic units with high surface areas and porosity, but unlike MOFs and COFs they form amorphous 3D networks with extended conjugation and can be easily processable using electrochemical,[86,87] surface functionalisation[88] and surface growth.[89,90]

Table 1.1 Summary of the physical properties of porous polymers. Micro- and meso- pores have pores sizes < nm or 2 – 50 nm respectively. Ultraporous materials have high pore volumes and surfaces areas. The term zeotype is a framework that is based upon a known zeolite topology. The term multivariate MOFs refers to MOFs comprised of more than one organic linker. Table reproduced from Science, 2015, 348, 8075–8075.[34]

	Porous molecular solids	Porous organic polymer	Covalent organic framework	Metal organic framework	Zeloite
	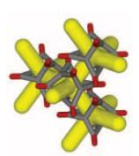			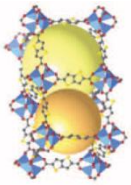	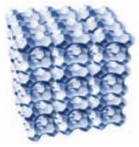
Porosity	Can be ultraporous/mesoporous, but this is rare so far	Can be ultraporous/mostly microporous; broader pore sizes	Can be ultraporous/ mesoporous; narrow pore size distributions	Can be ultraporous/mesoporous; narrow pore size distributiond	Microporous or mesoporous; narrow pore size distributions
Crystallinity	High, but amorphous examples too	Amorphous	Modest to high	Typically high	Typically high; can also be amorphous
Stability	Generally poor, though isolated examples of hydrothermal stability	Good to excellent, especially hydrothermal	Boronates generally poor; iminies generally good	Poor to good; growing number of water stable MOFs	Thermal stability generally excellent; can be acid/base sensitive
Modularity /diversity	Cocrystals possible, not widely exemplified yet	Very high; multiple linkers and liner functions possible	In principle high; less developed than MOFs	Very high even for single-linker MOFs; also multivariate MOFs	High; new structures can be based on known zeotypes
Processing	Soluble, as for PIMs could be advantage or disadvantage, depending	Modest processability, with exception of soluble PIMs	Insoluble, but examples of surface growth	Insoluble, though many recent examples of composite and films	Insoluble, but technologies for films, composites and pellets are well developed
Designability	Isolated cage can encode functions, but no general isoreticular	Composition control good;3D structure control more challenging	In principle good, as for MOFs; isorectiular approach possible	Excellent, isorecticular principles of nose/strut metal organic bonding are well developed	Excellent, though design of organic templates can still be challenging
Unique selling points	Solution processing ; physical properties intrinsic to cages	Extended conjugation for CMPs, solution processing for PIMs	Electronic properties	Structural and chemical control for diverse range of materials	Stability; low cost, commercially proven technology
Summary	New area with fewer examples, but early promise for specific molecular separations	Rapidly growing in number; diverse chemistry; commercial application for PIMs	Much less developed than MOFs, but early promise for organic electronics	Established and highly active field; as yet, no large scale applications	Developed but still actively growing area; zeolites have major commercial importance

1.3.4 Non-porous materials

In contrast to porous polymers, linear polymers have been shown to form semi-crystalline or amorphous structures upon aggregation and packing.[54] In this case, crosslinks are formed between polymer chains *via* Van Der Waals forces between aromatic groups of neighbouring chains. Planarity of amorphous π-conjugated polymer chains is advantageous in order to decrease torsional disorder. Torsional disorder results in a partial break in the overlap of π-orbitals decreasing the overall conjugation length creating localised regions of conjugation,[91,92] resulting in an increased HOMO/LUMO energies.[93] Therefore, the overall energy of the system is minimised through equilibria between torsional disorder and electron delocalisation. Conjugation is affected by both torsional disorder and the ordering of building blocks in a polymer chain to achieve reasonable conjugation lengths.[28,93] Sprick *et al.* have shown that by changing the relative monomer ratios a library of polymers can be synthesised, and that by doing so the band gap energies of CMPs can be altered by *ca.* 1 eV.[28] One of the monomer units used in this study was a pyrene-based monomer, and as the pyrene concentration was increased the band gap decreased (red shift in absorbance maxima) as a result of more aromatic rings which increased present within the structure increasing ring strain i.e. less torsional disorder due to resistance to bond twisting.[28]

Some linear polymers have been synthesised as the linear analogues of CMPs, by the incorporation of alkynyl groups to planarise the 3D structure.[59] As they are comprised of aromatic units they exhibit extended conjugation across the rigid backbone of the polymer chain. Typically linear polymers are insoluble, but processability can be improved by the incorporation of solubilising side chains resulting in soluble linear polymers, often only soluble in organic solvents.[94–97] Therefore linear polymers have received attention for photocatalytic water splitting applications due to ease of processability and device fabrication coupled with decreased particle size allowing for improved activity.[62]

1.3.5 Other organic materials

Alternatively to polymers, low molecular weight self-assembled structures can be used for solar fuel generation.[44,98–101] They are made solely of organic elements, and form 3D networks which can entrap large amounts of solvent, and can form either crystalline or amorphous structures with ease of processability.[102] Formation of the self-assembled network occurs *via* π-π stacking between the aromatic perylene core as well as other Van der Waals forces, promoting the formation of a conjugated pathway leading to good conductive properties,[103–106] and as a result have been used in OPV devices,[107,108] photocatalysis,[109–111] photoelectrochemistry[44] and sensors.[112]

1.4 Techniques for solar fuel generation

In chapter 2 we have used a CMP for the incorporation of a CO_2 reduction catalyst. Gas sorption was used to gain insight into the surface area and pore size distributions of the (un)metallated CMP, along with its ability to uptake CO_2. In chapters 3 and 4 we have developed photoelectrodes for water oxidation using linear polymers and gels. We used TA spectroscopy to investigate the mechanisms and charge carrier dynamics of the photochemical systems. In chapter 4 we use small angle neutron scattering (SANS) to gain meaningful insight into changes in structure of gel photoelectrodes upon various levels of hydration. Here, we introduce the basics of the theory for both of these techniques.

1.4.1 Transient Absorption (TA) spectroscopy

TA spectroscopy is a time-resolved spectroscopic technique which can give insight into the dynamic processes of a material upon photoexcitation at a given wavelength. Developments in the field of laser technology have produced TA spectroscopy systems with improved detection and sensitivity since the first report of the technique in 1949.[113,114] In this thesis we focus on the dynamic processes in organic materials in the UV-Visible absorption spectrum using an ultrafast TA system on the fs-ns timescale which is schematically shown in Figure 1.5.

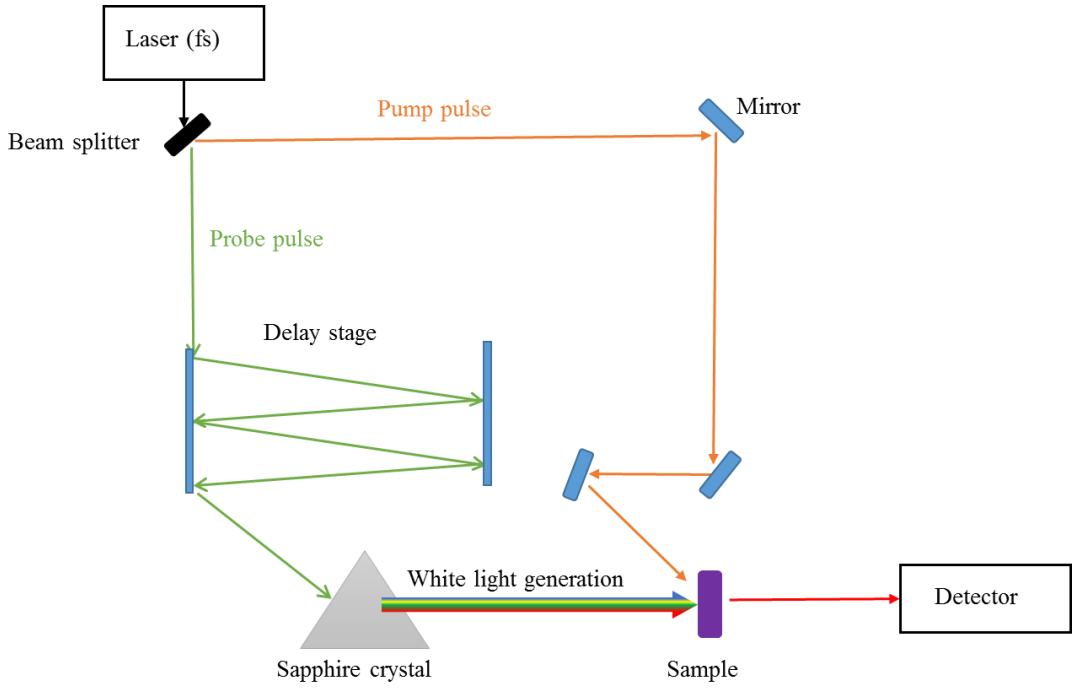

Figure 1.5 Schematic diagram showing the working principles of an ultrafast (fs –ns) transient absorption spectrometer. Such as the one used for our measurements.

A short ultrafast pulse is split into a pump and probe light by a beam splitter. The pump light is used to excite the material at a desired wavelength to a low energy excited state. The

probe light is passed through a variable delay line before passing through a sapphire crystal to generate white light, which then passes through the sample to a detector to generate a difference absorption spectrum (ΔA), i.e. the change in absorbance from the low energy excited state after white light excitation in comparison to the ground state at a single time point. This is carried out at various time delays, τ, by changing the variable delay line distance in order to acquire a 3D plot of the change in absorbance against time and wavelength. TA spectroscopy gives insight into processes related to a change in the optical density following excitation, and commonly observed signals can be assigned to:

(i) Ground state bleach: A fraction of the molecules in the ground state absorbance of the material are promoted to a low energy excited state upon excitation with the pump light, hence the number of molecules in the ground state adsorption decreases resulting in an inverse of the absorption profile of the absorbance of the ground state i.e. a negative absorbance signal.

(ii) Stimulated emission: Upon excitation of the material with the high energy laser pulse, an electron can drop to a lower energy level releasing a photon in phase with the incoming photons from the laser pulse, therefore hitting the detector and resulting in a negative absorption, often corresponding to the emission spectra of the material.

(iii) Excited state absorptions: The excitation of the low energy excited state molecules to higher energy excited states upon excitation with the probe light results in a positive absorption signal. If long-lived molecular states are generated such as triplet states or charge separated states, a positive signal is detected at longer timescales. As the spectra are recorded at various time delays, insight into the decay of the excited state as it relaxes back down the ground state, and any charge transfer, intersystem crossing and recombination processes can be gained from the kinetic analysis of these signals.

In this thesis TA spectroscopy was used in chapters 3 and 4, to gain insights in the charge carrier kinetics and electron/hole transfer processes for a PBI gel and linear polymers for overall water splitting applications. The full experimental details for each experiment are described in the respective materials and methods section of the chapters.

1.4.2 Small angle neutron scattering

SANS is a technique commonly used to probe the primary fibre dimensions and network within gels, as it has the ability to probe structures formed on the hundreds of nanometres scale. All SANS measurements shown in this thesis were carried out using the ISIS neutron source (STFC, Rutherford Appleton Laboratories), using an electric discharge method to form H- ions and electrons in the injector. Upon injection into the synchrotron alumina foil is used to remove electrons in order to produce a beam of photons. The photons are accelerated with the use of a radio-frequency electric field, around a 163 m ring with the use of strong magnets to direct the beam, and remove 84% of the protons from the synchrotron. Upon their removal, the fast travelling photons are directed towards a tungsten target, allowing for the production of neutrons *via* spallation. This reduces the speed at which the now formed neutrons travel, which are sent to the target stations for use in experiments, Figure 1.6.

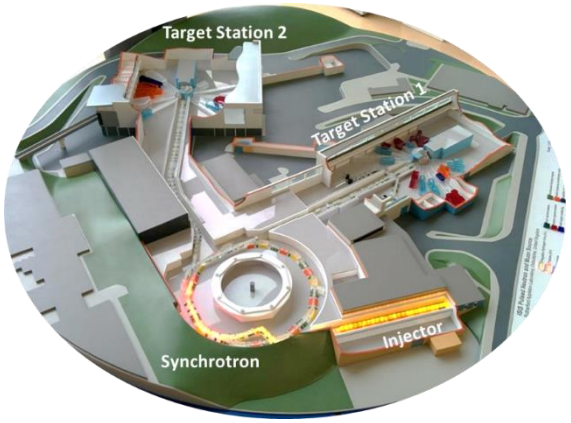

Figure 1.6 ISIS neutron facility showing the injector, synchrotron and target stations involved in the production of neutrons.

Neutrons can interact with the nucleus of an atom *via* elastic or inelastic scattering. Here we are interested in coherent elastic scattering of a neutron. Elastic scattering conserves energy meaning there is no energy losses or transfer occurring, and so the radiation of incident and scattered neutrons should in principle be the same. Elastic scattering only accounts for the energy of the neutron and not its momentum, and therefore only structural information can be obtained. There are two types of elastic scattering which can occur, coherent and incoherent scattering. Coherent scattering is governed by the neutron scattering interference from nearby atoms, allowing for the construction of the relative atomic positions of neutron centres in a material, giving insight into the materials size and shape.[115] Incoherent scattering has no scattering interference between neighbouring atoms, therefore no structural insight can be gained. For hydrogen, incoherent scattering is particularly large and greatly contributes to the background scattering noise. Since the scattering length density (SLD) is a measure of strength between the neutron and nucleus of an atom, this means that the SLD of isotopic elements will

have different scattering patterns as seen for hydrogen and deuterium. As deuterium has a smaller SLD, it can be used to reduce the background scattering noise. The SLD of an element is calculated as follows:

$$\rho_N = \frac{1}{V_m} \sum_i n_i b_i = \frac{\rho_m N_A}{M} \sum_i n_i b_i \qquad \text{Eq 1.11}$$

Where V_m is the molecular volume, ρ_m is mass density, M is molecular weight, η_i is the number of atoms in the molecule of type i and b_i is the scattering length of atom i. The SLD for a particular material is calculated *via* the equation above for powders and solids. As there is uncertainty in the total volume of water present in hydrogels, it is not clear how this affects the density of the material. Therefore, in order to obtain an accurate SLD value for non-solid materials, water content needs to be experimentally calculated. This is done by monitoring the SLD of the material in various ratios of solvent, for example H_2O:D_2O, and plotting it against the scattering intensity. When the SLD intensity is at a minimum, the low angle scattering vector (Q) is equal to 0, meaning the SLD has matched that of the molecule. A scattering pattern arises when there is a difference in scattering length between a solvent and a molecule, therefore when Q=0 the scattering length of solvent and molecule are the same, as shown in Figure 1.7.

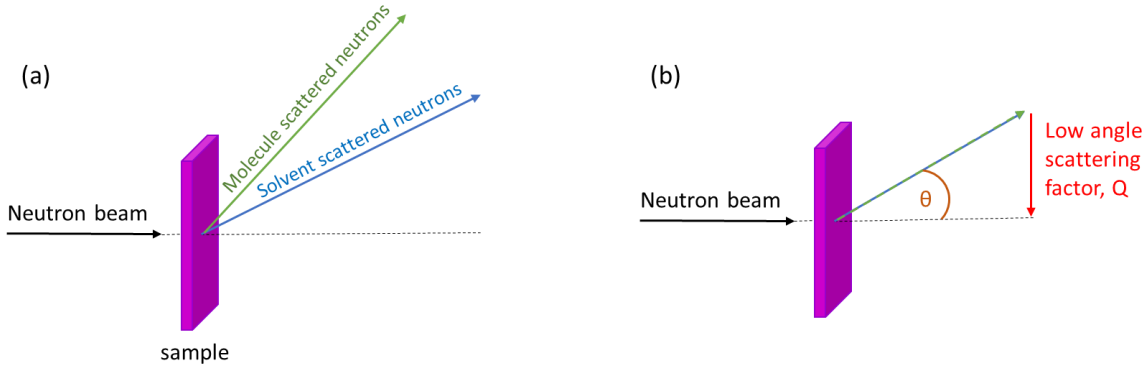

Figure 1.7 Neutron beam penetrates the sample and a difference in scattering length is seen for the molecule and solvent present within the sample (a), when the low angle scattering factor, Q, is equal to 0 this means that both the molecule and solvent have the same scattering pattern, allowing the SLD of the molecule to be determined (b).

The SLD can then be calculated from the ratio of solvents using the following equation, where V is the volume of the component and ρ is the SLD of the component:

$$\rho_{mix} = \frac{V_1\rho_1 + V_2\rho_2}{V_1 + V_2} \qquad \text{Eq. 1.12}$$

Analysis of the data is initially fitted to an assumed structure, in this case to a flexible cylinder and power law model, which is described by the following equation;

$$I(Q) = SF_O(SF_{PL}P(Q)_{PL} + SF_C P(Q)_C) + \text{Background} \qquad \text{Eq. 1.13}$$

There are three scaling factors present in the model used to determine the scattering intensity, I(Q):

1. An overall scale factor, SF_O, is present and fixed to 1, as the volume fraction is very low and so it is assumed the system is relatively dilute.[116]

2. A power law scaling factor, SF_{PL}, takes into account the radius, Kuhn length and contour length.[116] The flexible cylinder model describes a worm like chain of freely jointed units with a contour length, L, and each unit within the chain has a length, l_p, that is half of the Kuhn length, b, Figure 1.8. The contour length is the length of the chain if it was fully stretched out.[117] The Kuhn length is where a polymer chain is considered as a collection of Kuhn segments. A Kuhn segment describes how flexible and bent the chains are, as denotes the length at which the segments can be considered as rigid.[117] A short Kuhn length means there is more flexibility and random coil structure within the polymer, whereas a large Kuhn length represents a more sturdy and rod-like structure.

3. A worm-like cylindrical scaling factor, SF_C, takes into account the volume fraction of cylinders.[116]

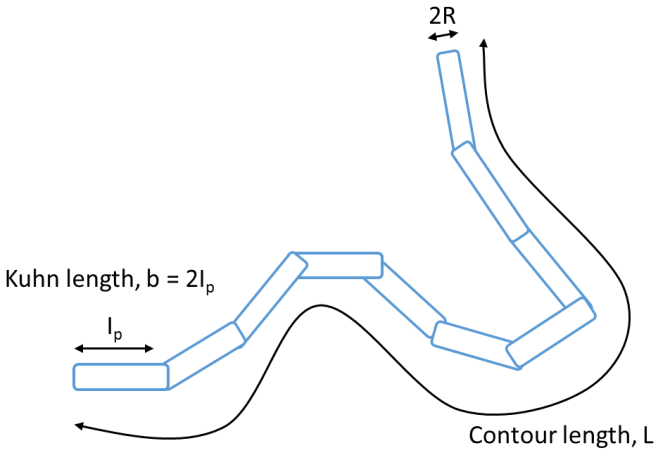

Figure 1.8 Schematic diagram for the fitting of SANS data to a flexible cylinder and power law model including parameters affecting the Porod's power law. Figure reproduced from Soft Matter, 2016, ***12****, 3612–3621.*[116]

For systems with isotropic scattering and mass fractal structures (a mass fractal structure consists of small molecules clustered together forming a 3D network containing crosslinks and branching points within its structure.), Porod's law is used to carry out data fitting to obtain the power law, $P(Q^{-N})$, where N is the mass fractal dimension. The background scattering noise is also considered due to the presence of a small amount of incoherent scattering from the sample. Incoherent scattering arises from hydrogen atoms in the PBI structure, the presence of a small amount of water in D_2O, and small incoherent scattering

contributions from other elemental atoms present within the PBI structure such as carbon, nitrogen and oxygen.

In this thesis we used SANS in chapter 4 to gain insight into the difference in structure of gels at various hydration levels. Full experimental details are given in the materials and methods section of chapter 4.

1.4.3 Gas sorption

Gas sorption is a technique used to characterise porous solids and fine powders giving insight into the porous structure of such materials. The absorption/desorption isotherms obtained from these measurements are a measure of the molar quantity of gas absorbed/released at a constant temperature. It is therefore important that the solid sample has a clean surface, achieved *via* the application of a vacuum at a given temperature, to prevent blockages in pores hence ensuring accurate pore measurements.[118] Once the solid sample has been degassed, the cell is then flushed with a known amount of the desired gas and the quantity of gas adsorbed is monitored against relative pressure, P/P_o, which gives insight into the porous structure. As the pressure of the system is increased the amount of gas absorbed increases; initially a build-up of gas occurs at the solid surface (1) until full monolayer coverage is achieved (2), and this gives insight into the surface area.[118] As the pressure is increased further, information into the mesopore size can be measured (3), followed by total pore volume and additional pore size information upon complete saturation (4) (Figure 1.9).[118,119]

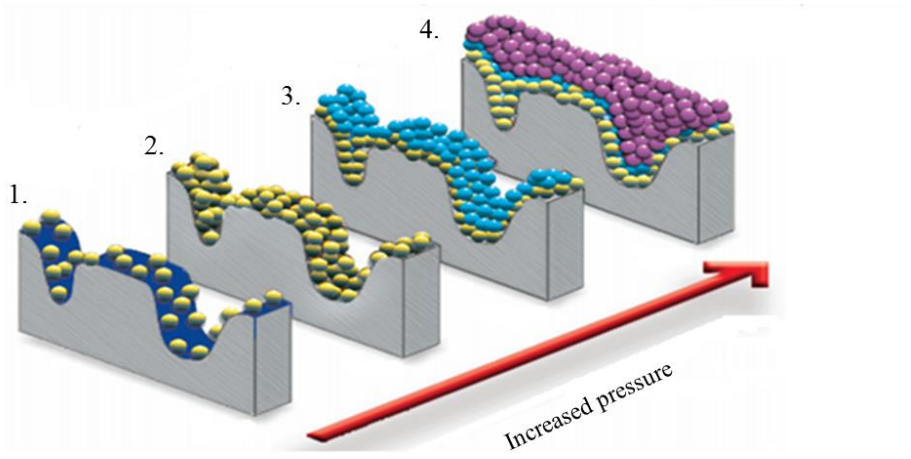

Figure 1.9 Schematic diagram of the filling of pores upon increasing pressure. Image taken from Micromeritics Instrument Corporation, Gas Adsorption Theory Poster.[119]

As the pressure is reduced, the amount of gas adsorbed decreases mirroring the adsorption profile. Adsorption/desorption isotherms are grouped into six types as shown in Figure 1.10.

Briefly:[118]

- Type I indicates narrow micropores and gas adsorption is limited by accessible micropore volumes.
- Type II + IV are given by either non-porous materials or macroporous solids.
- Type III + V are found in either non-porous or macroporous solids where weak adsorbent-adsorbate interactions are present.
- Type VI is found in non-porous materials with a uniform surface where adsorption occurs by layer by layer resulting in steps in the isotherm.

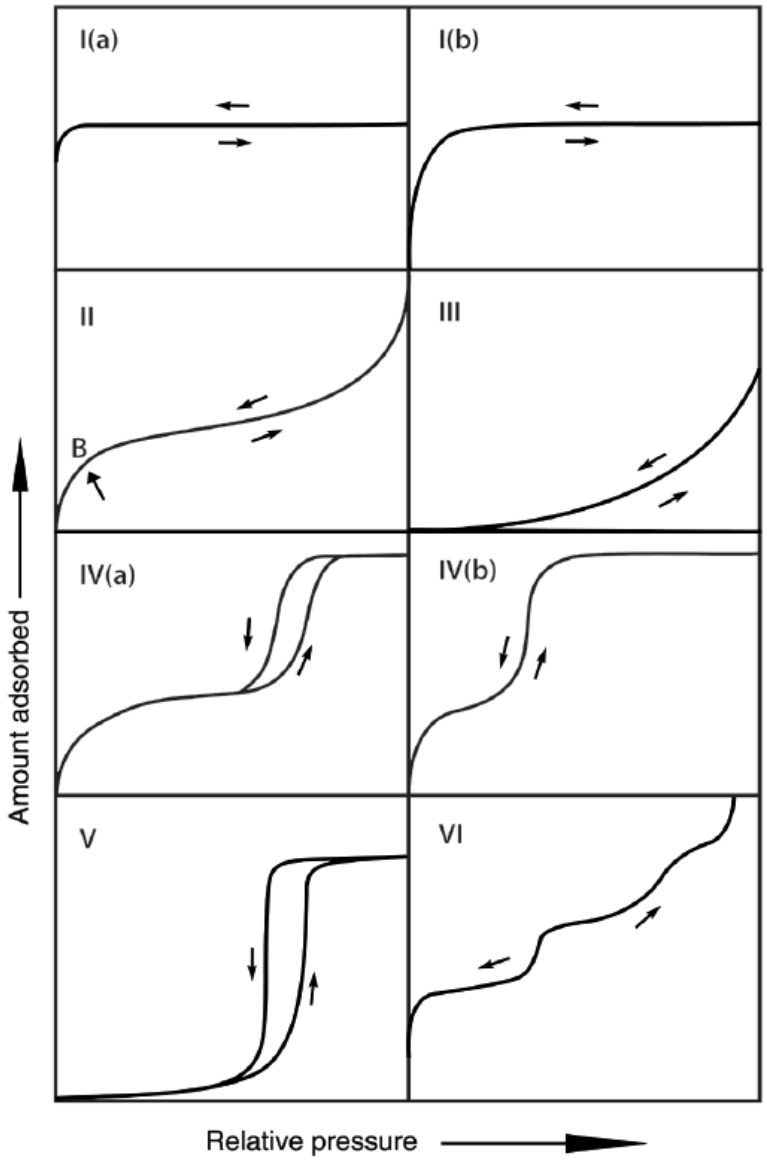

*Figure 1.10 Types of adsoption/desorption isotherms. Image taken from Pure Appl. Chem., 2015, **87**, 1051–1069.*[118]

A hysteresis loop is present when there is a difference between the adsorption and desorption data points as a result of the presence of meso- and macro- pores. The presence of a hysteresis

loop is generally due to capillary condensation, which arises due to gas condensing in a pore at a pressure (p) lower than the saturation pressure (p^o) of the bulk liquid.[118] Therefore, desorption is equivalent to a reversible liquid-vapour transition. Alternatively, hysteresis loops can be a result of network effects and pore blocking.[118] For example, if a narrow pore leads into a larger pore upon adsorption the larger pore will fill first, whereas upon desorption the narrower pore must empty first before desorption from the larger pore can occur.[118] There are 5 types of hysteresis loops reported and are shown in Figure 1.11, they are:[118]

- H1 loops are found in materials that have a narrow range of uniform mesopores.
- H2 loops are a result of a complex pore structures due to network effects. There are 2 types of H2 loops which are attributed to pore blocking due to narrow ranges of pore necks (a) and large size distribution of pore necks (b).
- H3 loops are distinguished by the adsorption isotherm mimicking that of a type II isotherm. It is commonly seen in clay materials, or macroporous materials which are not completely saturated.
- H4 loops are similar to H3 except the adsorption isotherm mimics that are a type I and II isotherm, and a distinct gas uptake is seen at early pressures due to the filling of micropores.
- H5 loops are due to a mixture of partially and non blocked mesopores.

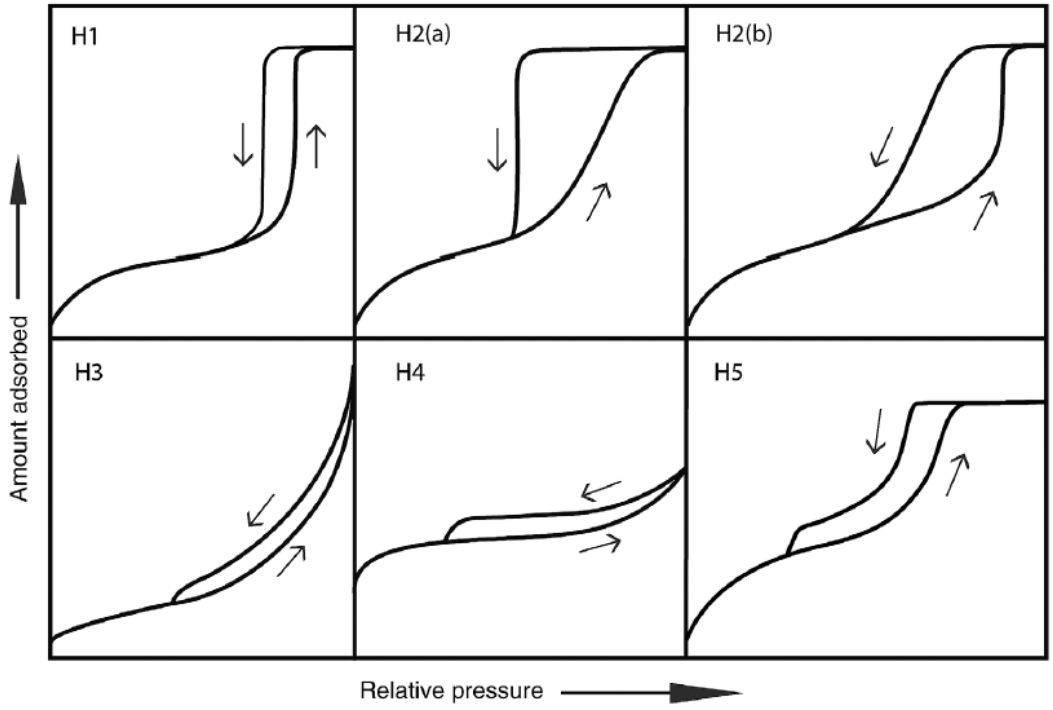

*Figure 1.11 Types of hysteresis loops. Image taken from Pure Appl. Chem., 2015, **87**, 1051–1069.*[118]

References

1 M. Höök and X. Tang, *Energy Policy*, 2013, **52**, 797–809.

2 M. Hoel and S. Kverndokk, *Resour. Energy Econ.*, 1996, **18**, 115–136.

3 G. Neri, M. Forster and A. J. Cowan, in *Issues in Environmental Science and Technology*, 2018, vol. 2019–Jan, pp. 184–209.

4 International energy agency, www.iea.org, (accessed 24 May 2019).

5 B. Zhang and L. Sun, *Chem. Soc. Rev.*, 2019, **48**, 2216–2264.

6 A. J. Bard and M. A. Fox, *Acc. Chem. Res.*, 1995, **28**, 141–145.

7 T. J. Jacobsson, V. Fjällström, M. Edoff and T. Edvinsson, *Energy Environ. Sci.*, 2014, **7**, 2056–2070.

8 C. K. Chan, H. Tüysüz, A. Braun, C. Ranjan, F. La Mantia, B. K. Miller, L. Zhang, P. A. Crozier, J. A. Haber, J. M. Gregoire, H. S. Park, A. S. Batchellor, L. Trotochaud and S. W. Boettcher, *Advanced and in situ analytical methods for solar fuel materials*, 2016, vol. 371.

9 C. Jiang, S. J. A. Moniz, A. Wang, T. Zhang and J. Tang, *Chem. Soc. Rev.*, 2017, **46**, 4645–4660.

10 K. A. Grice and C. P. Kubiak, *Recent Studies of Rhenium and Manganese Bipyridine Carbonyl Catalysts for the Electrochemical Reduction of CO2*, Elsevier Inc., 1st edn., 2014, vol. 66.

11 M. D. Sampson, A. D. Nguyen, K. a Grice, C. E. Moore, A. L. Rheingold and C. P. Kubiak, *J. Am. Chem. Soc.*, 2014, **136**, 5460–71.

12 C. Finn, S. Schnittger, L. J. Yellowlees and J. B. Love, *Chem. Commun.*, 2012, **48**, 1392–1399.

13 D. Boston, K.-L. Huang, N. de Tacconi, N. Myung, F. MacDonell and K. Rajeshwar, in *Photoelectrochemical Water Splitting: Materials, Processes and Architectures*, 2013, pp. 289–332.

14 J. Xing, W. Q. Fang, H. J. Zhao and H. G. Yang, *Chem. - An Asian J.*, 2012, **7**, 642–657.

15 P. Chowdhury, G. Malekshoar and A. Ray, *Inorganics*, 2017, **5**, 34.

16 K. Maeda, *ACS Catal.*, 2013, **3**, 1486–1503.

17 X. Chen, S. Shen, L. Guo and S. S. Mao, *Chem. Rev.*, 2010, **110**, 6503–6570.

18 *semiconductor*, IUPAC, Research Triagle Park, NC.

19 J. D. Yuen, A. S. Dhoot, E. B. Namdas, N. E. Coates, M. Heeney, I. McCulloch, D. Moses and A. J. Heeger, *J. Am. Chem. Soc.*, 2007, **129**, 14367–14371.

20 J. D. Rinehart, A. M. Schimpf, A. L. Weaver, A. W. Cohn and D. R. Gamelin, *J. Am. Chem. Soc.*, 2013, **135**, 18782–18785.

21 H. Liu, Y. Liu and D. Zhu, *J. Mater. Chem.*, 2011, **21**, 3335–3345.

22 Gratzel Michael, *Nature*, 2001, **414**, 338–344.

23 Q. Xu, L. Zhang, J. Yu, S. Wageh, A. A. Al-Ghamdi and M. Jaroniec, *Mater. Today*, 2018, **21**, 1042–1063.

24 A. Kudo and Y. Miseki, *Chem. Soc. Rev.*, 2009, **38**, 253–278.

25 L. M. Utschig, S. R. Soltau, K. L. Mulfort, J. Niklas and O. G. Poluektov, *Chem. Sci.*, 2018, **9**, 8504–8512.

26 A. J. Bard, *J. Photochem.*, 1979, **10**, 59–75.

27 P. Zhou, J. Yu and M. Jaroniec, *Adv. Mater.*, 2014, **26**, 4920–4935.

28 R. S. Sprick, J.-X. Jiang, B. Bonillo, S. Ren, T. Ratvijitvech, P. Guiglion, M. A. Zwijnenburg, D. J. Adams and A. I. Cooper, *J. Am. Chem. Soc.*, 2015, **137**, 3265–3270.

29 Y. Xu, N. Mao, C. Zhang, X. Wang, J. Zeng, Y. Chen, F. Wang and J. X. Jiang, *Appl. Catal. B Environ.*, 2018, **228**, 1–9.

30 C. Yang, B. C. Ma, L. Zhang, S. Lin, S. Ghasimi, K. Landfester, K. A. I. Zhang and X. Wang, *Angew. Chemie Int. Ed.*, 2016, **55**, 9202–9206.

31 R. Qin, J. Yang, P. Li, Q. Wu, Y. Zhou, H. Luo and F. Chang, *Sol. Energy Mater. Sol. Cells*, 2016, **145**, 412–417.

32 J.-X. Jiang, F. Su, A. Trewin, C. D. Wood, H. Niu, J. T. a Jones, Y. Z. Khimyak and A. I. Cooper, *J. Am. Chem. Soc.*, 2008, **130**, 7710–20.

33 D. Schwarz, A. Acharja, A. Ichangi, P. Lyu, M. V. Opanasenko, F. R. Goßler, T. A. F. König, J. Čejka, P. Nachtigall, A. Thomas and M. J. Bojdys, *Chem. - A Eur. J.*, 2018, **24**, 11916–11921.

34 A. G. Slater and A. I. Cooper, *Science*, 2015, 348, 8075–8075.

35 H. S. Choi, H. J. Jeon, J. H. Choi, G.-H. Lee and J. K. Kang, *Nanoscale*, 2015, **7**, 18923–18927.

36 Q. Shi, H. Sun, R. Yang, Z. Zhu, W. Liang, D. Tan, B. Yang, A. Li and W. Deng, *J. Mater. Sci.*, 2015, **50**, 6388–6394.

37 A. H. Alahmed, M. E. Briggs, A. I. Cooper and D. J. Adams, *J. Mater. Chem. A*, 2019, **7**, 549–557.

38 Y. Xu, S. Jin, H. Xu, A. Nagai and D. Jiang, *Chem. Soc. Rev.*, 2013, **42**, 8012.

39 D. J. Martin, P. J. T. Reardon, S. J. A. Moniz and J. Tang, *J. Am. Chem. Soc.*, 2014, **136**, 12568–12571.

40 C. Prasad, H. Tang and I. Bahadur, *J. Mol. Liq.*, 2019, **281**, 634–654.

41 S. Cao and J. Yu, *J. Phys. Chem. Lett.*, 2014, **5**, 2101–2107.

42 W.-J. Ong, L.-L. Tan, Y. H. Ng, S.-T. Yong and S.-P. Chai, *Chem. Rev.*, 2016, **116**, 7159–7329.

43 C. B. Nielsen, S. Holliday, H.-Y. Chen, S. J. Cryer and I. McCulloch, *Acc. Chem. Res.*, 2015, **48**, 2803–2812.

44 J. T. Kirner and R. G. Finke, *J. Mater. Chem. A*, 2017, **5**, 19560–19592.

45 L. Yao, A. Rahmanudin, N. Guijarro and K. Sivula, *Adv. Energy Mater.*, 2018, **8**, 1802585.

46 R. Li, W. Zhang and K. Zhou, *Adv. Mater.*, 2018, **30**, 1–31.

47 Z. Sun, T. Ma, H. Tao, Q. Fan and B. Han, *Chem*, 2017, **3**, 560–587.

48 M. Liu, L. Guo, S. Jin and B. Tan, *J. Mater. Chem. A*, 2019, **7**, 5153–5172.

49 V. D. Pokhodenko and V. A. Krylov, *Theor. Exp. Chem.*, 1994, **30**, 91–105.

50 W. R. Salaneck, R. H. Friend and J. L. Brédas, *Phys. Rep.*, 1999, **319**, 231–251.

51 S. Ling, S. Schumacher, I. Galbraith and M. J. Paterson, *J. Phys. Chem. C*, 2013, **117**, 6889–6895.

52 S. M. J. Rogge, A. Bavykina, J. Hajek, H. Garcia, A. I. Olivos-Suarez, A. Sepúlveda-Escribano, A. Vimont, G. Clet, P. Bazin, F. Kapteijn, M. Daturi, E. V. Ramos-Fernandez, F. X. Llabrés i Xamena, V. Van Speybroeck and J. Gascon, *Chem. Soc.*

Rev., 2017, **46**, 3134–3184.

53 K. H. Park, W. Kim, J. Yang and D. Kim, *Chem. Soc. Rev.*, 2018, **47**, 4279–4294.

54 F. Cacialli, J. S. Wilson, J. J. Michels, C. Daniel, C. Silva, R. H. Friend, N. Severin, P. Samorì, J. P. Rabe, M. J. O'Connell, P. N. Taylor and H. L. Anderson, *Nat. Mater.*, 2002, **1**, 160–164.

55 I. G. Austin and N. F. Mott, *Science*, 1970, **168**, 71–77.

56 T. P. Nguyen, *Mater. Sci. Semicond. Process.*, 2006, **9**, 198–203.

57 C. Schwarz, S. Tscheuschner, J. Frisch, S. Winkler, N. Koch, H. Bässler and A. Köhler, *Phys. Rev. B*, 2013, **87**, 155205.

58 R. Sebastian Sprick, Y. Bai, A. A. Y Guilbert, M. Zbiri, C. M. Aitchison, L. Wilbraham, Y. Yan, D. J. Woods, M. A. Zwijnenburg and A. I. Cooper, *Chem. Mater.*, 2018, **31**, 305–313.

59 R. S. Sprick, B. Bonillo, R. Clowes, P. Guiglion, N. J. Brownbill, B. J. Slater, F. Blanc, M. A. Zwijnenburg, D. J. Adams and A. I. Cooper, *Angew. Chemie - Int. Ed.*, 2016, **55**, 1792–1796.

60 Y. Xiang, X. Wang, L. Rao, P. Wang, D. Huang, X. Ding, X. Zhang, S. Wang, H. Chen and Y. Zhu, *ACS Energy Lett.*, 2018, **3**, 2544–2549.

61 C. Cheng, X. Wang, Y. Lin, L. He, J.-X. Jiang, Y. Xu and F. Wang, *Polym. Chem.*, 2018, **9**, 4468–4475.

62 G. Zhang, Z.-A. Lan and X. Wang, *Angew. Chemie Int. Ed.*, 2016, **55**, 15712–15727.

63 Q. Liu, Z. Tang, M. Wu and Z. Zhou, *Polym. Int.*, 2014, **63**, 381–392.

64 A. Dawson, Robert and Trewin, *Chapter 7 : Conjugated Microporous Polymers, in Porous Polymers: Design, Synthesis and Applications*, the Royal Society of Chemistry, Monographs., 2015.

65 A. I. Cooper, *Adv. Mater.*, 2009, **21**, 1291–1295.

66 S. Lin, C. S. Diercks, Y. Zhang, N. Kornienko, E. M. Nichols, Y. Zhao, A. R. Paris, D. Kim, P. Yang, O. M. Yaghi and C. J. Chang, *Science*, 2015, 349, 1208–1213.

67 S. Dalapati, S. Jin, J. Gao, Y. Xu, A. Nagai and D. Jiang, *J. Am. Chem. Soc.*, 2013, **135**, 17310–17313.

68 S. Bhunia, S. K. Das, R. Jana, S. C. Peter, S. Bhattacharya, M. Addicoat, A. Bhaumik

and A. Pradhan, *ACS Appl. Mater. Interfaces*, 2017, **9**, 23843–23851.

69 C. Wang, Y. V. Kaneti, Y. Bando, J. Lin, C. Liu, J. Li and Y. Yamauchi, *Mater. Horizons*, 2018, **5**, 394–407.

70 S. Zheng, X. Li, B. Yan, Q. Hu, Y. Xu, X. Xiao, H. Xue and H. Pang, *Adv. Energy Mater.*, 2017, **7**, 1–27.

71 S. Kempahanumakkagari, K. Vellingiri, A. Deep, E. E. Kwon, N. Bolan and K. H. Kim, *Coord. Chem. Rev.*, 2018, **357**, 105–129.

72 T. Zhang and W. Lin, *Chem. Soc. Rev.*, 2014, **43**, 5982–5993.

73 J. Lee, O. K. Farha, J. Roberts, K. A. Scheidt, S. T. Nguyen and J. T. Hupp, *Chem. Soc. Rev.*, 2009, **38**, 1450–1459.

74 H. V. Babu, M. G. M. Bai and M. Rajeswara Rao, *ACS Appl. Mater. Interfaces*, 2019, **11**, 11029–11060.

75 X. L. Zhang, L. Wang, L. Chen, X. Y. Ma and H. X. Xu, *Chinese J. Polym. Sci. (English Ed.*, 2019, **37**, 101–114.

76 Y. Kataoka, K. Sato, Y. Miyazaki, K. Masuda, H. Tanaka, S. Naito and W. Mori, *Energy Environ. Sci.*, 2009, **2**, 397–400.

77 C. G. Silva, I. Luz, F. X. Llabrés I Xamena, A. Corma and H. García, *Chem. - A Eur. J.*, 2010, **16**, 11133–11138.

78 J. Li, D. Luo, C. Yang, S. He, S. Chen, J. Lin, L. Zhu and X. Li, *J. Solid State Chem.*, 2013, **203**, 154–159.

79 S. Wang, W. Yao, J. Lin, Z. Ding and X. Wang, *Angew. Chemie - Int. Ed.*, 2014, **53**, 1034–1038.

80 Q. Liu, Z. X. Low, L. Li, A. Razmjou, K. Wang, J. Yao and H. Wang, *J. Mater. Chem. A*, 2013, **1**, 11563–11569.

81 O. Shekhah, J. Liu, R. A. Fischer and C. Wöll, *Chem. Soc. Rev.*, 2011, **40**, 1081–1106.

82 S. Kandambeth, A. Mallick, B. Lukose, M. V Mane, T. Heine and R. Banerjee, *J. Am. Chem. Soc.*, 2012, **134**, 19524–7.

83 C. R. Deblase, K. E. Silberstein, T. T. Truong, H. D. Abruña and W. R. Dichtel, *J. Am. Chem. Soc.*, 2013, **135**, 16821–16824.

84 W. Liu, Q. Su, P. Ju, B. Guo, H. Zhou, G. Li and Q. Wu, *ChemSusChem*, 2017, **10**, 664–669.

85 H. Wang, Z. Zeng, P. Xu, L. Li, G. Zeng, R. Xiao, Z. Tang, D. Huang, L. Tang, C. Lai, D. Jiang, Y. Liu, H. Yi, L. Qin, S. Ye, X. Ren and W. Tang, *Chem. Soc. Rev.*, 2019, **48**, 488–516.

86 V. S. Mothika, A. Räupke, K. O. Brinkmann, T. Riedl, G. Brunklaus and U. Scherf, *ACS Appl. Nano Mater.*, 2018, **1**, 6483–6492.

87 J. Lee, J. G. Kim and J. Y. Chang, *Sci. Rep.*, 2017, **7**, 1–8.

88 P. Lindemann, A. Schade, L. Monnereau, W. Feng, K. Batra, H. Gliemann, P. Levkin, S. Bräse, C. Wöll and M. Tsotsalas, *J. Mater. Chem. A*, 2016, **4**, 6815–6818.

89 Q. An, Y. Hassan, X. Yan, P. Krolla-Sidenstein, T. Mohammed, M. Lang, S. Bräse and M. Tsotsalas, *Beilstein J. Org. Chem.*, 2017, **13**, 558–563.

90 D. Wu, F. Xu, B. Sun, R. Fu, H. He and K. Matyjaszewski, *Chem. Rev.*, 2012, **112**, 3959–4015.

91 G. D. SCHOLES and G. RUMBLES, in *Materials for Sustainable Energy*, Co-Published with Macmillan Publishers Ltd, UK, 2010, vol. 5, pp. 12–25.

92 C. De Leener, E. Hennebicq, J. C. Sancho-Garcia and D. Beljonne, *J. Phys. Chem. B*, 2009, **113**, 1311–1322.

93 T. Tadesse, *J. Phys. Chem. Biophys.*, 2018, **08**, 1–6.

94 D. J. Woods, R. S. Sprick, C. L. Smith, A. J. Cowan and A. I. Cooper, *Adv. Energy Mater.*, 2017, **7**, 1700479.

95 L. Wang, R. Fernández-Terán, L. Zhang, D. L. A. Fernandes, L. Tian, H. Chen and H. Tian, *Angew. Chemie - Int. Ed.*, 2016, **55**, 12306–12310.

96 L. Li, R. G. Hadt, S. Yao, W. Y. Lo, Z. Cai, Q. Wu, B. Pandit, L. X. Chen and L. Yu, *Chem. Mater.*, 2016, **28**, 5394–5399.

97 S. Yanagida, T. Ogata, Y. Kuwana, Y. Wada, K. Murakoshi, A. Ishida, S. Takamuku, M. Kusaba and N. Nakashima, *J. Chem. Soc., Perkin Trans. 2*, 1996, 1963–1969.

98 J. T. Kirner, J. J. Stracke, B. A. Gregg and R. G. Finke, *ACS Appl. Mater. Interfaces*, 2014, **6**, 13367–13377.

99 J. T. Kirner and R. G. Finke, *ACS Appl. Mater. Interfaces*, 2017, **9**, 27625–27637.

100 F. Ronconi, Z. Syrgiannis, A. Bonasera, M. Prato, R. Argazzi, S. Caramori, V. Cristino and C. A. Bignozzi, *J. Am. Chem. Soc.*, 2015, **137**, 4630–4633.

101 D. Sun, D. Meng, Y. Cai, B. Fan, Y. Li, W. Jiang, L. Huo, Y. Sun and Z. Wang, *J. Am. Chem. Soc.*, 2015, **137**, 11156–11162.

102 E. R. Draper and D. J. Adams, *Chem*, 2017, **3**, 390–410.

103 H. Marciniak, X. Q. Li, F. Würthner and S. Lochbrunner, *J. Phys. Chem. A*, 2011, **115**, 648–654.

104 M. Burian, F. Rigodanza, N. Demitri, L. Dordević, S. Marchesan, T. Steinhartova, I. Letofsky-Papst, I. Khalakhan, E. Mourad, S. A. Freunberger, H. Amenitsch, M. Prato and Z. Syrgiannis, *ACS Nano*, 2018, **12**, 5800–5806.

105 Y. L. Wu, N. E. Horwitz, K. S. Chen, D. A. Gomez-Gualdron, N. S. Luu, L. Ma, T. C. Wang, M. C. Hersam, J. T. Hupp, O. K. Farha, R. Q. Snurr and M. R. Wasielewski, *Nat. Chem.*, 2017, **9**, 466–472.

106 J. J. Walsh, J. R. Lee, E. R. Draper, S. M. King, F. Jackel, M. A. Zwijnenburg, D. J. Adams and A. J. Cowan, *J. Phys. Chem. C*, 2016, **120**, 18479–18486.

107 E. R. Draper, J. R. Lee, M. Wallace, F. Jäckel, A. J. Cowan and D. J. Adams, *Chem. Sci.*, 2016, **7**, 6499–6505.

108 J. H. Oh, S. Liu, Z. Bao, R. Schmidt and F. Würthner, *Appl. Phys. Lett.*, 2007, **91**, 212107.

109 M. C. Nolan, J. J. Walsh, L. L. E. Mears, E. R. Draper, M. Wallace, M. Barrow, B. Dietrich, S. M. King, A. J. Cowan and D. J. Adams, *J. Mater. Chem. A*, 2017, **5**, 7555–7563.

110 A. S. Weingarten, R. V. Kazantsev, L. C. Palmer, D. J. Fairfield, A. R. Koltonow and S. I. Stupp, *J. Am. Chem. Soc.*, 2015, **137**, 15241–15246.

111 A. S. Weingarten, R. V. Kazantsev, L. C. Palmer, M. McClendon, A. R. Koltonow, A. P. S. Samuel, D. J. Kiebala, M. R. Wasielewski and S. I. Stupp, *Nat. Chem.*, 2014, **6**, 964–970.

112 A. Richter, G. Paschew, S. Klatt, J. Lienig, K. F. Arndt and H. J. P. Adler, *Sensors*, 2008, **8**, 561–581.

113 R. G. W. Norrish and G. Porter, *Nature*, 1949, **164**, 658–658.

114 R. Berera, R. van Grondelle and J. T. M. Kennis, *Photosynth. Res.*, 2009, **101**, 105–

118.

115 A. D. M. and A. Wilkinson, in *IUPAC Compendium of Chemical Terminology*, IUPAC, Research Triagle Park, NC, 2014, vol. 55, p. 932.

116 A. Z. Cardoso, L. L. E. Mears, B. N. Cattoz, P. C. Griffiths, R. Schweins and D. J. Adams, *Soft Matter*, 2016, **12**, 3612–3621.

117 H. Kumari, S. E. Armitage, S. R. Kline, K. K. Damodaran, S. R. Kennedy, J. L. Atwood and J. W. Steed, *Soft Matter*, 2015, **11**, 8471–8478.

118 M. Thommes, K. Kaneko, A. V. Neimark, J. P. Olivier, F. Rodriguez-Reinoso, J. Rouquerol and K. S. W. Sing, *Pure Appl. Chem.*, 2015, **87**, 1051–1069.

119 Micromeritics Instrument Corporation, Gas Adsorption Theory Poster, https://www.micromeritics.com/Repository/Files/Gas_Adsorption_Theory_poster.pdf, (accessed 18 June 2019).

“It is what it is”
Dr. Jamie Walsh

Chapter 2

A Conjugated Microporous Polymer For Electrocatalytic Carbon Dioxide Reduction

This work has been published: "A Conjugated Microporous Polymer For Electrocatalytic Carbon Dioxide Reduction” C. L. Smith, G. Neri, A. I. Cooper and A. J. Cowan, 2019, Sustainable Energy and Fuels.

2.1 Introduction

Molecular electrocatalysts for CO_2 reduction, based on transition-metal centres have been extensively explored, and catalysts that exhibit good selectivities towards carbon products and remarkable levels of activity with turn-over frequencies (TOFs) $>10^6$ are known.[1–3] A particularly attractive feature of molecular catalysts is that rational design is possible due to the well-defined nature of the catalyst. However, a general issue with many studies is that they are often studied when dissolved in organic solvents as homogenous catalysts. Frequently, a small amount of organic acid such as tetrafluoroethylene or water are added to act as a proton source to aid catalysis.[4,5] The large number of studies in organic solvents is due to the often poor solubility of the catalyst in aqueous media, the increased CO_2 solubility, and the ability to suppress undesired hydrogen evolution by tuning of the acid concentration. Although ideally, CO_2 electrocatalysts would be developed to have a high selectivity and activity in aqueous environments. For eventual deployment a sustainable source of H^+/e^- are required, and this is likely to be from water oxidation. Unfortunately, only a few homogeneous CO_2 reduction electrocatalysts are reported to be active in aqueous media,[1,6–9] however the fact that they have been known to exhibit Faradaic Efficiencies (FEs) as high as 98% for carbon based products[9] suggests that developing molecular electrocatalysts for use in water is a viable approach, Table 2.1.

Table 2.1 Some of the transition metal based electrocatalysts for CO_2 reduction that exhibit activity in aqueous media. GCE = glassy carbon electrode.

Catalyst	Electrolysis conditions	Overpotential (mV)	Major products	Faradaic efficiency (%)	Ref.
1. 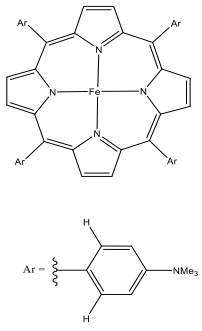	Aq. buffered 0.1 M KCl, pH 6.7, GCE	330	CO	98	[9]
2. 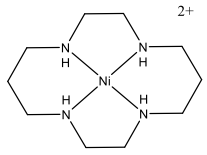	0.1 M KCl, GCE	770	CO	90	[8]

3. 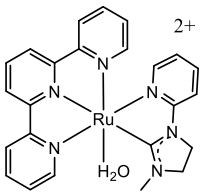	0.5 M $NaHCO_3$ aq. solution, , carbon cloth working electrode	670	CO	66	[7]
4. $[Fe_4N(CO)_{12}]^-$	Aq. buffered $KHCO_3/HCO_3^-$ pH 6.5, GCE	670	$HCOO^-$	96	[6]

An alternative approach to using homogenous molecular electrocatalysts is to attempt to directly reduce CO_2 on a metal or alloy electrode. Known metal electrodes for CO_2 reduction include Au, Ag, Zn, Pd, Hg, Sn, Cu and many metals have been shown to be effective catalytic surfaces able to achieve selectivity to CO or formate in water.[10] However, leading metal electrodes for CO production are based on costly elements (Au, Ag), and attempts to improve onset potentials are hampered by the inability to rationally design the active site. Therefore, the heterogenisation of molecular catalysts is an attractive option as it allows for a route to overcome such limitations. Such an approach also permits (i) experiments in aqueous media (for aqueous insoluble catalysts), (ii) easy product and reactant separation, (iii) improved electron transfer to the catalyst, and (iv) easy catalyst recycling.

There are three main families of molecular CO_2 reduction electrocatalysts are: (i) macrocyclic, (ii) phosphine and (iii) polypyridyl ligands and a full review of these is beyond the scope of this chapter, instead the reader is recommended the following excellent reviews.[3,11–14] Here we focus on bpy (2,2′-bipyridine) polypyridyl complexes containing metal centres such as, cobalt (Co), iron (Fe), rhenium (Re), manganese (Mn) and ruthenium (Ru) which have been shown to form particularly active catalysts for CO_2 reduction, and in particular on the heterogenisation of these catalysts.[1,2,15–17] Conjugated microporous polymers (CMPs) are also introduced, and a study of a CMP containing bpy sites which can be modified to contain a transition metal electrocatalyst based on the known solution electrocatalyst $[Mn(bpy)(CO)_3Br]$,[18] for CO_2 reduction is reported.

2.1.1 Mn molecular electrocatalysts for CO_2 reduction in solution

[*fac*-Re(bpy-R)$(CO)_3$Cl] (bpy-R = R groups substitution of bpy at the 4,4′- positions) and its analogues have been widely studied for CO_2 reduction to CO and formic acid (HCOOH), due to their facile synthetic modifications and reported excellent selectivities.[19,20]

From here onwards the *fac* label is omitted and instead geometry labels are included solely for *mer*-complexes. However, the natural abundance of rhenium is low and therefore limits practical application. In contrast, the Mn analogue, [Mn(bpy-R)$(CO)_3$Br], is based on abundant elements. Recently (2011) this complex has also been shown to be an excellent CO_2 reduction catalyst which has exhibited high catalytic turnover numbers (TONs),[3–5] and also a good selectivity in aqueous conditions at modest overpotentials as both a homogenous catalyst and when immobilised.[18,21–25]

The redox behaviour of [Mn(bpy-R)$(CO)_3$Br] was first reported by Hartl and co-workers over 20 years ago,[26] and several research groups have since further developed our understanding of the complex through the use of spectroelectrochemical techniques.[4,5,27–33] The mechanism is summarised in a recent review,[34] and key steps are shown in Figure 2.1. Under an inert argon atmosphere, in aprotic solvents such as acetonitrile (MeCN), [Mn(bpy)$(CO)_3$Br] displays two one electron reductions at -1.56 and -1.80$V_{Ag/AgNO3}$, (approx. -1.21 and -1.45 $V_{Ag/AgCl}$, the reference electrode that will be used in this study).[18] The first irreversible reduction at -1.56 $V_{Ag/AgNO3}$ is assigned to the loss of the labile bromide ligand. The subsequently formed [Mn(bpy)$(CO)_3$]$^{\bullet}$ species rapidly dimerizes (k_{dim} = 1.3 x 10^9 $M^{-1}s^{-1}$) at room temperature to form [Mn(bpy)$(CO)_3]_2$.[35] The second reduction at -1.80 $V_{Ag/AgNO3}$ results in dimer cleavage, forming [Mn(bpy)$(CO)_3]^-$. In a CV the return potential sweep shows the oxidation of [Mn(bpy)$(CO)_3]^-$ to reform [Mn(bpy)$(CO)_3]_2$, and then the oxidation of the dimer to form [Mn(bpy)$(CO)_3$X] at -1.39 and -0.51 $V_{Ag/AgNO3}$ (approx. -1.05 and -0.17 $V_{Ag/AgCl}$) respectively.[18] Here X represents that of either a bromide or solvent ligand, as when cycling through the potential window multiple times, a new reductive feature at -1.35 $V_{Ag/AgNO3}$ grows in due to the formation of the solvo-complex, [Mn(bpy)$(CO)_3$(MeCN)], as a result of ligand exchange. Intriguingly, it has been long known that during electrocatalytic reduction with [Re(bpy)$(CO)_3$Cl] that [Re(bpy)$(CO)_3]^-$ is formed (typically not *via* a dimerisation step) in two successive one electron reductions, is the active catalyst that binds CO_2, yet despite the formation of [Mn(bpy)$(CO)_3]^-$ being observed, early studies reported no catalytic activity with the Mn analogue.[29]

It was not until over 15 years after these initial spectroelectrochemical studies that Chardon-Noblat and Deronzier *et al.* reported how [Mn(bpy-R)$(CO)_3$Br], (R = H, or CH_3) could be used for electrocatalytic CO_2 reduction.[18,36] It was shown that when [Mn(bpy)$(CO)_3$Br] was reduced under a CO_2 atmosphere, no significant activity towards CO_2 reduction occurs, until a Brønsted acid (in the first studies H_2O) was added. In the presence of the acid and CO_2 a large increase in current density is observed at the second reduction, indicating that [Mn(bpy)$(CO)_3]^-$ can be an active electrocatalyst for CO_2 reduction.[18] It is now known that the Brønsted acid plays a key role in stabilising the initial formation of the M-CO_2

intermediate (where M represents the metal center).[31,37–39] The role of the acid strength has been investigated experimentally in work by Smieja *et al.* using [Mn(bpy-*t*Bu)(CO)$_3$Br] in the presence of a range of acids of differing pKa's (MeOH > 2,2,2-trifluoroethanol (TFE)~H_2O).[40] They saw that the stronger Brønsted acid gave the highest stabilisation of charge on Mn(I)-CO_2, resulting in greater current densities and higher TOFs. Although the trend mirrored that seen for [Re(bpy-*t*Bu)(CO)$_3$Br] with 100 ± 15% CO FE, activity of [Mn(bpy-*t*Bu)(CO)$_3$Br] was superior, with a 60% increase in TOF in MeCN with 1.4 M TFE, and a 400 mV reduction in overpotential.[18,40] Subsequently, numerous other groups, including our own[31,39] have shown experimentally[5,40] and computationally[37,41,42] that the strength of the acid actually controls not just the initial CO_2 binding, but also the pathway of catalysis, Figure 2.1. Following protonation of the M-CO_2 adduct to form M-CO_2H, by either electron transfer (reduction first) or protonation and cleavage of one of the CO bonds, where H_2O evolution also (protonation first) occurs, with the balance between the two being acid and potential dependent, Figure 2.1.[40,43,44] Remarkably, recent works have now modified the bpy ligand to incorporate a local proton source, which has enabled dominant activity, from the lower overpotential protonation first pathway, and even catalytic activity (albeit it short-lived) in the absence of an external proton source.[42,45–47]

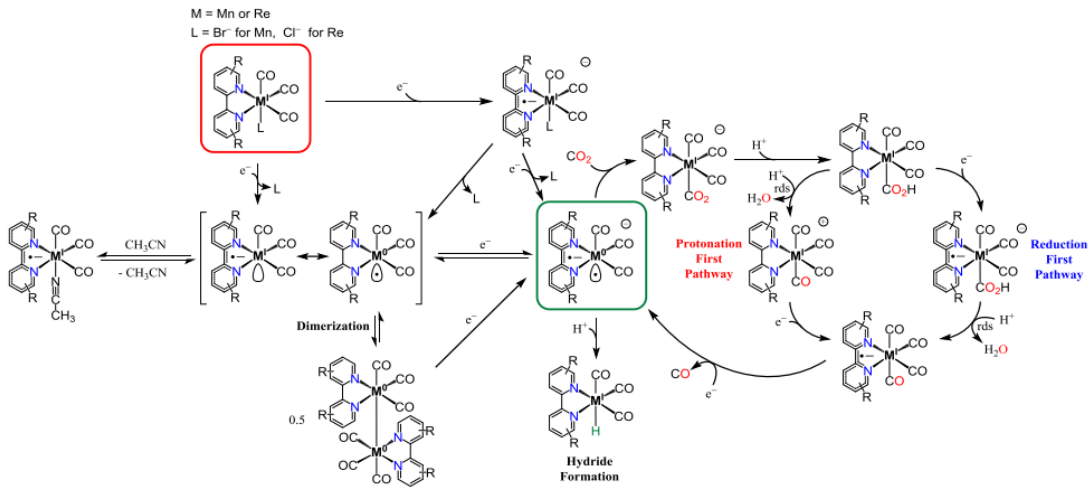

*Figure 2.1 Reaction mechanism for [Mn/Re(bpy-R)(CO)$_3$Br] (red box) when under a CO_2 atmosphere in the presence of a proton source, whereby reduction can occur via a protonation first pathway (red) and a reduction first pathway (blue). The catalytically active species, [M^0(bpy•$^-$)(CO)$_3$]$^-$, is highlighted in a green box. Figure reproduced from Coord. Chem. Rev., 2018, **374**, 173–217.*[34]

Interestingly, some studies have also shown an increase in current under CO_2 prior to the potential at which [Mn(bpy)(CO)$_3$]$^-$ is electrochemically formed.[5,37] Early works by Deronzier demonstrated that using [Mn(bpy-Me)(CO)$_3$]$_2$ (where bpy-Me is 4,4′-dimethyl-2,2′-bipyridine), CO_2 reduction could also occur without the formation of [Mn(bpy-Me)(CO)$_3$]$^-$ *via*

a dimer first pathway,[48] Figure 2.2. Similar behavior has also been proposed by several other groups, and recently Neri *et al.* confirmed that this third reduction pathway, also takes place with $[Mn(bpy)(CO)_3]_2$ through the use of in-situ vibrational sum frequency generation spectroscopy.[31] Again, it has been shown that for $[Mn(bpy)(CO)_3]_2$ to interact with CO_2 the Brønsted acid plays a key role in enabling this lower overpotential pathway for CO_2 reduction.[31] However, although catalysis is possible by direct interaction of the CO_2/H^+ with the dimer, the reported TOFs are well below those achieved following the generation of $[Mn(bpy)(CO)_3]^-$.[48]

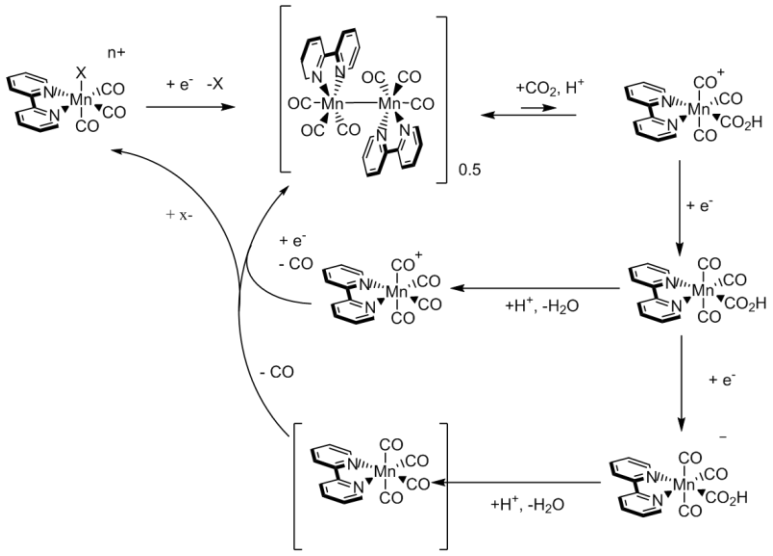

*Figure 2.2 Possible reaction mechanisms for [Mn(bpy-R)(CO)₃Br] when under a CO_2 atmosphere in the presence of a proton source where CO_2 reduction is proposed to go via the dimer. Figure adapted from Phys. Chem. Chem. Phys., 2019, **21**, 7389–7397.*[31]

Although the overpotential for CO_2 reduction by $[Mn(bpy\text{-}R)(CO)_3Br]$ is significantly smaller than its Re analogue, it has been proposed that the need to generate the active catalyst ($[Mn(bpy)(CO)_3]^-$) by the formation and subsequent reduction of $[Mn(bpy)(CO)_3]_2$ is undesirable[4,40] Therefore, several groups have been working on elimination of dimer formation with the anticipation that it will enable the generation of $[Mn(bpy)(CO)_3]^-$ at more positive potentials, and offer improved TOFs for catalysis at more moderate overpotentials. In particular, sterically bulky groups have been added to the bpy with complexes containing ligands such as 6,6′-dimesityl-2,2′-bipyridine (mesbpy) being developed to prevent two Mn center's from coming into close contact.[4] In this previous work a single reduction at -1.55 $V_{Fc+/Fc}$ (approx. -1.13 $V_{Ag/AgCl}$) in MeCN was reported for the formation of $[Mn(mesbpy)(CO)_3]^-$, *via* two one electron steps with reduction of the initially formed $[Mn(mesbpy)(CO)_3]^{\bullet}$ occurring at potentials positive of the starting material. However, although dimerisation was prevented, the overpotential for catalysis was not initially

improved. $[Mn(mesbpy)(CO)_3]^-$ was generated 300 mV positive of the potential required for $[Mn(bpy)(CO)_3]^-$ formation, but CO_2 reduction to CO only occurred ~400 mV negative of the potential at which $[Mn(mesbpy)(CO)_3]^-$ was electrochemically formed.[4] Only when a third electron was introduced *via* a bpy based reduction, at more negative overpotentials (-2.01 $V_{Fc+/Fc}$, approx. -1.58 $V_{Ag/AgCl}$), did catalysis occur.[4] Although preventing dimerisation did not aid the overpotential the TOF of the catalyst was improved, with the TOF = 5000 s^{-1} for CO_2 to CO (MeCN with 0.3 M TFE) being significantly higher than for other $[Mn(bpy\text{-}R)(CO)_3Br]$ catalysts. Building on work by Savéant and co-workers who previously reported improved stability and an increased rate in CO_2 reduction in the presence of Mg^{2+}, which acted as a Lewis acid when used with an iron tetraphenylporphyrin CO_2 reduction catalyst,[49] studies with $[Mn(mesbpy)(CO)_3Br]$ in the presence of Mg^{2+} were carried out.[5] These showed a ten-fold increase in TOF and the lowest overpotential for homogeneous electrocatalysts for CO_2 reduction (300 - 450 mV).[5]

An alternative approach to prevent dimerisation is through modification of the axial binding site. Replacement of the bromide ligand with a cyano (CN) group in place minimises axial ligand loss[50] and prevents $[Mn(bpy)(CO)_3]^0$ generation, which would otherwise rapidly dimerise. Solution phase electrochemistry in MeCN showed the presence of two reductions at -1.94 and -2.52 $V_{Fc+/Fc}$ (approx. -1.52 and -2.09 $V_{Ag/AgCl}$), assigned to ligand based reductions of the bpy and CN respectively, leading to the generation of $[Mn(bpy)(CO)_3]^-$ (Figure 2.3).[50] Although dimerization was prevented, formation of the catalytically active species occurred *ca.* 650 mV more negative than for $[Mn(bpy)(CO)_3Br]$. Again, although a large overpotential of *ca.* 1350 mV for CO_2 reduction to form CO was required, the catalyst exhibited good activity and selectivity with a 98% FE for CO.[50]

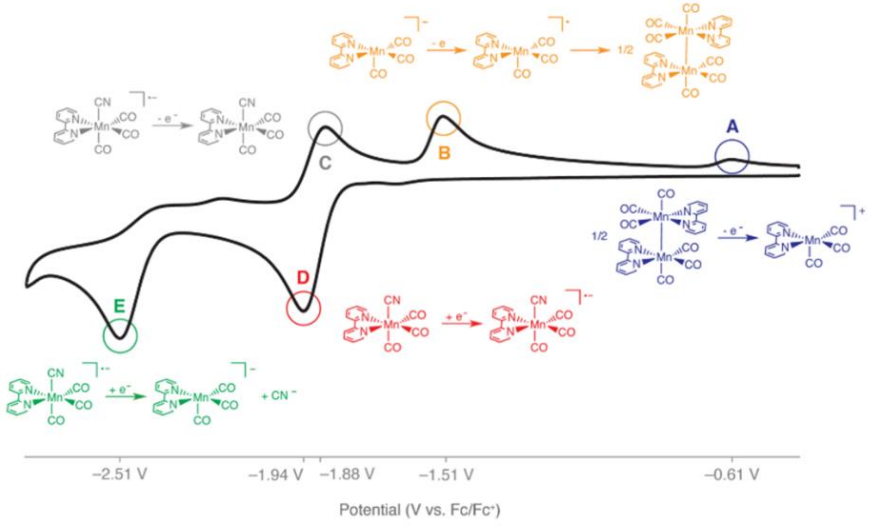

*Figure 2.3 CV of 1 mM $[Mn(bpy)(CO)_3CN]$ in MeCN with 0.1 M TBAP supporting electrolyte recorded at a scan rate of 100 mVs^{-1} under a CO_2 atmosphere, with the assigned mechanisms to each reduction. Figure was reproduced from Inorg. Chem., 2015, **54**, 8849–8856.*[50]

2.1.2 Heterogenised Mn catalysts for CO_2 conversion in water

There are relatively few known molecular electrocatalysts for CO_2 reduction that show activity when dissolved in water, most have been studied in organic media.[9,51–54] As noted above immobilisation of the catalyst onto the electrode offers a way to study otherwise aqueous insoluble molecules. Immobilisation of a [Re(bpy)$(CO)_3$Br] CO_2 reduction catalyst was reported by Yoshida *et al.* in 1993, where the complex was incorporated into a Nafion solution, spread onto a carbon electrode and allowed to dry in air.[55] Due to the ease of fabrication, and good stability of the immobilised electrode, the use of a supporting polymer such as Nafion has been widely used in multiple similar studies.[21,55,56] Yoshida *et al.* saw *ca.* 2:1 selectivity for CO_2 reduction (CO:H_2) in 60 mM phosphate buffer pH 7, unlike for homogenous catalysis of [Re(bpy)$(CO)_3$Br] in MeCN which has 100% selectivity.[55] Although, the immobilisation of the catalyst resulted in greater activity (TOF = 166 h^{-1}) when compared to in an MeCN solution (TOF = 21 h^{-1}), the electrode was limited by a lack of electroactive catalyst (~5%) within the membrane.[55] The vast majority of the Re complex deposited was inactive, and thought to be due to formation of large clusters of the catalyst upon drying. Nafion is an excellent cation/proton conductor,[57] however it does not provide an electroactive support making it possible for clusters of catalysts to become electrically isolated.

The first studies on [Mn(bpy)$(CO)_3$Br] in water were carried out within the Cowan group, in part by myself.[21,22] As the Mn catalysts require the use of a suitably strong acid for CO_2 reduction, Nafion membranes were hoped to also have a catalytic role, in addition to aiding immobilisation. A similar immobilisation method to that used by Yoshida was employed, and we were surprised to find that similar to solution phase electrochemistry, even when in Nafion, [Mn(bpy)$(CO)_3$Br] underwent rapid ligand loss and dimerisation.[21] Indicating that either diffusion of the catalyst occurs within the membrane, or in-line with the suggestions of Yoshida *et al.* the catalyst aggregates upon drying, resulting in [Mn(bpy)$(CO)_3$Br] residing close enough to each other permitting dimerisation.[55] Controlled potential electrolysis (CPE) of a Nafion/[Mn(bpy)$(CO)_3$Br] membrane, showed a 2:1 selectivity to CO:H_2 for potentials as low as -1.3 $V_{Ag/AgCl}$ at pH 7 in phosphate buffer with good stability over a 20 hour time frame.[21] Although, as previously reported by Yoshida *et al.* the system was limited by a lack of electroactive content of the catalyst. This was partially overcome by the addition of multi-walled carbon nanotubes (NTs) into the Nafion/[Mn(bpy)$(CO)_3$Br] membrane, where a ratio 1:1 of catalyst:NTs showed optimal activity.[21] Although the addition of NTs to the membrane resulted in *ca.* 10 fold current enhancement, *ca.* 100 mV more positive onset for CO production, and an increase in electroactive content from 0.25% to 11%, the electroactive content was still relatively low and the overall TON only reached a maximum of 101.[21] Further studies looked at modification of the bpy ligand in the 4,4′ position with electron withdrawing

(EWG) and donating (EDG) groups to examine how functionalisation could change the Mn reduction potentials and overpotential for CO_2 reduction for the immobilised catalyst.[22] The incorporation of an EWG (-COOH) to [Mn(bpy-R)$(CO)_3$Br] shifted the reduction potentials positive, however when immobilised within a NT/Nafion membrane little selectivity towards CO_2 reduction was seen.[22] Interestingly, [Mn(bpy-COOH)$(CO)_3$Br] is soluble in water and as a homogenous catalyst between pH 7-9 it was active with good selectivity towards CO_2 of 65 ± 15%.[23] Addition of EDG, such as tertiary butyl, to [Mn(bpy-R)$(CO)_3$Br]/NT/Nafion membrane gave a selectivity of ~1.04 for CO : H_2 as opposed to ~0.28 for the parent [Mn(bpy-H)$(CO)_3$Br] system, but improved TOFs.[22]

Immobilisation has also been achieved through the π-π bonding interactions between NTs and a Mn complex modified with a pyrene anchoring group, [Mn(bpy-pyr)$(CO)_3$Br], Figure 2.4.[24] For this study electrodes were prepared by drop casting NTs in *N*-methylpyrrolidone onto a glassy carbon electrode (GCE), once dry the electrode was immersed in an anhydrous solution of [Mn(bpy-pyr)$(CO)_3$Br] in DMF for 30 minutes. Product analysis under CO_2 showed CO and formate as the carbon-based products, although proton reduction to form H_2 was the dominant product. However, the electrodes did show good stabilities with TONs of up to 1790 ± 290 and 3920 ± 230 for CO and formate respectively being achieved at *ca.* -1 $V_{Ag/AgCl}$, which are far superior to those previously reported for an immobilised [Mn(bpy)$(CO)_3$Br] catalyst.[24] Interestingly, by altering the loading of [Mn(bpy-pyr)$(CO)_3$Br] a change in product selectivity was observed. Low [Mn(bpy-pyr)$(CO)_3$Br] loadings resulted in high levels of formate production, whilst higher loadings gave rise to CO as the main CO_2 reduction product.[24] The authors rationalised this as being the result of two different catalytic pathways, where low catalyst loadings resulted in the formation of a Mn-hydride complex, identified by in-situ FTIR SEC (Figure 2.4), which gave rise to formate following CO_2 binding. In contrast, at high concentrations dimer formation can occur enabling CO production.

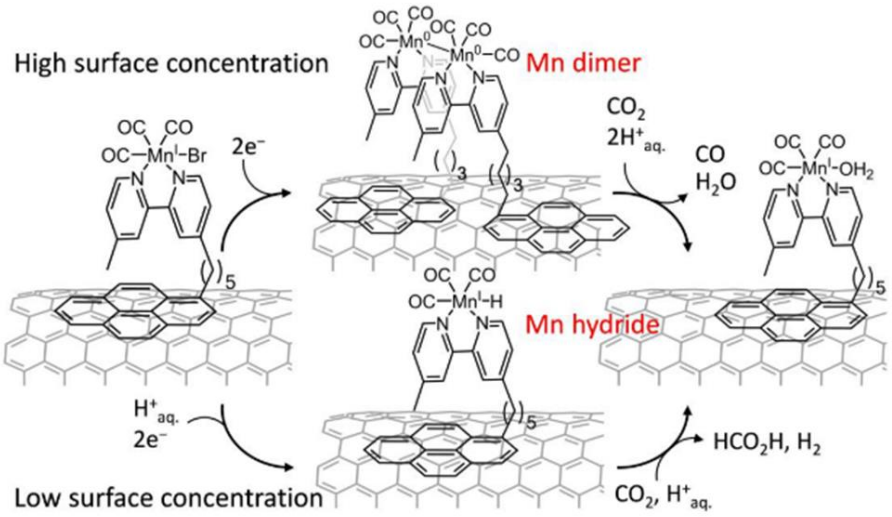

Figure 2.4 Concentration dependent proposed mechanism for CO_2 using [Mn(bpy-pyr)(CO)$_3$Br] immobilised onto NTs via π-π interactions with a pyrene linker. Figure reproduced from J. Am. Chem. Soc., 2017, ***139****, 14425–14435.*[24]

Immobilisation of CO_2 reduction molecular catalysts by polymerisation of functional groups attached to the bpy ligand is also a popular approach, and has commonly been achieved *via* electropolymerisation.[58,59] Meyer and co-workers were the first to report electropolymerisation of pyridine complexes containing metal centres for CO_2 reduction.[60–62] Electrode fabrication was achieved by modifying the bpy ligand in [Re(bpy)(CO)$_3$Cl] with a vinyl group. Cycling the potential from *ca.* 0 V to – 1.65 $V_{Ag/AgCl}$ resulted in a polymerised film on the surface of the electrode. They saw an increase in stability and reactivity towards CO_2 in comparison to homogenous studies, demonstrated by an increase in TON to 516 from *ca.* 20. However, undesirable side reactions from the formation of vinyl radicals upon electropolymerisation have led to film degradation.[59] Similar studies have been reported with Mn derivatives with bpy ligands modified with pyrrole groups.[63]

2.1.3 Porous polymer frameworks for catalysis

Immobilisation of the Mn catalyst onto supports has been a successful route to making active electrodes for CO_2 reduction in water. However, in the majority of cases studied the complex is still able to undergo dimerisation following the first one-electron reduction. Furthermore, partial current densities for CO and $HCOO^-$ formation have been relatively low, due to a combination of low concentrations of electroactive species on the support electrodes, and also possibly the low concentration of CO_2 within the structure of the immobilised materials. In principle, the ability to bind a catalyst into a conductive framework could allow for improved electroactive contents, and potentially enhanced catalytic activity when compared to solution based electrocatalysis.[64] Additional advantages may also occur. First the use of well-defined molecular catalytic centres that are synthetically addressable may combine

the advantages of homogenous electrocatalysts with heterogenous catalysts (e.g. recycling, product separation). Second, the high surface area of a porous conductive framework offers increased surface areas, and in some cases the framework can be designed to concentrate reactants (e.g. CO_2 capture) or exclude possible poisons. Therefore, covalent binding of [Mn(bpy-R)$(CO)_3$Br] into the rigid structural framework of a porous molecular solid[65] is of particular interest, both as a strategy to prevent dimerisation and as a way to improve the level of CO_2 catalysis.[56,66]

Crystalline porous frameworks such as metal organic frameworks (MOFs) and covalent organic frameworks (COFs) have begun to receive significant levels of interest for both the photo- and electrocatalytic reduction of CO_2.[64,67–71] However, even though MOFs and COFs have been extensively used in solar fuel generation applications,[71,72] they are hindered by their long-term instability.[73–75] Therefore we also discuss porous polymers constructed by the cross-coupling reactions of aromatic building blocks which give rise to a high degree of conjugation. These materials, known as conjugated microporous polymers (CMPs), can be tuned again through ligand design,[76,77] and through the selection of monomer struts of different sizes and chemical functionalities, it is possible to achieve fine control over the porosity, surface area and gas sorption properties of the resulting polymer.[76,78–83] Importantly, CMPs typically exhibit excellent stability making them ideal candidates for their applications in solar fuel generation. Although CMPs have been studied for use in a wide range of applications including gas storage, heterogeneous catalysis,[56,64,67,84,85] photocatalysis[72,86–89] and energy storage[90–93] there is limited literature precedence for electrocatalytic CO_2 reduction. Therefore following a brief summary of MOF/COF catalysts for CO_2 reduction, focusing on Re and Mn systems, CMP materials as potential electrocatalysts are introduced in the following section.

The first reported MOF-CO_2 electrocatalyst of which we are aware was by Hinogami *et al.* in 2012, where copper ethanedithioamidate was incorporated into a MOF, which achieved a FE >98% for formate production.[66] Since this report, the incorporation of metal porphyrins into porous materials has gained interest with a number of porphyrin and related catalysts being studied within MOFs,[94–96] and these are thoroughly discussed in a recent review.[97] Of particular relevance to the work reported here is a study from 2016 by Sun *et al.* where [Re(bpy)$(CO)_3$Cl] was incorporated into a MOF framework, following modification of the bpy ligand in the 5,5′ position with carboxylic acid groups allowing for attachment to the Zn nodes.[98] Thin film electrodes were prepared *via* sequentially spray coating ethanolic solutions of Zn acetate and [Re(bpy-COOH)$(CO)_3$Cl] onto conductive glass (FTO). Electrochemical analysis in MeCN with 0.1 M tetrabutylammonium hydroxide (TBAH) as the supporting electrolyte showed an initial bpy based reduction (-0.9 $V_{Ag/AgCl}$), followed by reduction of the Re metal centre and loss of Cl ligand (*ca.* -1.1 $V_{Ag/AgCl}$). Importantly under

CO_2 a drastic increase in current density was observed indicating CO_2 reduction.[98] Current densities up to 2.5 mA.cm^{-2} were achieved, with a FE of 93 ± 5% for CO production and a TON of 580 after 2 hours of bulk electrolysis at *ca.* -1.8 $V_{Ag/AgCl}$.[98] The FE obtained is one of the highest for MOF and COF based systems thus far. However, degradation of the MOF was apparent during CPE measurements indicated by a decrease in current over time.[98] Recently, Marinescu and co-workers have explored to the use of COFs for heterogeneous catalysis, as they have greater electrical conductivity and possess good stability in water under harsh acidic and basic conditions.[67] [Re(bpy)$(CO)_3$Cl], Co and Iron (Fe) porphyrins were each incorporated into COF structures to produce, COF-Re, COF-Re-Co and COF-Re-Fe respectively (Figure 2.5a), and drop cast onto carbon fabric and left to dry.[67] CPE was carried out in pH 7 aqueous phosphate buffer under a CO_2 atmosphere for one hour at -1.3 $V_{Ag/AgCl}$. However, the metallated COFs exhibited little to no activity towards CO_2 reduction with the bimetallic COF-Re-Co, which showed the most activity and a 18 ± 2% FE for CO and 55 ± 5% for H_2.[67] A significant factor behind the low activity was proposed to be the presence of multiple reductions on multiple different metal sites inhibiting CO_2 reduction, due to a competition of electrons preventing the generation of the doubly reduced catalytically active species, hence favouring H_2 evolution.[67] Additionally, although relatively modest Brunauer-Emmett-Teller (BET) surface areas < 700 m^2g^{-1} were reported for the COF systems, the small pore sizes of both systems, COF-Re and COF1-Re, may have also been limited by diffusion of CO_2 and/or products through the structures. FEs were later improved by the incorporation of [Re(bpy)$(CO)_3$Cl] into COF1 (Figure 2.5b). In this study a carbon ink method was used to immobilise COF1-Re onto the surface of a GCE, where it was mixed with carbon black and poly(vinylidene fluoride) in *N*-methyl-2-pyrrolidone.[64] An optimised current density of 2.2 mA cm^{-2} was achieved at the relatively negative potential of -2.37 $V_{Ag/AgCl}$ when 29.38 wt% Re was incorporated into COF1. However, after 30 minutes of CPE the FE decreased from a maximum value of 81%.[64] This was attributed to an instability of the catalyst under prolonged CPE measurements.

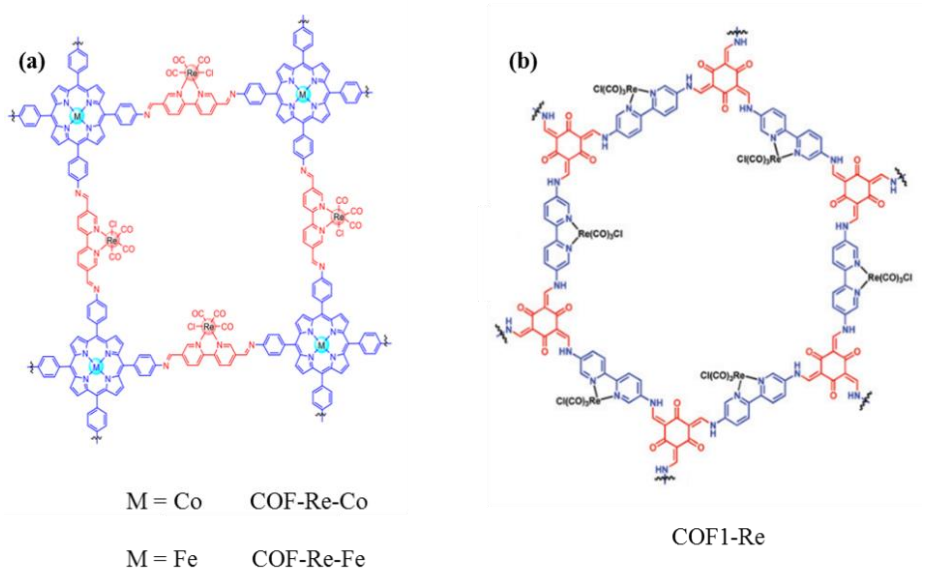

*Figure 2.5 The structure of two COFs used to immobilise [Re(bpy)(CO)$_3$Cl], with (a) and without (b) a second metal center. Figure adapted from Dalt. Trans., 2018, **47**, 17450–17460 and ACS Appl. Mater. Interfaces, 2018, **10**, 37919–37927 respectively.*[64,67]

A porous polymer (UiO-67 = $Zr_6O_4(OH)_4(bpdc)_6$) incorporated with a CO_2 reduction catalyst, [Re(dcbpy)(CO)$_3$Br] (dcbpy = 2,2′-bipyridine-5,5′-dicarboxylic acid), for photocatalyst was also reported in 2011 by Lin and co-workers for CO_2 photocatalysis (Figure 2.6).[73] A TON of 5 was reported for CO, with good selectivity in comparison to H_2 (10:1) when irradiated for 6 hours under >300 nm light source in acetonitrile with 5% trimethylamine (TEA) as a sacrificial electron donor.[73] Recyclability measurements of the catalyst showed that after 20 hours of irradiation 43.6% of Re had leached from UiO-67-Re.[73]

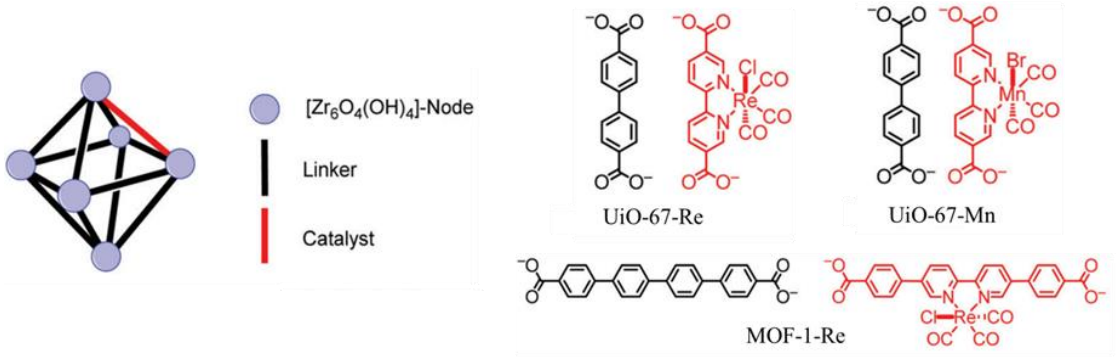

*Figure 2.6 Schematic diagram of the UiO-67 framework showing the $[Zr_6O_4(OH)_4]^{-}$ nodes (purple circles), linker units (black) and catalyst units (red) for the immobilisation of [M(bpy-R)(CO)$_3$Br] where M = Mn or Re. Figure adapted from Chem. Soc. Rev., 2017, **46**, 761–796.*[3]

[Mn(bpy)(CO)$_3$Br] derivatives have also been incorporated into other polymeric frameworks for use in photocatalysis,[75,89] although to the best of our knowledge they have not been applied as MOF or COF electrocatalysts. The immobilisation of [Mn(bpy-CO_2H)(CO)$_3$Br] into UiO-67 (UiO-67-Mn) was later reported by Kubiak and Cohen.[89] They

found UiO-67-Mn to be an active CO_2 photocatalyst to formate when a suitable sensitizer ([Ru(4,4′-dimethyl-2,2′-bipyridine)$_3$]$^{2+}$) and sacrificial electron donor (1-benzyl-1,4-dihydronicotinamide, BNAH) is present (Figure 2.6).[99] TONs of 110 were achieved after 18 hours under 470 nm irradiation, significantly higher than those reported for [Mn(bpy-R)(CO)$_3$Br] analogues under the same experimental conditions, demonstrating the high activity of [Mn(bpy-CO_2H)(CO)$_3$Br] when immobilised.[99] Stability measurements were performed by reusing UiO-67-Mn, and showed that after three 4 hour cycles activity was largely retained with a decrease in TON from 24 to 17.[99] The loss in activity was due to loss of CO ligands form Mn centres and degradation of UiO-67 when under prolong visible light exposure and alkaline experimental solution, which was confirmed by FTIR and Inductively Coupled Plasma-Optical Emission Spectrometry (ICP-OES) studies.[99]

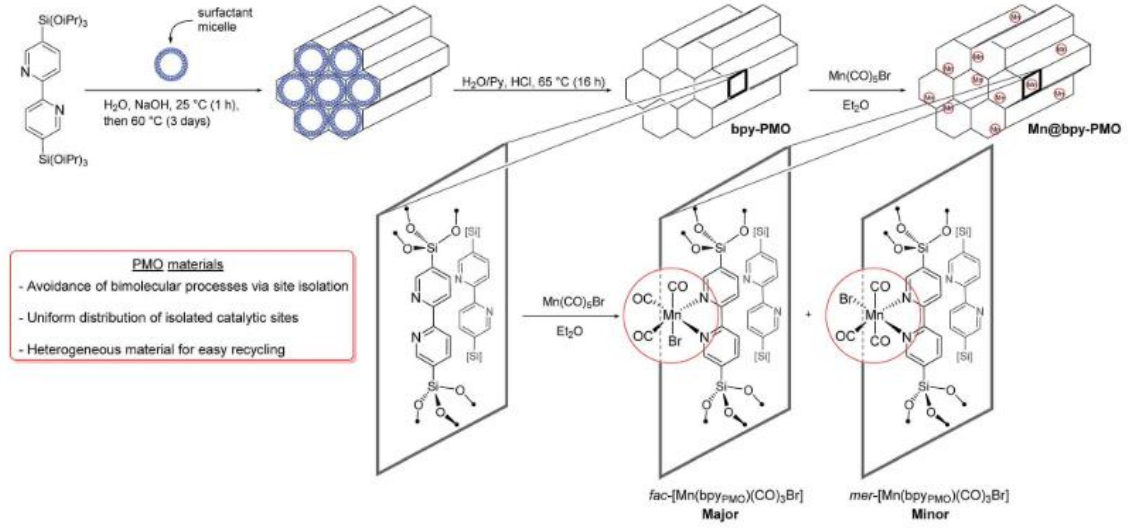

Figure 2.7 Synthetic pathway to Mn@bpy-PMO. Figure reproduced from Chem. Sci., 2017, ***8****, 8204–8213.*[75]

More recently, immobilisation of [MnBr(CO)$_3$] units at bpy sites within a periodic mesoporous organosilica (PMO), Mn@bpy-PMO, has been reported, Figure 2.7. Similarly to MOFs, PMOs exhibit high surface areas, uniform pores and are robust. Surprisingly, immobilisation of Mn into the bpy-PMO framework resulted in the formation of both the *fac*- and *mer*- isomers.[75] By adjusting the ratio of photosensitizer ([Ru(bpy)$_3$]Cl$_2$) and a sacrificial electron donor (1,3-dimethyl-2-phenyl-2,3-dihydro-1H-benzoimidazole, BIH) under visible light irradiation and catalyst loading, working experimental conditions were optimised. An excellent selectivity for carbon based products was reported and TONs of 168, 292 and 72 were also achieved for CO, formate and H_2 respectively after 16 hours of irradiation.[75] Recyclability studies showed that by separating and washing Mn@bpy-PMO the catalyst could be reused, and after 3 cycles of 5 hours of irradiation TONs of 484 and 239 for formate and CO were reached.[75] The photo-generation of formate and CO was rationalised by the

presence of two parallel reduction pathways; (i) *via* the formation of the hydride species or (ii) the binding of CO_2 to the Mn metal centre respectively and is shown in Figure 2.8.[75]

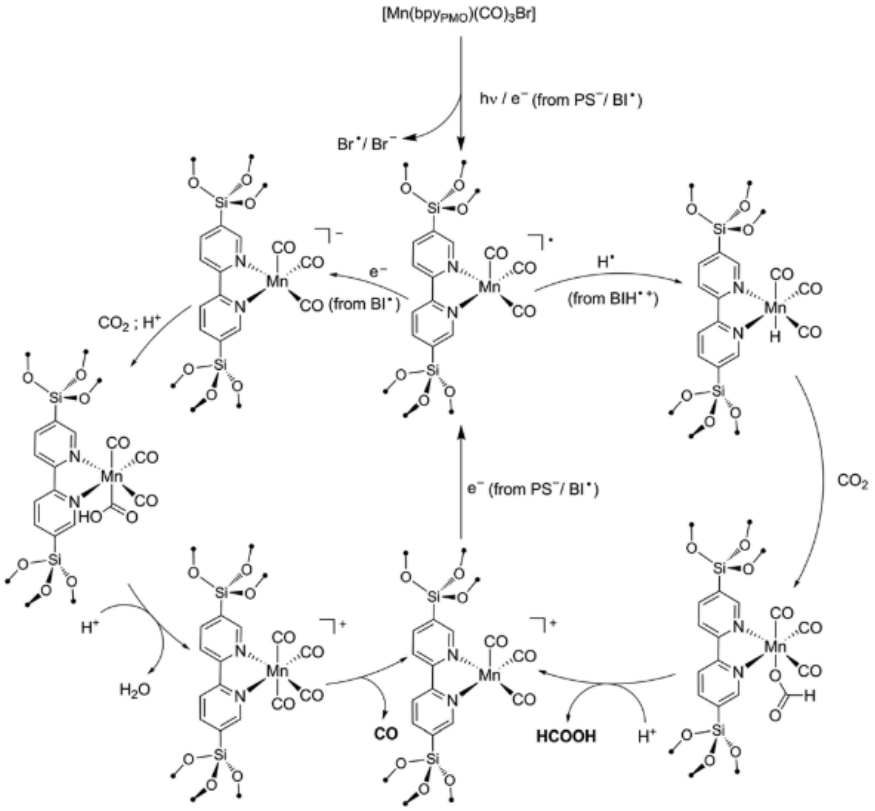

*Figure 2.8 Proposed mechanisms for two parallel photocatalytic CO_2 reduction pathways to form formate and CO with Mn@bpy-PMO. Figure taken from Chem. Sci., 2017, **8**, 8204–8213.*[75]

Modifications of the MOF framework have also been explored to improve CO_2 photocatalysis. UiO-67 was shown to be unstable in solution and when under prolonged visible light irradiation. Furthermore, activity was limited by the small pores restricting diffusion of products and reactants through the structure. In an attempt to overcome such limitations, Lin and co-workers have explored the use of an elongated modified linker unit in UiO-67 (MOF-1), Figure 2.6.[100] After 6 hours of irradiation with a 410 nm LED selective conversion of CO_2 to CO was achieved in an MeCN/TEA solvent were TONs of 0.40 and 6.44 for H_2 and CO respectively were reported.[100] By changing the solvent from MeCN to THF the selectivity was altered with TONs of 4.15 and 0.32 for H_2 and CO respectively being met.[100] However, decomposition of MOF-1-Re was still observed due to partial hydrogenation of the bpy ligand resulting in leaching of Re.[100] Addition of $–NH_2$ functional groups to MOF linker units has also been shown to improve photocatalytic activity for CO_2 reduction due to

intermolecular stabilisation of the initially formed carbamate with $–NH_2$ ligands as shown in Figure 2.9.[74]

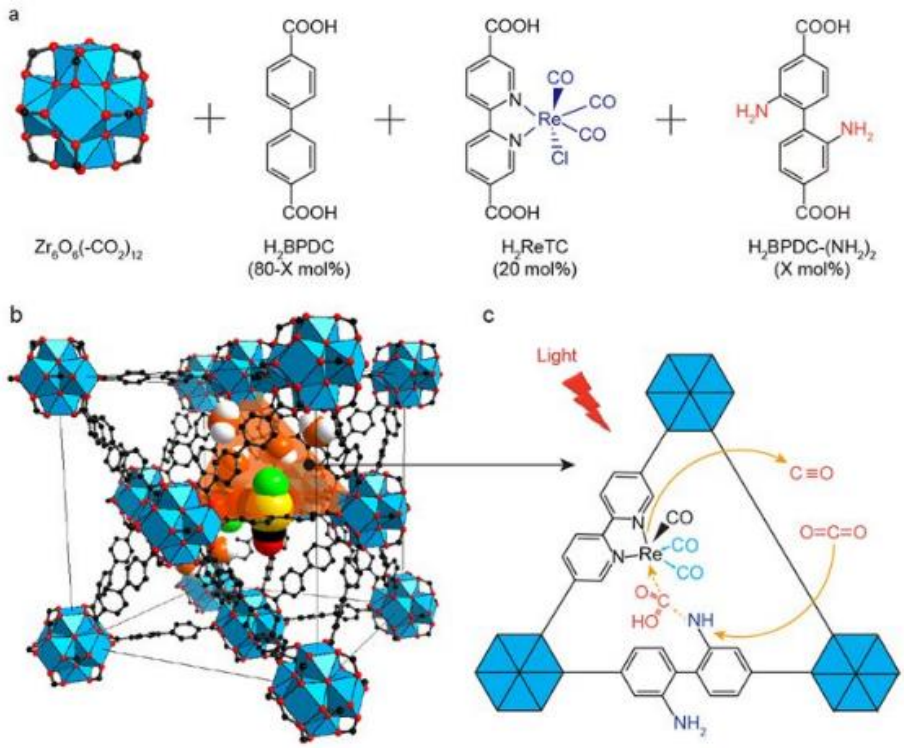

Figure 2.9 Schematic diagram showing the formation of UiO-67 type MOF with the immobilization of [Re(bpy-COOH)(CO)$_3$Br] and –NH$_2$ functionalised groups (a) where the presence of –NH$_2$ ligands aids photocatalytic CO$_2$ reduction by a cooperative effect via stabilization of the carbamate reaction intermediate (b and c). Figure taken from Sci. Rep., 2017, 7, 1–8.[74]

CMPs were first synthesised at the University of Liverpool by Cooper group in 2007.[101] These CMPs exhibited high apparent surface areas, up to1000 m^2g^{-1} in the dry state.[101] CMPs can also be modified with metal centres to produce a metal-organic CMP.[102] Many bpy based CMPs have since been reported, including the CMP-[Re(bpy)(CO)$_3$Cl] analogue which was synthesised by Sonogashira-Hagihara cross-coupling reaction using the monomer units shown in Figure 2.10, resulting in a porous material with a high surface area.[102] [Re(CO)$_5$Cl] was then reacted with the CMP structure by refluxing in toluene (boiling point 111˚C) to yield CMP-(bpy)$_x$Re. It was also shown that a CMP-(bpy)$_x$Re containing x=20% of 5,5′-dibromo-bipyridine units in the structure produced the highest BET surface area of 859 m^2g^{-1}, giving the highest rhenium content (15.06 wt%).[102] Although the CMP-(bpy)$_{20}$Re was synthesised, showing the catalyst can be successfully immobilised within CMP structures, it has yet to be used for electrocatalytic CO_2 reduction . There is however one study on the use of a closely related CMP, containing [Re(bpy)(CO)$_3$] subunits for the photocatalytic reduction of CO_2 which showed improved stability when compared to the parent [Re(bpy)(CO)$_3$Cl] complex in solution.[103]

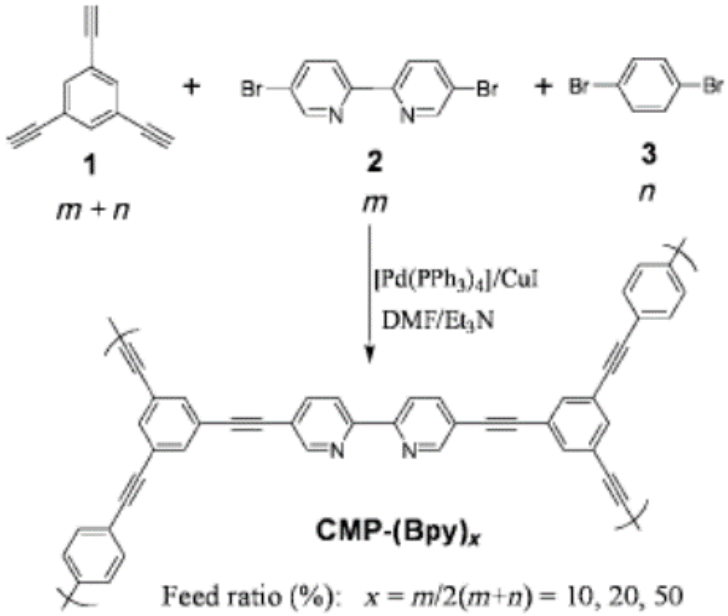

*Figure 2.10 Synthetic route to CMP-(bpy)$_x$Re of differing bpy loadings. Figure adapted from Angew. Chemie Int. Ed., 2011, **50**, 1072–1075.*[102]

CMPs are particularly interesting for CO_2 conversion as many CMP structures have been shown to be effective for CO_2 capture.[104–106] CO_2 capture by CMPs has been studied in detail, with the ability to add functionality into CMPs (e.g. amine and carboxylic acid groups) being particularly useful. These have been reported for selective CO_2 uptake in CMPs due to their strong affinity for CO_2, and ability to stabilise absorbed CO_2. CO_2 absorption using organic materials is of particular interest as it is cost effective, and does not need the high energy demands industrial methods of chemical sorption of CO_2 require.[104,106–108]

CMPs have been used in electrochemical applications such as supercapacitors,[109] batteries,[110] oxygen reduction.[111–113] However an issue is that in many cases they are not very conductive due to torsional disorder which is discussed in detail in chapter 1. Nonetheless, the ability to combine gas capture and conversion in a single device makes them of interest for CO_2 electrocatalysis. To the best of our knowledge there is only one report where a CMP has been used for electrocatalytic CO_2 reduction, where TPE-CMP prepared was synthesised using a Yamamoto coupling reaction (Figure 2.11) and was then deposited with 10 wt% Pt or Fe nanoparticles to give TPE-CMP-M (M = Pt or Fe).[114] A gas diffusion membrane was fabricated by depositing a homogeneous ink of CMP-M in ethanol onto a gas diffusion layer and compressing it onto a Nafion layer (Figure 2.11). In this case the catalyst particles (Pt or Fe) are not part of the CMP structure but are instead deposited/doped on the polymer. The Pt doped TPE-CMP resulted in $< 2 \times 10^{-5}$ mmol h^{-1} of carbon based products, which was increased to *ca.* 7×10^{-5} mmol h^{-1} upon the addition of 30% NTs to the homogeneous casting

ink.[114] The carbon based products detected were that of mainly alcohols, in particular methanol and acetone.[114] Although the authors report the detection of carbon based products from CO_2 reduction, the authors only report the total FE, > 95%, and note that majority of the 95% FE is hydrogen.[114] Even though selectivity is low for the system reported here, this study highlights that CMPs may be useful materials for electrocatalytic CO_2 reduction.

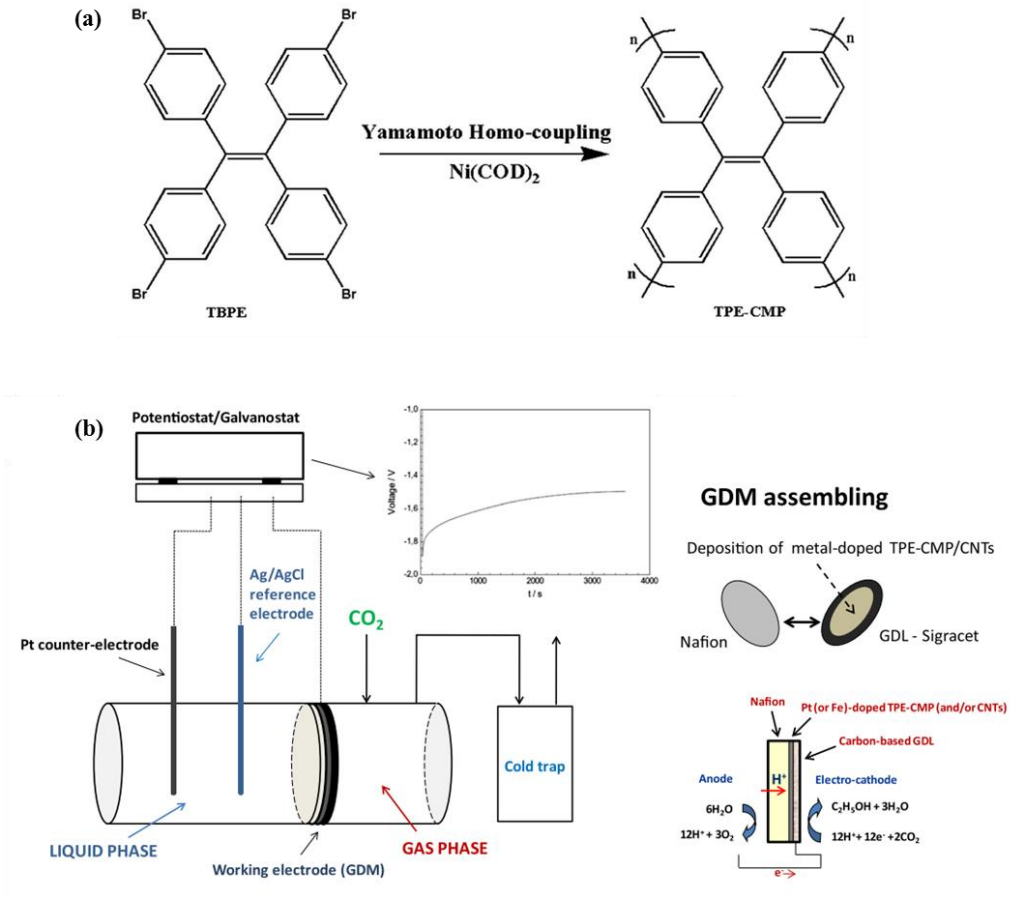

Figure 2.11 Schematic reaction scheme for the synthesis of TPE-CMP (a) and electrochemical set up of the cell and working gas diffusion electrode (b). Figure reproduced from J. Appl. Electrochem., 2015, ***45****, 701–713.*[114]

2.1.4 Scope of this chapter

[Mn(bpy)(CO)$_3$Br] has been previously shown to be selective for CO_2 reduction to CO and formate in organic solvents such as MeCN and in aqueous solution.[18,21] However, it has been postulated that Mn-Mn bond cleavage during dimer reduction results in a larger over-potential for the onset of CO_2 catalysis.[37,21] Some studies have explored the prevention of dimerisation through the addition of bulky groups to the bipyridine ligand, with varying degrees of success.[4,5,99] An alternative pathway to avoid dimerisation is the immobilisation of the catalyst. Previous electrochemical studies of [Mn(bpy)(CO)$_3$Br] deposited onto the surface of a GCE show that dimerisation still occurs, however immobilisation onto NTs using a flexible linker at low concentrations did prevent this pathway.[24] In principle, immobilisation into a rigid conductive framework is an attractive opportunity, as it should prevent dimerisation and provide a high concentration of electroactive catalytic sites.

CMPs offer a high surface area electroactive framework, and CMPs are also highly effective CO_2 uptake materials.[80,107,115,116] However, to date a CO_2 reduction electrode based on a metal organic CMP has not been reported. This chapter describes the synthesis, characterisation and electrochemical testing of a CMP modified with a [Mn(bpy)(CO)$_3$Br] derivative. The targeted structure is based on a modification of CMP-(bpy)$_{20}$, originally reported by the Cooper group.[102] The aim is to explore (i) if electrochemically triggered Mn dimerisation can be prevented using a CMP structure and (ii) the catalytic activity towards CO_2 and H^+ reduction.

Experiments also explore in detail the methods of electrode fabrication (e.g. the choice of supporting polymer to aid adhesion to the electrode). An issue with CMPs as electrode materials is that long-range charge transport is limited by twisting of the structure.[117,118] Here, we also explore a route to template the CMP directly onto carbon supports to achieve planarity and conjugation, which has significance to the wider field of CMP based electrochemical materials.

2.2 Results and Discussion

2.2.1 Synthesis and characterisation

The synthesis of CMP-$(bpy)_x$ (x = 10, 20, 50) has previously been reported, and the framework has also been modified by reaction with $[Re(CO)_5Cl]$ to provide $[Re(bpy)(CO)_3Cl]$ moieties within the structure, (Figure 2.10).[102] The notation for the bpy content of the polymer arises from the feed percentage of 5,5′-dibromo-2,2′-bipyridine in the polymerisation reaction. In this past study CMP-$(bpy)_{20}$ yielded the highest BET surface area and also the maximum Re loading (15%), therefore studies here are based on using CMP-$(bpy)_{20}$ for the immobilisation of the Mn analogue. Initial experiments, (method (a), Figure 2.12) followed the method described by Jiang *et al.* to prepare the CMP-$(bpy)_{20}$. Full synthetic details can be found in the materials and methods section (2.4).[102] Briefly, under an argon atmosphere 1,4-dibromobenzene, 5,5′-dibromo-2,2′-bipyridine and 1,3,5-triphenylbenzene were refluxed in DMF/NEt_3 for 3 days in the presence of CuI and $Pd(PPh_3)_4$, yielding a brown solid. Following ball milling to reduce the particle size, purification of CMP-$(bpy)_{20}$ was then achieved *via* soxhlet extraction in methanol at 90˚C for 3 days. Incorporation of the Mn catalysts was achieved by refluxing a suspension of CMP-$(bpy)_{20}$ in toluene with an excess of $[Mn(CO)_5Br]$ for 24 hours in the dark.

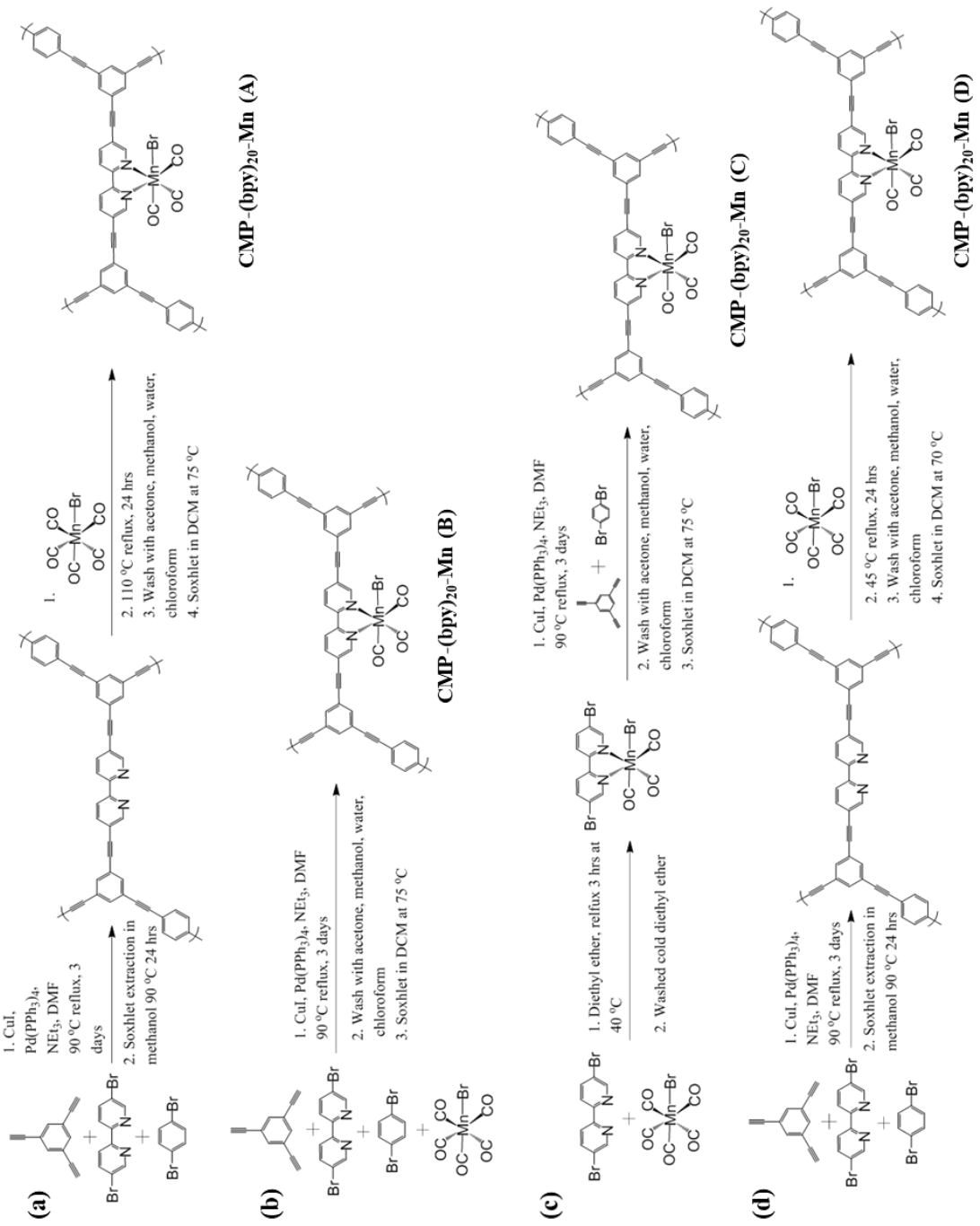

Figure 2.12 Synthetic routes (a-d) explored for optimised [Mn(bpy)(CO)$_3$Br] loading into the CMP-(bpy)$_{20}$ via post metalation of CMP-(bpy)$_{20}$ at 110˚C (a) and 45˚C (d), a one pot synthesis (b) and metalation of the bpy monomer unit prior to CMP-(bpy)$_{20}$ synthesis (c). Spectroscopic techniques described below, showed that synthetic route d gave optimal loading of the catalyst.

FTIR spectroscopy confirmed the presence of a *fac*-tricarbonyl complex, likely $[Mn(bpy)(CO)_3X]^{n+}$ (where X may be a solvent or Br^- and n = 0, 1), through the presence of three new ν(CO) bands at 2026, 1942 and 1921 cm^{-1} (compared to 2027, 1933 and 1924 cm^{-1} for a solid sample of $[Mn(bpy)(CO)_3Br]$ [22]), Figure 2.13. The sample prepared by method (a) in Figure 2.12 is here on described as CMP-$(bpy)_{20}$-Mn (A) and was found to contain 6.02 ± 0.07% Mn by weight through ICP-OES analysis, Table 2.2. Despite the soxhlet extraction and washing steps outlined in the methods section, 0.31 ± 0.013% of Pd from the initial coupling reaction was still present. The weight content of Mn in CMP-$(bpy)_{20}$-Mn (A) (*ca.* 6%) is roughly in-line with the highest achieved when CMP-$(bpy)_{20}$-Re was prepared (15%) taking into account the ratio of masses of the metal center (Re:Mn = 3.38, Re:Mn wt./wt. = 2.5). However, it was decided to explore a range of synthetic routes to incorporate $[Mn(CO)_5Br]$ into the CMP network in an attempt to minimise the change in surface area and optimize the Mn loading level. Although the theoretical maximum weight loading of Mn into CMP-$(bpy)_{20}$ is 6.4% (based on 100% reaction of all bpy units and the Mn complex formed maintain the Br ligand) was apparently reached by method (a), it was noted that the BET surface area was greatly decreased upon addition of the Mn center from 612 $m^2\ g^{-1}$ to 405 $m^2\ g^{-1}$, Table 2.2.

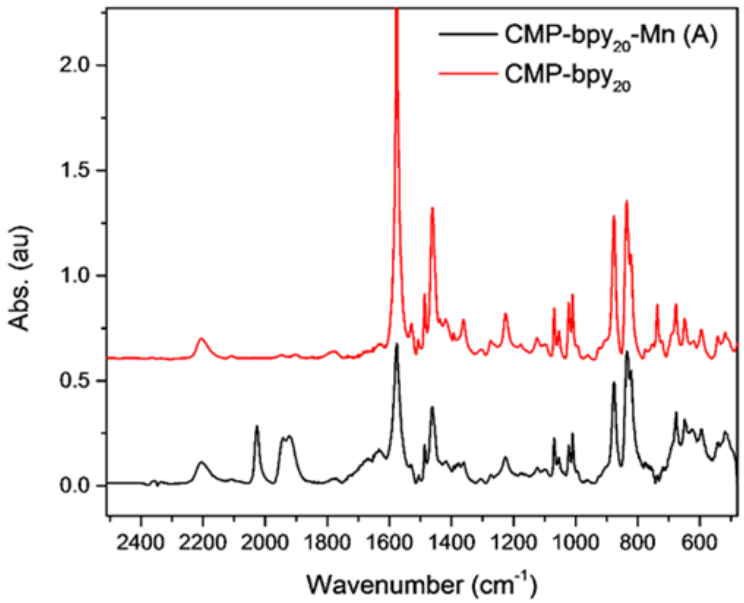

Figure 2.13 FTIR spectrum of CMP-$(bpy)_{20}$ (red) and CMP-$(bpy)_{20}$-Mn (A) (black), confirmed the presence of a Mn fac-tricarbonyl complex.

Table 2.2 Physical properties of CMP-(bpy)$_{20}$ and CMP-(bpy)$_{20}$- Mn, where CMP-(bpy)$_{20}$-Mn was synthesised via various synthetic routes for optimisation of catalyst content.

Synthetic route	BET surface area (m^2/g)[a]	Total pore volume (cm^3/g)[b]	Mn_{ICP} (%)[c]
CMP-(bpy)$_{20}$	636.86	0.24	-
CMP-(bpy)$_{20}$-Mn (A)	404.94	0.16	6.02 ± 0.07
CMP-(bpy)$_{20}$-Mn (B)	94.37	0.035	4.74 ± 0.52
CMP-(bpy)$_{20}$-Mn (C)	24.35	0.0082	2.12 ± 0.02
CMP-(bpy)$_{20}$-Mn (D)	549.25	0.21	5.47 ± 0.21

[a] BET Surface area calculated over the pressure range (P/P_0) 0.00017–0.1. [b] Total pore volume at $P/P_0 = 0.102$. [c] ICP-OES was used to determine Mn loading. Samples were prepared *via* microwave digestion in nitric acid.

Figure 2.12 provides an overview of the synthetic methods explored. We hypothesised prior incorporation of [Mn(CO)$_5$Br] into the brominated bpy monomer may lead to a change in porous structure and two methods were examined. Firstly, a one pot synthetic approach involved the addition of [Mn(CO)$_3$Br] into the starting polymerisation mixture, Figure 2.12b, which resulted in 4.74 ± 0.52% weight of Mn within CMP-(bpy)$_{20}$-Mn (B) and a very low BET surface area. FTIR analysis showed weak, broad, potentially multiple carbonyl stretches shown in Figure 2.14. Presence of a *fac*-tricarbonyl species is evident at *ca*. 2020, 1947 and 1930 cm^{-1}, some dimer species could also be present, indicated by stretches at *ca.* 1975, and 1878 cm^{-1} but it is difficult to assign all the expected *v*(CO) modes for the dimer due to most of them being masked by the tricarbonyl stretches ([Mn$_2$(bpy)$_2$(CO)$_6$] in THF has reported *v*(CO) at 1975, 1963, 1936, 1886 and 1866 cm^{-1} [119]).

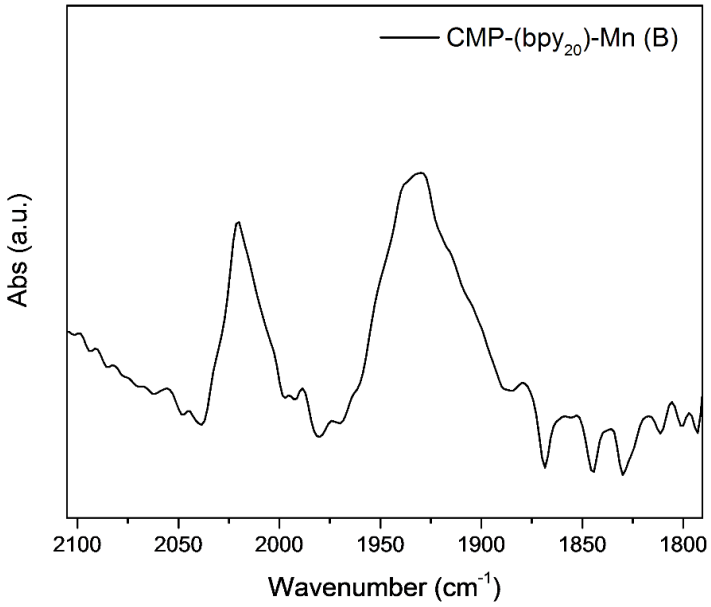

Figure 2.14 FTIR of CMP-(bpy)$_{20}$-Mn (B) showing the presence of carbonyl streches.

As an alternative synthetic route where the 5,5′-dibromo-2,2′-bipyridine monomer was reacted with [Mn(CO)$_5$Br] prior to synthesising the CMP-(bpy)$_{20}$ framework was also tested method (c), Figure 2.12. This was used as it should ensure that all bpy sites in the CMP-(bpy)$_{20}$ backbone were metalated. [Mn(bpy-Br$_2$)(CO)$_3$Br] was synthesised using the literature methods reported for [Mn(bpy)(CO)$_3$Br], section 2.4.[18] FTIR analysis of the product of the first step was consistent with the formation of a *fac*-tricarbonyl complex (ν(CO) = 2031 and 1934 cm^{-1} (broad, 2 stretching modes), and H^1-NMR recorded of the Mn confirmed the presence of [Mn(bpy-Br$_2$)(CO)$_3$Br], Figure 2.15 and Figure 2.16.

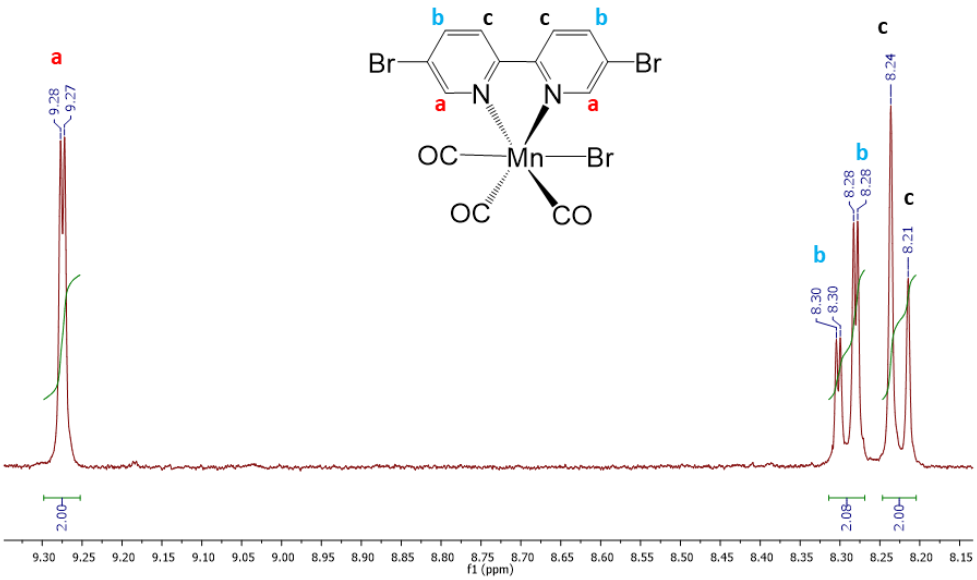

Figure 2.15 H^1-NMR of [Mn(bpy-Br_2)$(CO)_3$Br] in d_3-MeCN. Assignments to the protons present on the bpy ligand are shown as a,b and c which have been assigned to peaks in the spectra. ^{1}H NMR (400 MHz, CD_3CN) δ 9.27 (d, J = 1.9 Hz, 2H), 8.29 (dd, J = 8.7, 2.0 Hz, 2H), 8.23 (d, J = 8.7 Hz, 2H).

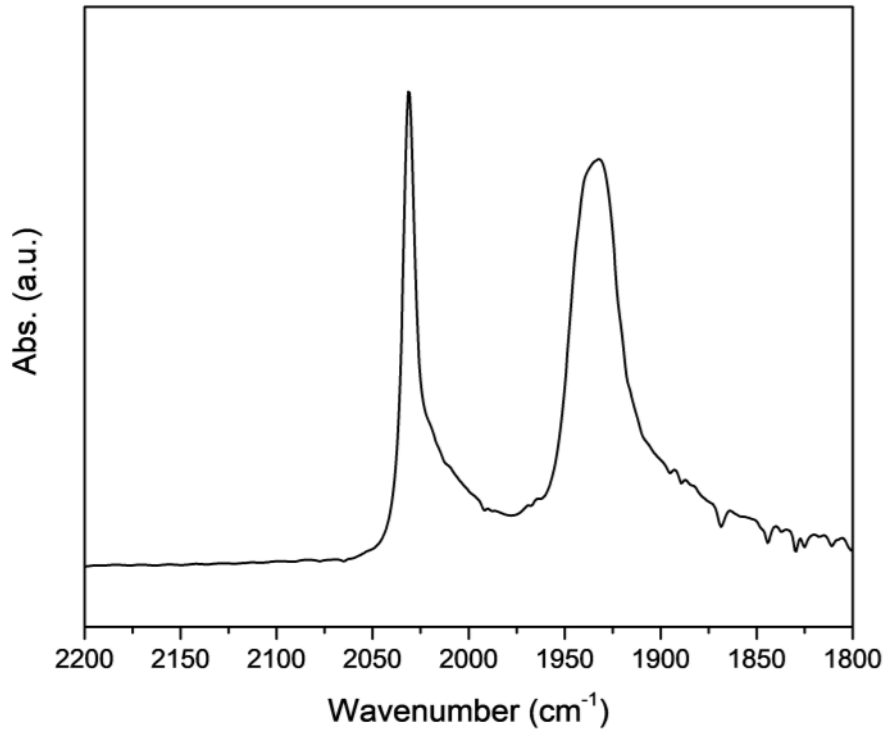

Figure 2.16 FTIR of [Mn(bpy-Br_2)$(CO)_3$Br] in MeCN showing a strong ν(CO) mode at 2031 and a broad band at 1934 cm^{-1} due to the overlap of two ν(CO).

Subsequent use of the [Mn(bpy-Br_2)$(CO)_3$Br] monomer unit in the Sonogashira-Hagihara cross-coupling reaction led to the formation of CMP-$(bpy)_{20}$-Mn (C), however this material had the lowest Mn wt% (2.12 ± 0.02%, Table 2.2) and BET surface area. Finally, a modified version of the synthesis, method (a), was tested where the temperature was decreased from 110˚C to 45˚C for the reaction CMP-$(bpy)_{20}$ with $[MnCO)_5Br]$. The lower temperature was more in-line with literature reports for the synthesis of [Mn(bpy)$(CO)_3$Br] in solution, where the yield decreases at higher temperature,[21] Figure 2.12(d). Using this method CMP-$(bpy)_{20}$-Mn (D) was obtained which contained 5.47 ± 0.21% by weight of Mn (Table 2.2), and significantly also an improved BET surface area (529 m^2 g^{-1}). FTIR spectroscopy of CMP-$(bpy)_{20}$-Mn (D) also showed ν(CO) bands at 2025, 1937 and 1918 cm^{-1}, Figure 2.17b, again consistent with the formation of a tricabonyl complex. It is notable that the ratio of the ν(CO) band at 2025 cm^{-1} to the ring mode at 1576 cm^{-1} in CMP-$(bpy)_{20}$-Mn (D) is ~2:1, in contrast the ratio in CMP-$(bpy)_{20}$-Mn (A) is ~1:3 (Figure 2.17). Although pathway A exhibits a slightly higher Mn content, it seems apparent that the lower temperature route actually provides a greater level of incorporation of the desired [Mn(bpy)$(CO)_3$Br] moieties, presumably with a range of MnO_x species being present in CMP-$(bpy)_{20}$-Mn (A). Therefore, synthetic route (D) was taken forward for all future studies.

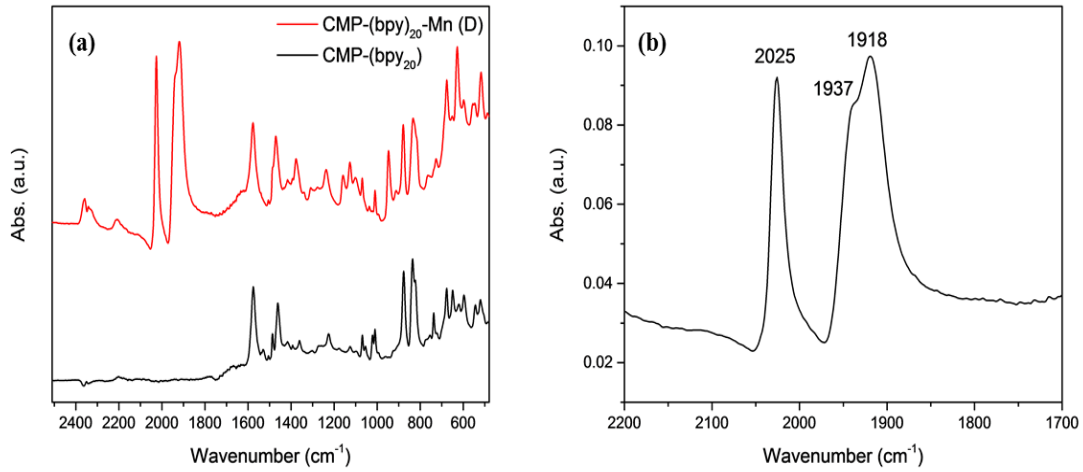

Figure 2.17 FTIR spectra overlay of CMP-(bpy_{20})-Mn (D) (red) and CMP-(bpy_{20}) (black) (a), showing the presence of three ν(CO) stretches indicative of the incorporation of [Mn(bpy)$(CO)_3$Br] catalyst into the CMP network (b).

UV-Visible absorption spectroscopy of the unmodified framework, CMP-$(bpy)_{20}$, shows the presence of a broad absorption with a maxima at *ca.* 400 nm, with an absorption tail out to 800 nm, likely due to the presence of a conjugated system with many different local environments as a result of torsional disorder affecting the conjugation lengths Figure 2.18a.[120] A shoulder in the solid-state UV-Visible absorption spectrum of CMP-$(bpy)_{20}$-Mn (D) at 500 nm is assigned to a metal (Mn) to ligand charge transfer (MLCT). The MLCT is significantly

shifted compared to the parent [Mn(bpy)(CO)$_3$Br] complex which has MLCT λ_{max} ~ 410 nm in MeCN solution, again indicating a marked difference in the electronic structure of the Mn center/ligands.[21] Thermogravimetric analysis (TGA) analysis showed ~7% mass loss between 300-500˚C, proposed to be due to the loss of CO ligands, further indicating the presence of [Mn(bpy)(CO)$_3$Br] incorporation, Figure 2.18b. Based on the Mn weight content (5.47%) the CO ligands would be anticipated to account for 8.26% of the weight of CMP-(bpy)$_{20}$-Mn (D), suggesting that the majority of the Mn centers are present as tricarbonyl complexes. Complete decomposition of the material did not occur until 900˚C showing the high stability of the CMP-(bpy)$_{20}$ polymer.

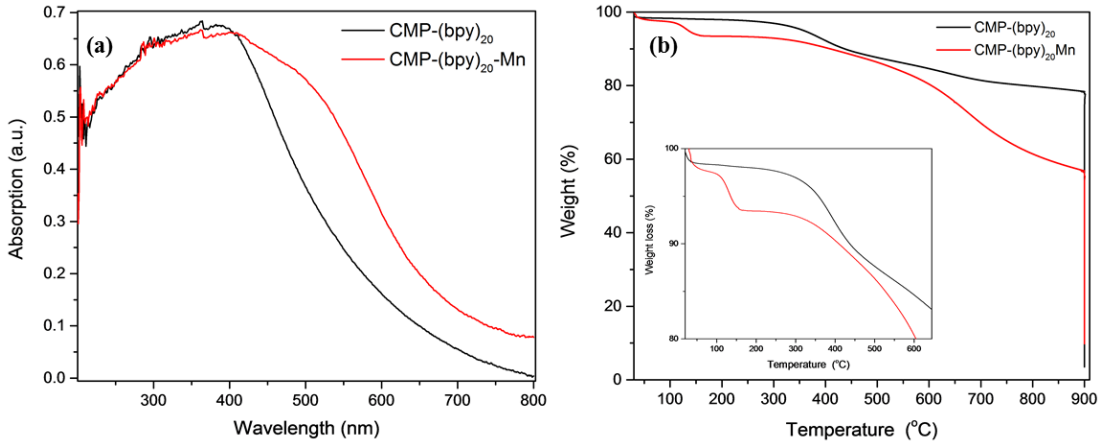

Figure 2.18 UV-Visible absorption spectroscopy of CMP-(bpy)$_{20}$ (black) and CMP-(bpy)$_{20}$-Mn (D) (red) (a). TGA analysis of CMP-(bpy)$_{20}$ (black) and CMP-(bpy)$_{20}$-Mn (D) (red) (b).

CMPs are known to form amorphous structures.[80] CMP-(bpy)$_{20}$-Mn (D) was confirmed to be amorphous by powder X-ray diffraction (PXRD), where only very weak broad signals were present, indicating a small degree of ordering of the network, likely due to stacking of polymer chains through intermolecular forces, Figure 2.19.[121] The PXRD pattern of the CMP showed three broad peaks at 2θ values of 17.37, 22.45 and 42.90˚. Addition of [Mn(bpy)(CO)$_3$Br] into the CMP show an additional peak at 10.76˚, which could be a result of a change in packing upon the immobilisation of the catalyst.

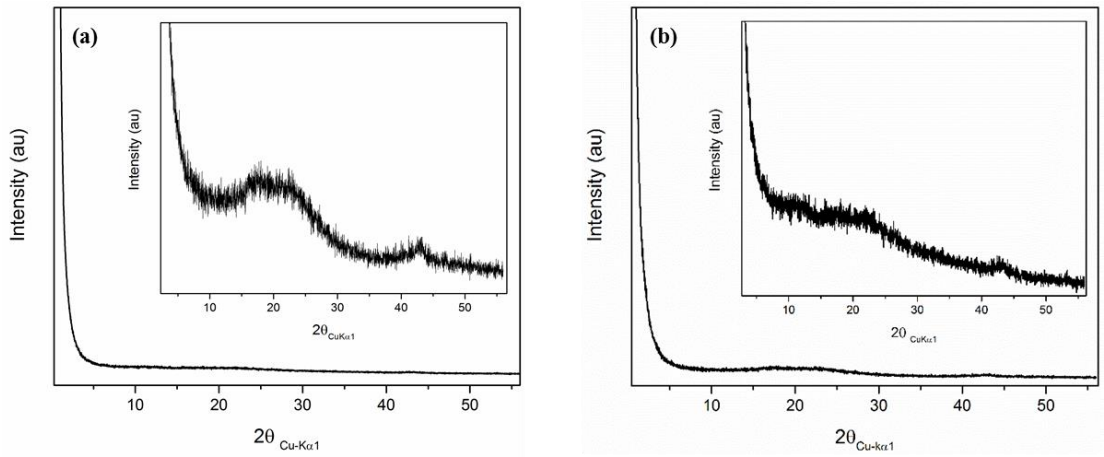

Figure 2.19 PXRD patterns of CMP-(bpy)$_{20}$ (a) and CMP-(bpy)$_{20}$-Mn (D) (b).

BET surface areas are reported in Table 2.2 and adsorption-desorption isotherms and pore volumes (77 K) are shown in Figure 2.20 providing insight into the porous networks. All materials show type I and type IV physisorption isotherms with hysteresis, where CMP-(bpy)$_{20}$-Mn (D) is the only material to display a clear H2 hysteresis loop, indicating the presence of a porous network. Analysis of the differential pore volume shows a broad range of pores are present in CMP-(by)$_{20}$ and CMP-(bpy)$_{20}$-Mn (D). Differential pore volume plots for CMP-(bpy)$_{20}$-Mn (B) and (C) are not shown due to the low surface areas making it difficult to fit the pore volumes within a reasonable error. In-line with expectations, addition of the Mn complex led to a lower surface area as a result of the increased weight of the polymer, Table 2.2.

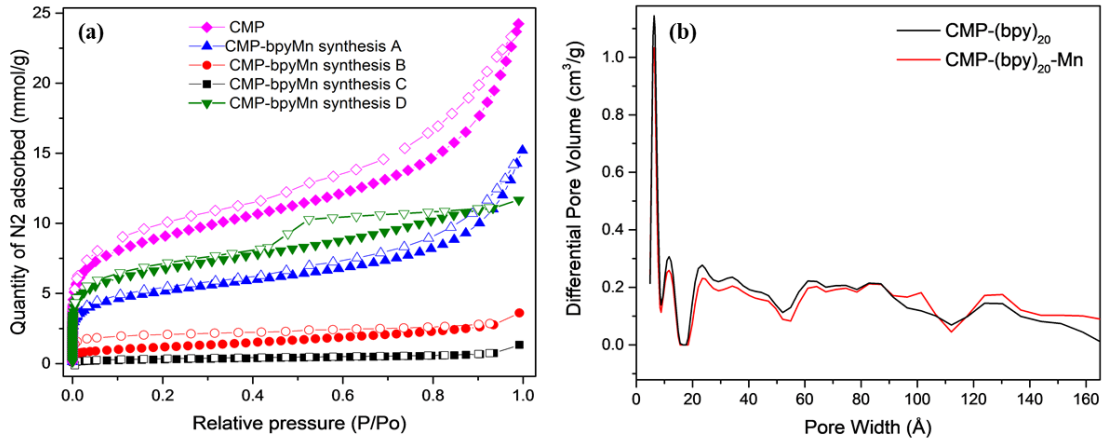

Figure 2.20 N_2 adsorption-desorption isotherms measured at 77.4 K for CMP-(bpy)$_{20}$ (black), CMP-(bpy)$_{20}$-Mn synthesis a (red), CMP-(bpy)$_{20}$-Mn synthesis b (pink), CMP-(bpy)$_{20}$-Mn synthesis c (blue). Adsorption data is shown with filled labels, and desorption data with open labels (a). Differential pore volume of CMP-(bpy)$_{20}$ (black) and CMP-(bpy)$_{20}$-Mn (D) (red) fitted to a DFT model.

The distribution of differential pore volumes is broadly the same for CMP-$(bpy)_{20}$-Mn-(D), and CMP-$(bpy)_{20}$, however decreased volume for the metallized samples is observed. The CO_2 absorption-desorption isotherm of CMP-$(bpy)_{20}$-Mn (D) at 298 K shows the ability of CO_2 to be absorbed and desorbed from the porous structure from its non-linear response (Figure 2.21).[105,122] The CO_2 uptake at atmospheric pressure and 298 K is approximately 1 mmol gm^{-1}, and is similar to those of previous metal free CMP materials with values ranging between ~1-2.2 mmol gm^{-1} being reported.[106,123,124] However it should be noted that although not the highest capacity, the sample prepared here still exceeds the CO_2 uptake levels of many reported activated carbon capture materials.[125,126] It is therefore apparent that CMP-$(bpy)_{20}$-Mn-(D) is a high surface area porous material that has the potential to provide high local concentrations of CO_2 to the catalytic sites.

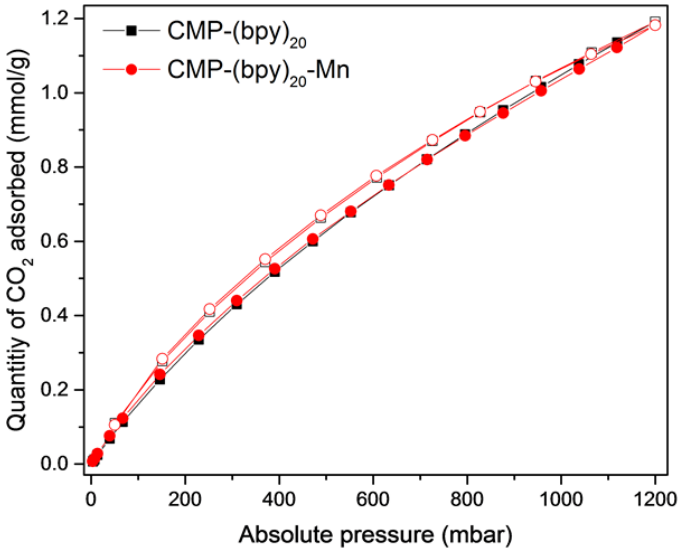

Figure 2.21 CO_2 adsorption-desorption isotherms measured at 298 K for CMP-$(bpy)_{20}$ (black) and CMP-$(bpy)_{20}$-Mn (red). No difference in CO_2 sorption is seen with the addition of Mn. Adsorption data is shown with filled labels, and desorption data with open labels.

2.2.2 Electrochemical analysis

The electrochemical behaviour of CMP-$(bpy)_{20}$-Mn (D) and CMP-$(bpy)_{20}$ was studied in pH 7 phosphate buffer electrolyte under both an argon and CO_2 atmosphere. For the remainder of this chapter CMP-$(bpy)_{20}$-Mn (D) is referred to as CMP-$(bpy)_{20}$-Mn as the materials prepared by the other synthetic methods were not further studied. A common approach often used to immobilise materials that are insoluble in the electrolyte of interest is to drop cast a small amount of material onto the surface of a glassy carbon electrode, in some cases without any additional binder that aids adhesion to the electrode surface.[21,22,55] As it was not possible to dissolve any of the CMP samples prepared, electrodes were initially drop cast from a suspension in toluene or acetonitrile after 15 minutes sonication, full sample

preparation details are in section 2.4. However, the poor stability of the electrode prevented detailed electrochemical studies. Samples detached upon either immersion of the electrode into electrolyte, or upon cycling during a standard electrochemical experiment, and this was evident from delamination of the film during electrochemical measurements as shown in Figure 2.22. To improve the adhesion of the sample to the carbon electrode two different approaches have bene used (i) the introduction of a supporting/binder polymer and (ii) grafting the CMP directly onto the surface of the electrode.

Figure 2.22 Photographs of a CMP-$(bpy)_{20}$-Mn electrode before (left) and after (right) electrochemical measurements.

2.2.2.1 Supporting polymer – Nafion

Nafion is the most widely used polymer for the immobilisation of CO_2 reduction electrocatalysts onto electrode surfaces.[21,55,127] As described above Nafion has previously been used to immobilise [Mn(bpy)$(CO)_3$Br] onto the surface of a GCE, which resulted in good stability with electrodes lasting > 48 hours under operating conditions.[21] Therefore the electrochemical behaviour of CMP-$(bpy)_{20}$ and CMP-$(bpy)_{20}$-Mn samples was initially studied using a Nafion support. Electrodes were prepared by casting 10 µL of a suspension of either CMP-$(bpy)_{20}$ or CMP-$(bpy)_{20}$-Mn (5.5 mg/mL) in a Nafion (at 0.5% weight) acetonitrile/alcohol solution onto a GCE (0.07 cm^2). Full details of the sample preparation are given in section 2.4.

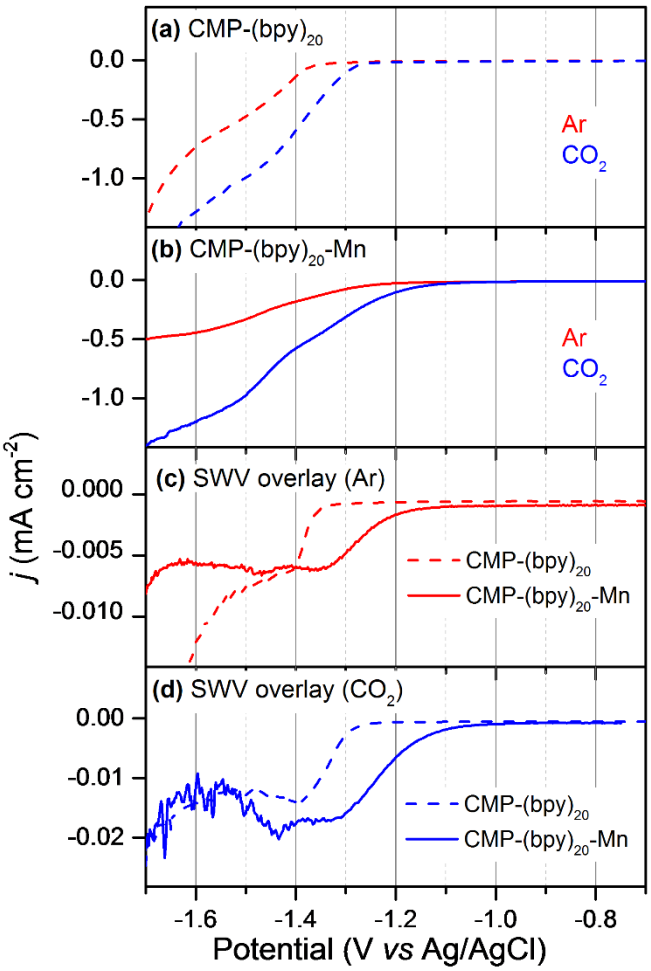

Figure 2.23 Linear sweep voltammogram of CMP-(bpy)$_{20}$ (a) and CMP-(bpy)$_{20}$-Mn (b) under an atmosphere of argon (red) and CO_2 (blue) at 10 mVs^{-1}. Square wave voltammograms of CMP-(bpy)$_{20}$ (dashed) and CMP-(bpy)$_{20}$-Mn (solid) under argon (red) and CO_2 (blue) at 5 Hz. All mesaurements were carried out in 0.1 M phosphate buffer electrolyte.

Linear sweep voltammetry and square wave voltammetry for the CMP-(bpy)$_{20}$ sample in the absence of the Mn catalytic site under both argon and CO_2 in pH 7 phosphate buffer (0.1 M) is shown in Figure 2.23 (a,c,d). Under argon a single reduction at -1.46 V is present that appears to shift to more positive potentials (-1.44 V) under CO_2. All potentials throughout the rest of this chapter are referenced against Ag/AgCl unless stated otherwise. This reduction for the CMP-(bpy)$_{20}$ sample is proposed to be either due to reduction of the CMP-(bpy)$_{20}$ sample backbone, or to be associated with residual Pd within the sample (0.24 ± 0.02%). Despite repeated washings in chloroform, acetone and methanol (50 mL each), followed by soxhlet extraction in DCM, the Pd could not be removed in-line with past studies on the framework by Jiang *et al.*[102] The slight shift in reduction potential under CO_2 may indicate that CO_2 binds to the reduced CMP-(bpy)$_{20}$ or Pd site (see below).

In addition to the reduction at -1.46 V under argon the LSV and square wave voltammogram (SWV) of CMP-$(bpy)_{20}$-Mn (Figure 2.23, b-d) also show a new reduction at -1.37 V which is assigned to a Mn based reduction. Under the same conditions, films of $[Mn(bpy)(CO)_3Br]$ in Nafion show two main reductions, at -1.15 V which is assigned to the reduction of $[Mn(bpy)(CO)_3Br]$ to form $½[Mn_2(bpy)_2(CO)_6]$, and at -1.47 V due to the reduction of $½[Mn_2(bpy)_2(CO)_6]$ to form $[Mn(bpy)(CO)_3]^-$ Figure 2.24.[21] When bulky substituents are placed on the bpy ligand dimerisation can be prevented, and in acetonitrile the formation of $[Mn(bpy\text{-}R)(CO)_3]^-$ has been reported to occur *via* a two-electron process at a single potential.[4] Here, the incorporation of the Mn centre into the CMP-$(bpy)_{20}$ structure would be expected to prevent dimerisation, and the presence of a single reduction assignable to the Mn centre allows us to tentatively assign the feature to the reduction of CMP-$[Mn(bpy)_{20}(CO)_3Br]$ by two electrons to form the catalytically active species, CMP-$[Mn(bpy)_{20}(CO)_3]^-$. Further comparison of the CV of CMP-$(bpy)_{20}$-Mn to that of $[Mn(bpy)(CO)_3Br]$ in Nafion also supports the conclusion that incorporation of the catalytic centre into the CMP-$(bpy)_{20}$ structure has prevented dimerisation upon reduction, Figure 2.24. In addition to the two reductions described above, the $[Mn(bpy)(CO)_3Br]$/Nafion sample (Figure 2.24a) also shows an oxidation at -0.35 V which has been shown elsewhere to be due to the oxidation of $[Mn_2(bpy)_2(CO)_6]$ which forms in small clusters within the film.[21] In contrast, CMP-$(bpy)_{20}$-Mn shows no oxidation feature that can be assigned to the dimer complex, indicating that the reductions identified in Figure 2.24 generate an unstable species, likely CMP-$[Mn(bpy)(CO)_3]^-$.

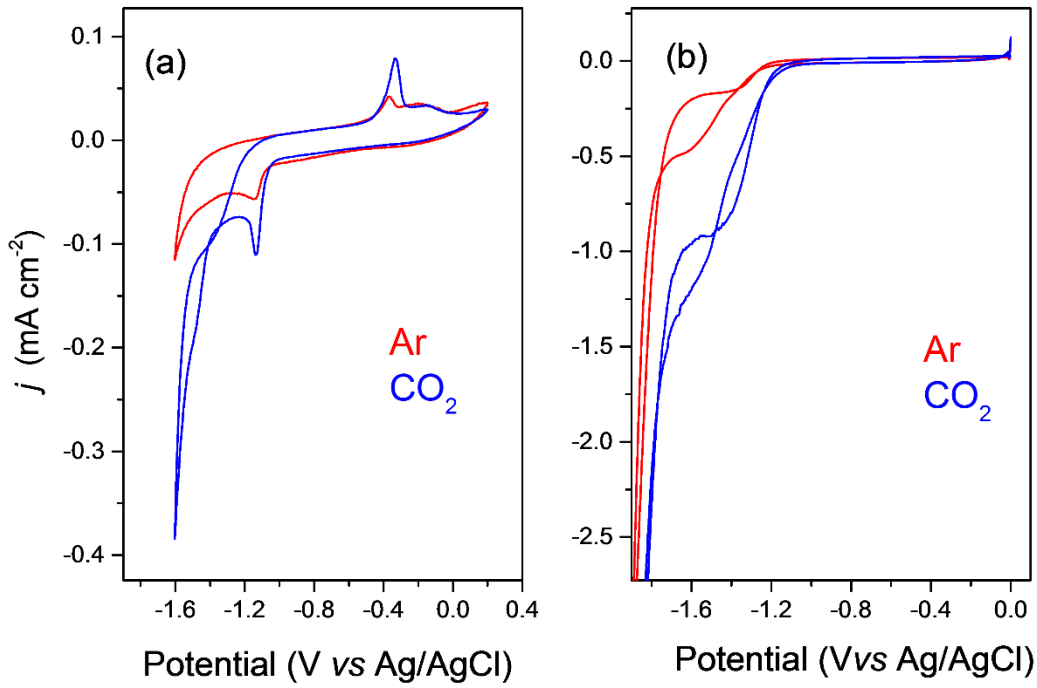

*Figure 2.24 CVs [Mn(bpy)(CO)$_3$Br]/Nafion$_{5\%}$ (a) and CMP-(bpy)$_{20}$-Mn/Nafion$_{0.5\%}$ (b) under argon (red) and CO_2 (blue) at a scan rate of 10 mVs^{-1}. Electrodes were prepared using 5.5 mg of [Mn(bpy)(CO)$_3$Br] or CMP-(bpy)$_{20}$-Mn in 5% wt or 0.5% wt. Nafion respectively. [Mn(bpy)(CO)$_3$Br]/Nafion$_{5\%}$ data shown here is reproduced from Chem. Commun. (Camb)., 2014, **50**, 12698–701.*[21]

In order to further study the behaviour of the Mn centre within CMP-(bpy)$_{20}$-Mn, CVs at a range of scan rates were recorded under argon, Figure 2.25. Attempts to plot the peak current versus scan rate were unsuccessful for the Mn based reduction at -1.37 V. However, the assignment to a Mn based reduction within the framework is also supported by the behaviour of CMP-(bpy)$_{20}$-Mn under CO_2. In addition to an increased current density and earlier onset potential under CO_2 (which is discussed fully in the catalysis section below) the SWV also shows a 30 mV shift positive for the Mn based reduction to -1.34 V, indicating that CO_2 may be binding to the reduced metal centre. Fujita *et al.* have previously described the relationship between observed reduction potential and CO_2 binding constant (K_{CO2}) for electrocatalysts that operate by a E_RC_{cat} mechanism, where the catalysis step is sufficiently slow to allow for electrochemical detection of the CO_2 adduct,[128] and is shown in Eq. 2.1. Where E and E^o are the peak potentials at which fast and slow catalysis occur.[4]

$$E = E° + \left(\frac{RT}{nF}\right)\ln\{1 + [CO_2]K_Q\} \quad Eq.\,2.1$$

Previous studies on similar Mn carbonyl complexes have reported shifts in potential on the order of 30 mV for the formation of the catalytically active [Mn(bpy-R)(CO)$_3$]$^-$ centre in the presence of 0.26 M CO_2 and a suitable proton source (to enable binding of CO_2 in the form of Mn^I-CO_2H) which corresponds to a CO_2 binding constant of 46 ± 10 M^{-1}.[4] Here CO_2 saturated

aqueous solutions are used ([CO_2] ~ 0.03 M), however the CMP-$(bpy)_{20}$-Mn structure is based on known CO_2 absorbent structures making it difficult to accurately determine the local CO_2 concentration. Assuming the formation of CMP-$[Mn(bpy)_{20}(CO)_3]^-$ by a two electron reduction an upper limit of K_{CO2} ~ 300 M^{-1} would be arrived at, however it must be reiterated that the very high apparent binding constant for CO_2 is more likely an indication of the ability of the CMP-$(bpy)_{20}$ structure to concentrate CO_2, instead of being a measure of the reduced Mn centre to bind to CO_2.

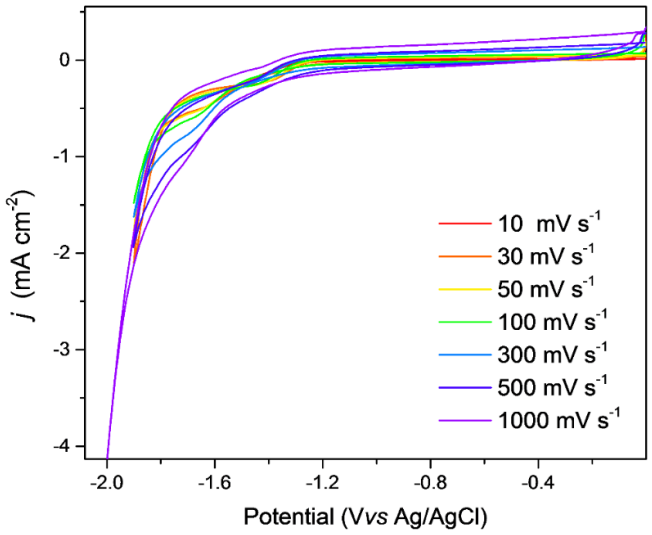

Figure 2.25 Various scan rates of CMP-$(bpy)_{20}$-Mn/Nafion$_{0.5\%}$ under an atmosphere of argon in 0.1 M pH 7 phosphate buffer.

Figure 2.24 also shows that the current densities for the reductions associated with CMP-$(bpy)_{20}$-Mn are significantly increased, particularly under CO_2, in Figure 2.24(b), despite the concentration of Mn being less on the CMP-$(bpy)_{20}$-Mn electrode compared to the $[Mn(bpy)(CO)_3Br]$/Nafion electrode. Determination of the electroactive content of Mn centres in the $[Mn(bpy)(CO)_3Br]$/Nafion sample has previously been reported to be 0.25% (3.5 x10^{-10} mol on a 0.07 cm^2 GCE).[21] Integration of the reductive feature in the SWV of CMP-$(bpy)_{20}$-Mn/Nafion$_{0.5\%}$ electrodes (Figure 2.26) which is assigned to the Mn centre, indicates 5.2 ×10^{-6} C is passed, corresponding to 2.7 ×10^{-11} mol of electroactive Mn on a 0.07 cm^2 GCE assuming a two electron reduction.

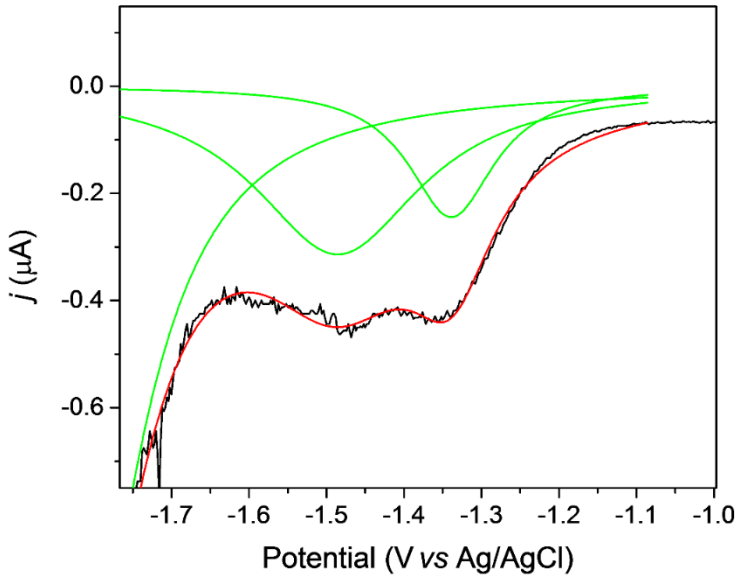

Figure 2.26 SWV of CMP-(bpy)$_{20}$-Mn/Nafion$_{0.5\%}$ under an atompshere of argon at a frequency of 10 Hz (black) and the fitting of the electrochemical features to obtain an area for the Mn based redution (green) accompanied by the overall fit (red).

It is therefore apparent that despite incorporation of the catalytic centre into the CMP-(bpy)$_{20}$ framework the vast majority (99%) of the Mn centres appear to be inactive, a point which will be discussed further below. The differences in the electrochemical behaviour of the Mn centre when incorporated within the CMP-(bpy)$_{20}$ framework and when freely deposited within Nafion are summarised in Figure 2.27.

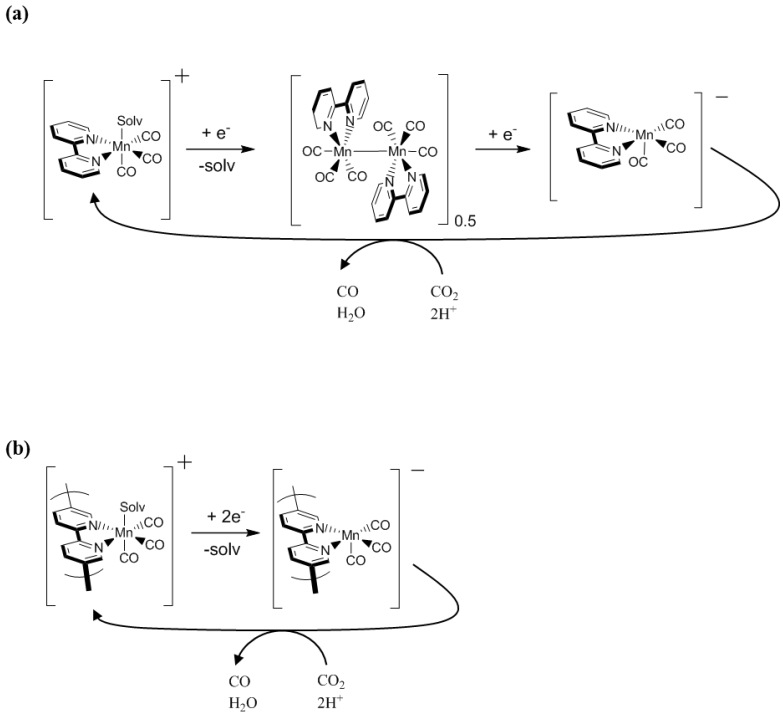

Figure 2.27 Schematic diagram of the different electrochemical reduction pathways of [Mn(bpy)(CO)$_3$Br] (a) and CMP-(bpy)$_{20}$-Mn (b).

2.2.2.2 Electrocatalytic behaviour of CMP-(bpy)$_{20}$-Mn in the presence of CO_2

In Figure 2.23, the low scan rate data (10 mV s^{-1}) shows enhancements in current density under CO_2 at potentials negative of -1.15 V, reaching a plateau at *ca.* -1.35 V with CMP-(bpy)$_{20}$-Mn. Using CMP-(bpy)$_{20}$, a sample that does not contain the Mn sites, an increased current density is still observed under CO_2, however the onset occurs at more negative potentials, -1.30 V, Figure 2.23. This indicates that electrocatalytic CO_2 reduction may be occurring at the Mn centre at relatively positive potentials. The electrochemical responses of both CMP-(bpy)$_{20}$ and CMP-(bpy)$_{20}$-Mn have also been studied under CO_2 at a range of scan rates, Figure 2.28. Interestingly, increasing the scan rate of the CV does not lead to an increase in measured current density for CMP-(bpy)$_{20}$-Mn between -1.15 and -1.35 V. Savéant *et al.* have discussed the scan-rate dependence of CVs during CO_2 electrocatalysis in several recent reviews,[129,130] and highlighted that such behaviour indicates that the catalysts TOF is not limited by substrate diffusion. In our case it indicates either slow catalysis between -1.15 and -1.35 V at the Mn centre, or that the substrate (CO_2/H^+) concentration is very high.

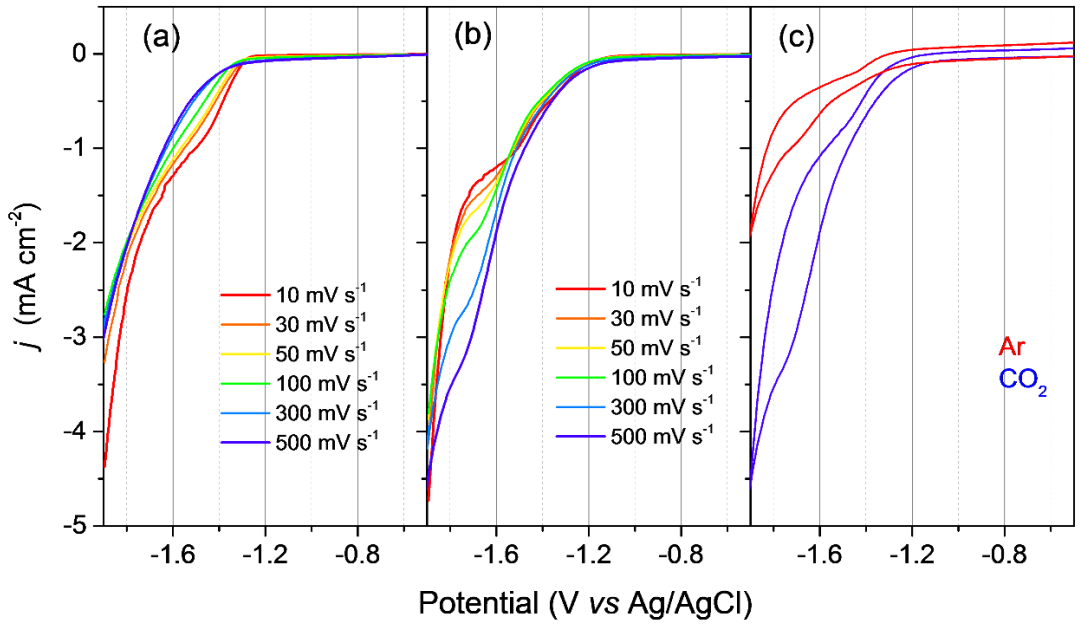

Figure 2.28 LSVs of CMP-(bpy)$_{20}$ (a) and CMP-(bpy)$_{20}$-Mn (b) at various different scan rates under an atmopshere of CO_2, accompanied by CV of CMP-(bpy)$_{20}$-Mn (c) under argon (red) and CO_2 (blue) in 0.1 M pH 7 phosphate buffer.

Increasing the scan rate does however lead to the growth of a new catalytic wave between -1.6 and -1.8 V under CO_2 using CMP-(bpy)$_{20}$-Mn, Figure 2.28b. Using CMP-(bpy)$_{20}$ we do not observe the same behaviour, indicating that the electrochemical activity in this region is due to the Mn centres within the material. The increasing current under CO_2 at high scan rates at more negative potentials indicates that substrate consumption (CO_2/H^+) is limiting catalysis in this potential region.[131] Therefore, it can be concluded that two CO_2 reduction pathways are

potentially occurring with the Mn centres within the CMP-$(bpy)_{20}$ material. At potentials positive of -1.6 V slow catalysis (which therefore is not limited by the availability of substrate) occurs. Negative of -1.6 V a faster catalytic pathway is available.

To asses if CO_2 reduction can occur, CPE experiments were carried out and are shown in Table 2.3. Gas-chromatography (GC) analysis was used to detect gaseous products formed and were recorded every hour. Such experiments are carried out in a gas tight cell, and the electrolyte (phosphate buffer) is stirred to promote gaseous products out of solution and into the head space. For all potentials, the FE for CO_2 reduction was low and the total FE is < 100% in all cases (maximum 85%). As no liquid products were detected from ion-chromatography (IC), the portion of unaccounted charge passed is likely to be due to (i) a leak present within the cell despite best efforts to keep the cell gas tight, or (ii) liquid product formation which was not seen after analysing post CPE electrolyte *via* IC. TONs up to *ca.* 1300 are observed at -1.6 V which is indicative of catalysis as opposed to catalyst degradation which would otherwise render a TON < 3 due to loss of the carbonyl ligands. To ensure the presence of CO was not due to degradation of the CMP-$(bpy)_{20}$-Mn, CPE under argon was carried out for 3 hours at -1.6 V with 610 mC of charged passed yielding FEs of 33.24% and 0.19% for H_2 and CO respectively. The FE was very low, meaning that either gas is leaking from the cell or that the sample is degrading. Repeated experiments under argon showed no improvement in FE suggesting that sample degradation may be a concern in the absence of CO_2. Regardless, the greatly decreased rate of CO production (*ca.* 6 times) under argon, coupled to the lower current density during the experiment strongly suggests that the CO does come from the CO_2.

Table 2.3 FE for CMP-$(bpy)_{20}$-Mn/Nafion$_{0.5\%}$ electrodes in 0.1 M phosphate buffer electrolyte. CPE was carried out at various potentials under a CO_2 atmosphere for 3 hours. TONs were determined based on 100% of bpy sites occupied with Mn catalyst, and 100% Mn centers being electrocatalytically active for a 10 µL drop, 54 nmol.† The TON was determined by using 2.7 × 10^{-11} mol of electroactive catalyst.‡

Potential ($V_{Ag/AgCl}$)	Charge passed (mC)	FE_{H2}%	FE_{CO}%	FE_{Total}%	$TON_{CO}^{\dagger}$ (total Mn content)	$TON_{CO}^{\ddagger}$ (electroactive content)
-1.4	531	69.68	0.44	70.12	0.22	448
-1.5	1318	56.17	0.16	56.33	0.19	393
-1.6	1589	84.57	0.43	85.00	0.71	1311

Analysis of charge versus time plot from CPE measurements shows a lack of stability during bulk electrolysis at all of the potentials tested, due to the presence of a slight curvature of the slope (Figure 2.29a-c). This instability is likely to be due to the formation of bubbles on the electrode surface during prolonged CPE measurements causing rupturing of the film, indicated by the sudden decrease in current at various times (Figure 2.29d).

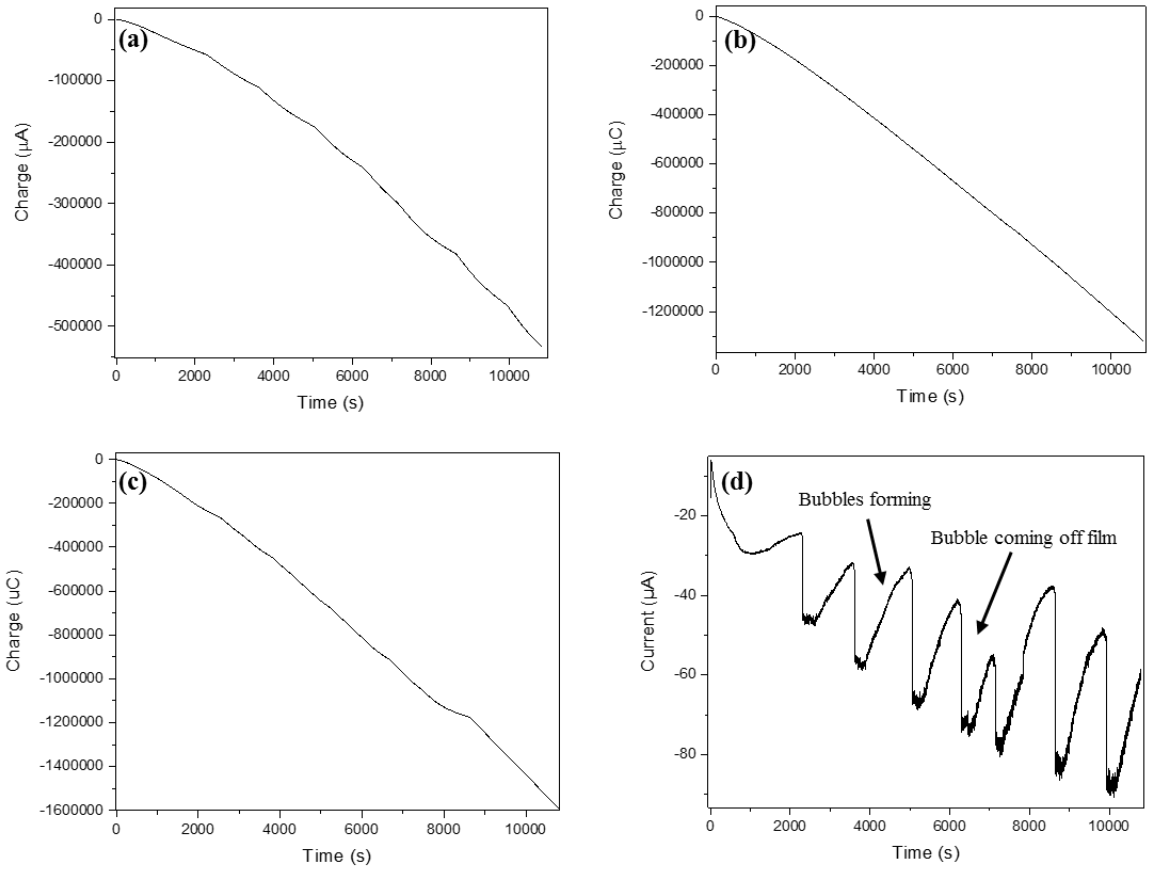

Figure 2.29 Charge vs time plot obtained from CPE measurements at -1.4 (a), -1.5 (b) and -1.6 V (c). The current vs time plot for -1.4 V is shown here as an example to show the formation of bubbles on the electrode surface during CPE measurements (d).

2.2.2.3 Improving the concentration of electrochemically active Mn sites in CMP-(bpy)$_{20}$-Mn/Nafion electrodes:

Nafion is a good proton conductor, however it is not a good electron conductor and therefore we investigated how changing the concentration of Nafion impacted the electrochemical activity. We tested the use of casting solutions containing different amounts of Nafion (5, 0.5 and 0.25% wt.) for the immobilisation of CMP-(bpy)$_{20}$-Mn on a GCE surface. Higher Nafion concentrations (5% wt.) did not form stable films by drop casting a mixture of CMP-(bpy)$_{20}$-Mn/Nafion, due to immiscibility between the hydrophobic CMP-(bpy)$_{20}$ and hydrophilic Nafion solution. Therefore, electrodes with 5% wt solutions were fabricated *via* a bilayer approach as shown in Figure 2.30, where CMP-(bpy)$_{20}$-Mn (5.5 mg/mL) was

suspended in acetonitrile (1 mL) and drop cast onto the surface of a GCE electrode. Once dry, 5 µL of 5% Nafion was deposited on top of CMP-$(bpy)_{20}$-Mn and allowed to dry in air.

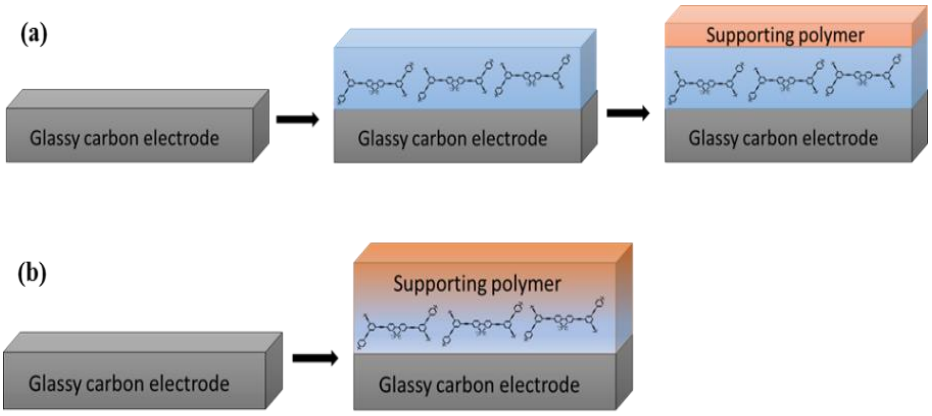

Figure 2.30 Schematic diagram representing the fabrication of a CMP-$(bpy)_{20}$-Mn/Nafion electrode via a bilayer (a) or mixed casting approach (b).

CVs of a CMP-$(bpy)_{20}$-Mn/$Nafion_{5\%}$ electrode showed no distinct electrochemical features, indicating either (i) a lack of electroactive catalytic centres present due too low conductivity of the CMP-$(bpy)_{20}$ backbone, or (ii) the lack of charge transport through a thick layer of Nafion, Figure 2.31. As we have shown so far in this chapter, using a mixed casting method with $Nafion_{0.5\%}$ the presence of electroactive Mn centres for CMP-$(bpy)_{20}$-Mn electrodes concluded the latter to be the limiting factor. Supporting this conclusion are experiments where the concentration of the Nafion casting solution (5%) was kept constant, but the volume deposited (2 µL) *via* a bilayer approach was decreased. These samples showed an improvement in the CV response with a clear reduction at -1.5 V under argon (Figure 2.31a). However, activity was still below that observed for the 0.5% wt. Nafion films prepared by casting a mixed CMP-$(bpy)_{20}$-Mn/Nafion suspension (described above).

Attempts to prepare films using Nafion concentration as low as 0.25% wt. *via* a mixed casting procedure produced unstable films upon both immersion and the application of a bias. As shown in the previous section, films prepared with 0.5% wt. Nafion concentration resulted in a good electrochemical stability when fabricated *via* a mixed casting method, therefore it was concluded that no further gains could be made by modifying the content of the supporting Nafion polymer.

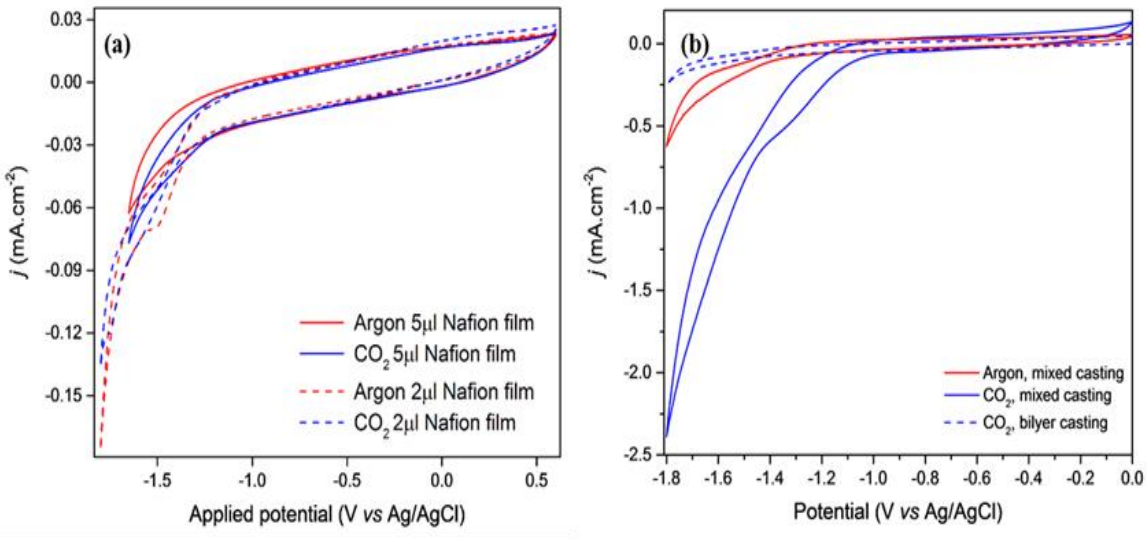

Figure 2.31 CV of CMP-(bpy)$_{20}$-Mn at 10 mVs^{-1} with a 5 µL (solid) and 2 µL (dashed) bilayer of Nafion under an argon (red) and CO_2 (blue) atmosphere (a). 100 mVs^{-1} CV under argon (red) and CO_2 (blue) of CMP-(bpy)$_{20}$-Mn in a mixed casting with Nafion$_{0.5\%}$ (solid lines) and 2 µL Nafion$_{5\%}$ under CO_2 (blue dashed) (b). 5 µL of CMP-(bpy)$_{20}$-Mn was deposited onto a GCE during electrode preparation. Electrochemistry was carried out in 60 mM phosphate buffer at ~pH 7, using a Pt counter electrode and Ag/AgCl reference electrode.

Soaking of the CMP-(bpy)$_{20}$-Mn/Nafion$_{0.5\%}$ electrode overnight, < 20 hours, did however increase the current density under both argon and CO_2 (Figure 2.32) likely to be due to increased wetting/hydration of the Nafion support polymer.[132,133] Broad reductions were present under argon at -1.30 and -1.47 V (Figure 2.32). Upon the addition of CO_2, the reduction features became more pronounced with an increase in current density to *ca.* 3 mA cm^{-2}.

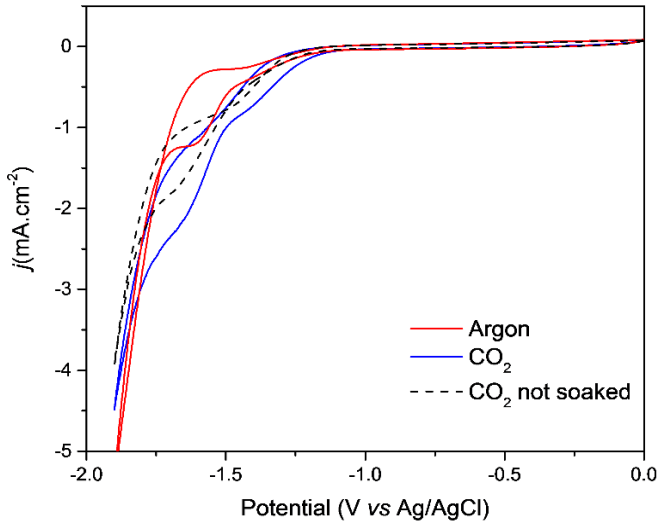

Figure 2.32 CV of CMP-(bpy)$_{20}$-Mn /Nafion electrode at a scan rate of 100 mVs^{-1}, showing soaking of the electrode prior to use gave increased activity under argon (red, solid) and CO_2 (blue, solid) in comparison to no prior soaking under CO_2 (black, dashed). Analysis was carried out in 0.1 M phosphate buffer pH 7 with a Pt counter electrode and Ag/AgCl reference electrode.

Although the CMP-$(bpy)_{20}$ framework is made up of aromatic groups and is therefore expected to be highly conductive, the presence of sp bonds within its structure allows for free rotation around the bonds. Therefore, limited long-range regions of localised conjugation are present, but long-range electron transport may be limited. This results in a low concentration of the Mn centres being electroactive. It is proposed, that in the electrodes described so far, only sites very close to/on the carbon electrode interface will be electroactive. As previously discussed in the introduction to this chapter, the addition of NTs has been shown to increase the electroactive concentration in CO_2 reduction electrodes containing molecular catalysts.[21] Therefore, NTs were added into the film preparation in a 1:1 mass ratio with CMP-$(bpy)_{20}$-Mn. As the previous section showed, soaking the electrode exhibited optimal activity, and so the electrode were soaked for a minimum of 20 hours prior to use. Figure 2.33 shows a significant increase in current density, to *ca.* 30 mA cm^{-2} (*vs* 3 $mA.cm^{-2}$ Figure 2.32, in the absence of NTs) under CO_2, indicating an increase in electroactive Mn centres upon the addition of NTs. The current densities achieved here are among the highest reported for this class of molecular catalyst in aqueous electrolyte,[22–24,40] however films were found to be unstable under catalytic conditions, regularly breaking apart due to the presence of gas bubbles. A CPE experiment was achieved at -1.4 V, but relatively poor selectively was still observed (FE_{H_2}% = 110 and FE_{CO}% = 4).

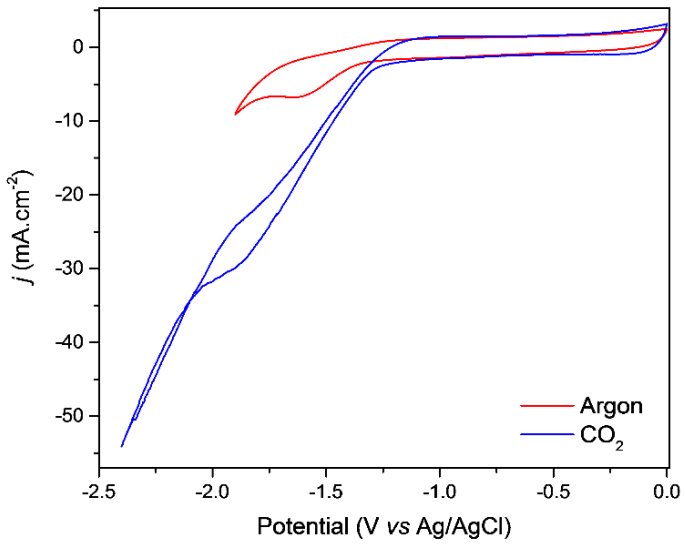

Figure 2.33 CV of CMP-$(bpy)_{20}$-Mn/Nafion/NT after soaking for ~ 20 hours under an argon (red) and CO_2 atmosphere (blue) in 0.1 M phosphate buffer, pH 7, at a scan rate of 100 mVs^{-1}. Voltammogram's were recorded using a Pt counter electrode and Ag/AgCl reference electrode.

2.2.2.4 CMP-(bpy)$_{20}$-Mn/Polyaniline electrodes for CO_2 reduction

Polyaniline (PANI) is a known conducting polymer, therefore experiments were attempted using films coated with the emeraldine salt of PANI, as it was hoped to both increase the surface-active catalyst content in addition to improving film stability. Intimate mixing of the PANI with CMP-(bpy)$_{20}$-Mn may overcome the known issues related to the low levels of conjugation of the framework. However, PANI has also been reported to act both as a CO_2 reduction electrocatalyst[134–136] and photoelectrode[137] in its own right. Therefore, initial control electrochemical experiments of PANI films were carried out on a GCE by drop casting 10 µL of PANI (25 mg) dissolved in DMF (1 mL) and left to dry for < 20 hours. Experiments at higher scan rates (100 mV s^{-1}, Figure 2.34a) in pH 7 phosphate buffer (60 mM) under argon are dominated by PANI based reductions at -0.02 and -0.35 V and an oxidation at 0.03 V, attempts to go to more positive potentials led to instability of the films. The reductions show a significant shift in the presence of CO_2 to -0.25 and -0.60 V, Figure 2.34a. Previous electrochemical studies of PANI have assigned these features to the fully reduced form owed to the electrochemical formation known as a leucoemeraldine base, through to the fully oxidised form of pernigrailine.[138] As the emeraldine salt is protonated it is electrically conducting.[138] At slower scan rates (Figure 2.34b), comparable to those used in the electrocatalysis studies below (5 - 10 mV s^{-1}) it can be seen that at potentials negative of -1.6 V (more negative than CMP-(bpy)$_{20}$-Mn based reductions) a marked increase in current does occur under CO_2 using the PANI film.

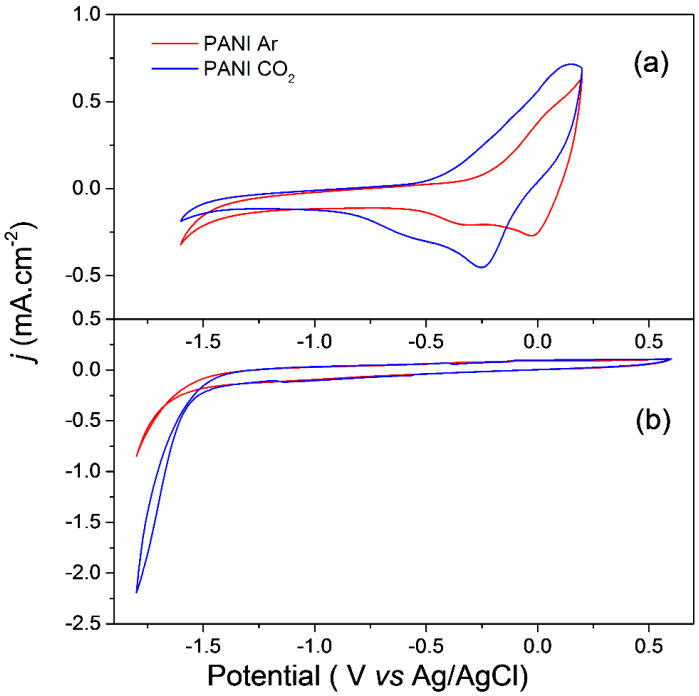

Figure 2.34 CV of PANI under an argon (red) and CO_2 (blue) atmopshere in 60 mM phosphate buffer electrolyte, pH 7, using a Ag/AgCl reference electrode and a Pt counter electrode at a scan rate of 100 mVs^{-1} (a) and 5 mVs^{-1} (b).

Stable electrodes of CMP-$(bpy)_{20}$-Mn/PANI as shown in Figure 2.35, were prepared by casting a suspension of 5 µL or 10 µL of CMP-$(bpy)_{20}$-Mn (5.5 mg/mL) in DMF onto the surface of an electrode, and once dry 5 µL of 2.5% wt. PANI in DMF was cast on-top of the electrode and left to dry in the dark. Attempts to make films from mixtures of PANI and CMP-$(bpy)_{20}$-Mn directly exhibited lower activity.

Figure 2.35 Photograph of CMP-$(bpy)_{20}$-Mn/PANI electrode before and after electrochemical analysis.

CVs of the CMP-$(bpy)_{20}$-Mn/PANI electrode in 60 mM phosphate buffer under an argon atmosphere showed a broad reduction at *ca.* -1.65 V. When under a CO_2 atmosphere current densities up to -0.46 mA.cm^{-2} were achieved Figure 2.36a. Due to the broadness of the reduction in the CV, square wave voltammetry was used to examine the sample. SWV of CMP-$(bpy)_{20}$-Mn/PANI under argon showed the presence of two reductions at *ca.* -1.45 and -1.6 V, Figure 2.36b. SWV of CMP-$(bpy)_{20}$/PANI and PANI electrodes has also been carried out. These indicate that the reduction at -1.45 V can be assigned to a CMP-$(bpy)_{20}$ reduction, or to the reduction of residual Pd in the CMP-$(bpy)_{20}$ from the synthesis. The second reduction at -1.60 V is therefore assigned to that of the direct two electron reduction of the [Mn(bpy)$(CO)_3$] moieties within CMP-$(bpy)_{20}$-Mn/PANI to form the catalytically active species, CMP-[Mn$(bpy)_{20}(CO)_3]^-$, in a manner similar to seen in the previous section when Nafion was used as the supporting polymer. Again, these results indicate that the immobilisation of the catalyst within the CMP-$(bpy)_{20}$ framework has prevented dimerisation. An increase in current density up to *ca.* 0.5 mA cm^{-2} at -1.6 V was obtained when CO_2 was present within the cell with a current increase at the potentials where the Mn based reduction is proposed to occur, suggesting that the complex remains catalytically active towards CO_2. Surprisingly, when PANI is used as a supporting polymer the electrochemical potentials for both CMP-$(bpy)_{20}$ and Mn based reductions are shifted to more negative potentials, which could indicate that the PANI interacts more strongly with CMP-$(bpy)_{20}$-Mn.

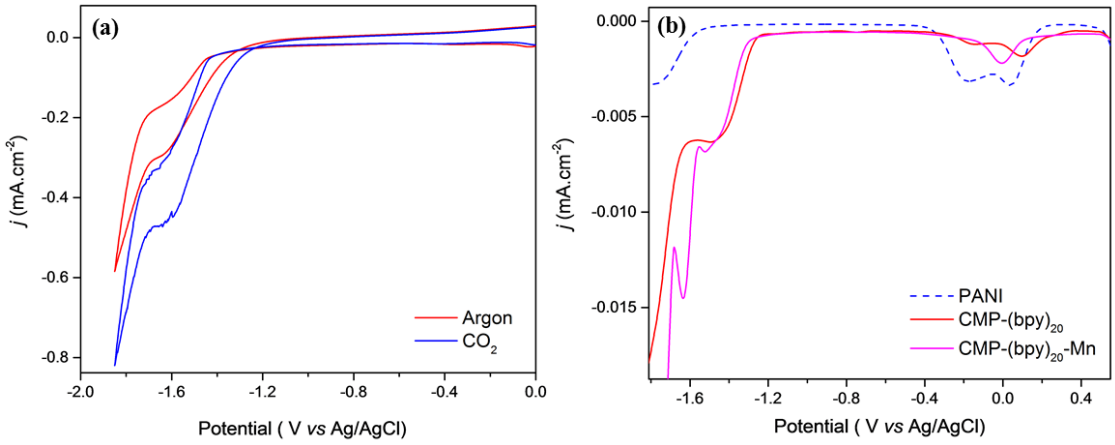

Figure 2.36 CV analysis of CMP-(bpy)$_{20}$-Mn/PANI under an argon (red) and CO_2 (blue) at a scan rate of 10 mVs^{-1} (a). SWV under argon of PANI (blue), CMP-(bpy)$_{20}$ (red) and CMP-(bpy)$_{20}$-Mn (pink) recorded at 5 Hz (b). Voltammograms were recorded in 60 mM phosphate buffer electrolyte, pH 7, using a Ag/AgCl reference electrode and a Pt counter electrode.

Although PANI was anticipated to help increase the concentration of electroactive catalyst, the current densities obtained were lower, in comparison to the CMP-(bpy)$_{20}$-Mn/Nafion electrodes discussed earlier in this chapter. Using square wave voltammetry an electroactive content of 8.55 × 10^{-13} mol was determined for CMP-(bpy)$_{20}$-Mn/PANI electrodes, Figure 2.37. The lower activity observed in comparison to Nafion electrodes (2.7 × 10^{-11} mol) could be due to (i) PANI not penetrating the CMP-(bpy)$_{20}$ network efficiently to increase the concentration of active Mn centres or (ii) increased proton source at Mn sites in the presence of PANI resulting in increased proton reduction.

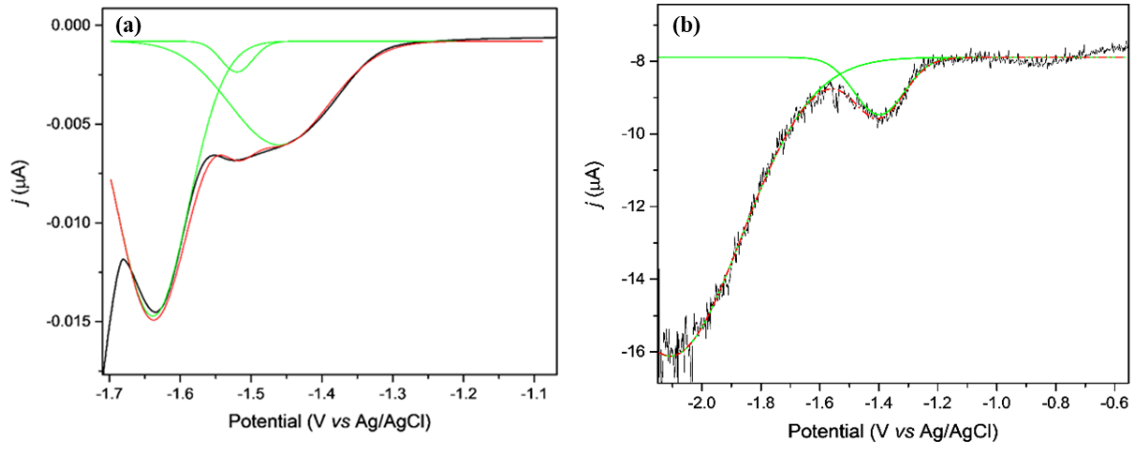

Figure 2.37 SWV of CMP-(bpy)$_{20}$-Mn/PANI (a) and CMP-(bpy)$_{20}$-Mn/PANI/NT (b) under an atmopshere of argon at a frequency of 5 Hz in 60 mM phosphate buffer electrolyte, ~pH 7.

Addition of NTs to the electrode was also investigated to increase the electroactive content of CMP-(bpy)$_{20}$-Mn/PANI electrodes,[21,22,24] by a mixed casting of CMP-(bpy)$_{20}$-Mn/NTs in a 1:1 weight ratio in PANI (Figure 2.38). Addition of NTs to the mixed CMP-(bpy)$_{20}$-Mn/PANI electrode resulted in a large increase in current density *ca.* 10 fold to *ca.*12 mA cm^{-2} under CO_2 at -1.6 V (compared to *ca.* 1.2 mA cm^{-2} in the absence of NTs, Figure 2.38b), and an increase in electroactive content to 5.1 nmol from fitting of the SWV shown in Figure 2.37b.

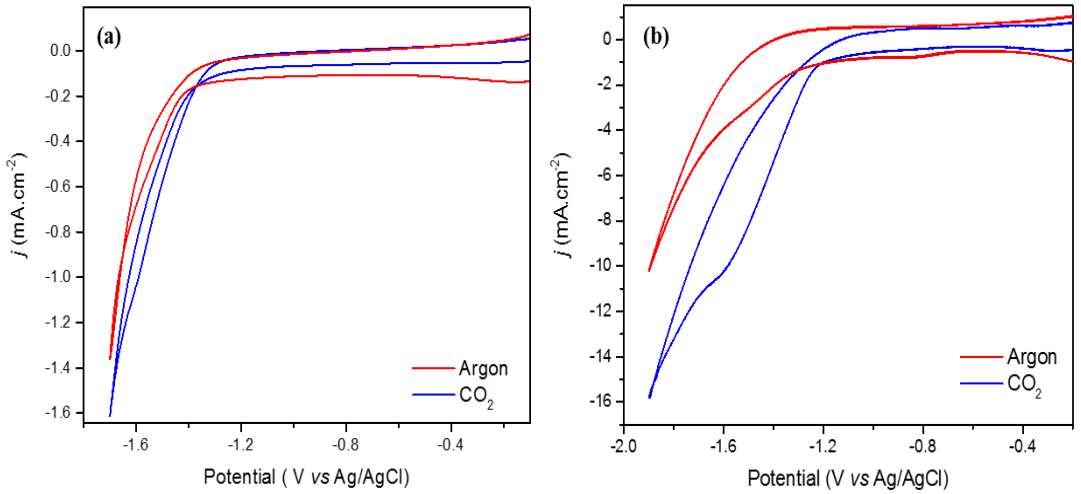

Figure 2.38 CV analysis of CMP-(bpy)$_{20}$-Mn/PANI (a) and CMP-(bpy)$_{20}$-Mn/PANI/NT (b) electrodes at a scan rate of 100 mVs^{-1} in 60 mM phosphate buffer, pH 7, under an argon (red) and CO_2 (blue) atmosphere. Electrodes were prepared by drop casting 5 µL of material as a mixed casting. NTs were added in a 1:1 mass ratio with CMP-(bpy)$_{20}$-Mn. Ag/AgCl reference electrode and Pt counter electrode were used.

Although good current densities were achieved during CV measurements for CMP-(bpy)$_{20}$-Mn/NT/PANI product analysis was hampered due to instability of the electrode during CPE measurements. As with the CMP-(bpy)$_{20}$-Mn/NT/Nafion samples the films were found to rupture, likely due to the high levels of gas (CO, H_2) being produced. Therefore, product analysis of CMP-(bpy)$_{20}$-Mn/PANI electrodes at -1.6 and -1.7 V was carried out. Total FEs > *ca.* 55% were obtained at -1.6 and -1.7, Table 2.4.

Table 2.4 FEs for CMP-(bpy)$_{20}$-Mn/PANI on a 0.07 cm^2 GCE at -1.6 V and -1.7 $V_{Ag/AgCl}$ after 2.2 hours† and 4 hours‡ of CPE under a CO_2 atmosphere in pH7 phosphate buffer. TONs were determined based on 100% of bpy sites occupied with Mn catalyst, and 100% Mn centers being electrocatalytically active for a 5 µL drop, 27 nmol.†Electroactive content was detrermined by integration of the Mn reduction from SWV, 8.55 × 10^{-13} mol.‡

Potential ($V_{Ag/AgCl}$)	Charged passed (mC)	FE_{H2}%	FE_{CO}%	Total FE%	$TON_{CO}^{\dagger}$ (total Mn content)	$TON_{CO}^{\ddagger}$ (electroactive content)
-1.6†	1830	34.47	0.13	34.60	0.47	14,766
-1.7‡	1500	54.70	0.05	54.75	0.15	4584

Again, hydrogen remains the dominant product from CPE measurements, and the low overall FEs indicated that gases may be being lost during the experiment. However, as the selectivity towards CO_2 reduction was low this was not further investigated. From CPE measurements we can also gain insight into the stability of the electrode over a prolonged time. The linear response obtained for the amount of charge generated over a 3-hour electrolysis period indicates good stability of the electrode (Figure 2.39).

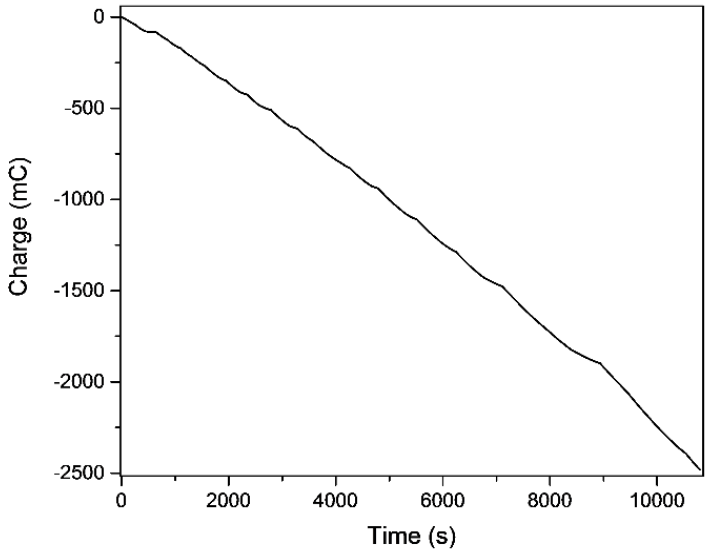

Figure 2.39 CPE of CMP-(bpy)$_{20}$-Mn/PANI held at -1.6 V for 3 hours under a CO_2 atmosphere at pH 7 in 60 mM phosphate buffer electrolyte.

2.2.2.5 Investigating the behaviour of [Mn(bpy)(CO)$_3$Br]/NT/PANI electrodes

The use of PANI as a supporting polymer for the immobilisation of the parent molecular catalyst ([Mn(bpy)(CO)$_3$Br]) has not previously been reported in the literature. Previous experiments on [Mn(bpy)(CO)$_3$Br]/NT/Nafion electrodes showed reasonable levels of activity towards CO_2 reduction. Therefore, it was decided to also test [Mn(bpy)(CO)$_3$Br]/NT/PANI electrodes. [Mn(bpy)(CO)$_3$Br]/NT/PANI electrodes were prepared in a similar way to that of CMP-(bpy)$_{20}$-Mn, where 5 µL [Mn(bpy)(CO)$_3$Br] (5.5 mg/mL) and NTs (5.5 mg/mL) were suspended in a solution of 2.5% w.t PANI, and films were fabricated *via* drop casting. CV analysis under argon shows three reduction features *ca.* -0.95, -1.12 and -1.40 V in 0.1 M K_2CO_3 electrolyte (Figure 2.40). The first two reductions are assigned to the formation of the dimer species upon loss of a bromide or solvent ligand respectively, which is further confirmed by the presence of a large re-oxidation at *ca.* +0.3 V, due to cleavage of the dimer bond by comparison to the known electrochemical behaviour of

the complex in MeCN solution, and when immobilised in a Nafion polymer.[18,21] The third reduction at -1.40 V is assigned to the formation of $[Mn(bpy)CO)_3]^-$. When under a CO_2 atmosphere, the current density increases significantly at potentials negative of -1.1 V, reaching a maximum of *ca.* 7 mA cm^{-2} at -1.3 V and *ca.* 11 mA cm^{-2} at -1.6 V, indicative of catalytic CO_2 reduction. The presence of two catalytic regions in Figure 2.40 indicates that in a manner similar to that seen in solution, both $[Mn_2(bpy)_2(CO)_6]$ and $[Mn(bpy)(CO)_3]^-$ are electrocatalytically active.[34]

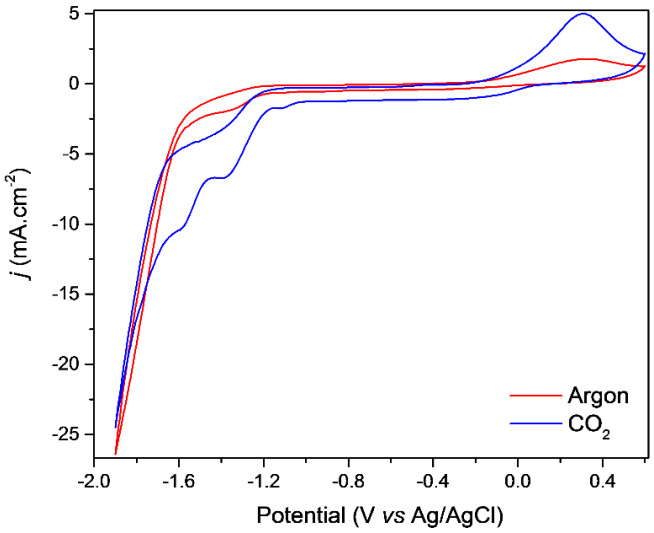

Figure 2.40 CV of [Mn(bpy)(CO)₃Br]/PANI/NT under an argon (red) and CO_2 (blue) atmosphere. Voltammograms were recorded at a scan rate of 50 mVs^{-1} in 0.1 M K_2CO_3 electrolyte with a Pt counter electrode and Ag/AgCl reference electrode.

Comparison of the CVs of both $[Mn(bpy)(CO)_3Br]$/PANI and CMP-$(bpy)_{20}$-Mn/PANI electrodes further supports the proposed 2 electron reduction to CMP-$[Mn(bpy)_{20}(CO)_3]^-$, Figure 2.41. At slower scan rates (10 mVs^{-1}), only one broad reduction for CMP-$(bpy)_{20}$-Mn is measured. In contrast, $[Mn(bpy)(CO)_3Br]$/PANI has two reductions at -1.15 and -1.49 V assignable to the two one electron reduction pathway. Upon reoxidation, three oxidations are assigned to dimer and PANI oxidations at -0.66, 0.35 and 0.15 V (Figure 2.41).

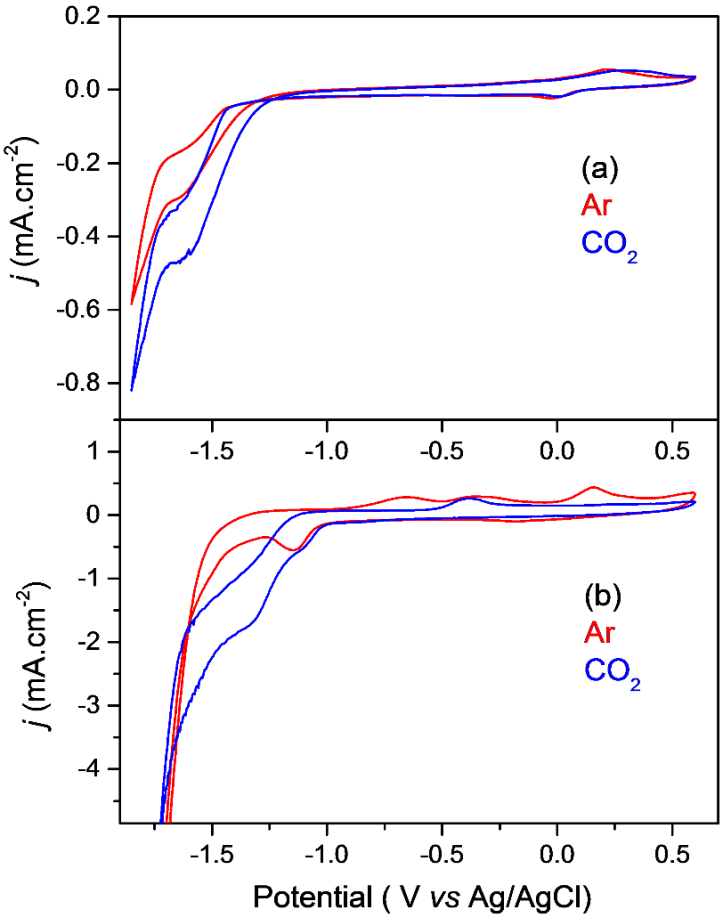

Figure 2.41 CV of CMP-(bpy)$_{20}$-Mn/PANI (a) and [Mn(bpy)(CO)$_3$Br]/PANI (b) under argon (red) and CO_2 (blue) at a scan rate of 50mVs^{-1} in 0.1 M K_2CO_3 electrolyte.

CPE measurements have been carried out at a range of potentials under CO_2. Potentials tested include those where $[Mn_2(bpy)_2(CO)_6]$ would be dominant (-1.2, -1.3 V), and where $[Mn(bpy)(CO)_3]^-$ can be formed (-1.45 V) in order to assess if each species is active towards CO_2 reduction. In all cases hydrogen was the dominant product, however at -1.2 V a FE of 22% was achieved for CO production, Table 2.5.

Table 2.5 FEs for 10 µL [Mn(bpy)(CO)$_3$Br]/PANI/NT electrodes in aqueous (0.1 M K_2CO_3) electrolyte. CPE was carried out at various potentials under a CO_2 atmosphere for 3 hours. The TON was determined by using the total [Mn(bpy)(CO)$_3$Br] deposited, 146.7 nmol,† and the electroactive content of [Mn(bpy)(CO)$_3$Br], 2.7 nmol, was determined from the integration of the reduction under Ar.‡

Potential ($V_{Ag/AgCl}$)	Charged passed (mC)	FE_{H2}%	FE_{CO}%	Total FE%	TON_{CO} † (total Mn content)	TON_{CO}‡ (electroactive content)
-1.2	919	54.20	22.0	76.24	7.14	385.19
-1.3	2570	91.80	1.98	93.78	1.80	97.7
-1.45	1973	63.04	1.52	64.56	1.06	57.41

At -1.2 V very high TONs were achieved (385) based on the electroactive content of Mn (determined from SWV, Figure 2.42), and even when the TON is calculated based on the total Mn content it is greater than 3 at -1.2 V, confirming catalysis and that CO cannot have solely come from [Mn(bpy)$(CO)_3$Br] complex degradation.

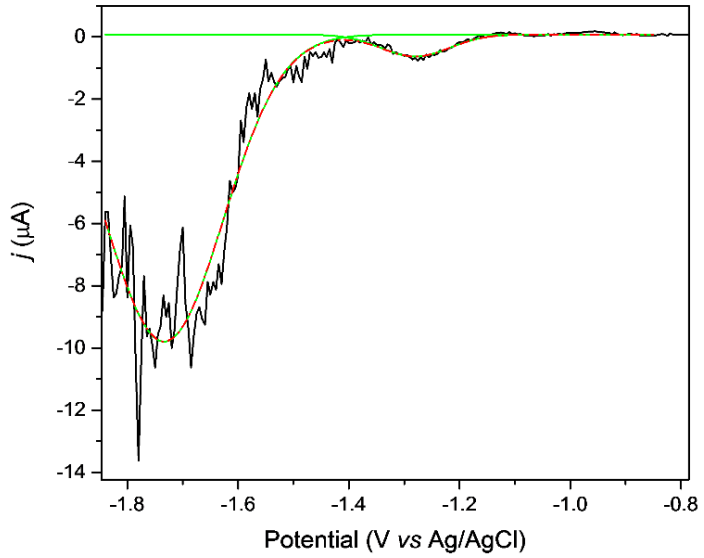

Figure 2.42 SWV of [Mn(bpy)$(CO)_3$Br]/PANI/NT under an atmopshere of argon at a frequency of 5 Hz in 0.1 M K_2CO_3 electrolyte, pH 7, with fitting (green) and overall fit (red) also shown.

2.2.2.6 Templating CMP-$(bpy)_{20}$-Mn onto the surface of a GCE

As discussed earlier, we anticipate the concentration of electroactive catalyst to be lower than the total concertation of Mn centres present within the CMP-$(bpy)_{20}$, due to breaks in the long-range conjugation due to rotation around sp bonds within the CMP-$(bpy)_{20}$ framework. To overcome this in the previous section we added NTs to the electrode film. In the final part of this chapter, an alternative route that exploits the strong π-π interactions that can be formed between the CMP-$(bpy)_{20}$ and a GCE are presented. The aim is to template the CMP-$(bpy)_{20}$ directly on the surface of a GCE or NT as schematically shown in Figure 2.43. The templating of a thin film also allows for the removal of the supporting polymer, which was hoped to further improve the catalytic activity.

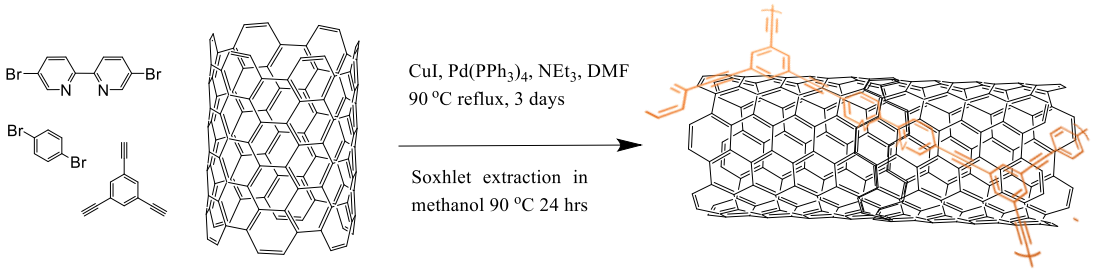

Figure 2.43 Schematic diagram to demonstrate templating CMP-(bpy)$_{20}$-Mn onto a carbon surface such as a GCE, or as shown in the figure for ease NTs.

Electrodes were prepared by adding a GCE into the CMP-(bpy)$_{20}$ synthesis method (D) during the first step, Figure 2.12. After polymerisation had occurred the electrode was removed from the bulk of the CMP-(bpy)$_{20}$ material, and dried in a vacuum over overnight at 110˚C. The electrode was then sonicated for *ca.* 15 minutes in water to remove any remaining bulk material to leave only a thin film on the surface of the GCE, indicative by a brown glaze across the electrode surface. Addition of [Mn(CO)$_5$Br] was incorporated by soaking the electrode in a solution of [Mn(CO)$_5$Br] in diethyl ether, refluxing at 45˚C overnight. The electrode was then washed and left stirring in DCM overnight to remove any unbound [Mn(CO)$_5$Br] and dried at 50˚C.

Raman spectroscopy is a quick and none invasive method used to determine if there was a change from the pristine GCE surface upon templating. Features at 1345, 1592 and *ca.* 2700 cm^{-1} are bands associated to sp2 hybridised carbons known as D, G and G′ bands.[139] The G bands are often seen in graphene and graphite, whereas the D band is observed in NT like materials indicating disorder or defects within the material.[139] When CMP-(bpy)$_{20}$-Mn has been templated on the surface of a GCE, a change to the bands occurs as a result of the increased presence of sp2 carbon bonds on the GCE surface. A change in the ratio of D and G bands, indicate an increase in sp2 hybridised defects and C-H stretches, which are consistent with the type of stretches expected from the CMP-(bpy)$_{20}$ framework (Figure 2.44).

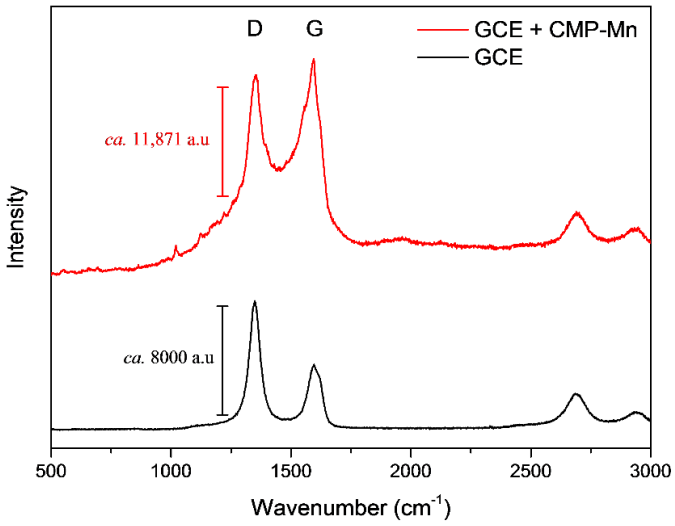

Figure 2.44 Raman spectroscopy of a pristine GCE (black) and a GCE with CMP-(bpy)$_{20}$-Mn templated on the surface (red). Spectra were recorded with Dr. M. Forster.

FTIR spectroscopy was unable to detect the presence of the metal carbonyl complex or the CMP-(bpy)$_{20}$ material. The most facile method to characterise the electrode was by electrochemical methods as no redox features were visible from CV analysis. Therefore, square wave voltammetry was used to gain insight into the electrochemical behaviour of the electrodes. Two reductions at -1.5 and -1.65 V were observed, which are more negative than that reported for the PANI or Nafion systems. Comparing the SWV of both templated CMP-(bpy)$_{20}$ and CMP-(bpy)$_{20}$-Mn, the electrochemical characterisation of the templated system is similar to what has previously been discussed in this chapter. Two reduction features were observed for CMP-(bpy)$_{20}$-Mn one of which (-1.5 V) is assigned to reductions of the CMP-(bpy)$_{20}$ or Pd, and the other to the two electron reduction of the Mn catalyst (-1.65 V) (Figure 2.45).

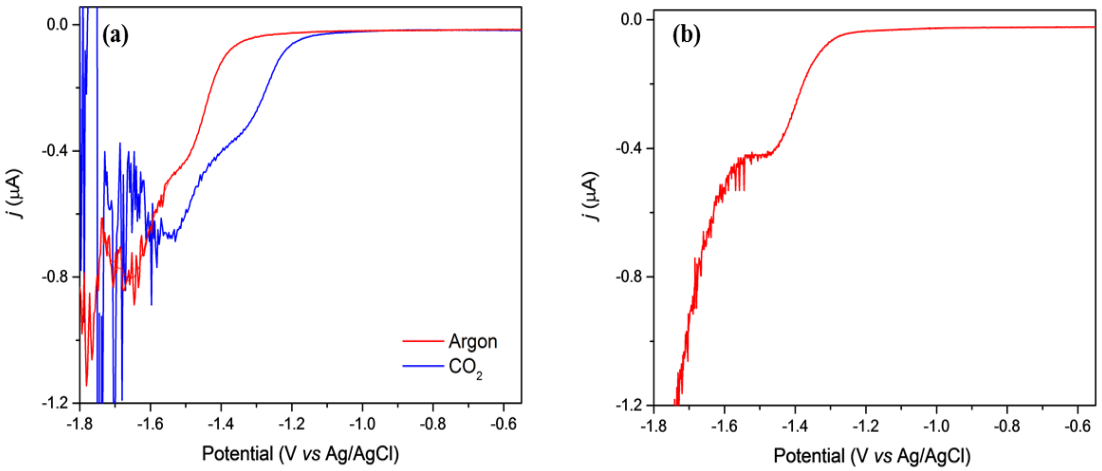

Figure 2.45 SWV of CMP-(bpy)$_{20}$-Mn templated on the surface of a GCE under argon (red) and CO_2 (blue) (a). SWV of CMP-(bpy)$_{20}$ templated on the surface of a GCE under argon (b). SWVs were recorded at a frequency of 5 Hz in 60 mM phosphate buffer with a Pt counter electrode and Ag/AgCl reference electrode.

To determine if the fabrication of a thin film had any catalytic activity, we carried out CPE of the electrode at various potentials under CO_2 using GC and IC for product determination. Differential pulse voltammetry (DPV) was used to determine the electroactive content (Mn) of CMP-(bpy)$_{20}$-Mn, Figure 2.45. Over the course of the 1 hour CPE measurements, the electrode exhibited good stability overall (Figure 2.46), however as with previous studies the dominant product was H_2 with minimal CO production.

Table 2.6 FEs for CMP-(bpy)$_{20}$-Mn templated on the surface of a GCE in 0.1 M phosphate buffer electrolyte. CPE screening was carried out at various potentials under a CO_2 atmosphere for 1 hour. The TON was determined from DPV measurements.

Potential ($V_{Ag/AgCl}$)	Charge passed (mC)	FE_{H2}%	FE_{CO}%	FE_{Total}%	TON_{CO}[a]
-1.3	151	41.56	0.169	41.73	4.7
-1.4	417	69.35	0.057	67.41	4.3
-1.5	331	87.97	0.098	88.07	5.9
-1.6	476	88.61	0.078	88.69	6.8

[a]Electroactive content determined from DPV measurements = 2.8×10^{-10} mol.

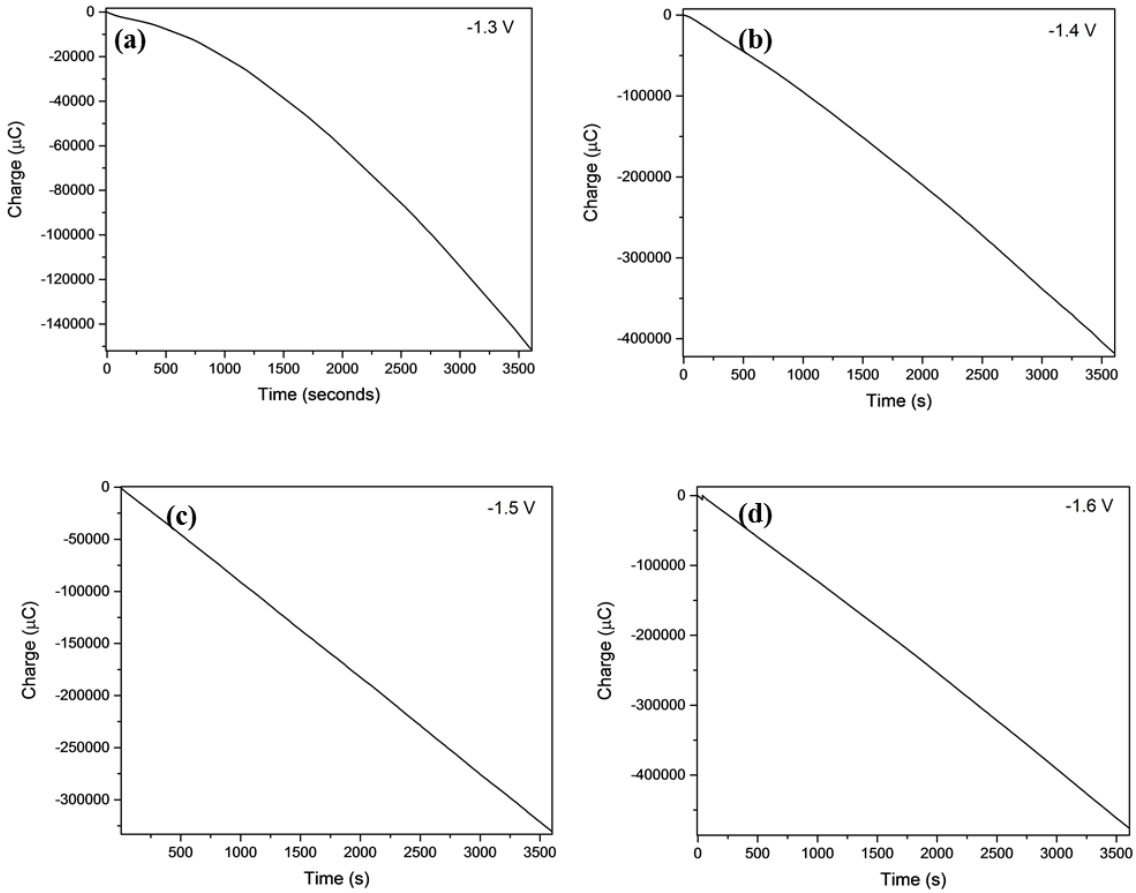

Figure 2.46 CPE of CMP-(bpy)$_{20}$-Mn templated on a GCE, held at -1.3 (a), -1.4 (b), -1.5 (c) and -1.6 V (d) for 1 hour under a CO_2 atmosphere.

Although the FE and yield of CO was low during CPE measurements under CO_2, CPE under an argon atmosphere at -1.5 V showed no CO production only that of hydrogen, confirming that CO produced is not from degradation of the Mn catalyst of CMP-(bpy)$_{20}$ framework. Importantly, when under CO_2 a TON > 3 was obtained, confirming that CO produced was not from the degradation of [Mn(bpy)(CO)$_3$Br] *via* loss of CO ligands, indicating catalysis of the Mn catalyst. To ensure the CMP-(bpy)$_{20}$ itself was not responsible for the formation of CO, CPE of a templated CMP-(bpy)$_{20}$ electrode was carried out under CO_2. After 1 hour of CPE at -1.5 V, in-line with CMP-(bpy)$_{20}$-Mn measurements, more charge was passed (681 mC) and CO and H_2 FEs of 0.025% and 61.97% were obtained. This indicates that for templated samples the CMP-(bpy)$_{20}$ framework can also reduce CO_2, and that further studies of this interesting system are required to fully understand its behaviour.

2.3 Conclusions

[Mn(bpy)$(CO)_3$Br] has been shown to be a selective heterogeneous catalyst in aqueous electrolyte,[21,22,24] allowing for easier recovery of catalyst and products and more efficient electron transfer. The catalytic cycle of [Mn(bpy)$(CO)_3$Br] has been well studied, and is shown that dimerisation of the catalyst is a prerequisite for [Mn(bpy)$(CO)_3]^{-}$ formation, resulting in an increased over-potential for CO_2 reduction to form CO at high rates. Although the dimer complex can be catalytically active it operates at reduced TOFs. Here, we present the incorporation of [Mn(bpy)$(CO)_3$Br] into a CMP framework containing bpy sites to prevent dimerisation.

An optimal loading, *ca.* 5.5% wt, of [Mn(bpy)$(CO)_3$Br] was achieved by post metalation of the CMP-$(bpy)_{20}$ at low temperatures of 45˚C without affecting the porosity of the CMP-$(bpy)_{20}$. Initial studies focused on the immobilisation of CMP-$(bpy)_{20}$-Mn using a Nafion supporting polymer. These works demonstrated that an electroactive Mn complex was present within the CMP-$(bpy)_{20}$ structure, and that the behaviour was markedly different to [Mn(bpy)$(CO)_3$Br] in solution, with the rigid framework preventing dimerisation. However, the electroactive contents of Mn within the CMP-$(bpy)_{20}$ framework were very low. The addition of NTs as an electroactive filler increased current densities to *ca.* 40 $mAcm^{-2}$ under CO_2 for electrodes that were soaked prior to use. Although these initial studies demonstrate it is possible to form an active electrocatalyst within the CMP-$(bpy)_{20}$ framework, bulk electrolysis experiments showed a lack of selectively for CO production with H_2 being the main product.

In an attempt to increase the electroactive content, the use of a conducting polymer, PANI, was also explored. Higher current densities of *ca.* 0.5 $mAcm^{-2}$ were achieved for CMP-$(bpy)_{20}$-Mn/PANI electrodes, *ca.* 5 times greater than the equivalent Nafion electrodes in the absence of NTs. Similarly to Nafion electrodes, selectivity was poor with hydrogen being the dominant product detected and very little CO. Since [Mn(bpy)$(CO)_3$Br]/PANI has yet to be reported in the literature, we explored how the presence of PANI affects the electrochemical behaviour of [Mn(bpy)$(CO)_3$Br]. Product analysis showed selectivity of [Mn(bpy)$(CO)_3$Br] was improved for CO_2 reduction and catalytic activity for CO_2 reduction at -1.2 V was achieved.

To overcome the diffusion limitations observed from lowering the Nafion concentration, and to improve the overall electroactive Mn centres, we templated the CMP-$(bpy)_{20}$ on the surface of the GCE to produce a thin film for reactants and products to diffuse across more facile. TONs up to *ca.* 7 was achieved indicating that activity was not improved by the removal of a supporting polymer. As observed previously, although dimerisation was

prevented, selectivity was poor. Although the local concentration of CO_2 is thought to be high due to the CMPs ability for good CO_2 uptake, low selectivity could be due to diffusion limitations hindering replenishment of CO_2 at the active sites. Other studies have shown that by changing the functional group in the 5,5′ position to EWG or EDG selectivity of this catalyst can be altered.[22] Therefore, it is not unreasonable to suggest that the poor selectivity could be due to the incorporation of the catalyst into the CMP-$(bpy)_{20}$ backbone, which has altered the electron density on the metal centre. Although TONs are low for the system we report here, this is one of the first examples that shows immobilisation of $[Mn(bpy)(CO)_3Br]$ into a porous framework for dimer prevention exhibiting CO_2 reduction, albeit with poor selectivity.[64,67]

2.4 Materials and Methods

2.4.1 Materials

Milli-Q water (18.2 MΩ) was used throughout (Millipore Corp). All chemicals were purchased from Sigma Aldrich except for 5,5′-dibromo-2,2′-bipyridyl which was purchased from TCI chemicals. 3 mm GCE were purchased from IJ Cambriam Scientific Ltd. Argon and helium N6 grade, and CO_2 CP grade were purchased from BOC. Calibrant gas for the GC was a custom order of 500 ppm H_2 and 200 ppm CO in helium.

2.4.2 Methods

Synthesis of CMP-$(bpy)_{20}$: Under an argon atmosphere 1,4 dibromobenzene (0.35 g), 5,5′-dibromo-2,2′-bipyridine (0.34 g) and 1,3,5 triphenylbenzene (0.375 g) were stirred under reflux at 90˚C for 3 days in DMF (8 mL) and NEt_3 (8 mL) with CuI (20 mg) and $Pd(PPh_3)_4$ (40 mg). Over the 3 day period the mixture had turned from a brown suspension to a brown solid. The polymer was then ball milled for 30 minutes, to obtain a powder which was then washed and purified *via* soxhlet extraction in methanol at 90˚C for 3 days. *Yield: 322 mg. Elemental analysis calculated (%): C 92.3, H 3.35, N 4.23; Found: C 82.17, H 3.42, N 4.14. BET surface area: 716 m^2/g. Median pore width: 7.504 Å.*

Synthetic routes of CMP-$(bpy)_{20}$-Mn:

a) CMP-$(bpy)_{20}$ (0.4 g) was suspended in toluene with $[Mn(CO)_5Br]$ (0.25 g) at 110˚C for 24 hours, and washed with methanol, water and chloroform (50 mL each). Followed by stirring in DCM for 2 days to remove any residual $[Mn(CO)_5Br]$. *Yield: 500 mg. BET surface area: 400 m^2/g. Median pore width: 7.326 Å.*

b) All CMP-$(bpy)_{20}$ monomer units were added into a mixture of DMF and NEt_3 as described above, $[Mn(CO)_5Br]$ was added also and the reaction mixture was left to polymerise for 3 days at 90˚C. Soxhlet extraction was then carried out in DCM at 75˚C. *Yield:380 mg Elemental*

analysis calculated (%): C 72, H 2.24, N 3.93; Found: C 56.96, H 2.97, N 3.47. BET surface area: 94.37 m^2/g. Median pore width: 8.273 Å.

c) 1,4 dibromo bipyridine (0.13g) and $[Mn(CO)_5Br]$ (0.2g) were mixed in diethyl ether (30 ml) at 40˚C for 3 hours, and washed with cold diethyl ether yielding an orange product. $[Mn(bpy\text{-}Br_2)(CO)_3Br]$ (0.13 g) was added to a reaction mixture of 1,3,4 triphenylbenzene (0.093 g) and 2,4 dibromobenzene (0.088 g) and stirred under reflux at 90˚C for 3 days in DMF (4 mL) and NEt_3 (4 mL) with CuI (5 mg) and $Pd(PPh_3)_4$ (10 mg). Brown product was washed with chloroform, acetone and methanol (50 mL each) and soxhlet extraction in DCM at 90˚C for 3 days. *Yield of $[Mn(bpy\text{-}Br_2)(CO)_3Br]$:0.17 g. Elemental analysis calculated for $[Mn(bpy\text{-}Br_2)(CO)_3Br]$ (%): C 29.28, H 1.13, N 5.25; Found: C 28.99, H 1.10 N 5.06. ^{1}H NMR (400 MHz, CD_3CN) δ 9.27 (d, J = 1.9 Hz, 2H), 8.29 (dd, J = 8.7, 2.0 Hz, 2H), 8.23 (d, J = 8.7 Hz, 2H). Elemental analysis calculated for CMP-$(bpy)_{20}$-Mn (%):C 72, H 2.24, N 3.93; Found: C 64.67, H 2.60, N 3.31. Yield for CMP-bpyMn: 132 mg BET surface area: 24.34 m^2/g. Median pore width: 9.049 Å.*

d) CMP-$(bpy)_{20}$ (0.25 g) was suspended in diethyl ether with $[Mn(CO)_5Br]$ (0.25 g) at 45˚C for 24 hours, and washed with methanol, water and chloroform (50 mL each), followed by soxhlet extraction in DCM at 75˚C. *Yield: 300 mg. Elemental analysis calculated (%): C 72, H 2.24, N 3.93; Found: C 57.35, H 2.72, N 3.28.*

UV-Visible absorption spectroscopy: Recorded on a Shimadzu UV-2550 UV-VisNIR spectrometer as powders in the solid state in absorption mode.

Fourier-transform infrared (FTIR) spectroscopy: Spectra recorded using a JASCO 4000 FTIR in either absorbance or transmission mode using the appropriate mounting apparatus for solid and liquid samples.

^{1}H-NMR: Recorded on a Bruker 400 MHz spectrometer. Chemical shifts (δ) are reported against d_3-MeCN solvent signal. ^{1}H NMR (400 MHz, CD_3CN) δ 9.27 (d, *J* = 1.9 Hz, 2H), 8.29 (dd, *J* = 8.7, 2.0 Hz, 2H), 8.23 (d, *J* = 8.7 Hz, 2H). The coupling constants, J, are given in Hz, and the multiplicity of the peaks are denoted as: d, doublet and dd, doublet of doublets.

Powder x-ray diffraction (PXRD): Measurements were performed on a PANalytical X'Pert PRO MPD, with a Cu X-ray source, used in high throughput transmission mode with Kα focusing mirror and PIXCEL 1D detector.

Gas sorption: Surface area and pore size distributions were performed on a Micromeritics ASAP 2020 volumetric adsorption analyzser under nitrogen and CO_2 adsorption and desorption at 77.4 K. Samples were degassed at 120˚C or 60˚C for 15 hours under vacuum (10^{-5} bar) prior to analysis.

Thermogravimetric analysis (TGA): Measurements were performed on an EXSTAR6000 by heating samples at rate of 5˚C min^{-1} under an air flow of 25 mL/min and nitrogen flow of 10 mL/min, in open aluminium pans from 40 to 600˚C and holding at 600˚C for 30 minutes.

ICP-OES and CHN analysis: Carried out by the University of Liverpool analytical services. ICP-OES samples were prepared *via* microwave digestion as described below.

Microwave digestion: A PerkinElmer titan MPS microwave sample preparation system was used. A method developed for the digestion of conjugated polymers was used. A full carrousel was used, and the temperature was ramped to 170˚C over a ramp time of 5 minutes at 30 bar and held for 5 minutes. The temperature was then increased to 210˚C over 3 minutes at 30 bar for 45 minutes. Finally, the temperature was lowered to 50˚C over 1 minute at 30 bar and held for 15 minutes. Digestion was carried out in concentrated nitric acid, and diluted with water to 14% nitric acid before ICP-OES analysis.

Electrode preparation of CMP-$(bpy)_{20}$-Mn: CMP-$(bpy)_{20}$-Mn (5.5 mg/mL) in toluene was sonicated for 15 minutes, and then 5 µL of the suspension was deposited onto the surface of a cleaned glassy carbon working electrode, and allowed to dry in the dark.

Electrode preparation of CMP$(bpy)_{20}$-Mn/Polyaniline and Nafion: PANI was prepare by dissolving PANI in DMF and sonicating for 20 minutes, followed by centrifuged to remove any residual undissolved PANI. Different Nafion concentrations were prepared by diluting Nafion 5% wt. in MeCN. Bilayer casting films were prepared as follows: CMP-$(bpy)_{20}$-Mn (5.5 mg/mL) was suspended in toluene or MeCN by 15 minutes sonication. Once dry a layer of PANI or Nafion was drop cast ontop and allowed to dry in the dark. Mixed casting films were prepared as follows: CMP-$(bpy)_{20}$Mn (5.5 mg/mL) in toluene (500 µL) and PANI (500 µL) was sonicated for 15 minutes, or CMP$(bpy)_{20}$-Mn was suspended in Nafion 0.5% wt. (1000 µL in MeCN) and drop cast onto a glassy carbon electrode and left to dry in the dark. For electrodes containing NTs, the NTs were added in a 1:1 mass ration with CMP$(bpy)_{20}$-Mn, typically 5.5 mg/mL of both NTs and CMP$(bpy)_{20}$-Mn in solution.

Cleaning of multi-walled carbon nanotubes (NTs): NTs (1.5 g) were stirred in 6 M nitric acid (26 mL) overnight at 80˚C. The NTs were then filtered and rinsed with water. The NTs were then centrifuged in water until the pH of the water was neutral. The NTs were rinsed with acetone and left to dry under vacuum overnight.

Electrochemical analysis: Experiments were carried out in a 3 neck flask using Ag/AgCl reference electrode, Pt counter electrode and glassy carbon working electrode. The electrolyte used was either 60 mM or 0.1 M phosphate buffer for CMP$(bpy)_{20}$-Mn experiments, and 0.1 M K_2CO_3 for [Mn(bpy)$(CO)_3$Br]/PANI experiments. The cell was kept in the dark using

aluminium foil for the entire experiment. The cell was purged with argon or CO_2 for 20-30 minutes before starting the experiment. Palmsens or emstat potentiostats were used.

Gas chromatography (GC): Performed using an Agilent 6890N with N6 helium as the carrier gas (5 $ml.min^{-1}$). A 5 Å molecular sieve column (ValcoPLOT, 30 m length, 0.53 mm ID) and a pulsed discharge detector (D-3-I-HP, Valco Vici) were employed. 100 µL injections were recorded of the cell headspace periodically. Calibrant injections were also obtained for each experiment.

Ion chromatography (IC): Performed on an Eco IC set up for the detection of anions. A metrosep A sup 5-150/4. Column was used, and a metrosep A sup 5 guard/4.0 with a pump rate of 0.7 mL/min, pressure of 7.3 MPa and conductivity of ca. 16.17 $\mu S.cm^{-1}$. An eluent of 3.8 mM potassium carbonate and 1.2 mM potassium bicarbonate, and a regen solution containing sulphuric acid (350 mM), oxalic acid (100 mM) and acetone (5%) was used. Liquid products were tested for by injection 2 mL of post experimental electrolyte. The system was calibrated using a primary multi-anion standard solution.

Controlled potential electrolysis (CPE): Experiments were carried out in a custom made gas tight cell with bola fittings. The cell was purged for 30 minutes with argon or CO_2. For experiments using an organic media as the electrolyte, Ag^+ wire was used and calibrated against ferrocene, whereas for aqueous electrolyte Ag/AgCl reference electrode was used. The Pt counter electrode was kept being a Vycor tip containing ferrocene carboxylic acid in 0.1 M KOH. The electrolyte was stirred through the experiment, and 100 µL injections were taken periodically. Faradaic efficiencies were calculated by measuring the gaseous products of CO and H_2 from GC analysis and the charge passed (Q), accounting for the 2 electrons to produce one molecule of CO. The calculations for determining the Faradaic efficiency and turn over number (TON) are shown below.

$$FE_{co}(\%) = \left[\frac{CO\ (mol)}{\left({}^{Q(C)}/_{2\ \times 96485\ (Cmol^{-1})}\right)}\right] \times 100$$

$$TON_{CO} = \frac{CO\ (mol)}{electroactive\ catalyst\ (mol)}$$

References

1 R. Francke, B. Schille and M. Roemelt, *Chem. Rev.*, 2018, **118**, 4631–4701.

2 E. E. Benson, C. P. Kubiak, A. J. Sathrum and J. M. Smieja, *Chem. Soc. Rev.*, 2009, **38**, 89–99.

3 N. Elgrishi, M. B. Chambers, X. Wang and M. Fontecave, *Chem. Soc. Rev.*, 2017, **46**, 761–796.

4 M. D. Sampson, A. D. Nguyen, K. A. Grice, C. E. Moore, A. L. Rheingold and C. P. Kubiak, *J. Am. Chem. Soc.*, 2014, **136**, 5460–5471.

5 M. D. Sampson and C. P. Kubiak, *J. Am. Chem. Soc.*, 2016, **138**, 1386–1393.

6 A. Taheri, E. J. Thompson, J. C. Fettinger and L. A. Berben, *ACS Catal.*, 2015, **5**, 7140–7151.

7 P. Kang, Z. Chen, A. Nayak, S. Zhang and T. J. Meyer, *Energy Environ. Sci.*, 2014, **7**, 4007–4012.

8 J. D. Froehlich and C. P. Kubiak, *Inorg. Chem.*, 2012, **51**, 3932–3934.

9 C. Costentin, M. Robert, J.-M. Savéant and A. Tatin, *Proc. Natl. Acad. Sci.*, 2015, **112**, 6882–6886.

10 Y. Hori, K. Kikuchi and S. Suzuki, *Chem. Lett.*, 1985, **14**, 1695–1698.

11 C. Yan, L. Lin, G. Wang and X. Bao, *Chinese J. Catal.*, 2019, **40**, 23–37.

12 J. Bonin, A. Maurin and M. Robert, *Coord. Chem. Rev.*, 2017, **334**, 184–198.

13 D. L. Dubois, *Comments Inorg. Chem.*, 1997, **19**, 307–325.

14 S. K. Lee, M. Kondo, G. Nakamura, M. Okamura and S. Masaoka, *Chem. Commun.*, 2018, **54**, 6915–6918.

15 H. Takeda, C. Cometto, O. Ishitani and M. Robert, *ACS Catal.*, 2017, **7**, 70–88.

16 J. Qiao, Y. Liu, F. Hong and J. Zhang, *Chem. Soc. Rev.*, 2014, **43**, 631–675.

17 C. D. Windle and E. Reisner, 2014, **44**, 1–19.

18 M. Bourrez, F. Molton, S. Chardon-Noblat and A. Deronzier, *Angew. Chemie Int. Ed.*, 2011, **50**, 9903–9906.

19 J. Hawecker, J. Lehn and R. Ziessel, *J. Chem. Soc., Chem. Commun.*, 1983, **286**, 536–538.

20 J. Hawecker, J. Lehn and R. Ziessel, *J. Chem. Soc., Chem. Commun.*, 1984, **984**, 328–330.

21 J. J. Walsh, G. Neri, C. L. Smith and A. J. Cowan, *Chem. Commun.*, 2014, **50**, 12698–701.

22 J. J. Walsh, C. L. Smith, G. Neri, G. F. S. Whitehead, C. M. Robertson and A. J. Cowan, *Faraday Discuss.*, 2015, **00**, 1–14.

23 J. J. Walsh, G. Neri, C. L. Smith and A. J. Cowan, *Organometallics*, 2019, **38**, 1224–1229.

24 B. Reuillard, K. H. Ly, T. E. Rosser, M. F. Kuehnel, I. Zebger and E. Reisner, *J. Am. Chem. Soc.*, 2017, **139**, 14425–14435.

25 M. Stanbury, J.-D. Compain and S. Chardon-Noblat, *Coord. Chem. Rev.*, 2018, **361**, 120–137.

26 F. Hartl, B. D. Rossenaar, G. J. Stor and D. J. Stufkens, *Recl. des Trav. Chim. des Pays-Bas*, 1995, **114**, 565–570.

27 B. D. Rossenaar, F. Hartl, D. J. Stufkens, C. Amatore, E. Maisonhaute and J.-N. Verpeaux, *Organometallics*, 2002, **16**, 4675–4685.

28 C. J. Kleverlaan, F. Hartl and D. J. Stufkens, *J. Photochem. Photobiol. A Chem.*, 1997, **103**, 231–237.

29 F. P. A. Johnson, M. W. George, F. Hartl and J. J. Turner, *Organometallics*, 1996, **15**, 3374–3387.

30 G. Neri, P. M. Donaldson and A. J. Cowan, *J. Am. Chem. Soc.*, 2017, **139**, 13791–13797.

31 G. Neri, P. M. Donaldson and A. J. Cowan, *Phys. Chem. Chem. Phys.*, 2019, **21**, 7389–7397.

32 M. L. Clark, A. Ge, P. E. Videla, B. Rudshteyn, C. J. Miller, J. Song, V. S. Batista, T. Lian and C. P. Kubiak, *J. Am. Chem. Soc.*, 2018, **140**, 17643–17655.

33 D. C. Grills, J. A. Farrington, B. H. Layne, S. V. Lymar, B. A. Mello, J. M. Preses and J. F. Wishart, *J. Am. Chem. Soc.*, 2014, **136**, 5563–5566.

34 D. C. Grills, M. Z. Ertem, M. McKinnon, K. T. Ngo and J. Rochford, *Coord. Chem. Rev.*, 2018, **374**, 173–217.

35 D. C. Grills, J. A. Farrington, B. H. Layne, S. V. Lymar, B. a Mello, J. M. Preses and J. F. Wishart, *J. Am. Chem. Soc.*, 2014, **136**, 5563–5566.

36 J.-D. Compain, M. Bourrez, M. Haukka, A. Deronzier and S. Chardon-Noblat, *Chem. Commun.*, 2014, **50**, 2539–2542.

37 C. Riplinger, M. D. Sampson, A. M. Ritzmann, C. P. Kubiak and E. A. Carter, *J. Am. Chem. Soc.*, 2014, **136**, 16285–16298.

38 Y. C. Lam, R. J. Nielsen, H. B. Gray and W. A. Goddard, *ACS Catal.*, 2015, **5**, 2521–2528.

39 G. Neri, J. J. Walsh, G. Teobaldi, P. M. Donaldson and A. J. Cowan, *Nat. Catal.*, 2018, **1**, 952–959.

40 J. M. Smieja, M. D. Sampson, K. a. Grice, E. E. Benson, J. D. Froehlich and C. P. Kubiak, *Inorg. Chem.*, 2013, **52**, 2484–2491.

41 J. A. Keith, K. A. Grice, C. P. Kubiak and E. A. Carter, *J. Am. Chem. Soc.*, 2013, **135**, 15823–15829.

42 K. T. Ngo, M. McKinnon, B. Mahanti, R. Narayanan, D. C. Grills, M. Z. Ertem and J. Rochford, *J. Am. Chem. Soc.*, 2017, **139**, 2604–2618.

43 M. D. Sampson, J. D. Froehlich, J. M. Smieja, E. E. Benson, I. D. Sharp and C. P. Kubiak, *Energy Environ. Sci.*, 2013, **6**, 3748–3755.

44 K.-Y. Wong, W.-H. Chung and C.-P. Lau, *J. Electroanal. Chem.*, 1998, **453**, 161–170.

45 F. Franco, C. Cometto, L. Nencini, C. Barolo, F. Sordello, C. Minero, J. Fiedler, M. Robert, R. Gobetto and C. Nervi, *Chem. - A Eur. J.*, 2017, **23**, 4782–4793.

46 J. Agarwal, T. W. Shaw, H. F. Schaefer and A. B. Bocarsly, *Inorg. Chem.*, 2015, **54**, 5285–5294.

47 F. Franco, C. Cometto, F. Ferrero Vallana, F. Sordello, E. Priola, C. Minero, C. Nervi and R. Gobetto, *Chem. Commun.*, 2014, **50**, 14670–14673.

48 M. Bourrez, M. Orio, F. Molton, H. Vezin, C. Duboc, A. Deronzier and S. Chardon-Noblat, *Angew. Chemie Int. Ed.*, 2014, **53**, 240–243.

49 I. Bhugun, D. Lexa and J.-M. Savéant, *J. Phys. Chem.*, 1996, **100**, 19981–19985.

50 C. W. Machan, C. J. Stanton, J. E. Vandezande, G. F. Majetich, H. F. Schaefer, C. P.

Kubiak and J. Agarwal, *Inorg. Chem.*, 2015, **54**, 8849–8856.

51 G. Seshadri, C. Lin and A. B. Bocarsly, *J. Electroanal. Chem.*, 1994, **372**, 145–150.

52 P. Kang, T. J. Meyer and M. Brookhart, *Chem. Sci.*, 2013, **4**, 3497.

53 P. Kang, Z. Chen, A. Nayak, S. Zhang and T. J. Meyer, *Energy Environ. Sci.*, 2014, **7**, 4007–4012.

54 J. D. Froehlich and C. P. Kubiak, *Inorg. Chem.*, 2012, **51**, 3932–3934.

55 T. Yoshida, K. Tsutsumida, S. Teratani, K. Yasufuku and M. Kaneko, *J. Chem. Soc., Chem. Commun.*, 1993, 631–633.

56 C. A. Downes and S. C. Marinescu, 2017, 4374–4392.

57 R. S. Yeo, J. McBreen, G. Kissel, F. Kulesa and S. Srinivasan, *J. Appl. Electrochem.*, 1980, **10**, 741–747.

58 J. E. Pander, A. Fogg and A. B. Bocarsly, *ChemCatChem*, 2016, **8**, 3536–3545.

59 N. M. Orchanian, L. E. Hong, J. A. Skrainka, J. A. Esterhuizen, D. A. Popov and S. C. Marinescu, *ACS Appl. Energy Mater.*, 2019, **2**, 110–123.

60 T. R. O'Toole, B. P. Sullivan, M. R. M. Bruce, L. D. Margerum, R. W. Murray and T. J. Meyer, *J. Electroanal. Chem.*, 1989, **259**, 217–239.

61 P. Denisevich, H. D. Abruna, C. R. Leidner, T. J. Meyer and R. W. Murray, *Inorg. Chem.*, 1982, **21**, 2153–2161.

62 P. Christensen, A. Hamnett, A. V. G. Muir, J. A. Timney and S. Higgins, *J. Chem. Soc. Faraday Trans.*, 1994, **90**, 459.

63 E. Torralba-Penalver, Y. Luo, J. D. Compain, S. Chardon-Noblat and B. Fabre, *ACS Catal.*, 2015, **5**, 6138–6147.

64 D. A. Popov, J. M. Luna, N. M. Orchanian, R. Haiges, C. A. Downes and S. C. Marinescu, *Dalt. Trans.*, 2018, **47**, 17450–17460.

65 A. I. Cooper, *ACS Cent. Sci.*, 2017, **3**, 544–553.

66 R. Hinogami, S. Yotsuhashi, M. Deguchi, Y. Zenitani, H. Hashiba and Y. Yamada, *ECS Electrochem. Lett.*, 2012, **1**, H17–H19.

67 E. M. Johnson, R. Haiges and S. C. Marinescu, *ACS Appl. Mater. Interfaces*, 2018, **10**, 37919–37927.

68 R. Hinogami, S. Yotsuhashi, M. Deguchi, Y. Zenitani, H. Hashiba and Y. Yamada, *ECS Electrochem. Lett.*, 2012, **1**, H17–H19.

69 S. M. J. Rogge, A. Bavykina, J. Hajek, H. Garcia, A. I. Olivos-Suarez, A. Sepúlveda-Escribano, A. Vimont, G. Clet, P. Bazin, F. Kapteijn, M. Daturi, E. V. Ramos-Fernandez, F. X. Llabrés i Xamena, V. Van Speybroeck and J. Gascon, *Chem. Soc. Rev.*, 2017, **46**, 3134–3184.

70 J. Lee, O. K. Farha, J. Roberts, K. A. Scheidt, S. T. Nguyen and J. T. Hupp, *Chem. Soc. Rev.*, 2009, **38**, 1450–1459.

71 V. S. Vyas, V. W. H. Lau and B. V. Lotsch, *Chem. Mater.*, 2016, **28**, 5191–5204.

72 G. Zhang, Z.-A. Lan and X. Wang, *Angew. Chemie Int. Ed.*, 2016, **55**, 15712–15727.

73 C. Wang, Z. Xie, K. E. Dekrafft and W. Lin, *J. Am. Chem. Soc.*, 2011, **133**, 13445–13454.

74 U. J. Ryu, S. J. Kim, H. K. Lim, H. Kim, K. M. Choi and J. K. Kang, *Sci. Rep.*, 2017, **7**, 1–8.

75 X. Wang, I. Thiel, A. Fedorov, C. Copéret, V. Mougel and M. Fontecave, *Chem. Sci.*, 2017, **8**, 8204–8213.

76 Y. Xu, S. Jin, H. Xu, A. Nagai and D. Jiang, *Chem. Soc. Rev.*, 2013, **42**, 8012.

77 Q. Liu, Z. Tang, M. Wu and Z. Zhou, *Polym. Int.*, 2014, **63**, 381–392.

78 J.-X. Jiang, F. Su, A. Trewin, C. D. Wood, H. Niu, J. T. a Jones, Y. Z. Khimyak and A. I. Cooper, *J. Am. Chem. Soc.*, 2008, **130**, 7710–7720.

79 D. Schwarz, A. Acharja, A. Ichangi, P. Lyu, M. V. Opanasenko, F. R. Goßler, T. A. F. König, J. Čejka, P. Nachtigall, A. Thomas and M. J. Bojdys, *Chem. - A Eur. J.*, 2018, **24**, 11916–11921.

80 A. G. Slater and A. I. Cooper, *Science*, 2015, 348, 8075–8075.

81 H. S. Choi, H. J. Jeon, J. H. Choi, G.-H. Lee and J. K. Kang, *Nanoscale*, 2015, **7**, 18923–18927.

82 Q. Shi, H. Sun, R. Yang, Z. Zhu, W. Liang, D. Tan, B. Yang, A. Li and W. Deng, *J. Mater. Sci.*, 2015, **50**, 6388–6394.

83 A. H. Alahmed, M. E. Briggs, A. I. Cooper and D. J. Adams, *J. Mater. Chem. A*, 2019, **7**, 549–557.

84 L. Chen, Y. Yang and D. Jiang, *J. Am. Chem. Soc.*, 2010, **132**, 9138–9143.

85 Y. B. Zhou and Z. P. Zhan, *Chem. - An Asian J.*, 2018, **13**, 9–19.

86 M. Liu, L. Guo, S. Jin and B. Tan, *J. Mater. Chem. A*, 2019, **7**, 5153–5172.

87 Y. Ma, Z. Wang, X. Xu and J. Wang, *Chinese J. Catal.*, 2017, **38**, 1956–1969.

88 C. Wang, Z. Xie, K. E. DeKrafft and W. Lin, *J. Am. Chem. Soc.*, 2011, **133**, 13445–13454.

89 H. Fei, M. D. Sampson, Y. Lee, C. P. Kubiak and S. M. Cohen, *Inorg. Chem.*, 2015, **54**, 6821–6828.

90 M. E. Bhosale, R. Illathvalappil, S. Kurungot and K. Krishnamoorthy, *Chem. Commun.*, 2016, **52**, 316–318.

91 S. Bi, C. Lu, W. Zhang, F. Qiu and F. Zhang, *J. Energy Chem.*, 2018, **27**, 99–116.

92 K. Cousins and R. Zhang, *Polymers (Basel).*, 2019, **11**, 690.

93 Z. Liu, X. Yuan, S. Zhang, J. Wang, Q. Huang, N. Yu, Y. Zhu, L. Fu, F. Wang, Y. Chen and Y. Wu, *NPG Asia Mater.*, 2019, **11**, 12.

94 S. Lin, C. S. Diercks, Y. Zhang, N. Kornienko, E. M. Nichols, Y. Zhao, A. R. Paris, D. Kim, P. Yang, O. M. Yaghi and C. J. Chang, *Science*, 2015, **349**, 1208–1213.

95 W. Zheng, C.-S. Tsang, L. Y. S. Lee and K.-Y. Wong, *Mater. Today Chem.*, 2019, **12**, 34–60.

96 N. Kornienko, Y. Zhao, C. S. Kley, C. Zhu, D. Kim, S. Lin, C. J. Chang, O. M. Yaghi and P. Yang, *J. Am. Chem. Soc.*, 2015, **137**, 14129–14135.

97 F. N. Al-Rowaili, A. Jamal, M. S. Ba Shammakh and A. Rana, *ACS Sustain. Chem. Eng.*, 2018, **6**, 15895–15914.

98 L. Ye, J. Liu, Y. Gao, C. Gong, M. Addicoat, T. Heine, C. Wöll and L. Sun, *J. Mater. Chem. A*, 2016, **4**, 15320–15326.

99 H. Fei, M. D. Sampson, Y. Lee, C. P. Kubiak and S. M. Cohen, *Inorg. Chem.*, 2015, **54**, 6821–6828.

100 R. Huang, Y. Peng, C. Wang, Z. Shi and W. Lin, *Eur. J. Inorg. Chem.*, 2016, **2016**, 4358–4362.

101 J.-X. Jiang, F. Su, A. Trewin, C. D. Wood, N. L. Campbell, H. Niu, C. Dickinson, A.

Y. Ganin, M. J. Rosseinsky, Y. Z. Khimyak and A. I. Cooper, *Angew. Chemie Int. Ed.*, 2007, **46**, 8574–8578.

102 J.-X. Jiang, C. Wang, A. Laybourn, T. Hasell, R. Clowes, Y. Z. Khimyak, J. Xiao, S. J. Higgins, D. J. Adams and A. I. Cooper, *Angew. Chemie Int. Ed.*, 2011, **50**, 1072–1075.

103 W. Liang, T. L. Church, S. Zheng, C. Zhou, B. S. Haynes and D. M. D'Alessandro, *Chem. - A Eur. J.*, 2015, **21**, 18576–18579.

104 R. Dawson, A. I. Cooper and D. J. Adams, *Polym. Int.*, 2013, **62**, 345–352.

105 Y. Xie, T.-T. Wang, X.-H. Liu, K. Zou and W.-Q. Deng, *Nat. Commun.*, 2013, **4**, 1960.

106 R. Dawson, D. J. Adams and A. I. Cooper, *Chem. Sci.*, 2011, **2**, 1173.

107 I. P. Koronaki, L. Prentza, V. Papaefthimiou, Z. Xiang, R. Mercado, J. M. Huck, H. Wang, Z. Guo, W. Wang, D. Cao, M. Haranczyk and B. Smit, *Renew. Sustain. Energy Rev.*, 2015, **50**, 547–566.

108 C. R. Mason, L. Maynard-Atem, K. W. J. Heard, B. Satilmis, P. M. Budd, K. Friess, M. Lanč, P. Bernardo, G. Clarizia and J. C. Jansen, *Macromolecules*, 2014, **47**, 1021–1029.

109 Y. Kou, Y. Xu, Z. Guo and D. Jiang, *Angew. Chemie - Int. Ed.*, 2011, **50**, 8753–8757.

110 F. Xu, X. Chen, Z. Tang, D. Wu, R. Fu and D. Jiang, *Chem. Commun.*, 2014, **50**, 4788–4790.

111 G. Lu, H. Yang, Y. Zhu, T. Huggins, Z. J. Ren, Z. Liu and W. Zhang, *J. Mater. Chem. A*, 2015, **3**, 4954–4959.

112 G. Lu, Y. Zhu, K. Xu, Y. Jin, Z. J. Ren, Z. Liu and W. Zhang, *Nanoscale*, 2015, **7**, 18271–18277.

113 J. Hynek, J. Rathouský, J. Demel and K. Lang, *RSC Adv.*, 2016, **6**, 44279–44287.

114 C. Ampelli, C. Genovese, M. Errahali, G. Gatti, L. Marchese, S. Perathoner and G. Centi, *J. Appl. Electrochem.*, 2015, **45**, 701–713.

115 A. I. Cooper, *Adv. Mater.*, 2009, **21**, 1291–1295.

116 A. Dawson, Robert and Trewin, *Chapter 7 : Conjugated Microporous Polymers, in Porous Polymers: Design, Synthesis and Applications*, the Royal Society of

Chemistry, Monographs., 2015.

117 R. S. Sprick, B. Bonillo, R. Clowes, P. Guiglion, N. J. Brownbill, B. J. Slater, F. Blanc, M. A. Zwijnenburg, D. J. Adams and A. I. Cooper, *Angew. Chemie - Int. Ed.*, 2016, **55**, 1792–1796.

118 C. De Leener, E. Hennebicq, J. C. Sancho-Garcia and D. Beljonne, *J. Phys. Chem. B*, 2009, **113**, 1311–1322.

119 F. Hartl, T. Mahabiersing, P. Le Floch, F. Mathey, L. Ricard, P. Rosa and S. Záliš, *Inorg. Chem.*, 2003, **42**, 4442–4455.

120 R. S. Sprick, B. Bonillo, M. Sachs, R. Clowes, J. R. Durrant, D. J. Adams and A. I. Cooper, *Chem. Commun.*, 2016, **52**, 10008–10011.

121 A. B. Koren, M. D. Curtis, A. H. Francis and J. W. Kampf, *J. Am. Chem. Soc.*, 2003, **125**, 5040–5050.

122 C. F. Martín, E. Stöckel, R. Clowes, D. J. Adams, A. I. Cooper, J. J. Pis, F. Rubiera and C. Pevida, *J. Mater. Chem.*, 2011, **21**, 5475.

123 D. Lee, C. Zhang and H. Gao, *Macromol. Chem. Phys.*, 2015, **216**, 489–494.

124 A. Modak and S. Jana, *Microporous Mesoporous Mater.*, 2019, **276**, 107–132.

125 M. Younas, M. Sohail, L. L. Kong, M. J. K. Bashir and S. Sethupathi, *Int. J. Environ. Sci. Technol.*, 2016, **13**, 1839–1860.

126 Y. Zou and A. E. Rodrigues, *Adsorpt. Sci. Technol.*, 2002, **19**, 255–266.

127 J. Zhang, W. J. Pietro and A. B. P. Lever, *J. Electroanal. Chem.*, 1996, **403**, 93–100.

128 E. Fujita, C. Creutz, N. Sutin and D. J. Szalda, *J. Am. Chem. Soc.*, 1991, **113**, 343–353.

129 J.-M. Savéant, *Chem. Rev.*, 2008, **108**, 2348–2378.

130 C. Costentin, M. Robert and J.-M. M. Savéant, *Acc. Chem. Res.*, 2015, **48**, 2996–3006.

131 C. Costentin, M. Robert and J. M. Savéant, *Chem. Soc. Rev.*, 2013, **42**, 2423–2436.

132 M. Sachs, R. S. Sprick, D. Pearce, S. J. Hillman, A. Monti, A. A. Y. Guilbert, N. J. Brownbill, S. Dimitrov, F. Blanc, M. A. Zwijnenburg, J. Nelson, J. R. Durrant and A. I. Cooper, *Nat. Commun.*, 2018, 1–11.

133 D. J. Woods, R. S. Sprick, C. L. Smith, A. J. Cowan and A. I. Cooper, *Adv. Energy Mater.*, 2017, **7**, 1700479.

134 D. Hursá, A. Kormá, K. Rajeshwar and C. Janá, *Chem. Commun. Chem. Commun*, 2016, **8858**, 8858–8861.

135 F. Köleli, T. Röpke and C. H. Hamann, *Synth. Met.*, 2004, **140**, 65–68.

136 W. Zheng, S. Nayak, W. Yuan, Z. Zeng, X. Hong, K. A. Vincent and S. C. E. Tsang, *Chem. Commun.*, 2016, **52**, 13901–13904.

137 D. Hursán, A. Kormányos, K. Rajeshwar and C. Janáky, *Chem. Commun.*, 2016, **52**, 8858–8861.

138 A. G. MacDiarmid and A. J. Epstein, *Faraday Discuss. Chem. Soc.*, 1989, **88**, 317.

139 M. S. Dresselhaus, A. Jorio, A. G. Souza Filho and R. Saito, *Philos. Trans. R. Soc. A Math. Phys. Eng. Sci.*, 2010, **368**, 5355–5377.

“Things will look better in the morning”

- Bagheera

Chapter 3

Linear polymers for overall water splitting

Part of this work has been published: “A solution-processable polymer photocatalyst for hydrogen evolution from water”, D. J. Woods, R. S. Sprick, C. L. Smith, A. J. Cowan and A. I. Cooper, 2017, Advanced Energy Materials.

3.1 Introduction

In this chapter we explore the application of organic linear polymers for overall water splitting. Initially we discuss the recent advances in the field of photocatalytic hydrogen evolution, followed by photoelectrochemical (PEC) water oxidation using organic polymer materials.

3.1.1 Photocatalytic hydrogen evolution

The first report of an organic semiconductor for photocatalytic hydrogen evolution was published in 1985, using a poly(*p*-phenylene) polymer which showed a low apparent quantum yield (AQY) of *ca.* 0.04% in the presence of an electron donor, trimethylamine (TEA), excited with λ>290 nm.[1] However, it was not until 2009 when 2D graphitic carbon nitride (g-C_3N_4) was reported for visible light photocatalytic hydrogen evolution using a sacrificial donor and Pt co-catalyst which produced >106 $\mu molh^{-1}g^{-1}$ H_2,[2] that the use of organic semiconductors for hydrogen evolution received significant levels of attention.[3–5] To date, g-C_3N_4 and its related structures have been widely studied for photocatalytic water splitting applications due high AQYs of *ca.* 50%.[6] However, the high temperatures used during synthesis leads to lack of control over the exact structure of g-C_3N_4. g-C_3N_4 is usually described as comprising solely of heptazine or triazine units, however in reality analysis by FTIR, CHN and XPS shows both a deviation from the expected C:N ratios and the presence of a wide range of unexpected functional groups (e.g. –CN, -CO), making it difficult to rationally fine tuning the structure-properties for desired applications. Recently, many other π-conjugated polymers have also been discovered and shown to be active hydrogen evolution photocatalysts under both UV and Visible light. Examples include; COFs, CTFs, CMPs, and linear polymers,[7–9] and organic semiconductors have now been shown to reach hydrogen evolution reaction (HER) rates comparable to common inorganic photocatalysts.[10–13] Here, we briefly discuss some of the most commonly studied classes of organic materials for photocatalytic hydrogen evolution, before focusing on linear polymers.

3.1.1.1 Covalent Organic Frameworks (COFs)

COFs are highly ordered 2D or 3D crystalline structures that possess high surface areas and uniform pore sizes. They have been shown to be promising materials for photocatalysis as the structure-properties of COFs allows for good charge carrier mobilities, rapid diffusion of reactants and products, they are highly stable and robust and are good light harvesting materials which can be easily tailored for their desired application.[14] Stegbauer *et al.* were the first to report visible light (> 420 nm) photoactivity with a hydrazone-based COF for hydrogen evolution. In this study they achieved HERs as high as *ca.* 1900 $\mu mol\ h^{-1}g^{-1}$ in the presence of a triethanolamine (TEOA) sacrificial electron donor and a Pt co-catalyst, (Figure 3.1).[15] The application and development of COFs for photocatalytic hydrogen

evolution have been well reviewed elsewhere in detail and it is apparent that although challenging to prepare, and often unstable during photocatalysis, these highly ordered materials can achieve high levels of activity for the HER.[14,16–19]

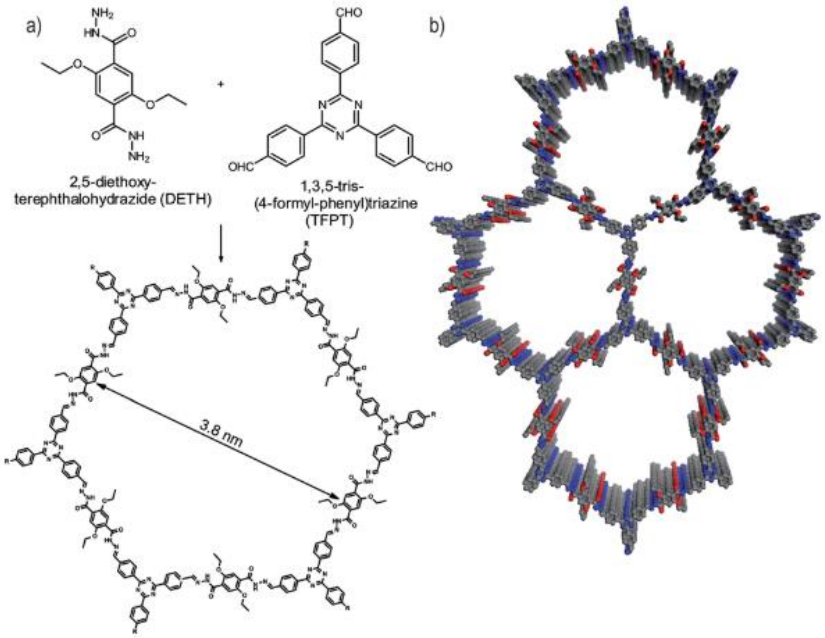

*Figure 3.1 Condensation reaction scheme of 1,3,5-tris-(4-formyl-phenyl)triazine (TFPT) and 2,5-diethoxy-terephthalohydrazide (DETH) building blocks for the synthesis of a hydrazone-based COF catalysed by acetic acid (a). The hydrazone-based COF exhibits a hexagonal 2D crystalline structure and is an effective HER photocatalyst. Figure taken from Chem. Sci., 2014, **5**, 2789–2793.*[15]

3.1.1.2 Covalent Triazine Frameworks (CTFs)

CTFs offer an alternative porous organic photocatalyst. CTFs are structurally related to g-C_3N_4 and have high chemical stability and good HER due to encompassing the use of triazine units to gain high nitrogen content, which is hypothesised to correlate with improved HER due the ability of nitrogen to act as a catalytic site.[2,7] CTFs are often synthesised by high temperature ionothermal approaches,[3,20] although low temperature and/or microwave assisted synthetic routes also exist.[21–23] Due to the presence of triazine or heptazine linker units CTFs exhibit good stability as, unlike COFs, they are not susceptible to hydrolysis.[24,25] CTFs exhibit high surface areas, porosity, good thermal and chemical stabilities and form amorphous or crystalline structures giving them potential applications in catalysis and energy storage.[25] Guo *et al.* have reported the highest HER for CTFs and, to the best of our knowledge, organic porous materials using a nitrogen doped CTF for photocatalytic hydrogen evolution (10760 µmol $h^{-1}g^{-1,}$ >420 nm light) in the presence of a TEOA sacrificial electron donor and a Pt co-catalyst under visible light, (Figure 3.2).[26]

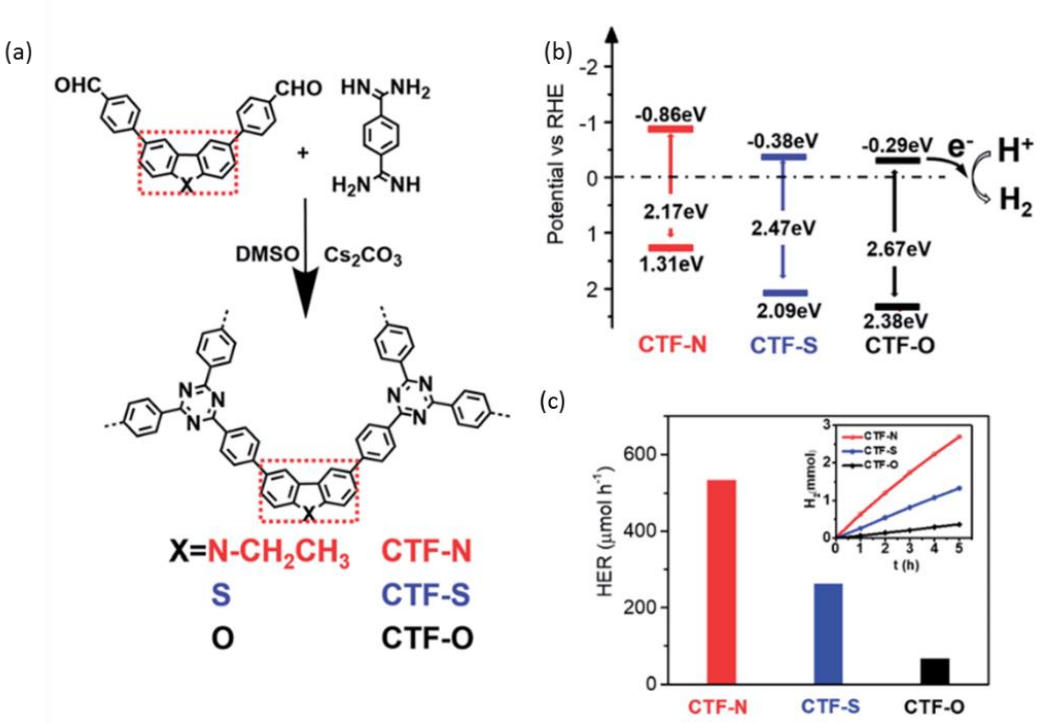

Figure 3.2 CTFs were synthesised by a condensation reaction and doped with N-CH_2CH_3, S or O yielding CTF-N (red), CTF-S (blue) and CTF-O (black) (a). Energy diagram of CTFs (b) and HER under >420 nm irradiation in the presence of a TEOA sacrificial donor and Pt co-catalyst (c). Figures taken from J. Mater. Chem. A, 2018, ***6****, 19775–19781.*[26]

3.1.1.3 Conjugated Microporous Polymers (CMPs)

CMPs are amorphous and exhibit high surface areas, porosity and are thermally and chemically robust. CMPs were first reported for photocatalytic hydrogen evolution in 2015 by the Cooper group at the University of Liverpool.[27] A series of CMPs were co-polymerised, demonstrating how the optical gap can simply be tuned. In this work H_2 evolution reactions were carried out with the polymer as a suspension in water, in the presence of a sacrificial electron donor (diethylamine, DEA) and HER rates as high as 174 ± 9 μmol $h^{-1}g^{-1}$ under visible light irradiation (> 420 nm) were measured. Interestingly, as the optical gap of the CMPs decreased HER activity increased, before decreasing below an optical gap of 2.33 eV.[27] The highest HER reported in this series of CMPs was higher than that for g-C_3N_4, and a linear polymer under the same experimental conditions.[27] All CMPs in this study were active under visible light irradiation, unlike most g-C_3N_4s demonstrating a route to achieving highly active photocatalysts under visible light. However, the activity of CMPs was limited to a small portion of the visible spectrum with the AQY at wavelengths > 420 nm being relatively low.[7,28,29] This has been proposed to be due to inefficient charge separation in polymers with small optical gaps, that absorb light more strongly at longer wavelengths.

The use of donor-acceptor groups has since been suggested to provide a way to achieve effective charge separation and band gap narrowing due to orbital overlap interactions between the donor and acceptor units, and hence improved visible light activity with narrow optical gap materials and studies have achieved visible light activity for the HER at wavelengths that corresponds to >50% of the solar spectrum.[30–35] Of note is a recent report by Zhang *et al.* on nitrogen containing CMPs with donor-acceptor units (Figure 3.3).[35] A cyano unit was employed as the acceptor group, whilst carbazole and diphenylamine units were electron donor units. By altering the substitution positions and the number and type of electron donor units, narrow band gaps from 1.64 - 2.29 eV were achieved, along with high AQYs (6.4% at 420 nm, overall HER of 2103 μmol $h^{-1}g^{-1}$), with *para* substitution by acceptor groups providing the most active photocatalysts.[35] Co-polymerisation of donor and acceptor groups to synthesise CMPs for photocatalytic hydrogen evolution has been shown as an effective route to increasing AQYs and HER to as high as 1.93% and 8633 μmol h $^{1}g^{-1}$.[36]

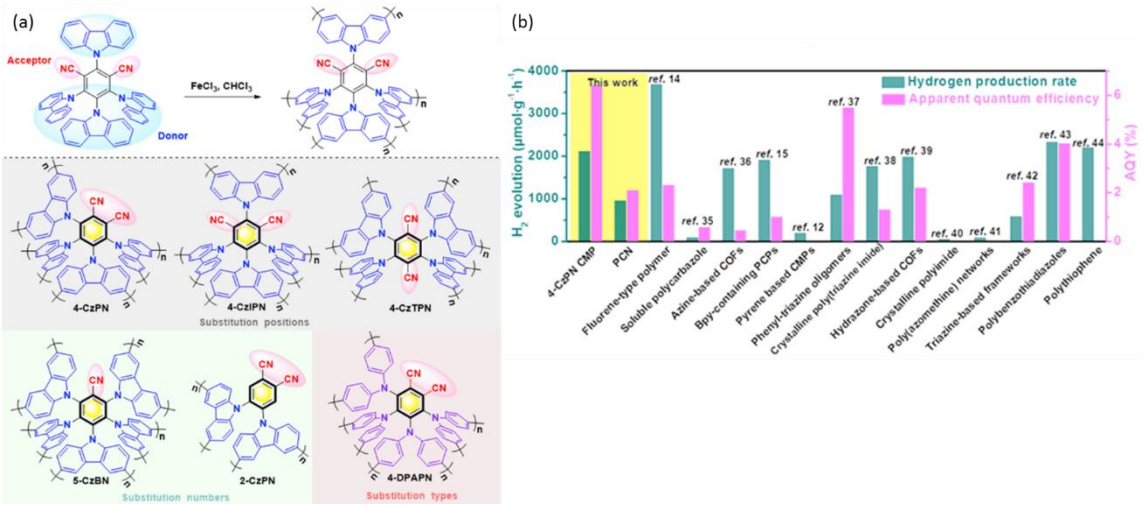

Figure 3.3 Modified CMPs with cyano groups (CN) where the substitution position, numbers and types of substitutions is altered (a). Comparison of the most active CMP from the study by Zhang et al. in the presence of a Pt co-catalyst (3% wt.) and TEOA sacrificial donor with other reported organic polymers form H_2 evolution (b). Figures taken from Appl. Catal. B Environ., 2019, ***245****, 114–121.*[35]

3.1.1.4 Linear polymers

Despite it being widely anticipated that porosity would be an important property of effective HER photocatalysts, studies have shown in several cases that the non-porous analogues of CMPs are superior HER photocatalysts, suggesting microporosity may not be essential.[37,38] Although in some instances the porous CMP analogue have had greater activity, the role of the porosity is not clear and it may be that the change in behaviour can be assigned to differences in charge transport and wettability of the specific CMPs used.[39] Therefore there is increasing interest in the study of linear polymer photocatalysts for the HER. Synthesis of

CMP linear analogues is achieved by the addition of alkyl chains to the polymer backbone which blocks the formation of a 3D network.[28,40] Additionally the alkyl chains shift the LUMO to more negative potentials, leading to a narrowed optical gap and increased visible light activity. Furthermore, it has been suggested that the addition of long chains restricts torsional disorder with the planarization of the polymer chains increasing charge migration and hence HER rates. Xiang *et al.* have shown that the addition of alkyl chains to a donor-acceptor CMP to linearize the structure results in a superior HER rate of 9600 μmol $h^{-1}g^{-1}$, and an AQY of 1.8%.[40]

In addition to linear polymers based on CMP analogues a number of studies have also examined polymer chains based on modification of the original poly(*p*-phenylene) structure.[1] The incorporation of heteroatoms such as nitrogen, sulphur and fluorine, has been shown to increase AQYs and HER rates.[26,29,39] In the same study by Xiang *et al.* they showed fluorination of donor-acceptor linear polymers increased the AQY by >30% (maximum AQY *ca.* 5%) with optimal HER rates of 13,300 $h^{-1}g^{-1}$ where F substitution *para* to the electron donating group showed greatest activity.[40] This was rationalised *via* computational studies, where the electron donating ability of F promoted greater electron density on the carbon atom in the *meta* position (relative to F) resulting in greater overlap with the nitrogen heteroatom in neighbouring polymer chains, and so promoting electron transfer.[40] Sprick *et al.* have gone on to show that the use of sulfone polymers outperform their fluorine analogues for a class of CMPs and linear polymers when under sacrificial conditions.[39] This was rationalised from water uptake measurements, where it was found fluorine analogues exhibited a lower water uptake in comparison to the sulfone polymers, as water is able to better penetrate the pores of the more polar sulfone polymer.[39] Sprick *et al.* also conducted an investigation into how the difference in residual palladium (Pd) content from the polymer synthesis in the fluorine and sulfone polymers affected the photocatalytic activity, to ensure Pd was not acting as a co-catalyst, and hence contributing to the difference in HER. By varying the concentration of Pd within the polymers by washing samples with a Pd scavenger, a decrease of *ca.* 94% in HER rates from 3106 μmol $h^{-1}g^{-1}$ to 110 μmol $h^{-1}g^{-1}$ were observed.[39] However, the difference in HER rates between fluorine and sulfone polymers cannot be fully attributed to Pd content. Sprick *et al.* along with other groups[41,42] have shown that although a linear increase in HER rates occur upon increased Pd content, at high levels of Pd content (*ca.* 100 ppm) as seen for those reported by Sprick *et al.* the HER saturates,[39] whereas at low Pd levels (< 1 ppm) the Pd concentration can have a profound effect on activity.[41]

CMP analogues of linear polymers can be synthesised by fusing phenylene units together with the use of bridging functionalities, as shown in Figure 3.4, and has also been explored as a way to increase rigidity along linear polymer chains with the aim of restricting torsional distortion. Comparison of fused polymer chains with unfused chains with similar optical band gaps showed that the fused polymers gave higher HER rates.[29] Interestingly computational studies indicated that the main effect of the bridging groups was to make the ionization potentials of the fused polymers more negative, resulting in a greater driving force for electron migration onto water.[29]

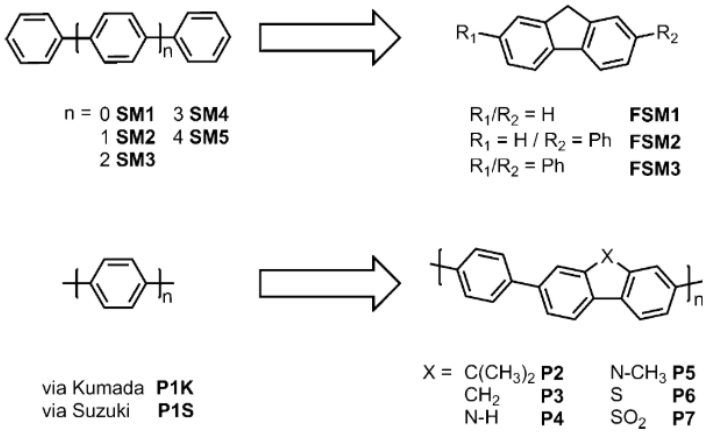

*Figure 3.4 Schematic diagram showing the planarization of conjugated phenylene oligomers (SM1-SM5) and poly(o-phenylenes)s (P1K,P1S) by the fusion of the phenylene rings to produce the fluorene analogues. Figure reproduced from Angew. Chemie - Int. Ed., 2016, **55**, 1792–1796.*[29]

Most organic materials for photocatalytic hydrogen evolution are insoluble in organic solvents making it difficult to process the materials for applications in PEC water splitting, and also gives rise to a loss in photoactivity due to the necessary need to suspend the polymer in solution during reactions.[43] One way in which this can be overcome is by the fabrication of solution processable polymers, for ease of fabrication of photoelectrodes or deposition onto supporting substrates.[44] In addition to providing a route to controlling the torsional distortion of the structure the incorporation of side chains, such as alkyl chains, can also aid solubility enabling solution processing. Similar approaches have been used in OPV devices to synthesise solution processable conjugated polymers, where branched alkyl chains such as 2-ethykhexyl have been shown to give rise to good solubility in comparison to linear chains.[45] Of particular note is recent work at Liverpool which has developed a π-conjugated linear polymer, P8s modified with alkyl groups, shown in Figure 3.5, that could be cast into films from a chloroform solution and was shown during this project to be an effective photocatalyst for the HER in the presence a sacrificial electron donor solution of MeOH and TEOA.[46]

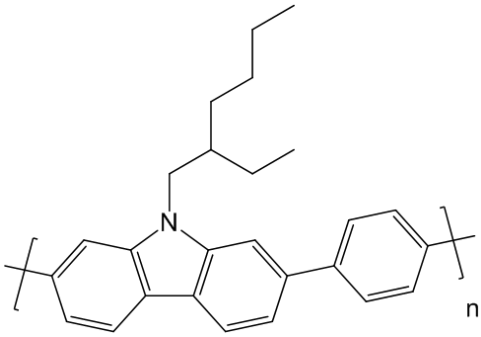

Figure 3.5 Structure of P8 polymer.

Over recent years, much work has focused on optimising the activity of organic semiconductors for photocatalytic hydrogen evolution by modification of the electronic properties. Computational studies have paved a way to rationalise the mechanism by which photocatalysis occurs. But remarkably, little in the way of spectroscopic studies to gain meaningful insight into the excited state dynamics and the role of the different solvent/electron donor has been reported[28,39,47,48] – and this is a topic we explore in this chapter.

3.1.2 Polymers for water oxidation

The first example of photoelectrochemical (PEC) water splitting was reported by Fujishima and Honda in 1972, where a TiO_2 photoanode was illuminated with UV light to achieve water oxidation, and was combined with a Pt counter electrode were hydrogen evolution occured.[49] Since, many inorganic semiconductors have been studied for their application in overall water splitting PEC cells, and have shown impressive solar-to-hydrogen efficiencies > 10%.[50–52] Although this is above the practical commercialisation threshold, they are limited by the following: (i) expensive to fabricate, (ii) use of non-abundant elements and (iii) lack of utilisation of the visible region of the spectrum as most require UV light. The use of organic semiconductors overcomes some of these limitations, as they are cheap to fabricate as they are comprised of earth abundant elements, can be designed to have narrower band gaps and so utilise a larger portion of the solar spectrum and the structure-properties can be easily fine-tuned.

However, despite the high levels of interest in polymer photocatalysts for the HER to date there are few reports of organic photoanodes and photocathodes for PEC cells for overall water splitting. Those that are known are summarised in Table 3.1 and it is apparent that photocurrents as high as *ca.* 6 mA cm^{-2} for organic photocathodes can be achieved. However, in contrast the highest photocurrents for PEC devices with organic photoanodes for water oxidation are ~150 µA cm^{-2},[53] and the majority of photoanodes achieve less than 100 µA cm^{-2}.

*Table 3.1 Summary of organic semiconductor photoelectrodes for solar water splitting. Table taken from Adv. Energy Mater., 2018, **8**, 180258.*[74]

Photoelectrode type	Photoactive layer	HTL[a]	ETL[b]	Catalyst[c]	J_{ph}[d]	Electrolyte	Ref.
Photocathode	P3HT:$PC_{61}BM$	–	–	–	<1 μA cm^{-2}	0.2 M NaCl	[94]
Photocathode	BDT-ETTA COF	–	–	Pt nanoparticles	≈10 μA cm^{-2}@0 V vs RHE	0.1 M Na_2SO_4	[90]
Photocathode	PTBh	–	–	–	≈100 μA cm^{-2}@0.11 V vs RHE (1.6 suns)	1 M phosphate buffer (pH 7)	[80]
Photocathode	PTTh	–	–	–	≈120 μA cm^{-2}@0 V vs RHE	1 M phosphate buffer Adj. w/NaOH (pH 11)	[81]
Photocathode	P3HT:$PC_{61}BM$	PEDOT:PSS	TiO_2	MoS_3	200 μA cm^{-2}@0 V vs RHE	0.5 M H_2SO_4	[95]
Photocathode	P3HT:$PC_{61}BM$	Cross-linked PEDOT:PSS	AZO	Pt	1.2 mA cm^{-2}@0 V vs RHE	0.2 M KCl in phosphate buffer (pH 6.9)	[104]
Photocathode	P3HT:$PC_{61}BM$	MoS_2	TiO_2	MoS_3	1.21 mA cm^{-2}@0 V vs RHE	0.5 M H_2SO_4	[101]
Photocathode	P3HT:$PC_{61}BM$	MoO_x	–	MoS_3	2.2 mA cm^{-2}@0 V vs RHE	0.5 M H_2SO_4	[99]
Photocathode	P3HT:$PC_{61}BM$	Cross-linkable PEDOT:PSS	TiO_x	Pt	≈3 mA cm^{-2}@–0.10 V vs RHE	0.1 M Na_2SO_4 Adj. w/H_2SO_4 (pH 2)	[100]
Photocathode	P3HT:$PC_{61}BM$	MoO_3	TiO_2	Pt	≈3 mA cm^{-2}@0 V vs RHE	0.1 M H2SO4 Adj. w/Na_2SO_4 (pH 1.4)	[103]
Photocathode	P3HT:$PC_{61}BM$	CuI	TiO_2	RuO_x	≈3.7 mA cm^{-2}@0 V vs RHE	0.5 M Na_2SO_4 + 0.1 M NaH_2PO_4 (pH 5)	[102]
Photocathode	P3HT:$PC_{61}BM$	GO	TiO_2	Pt/C–Nafion	6.01 mA cm^{-2}@0 V vs RHE	0.5 M H_2SO_4	[112]
Photocathode	P3HT:$PC_{61}BM$	CuI	TiO_2	Pt	5.25 mA cm^{-2}@0 V vs RHE	0.1 M H_2SO_4–Na_2SO_4 (pH 1)	[111]
Photocathode	P3HT:$PC_{61}BM$	CuI	TiO_2	Pt	7.1 mA cm^{-2}@0 V vs RHE	0.1 M H_2SO_4 + 0.1 M Na_2SO_4 (pH 1)	[107]
Photocathode	P3HT:$PC_{61}BM$	PEDOT:PSS	LiF/Al/Ti	MoS_3	8.4 mA cm^{-2}@0 V vs RHE	0.5 M H_2SO_4	[105]
Photoanode	PTCBI	–	–	CoPc	≈20 μA cm^{-2}@1.2 V vs RHE	1×10^{-3} M NaOH (pH 11)	[115]
Photoanode	BBL	–	–	Ni–Co	≈30 μA cm^{-2}@1.23 V vs RHE	0.6 M sulfate/phosphate buffer (pH 7)	[119]
Photoanode	$PC_{71}BM$	ZnO	ZnO	–	≈60 μA cm^{-2}@1.23 V vs RHE	0.1 M KOH (pH 13)	[118]
Photoanode	PTCDA:$PC_{61}BM$	–	–	–	≈100 μA cm^{-2}@1.2 V vs RHE	35×10^{-3} M KNO_3 Adj. w/H_2SO_4 (pH 2)	[116]
Photoanode	PMPDI	–	–	CoO_x	≈150 μA cm^{-2}@1.56 V vs RHE	0.1 M KPi buffer (pH 7)	[117]

[a]Hole transport layer; [b]Electron transport layer; [c]HER catalyst (photocathode), OER catalyst (photoanode); [d]Under 1 sun simulated solar illumination unless noted.

In contrast to organic photoelecrodes, nanostructured inorganic photoanodes reported such as α-Fe_2O_3,[54] TiO_2,[55] $BiVO_4$[56] and WO_3[57] are known to achieve photocurrents > 1 $mAcm^{-2}$. A further drawback of the organic photoelectrodes is often their lack of stability under the working conditions required, which results in degradation of the photoelectrodes from prolonged periods in acidic/basic electrolyte and/or due to the application of a bias and prolonged light irradiation. Ways in which this can be overcome is by the use of protecting over layers such as TiO_2 or Al_2O_3,[58,59] which not only improve the stability of the electrode, but also aid charge separation upon photoexcitation of the absorber. As there are relatively few examples of solely organic materials that can carry out overall water splitting, here we focus on the use of polymers as sensitizers of inorganic materials for water oxidation either by transfer of the hole or electron into the inorganic support. In chapter 4, a new fully organic system based on the use of a PBI gel for water oxidation is introduced.

In 2011 g-C_3N_4 was first reported for PEC water oxidation in the presence of a TiO_2 heterojunction.[60] TiO_2/g-C_3N_4 electrodes were prepared by heating the TiO_2 electrode at 425˚C in a gaseous urea pyrolysis which resulted in a 1-3 nm layer of g-C_3N_4 on the surface of the TiO_2.[61] PEC measurements of the TiO_2/g-C_3N_4 photoelectrode were carried out in pH 7 0.1 M phosphate buffer. Photocurrents < *ca.* 100 μAcm^{-2} have been reported for TiO_2/g-C_3N_4 photoanodes, which exhibit visible region activity.[61] In the absence of a co-catalyst no oxygen

was detected for TiO_2/g-C_3N_4 photoanodes under 420 nm illumination. Upon the addition of an IrO_x WOC an oxygen Faradaic efficiency (FE) of 19% was reported at +0.5 $V_{Ag/AgCl}$.[61] The low FE obtained was assigned to poor adhesion of g-C_3N_4 to TiO_2 resulting in inadequate electronic coupling between g-C_3N_4 and TiO_2.[61] Further studies optimising g-C_3N_4 photoelectrodes have consisted of exploring different water oxidation co-catalysts (WOCs), doping the TiO_2 heterojunction and altering the working pH of the electrolyte.[62–66] Optimal photocurrents of 49,500 µA cm^{-2} at +1$V_{Ag/AgCl}$ in 0.1 M Na_2SO_4 electrolyte for pristine g-C_3N_4 with 1 wt% Au nanoparticles has since been reported under visible light illumination.[67]

The use of wide band-gap inorganic semiconductors, such as TiO_2, as heterojunctions for improved PEC response is a common technique used to improve photoactivity.[68,69] Dai *et al.* fabricated photoelectrodes by spin coating 10 mg/mL of a soluble fluorene-dibenzothiophene-S,S-dioxide-based conjugated polymer, C12, from THF on the surface of a TiO_2/FTO electrode to improve electron-hole pair separation.[70] An improved photocurrent of 32.5 µA cm^{-2} was obtained under visible light irradiation (>420 nm), 29.5 times that of C12/FTO electrodes, confirming electron transport through the organic semiconductor was limited.[70] These photocurrents reported are of significant size for organic semiconductors in the absence of a co-catalyst. Although C12 photoanodes were optimised, no FEs for O_2 generation were reported. Alternatively, Xiao *et al.* have used ZnO nanorods to improve charge separation of a poly-pyrrole (PPy) conducting polymer in 0.5 M Na_2SO_4 pH 7 electrolyte.[71] Steady state photocurrents *ca.* 680 µA cm^{-2} at +0.8 $V_{Ag/AgCl}$ were observed, double than that for ZnO alone under white light irradiation.[71] Although the authors conclude that the photo-generated holes can oxidise H_2O, no O_2 measurements were reported. ZnO is known to be susceptible to photocorrosion and have stability limitations in acidic and basic pHs,[72,73] and therefore further study is warranted into both O_2 generation and stability.

Organic semiconductor photoanodes have been shown to have poor stability under the harsh working conditions required for water oxidation,[71,74–76] and efforts have been made to improve stability by the use of protecting layers on the organic semiconductor, and by the use of robust organic semiconductor materials.[77] In 2015 Bornoz *et al.* were the first to report an organic semiconductor exhibiting sustained solar driven water oxidation using poly(benzimidazobenzophenanthroline) (BBL), as it is a highly robust organic semiconductor with moderate electron mobility.[75] Thin film photoanodes were prepared by dispersion spray

coating which resulted in the film possessing a rough nanofiber morphology, and optimal photocurrents (Figure 3.6).

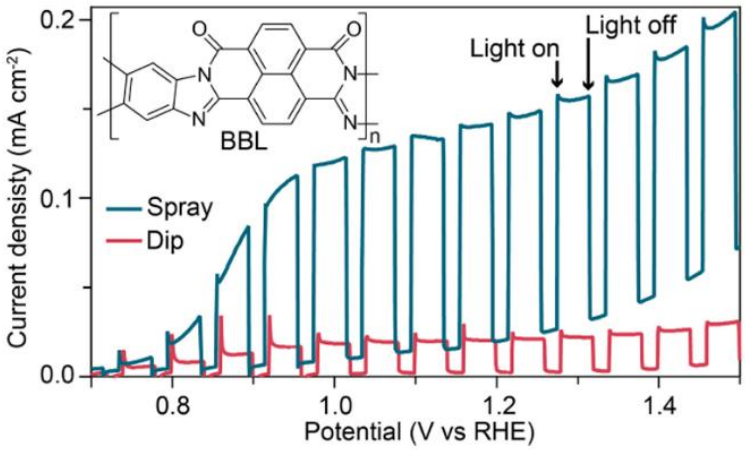

*Figure 3.6 Chopped PEC of BBL (structure shown as insert) dip-coated (red) or spray coated from a dispersion (blue) onto FTO under white light illumination in 0.5 M Na_2SO_3 electrolyte, pH 7. Electrodes were back irradiated, from FTO face. Figure taken from J. Am. Chem. Soc., 2015, **137**, 15338–15341.*[75]

They found films with a thickness of 120 nm gave excellent photocurrents of *ca.* 20 µA cm^{-2} at +1.23 V pH 7 for organic semiconductors, whereas thicker films showed decreased photoactivity.[75] Coupled with back illumination resulting in greater photocurrents, electron transport was seen to be limited which was thought to be due to the presence of grain boundaries between nanofibers. Initial O_2 measurements did not show O_2 generation, but instead that of •OH, detected *via* a florescence probe technique where coumarin reacts with •OH to produce umbelliferone which can be spectroscopically detected. As no self-oxidation was detected, a Ni-Co co-catalyst was added to the BBL electrode in conjunction with a thin layer of TiO_2 to act as a tunnel junction to improve co-catalyst stability.[75] The addition of TiO_2 did not affect the photocurrent obtained, however a 10 µA cm^{-2} increase was observed in the presence of Ni-Co. O_2 measurements of the BBL/TiO_2/Ni-Co photoanode showed a FE of 82 ± 16% for O_2 evolution.[75] Although the photocurrents achieved do not meet those required for practical applications, this study demonstrates promise for the future of organic semiconductors which can not only overcome stability limitations but also carry out efficient water oxidation with high FEs.

The use of a protecting layer to stabilise inorganic photoanodes and improve photocurrents was first actively reported by the McIntyre group.[58] Recently, Wang *et al.* improve the stability of a [6,6]- phenyl C_{71} butyric acid methyl ester ($PC_{71}BM$) electrode which was spin coated onto indium ton oxide (ITO) by atomic layer deposition of an ultrathin ZnO passivation layer (< 2 nm thickness) for visible light water oxidation (Figure 3.7).[78] Excellent stability of the $PC_{71}BM$/ZnO/ITO photoanode was observed in 0.1 M KOH pH 13

electrolyte. A half-life ($t_{50\%}$) of *ca.* 1000 s was reported which was *ca.* 300% greater than $PC_{71}BM$/ITO photoanodes.[78] Optimised photocurrents of 60 µA cm^{-2} were achieved. The addition of a passivation layer aids charge separation, by hole injection from $PC_{71}BM$ to ZnO/electrolyte interface for water oxidation, where an optimal ZnO thickness of ≤ 1.3 nm was found.[78]

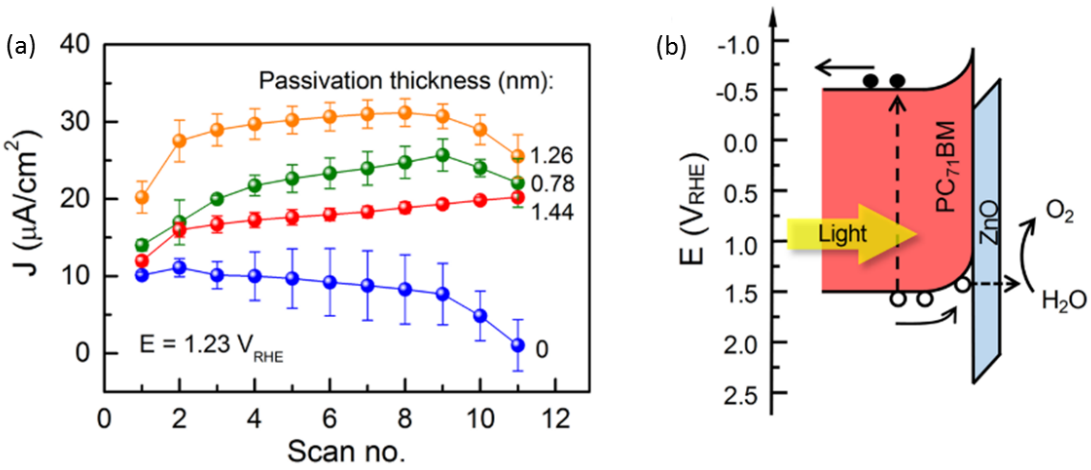

*Figure 3.7 Plot of current vs scan number for $PC_{71}BM$/ZnO electrodes with ZnO passivation layer thickness of 1.44 (red) 1.26 (orange), 0.78 (green) and 0 (blue) nm (a). Energy diagram of $PC_{71}BM$/ZnO (b). Figures reproduced from Chem. Mater., 2018, **30**, 324–335.*[78]

3.1.3 Scope of this chapter

Polymer photocatalysts and electrodes have great potential as water splitting materials due to good synthetic control permitting fine tuning of the materials properties (e.g. optical gap, driving force for charge transfer) possible. However, to date this emerging field has largely been based on chemical intuition and calculations of materials properties. Relatively few studies have examined the photophysics of the polymer photocatalysts. In this chapter we initially use TA spectroscopy to understand the excited states formed and their lifetimes upon excitation and to investigate the mechanism of hydrogen evolution for such systems. Experiments are carried out on a solution processable polymer prepared as a thin film photocatalyst on glass (P8s, Figure 3.8) and also a related linear polymer (P56) both of which were prepared within the Cooper group at Liverpool. In particular we demonstrate the role of the individual components in the reaction mixtures during HER, as it was found empirically that a mixture of water, triethanolamine and methanol gave the highest hydrogen yields but the reason behind this was unknown.

In the second part of the chapter the solubility in organic solvents of P8s is exploited to develop a photoanode with the aim of achieving an overall water splitting device. Such an approach requires preparation of high-quality electrodes on conductive supports, a challenging task with insoluble polymers. To explore the water oxidation activity of P8s for use in overall water splitting, we have used the polymer as a photoanode. The initial activity has been measured, and the photoanode has been optimised for its efficiency of water oxidation by combining with an inorganic support/heterojunction material. Although initial FEs for O_2 production are low, the design approach developed is likely to be of relevance to future studies.

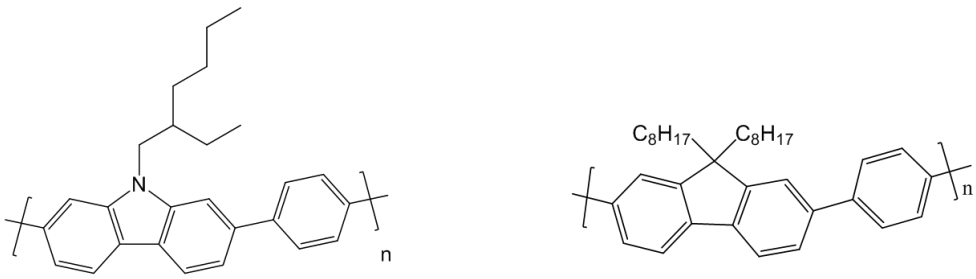

P8s P56

Figure 3.8 Structures of two polymer repeating units explored within this chapter, whereby we aim to understand the role of different solvents and how they affect charge separation during photocatalytic hydrogen evolution experiments.

3.2 Results and Discussion

3.2.1 Photocatalytic excited state dynamics of P8s

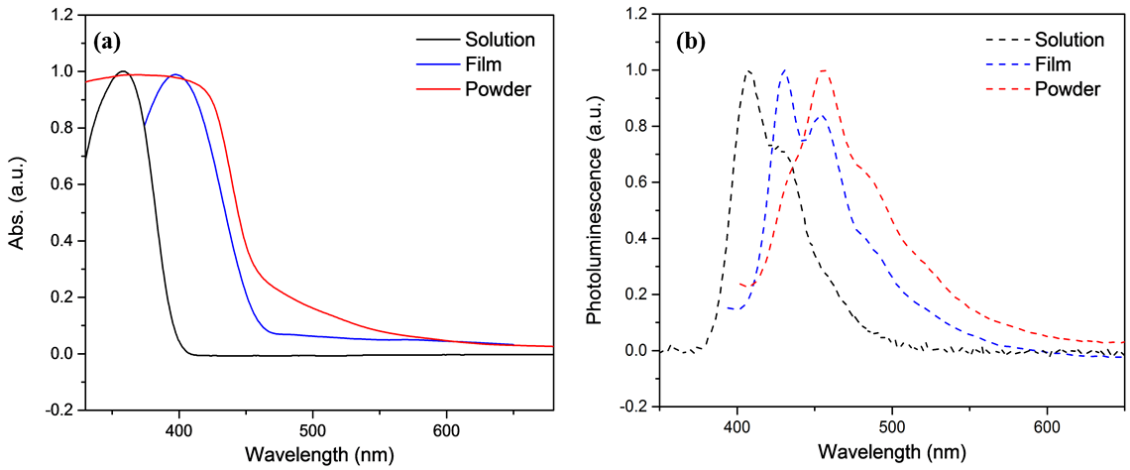

Figure 3.9 UV-Visible absorption (a) and emission (b) spectra for P8s as a solution in chloroform (black), film on glass (drop cast from chloroform, blue) and powder (red). Figure adapted from Adv. Energy Mater., 2017, 7, 1700479. [46]

Cooper and co-workers have previously reported photocatalytic hydrogen evolution with organic polymers such as CMPs and linear polymers.[27,29] A typical experimental set up consists of a mixture or a suspension of the polymer in a solvent mixture, with the addition of a sacrificial electron donor such as methanol (MeOH), diethylamine (DEA), trimethylamine (TEA), triethanolamine (TEOA) and sodium sulphide. Sprick *et al.* have found that for a family of low molecular weight linear polymers a mixture of H_2O/MeOH/TEA (1:1:1) leads to the highest hydrogen evolution activity, although prior to this work the role of the individual components, and need for a solvent mixture was unclear.[29] Here TA spectroscopy was used to study P8s that had been deposited onto a glass substrate as a support material by spin-coating from chloroform in the presence and absence of the scavenger mixes. The films had a UV-Visible absorption maxima at 400 nm, Figure 3.9a, and under an Argon atmosphere showed an emission maxima at 430 nm, Figure 3.9b, with multiple shoulders present due to the presence of many different local environments as a result of torsional disorder and changes in the degrees of freedom within the structure when as a solid in comparison to in solution, therefore resulting in a change in the ratio of vibronic transitions upon excitation for a solid, film or powder.

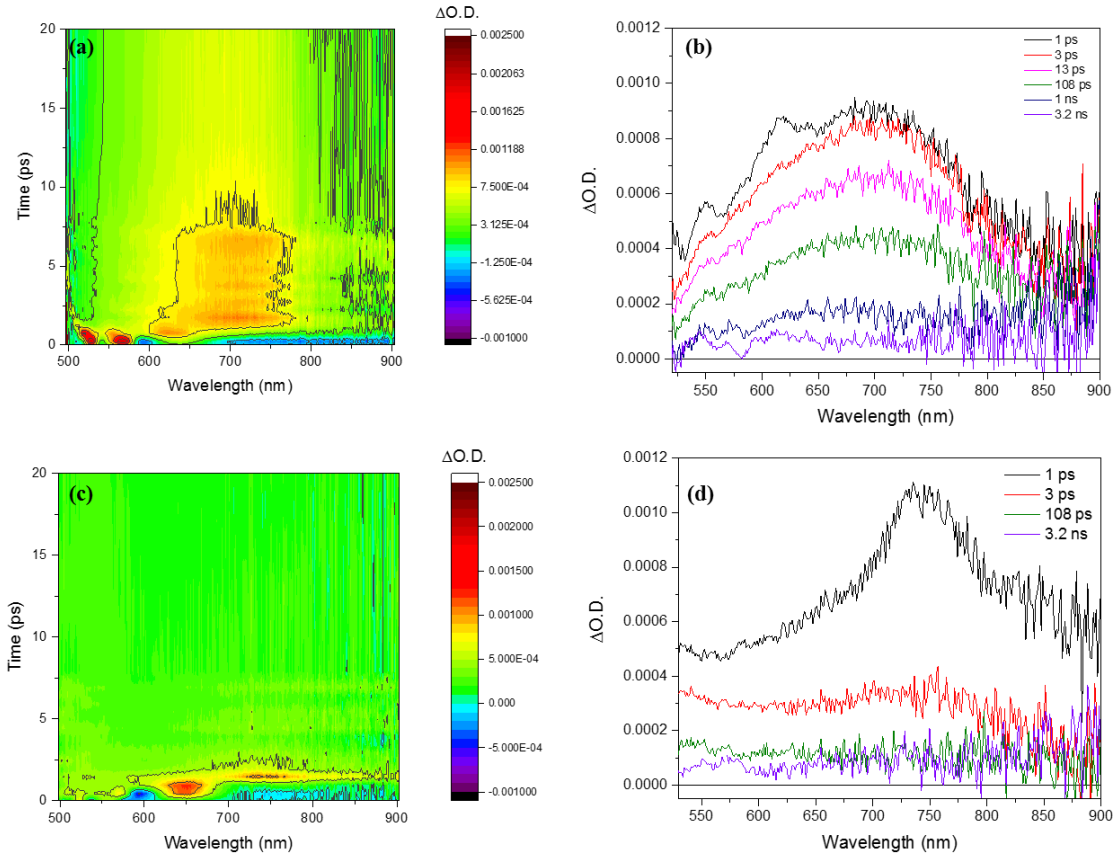

Figure 3.10 TA spectra of P8s film on a glass substrate in a mixture of H_2O/MeOH/TEA (1:1:1) shown as a 3D contour plot (a) and time slices (b) and for P8s in H_2O respectively (c and d). Spectra were recorded on the fs-ns timescale with an excitation wavelength of 365 nm and a pump energy of 150 µW with Ar purged suspensions.

Initially, TA measurements were carried out in H_2O under an inert argon atmosphere with an excitation wavelength of 365 nm (150 µW, 5 kHz repetition rate). The excitation wavelength was chosen to overlap with the maxima of the UV-Visible absorption spectrum, and π-conjugated polymers are predominantly photocatalytically active under UV irradiation.[29,46] Transient spectra of a P8s films in H_2O at various time delays are shown in Figure 3.10c and d. Upon photoexcitation, at early times of < 1 ps, positive features appear at 525nm (weak) and 640 nm. At ~ 1 ps a band 730 nm (br.) is present, and blue shifts as it rapidly decays back down to the ground state. The earliest features are assigned to short-lived photo-induced absorptions (PIA). $T_{50\%}$ is commonly used as an indication of the rate of decay of a feature,[79] and it corresponds to the time where the signal (in this case the PIA) has decayed to 50% of its intensity. The short-lived PIA in H_2O at ~715 nm exhibits a $t_{50\%}$ of ~ 2 ps (Figure 3.11), in-line with literature president for other π-conjugated polymers,[47,80] permitting the assignment of an exciton species. Such fast exciton recombination rates are not surprising, due to the presence of Coulombic interactions present between electrons and holes of the excitonic pair which are only weakly screened in the polymer material, promoting recombination.[81] As

a result of such a short-lived exciton lifetimes, the formation of free charge carriers is therefore prevented.

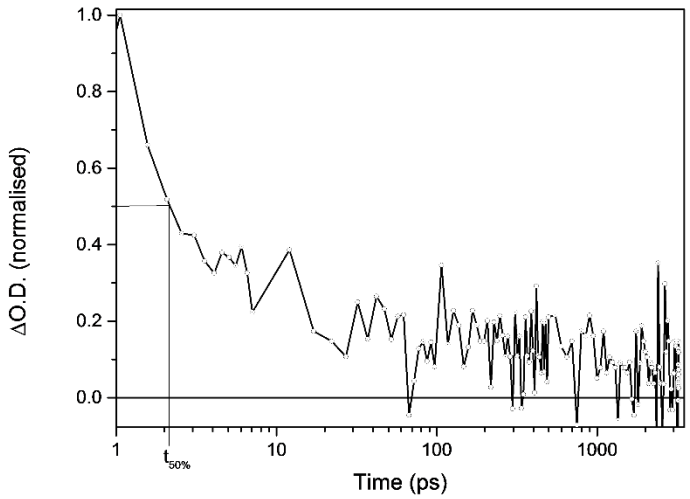

Figure 3.11 Kinetic trace of P8s in H_2O recorded at 715 nm following 365 nm excitation under an atmosphere of argon.

TA spectra of P8s films in a mixture of H_2O/MeOH/TEA (1:1:1) showed TA features that had significantly increased lifetimes when compared to the experiments recorded in water alone, Figure 3.10 a and b. The TA spectra show the formation of short-lived PIAs at approximately 525 nm and 625 nm in less than 1 ps, which are quenched upon the formation of a broad long-lived species at 715 nm. The formation of the 715 nm band within 2 ps occurs at a rate that roughly matches the decay of the 525 and 625 nm bands, Figure 3.12.

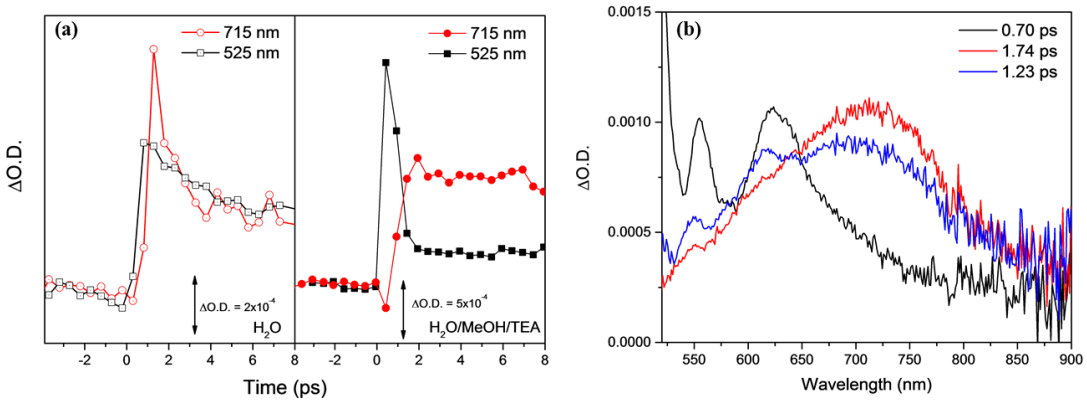

Figure 3.12 Kinetic overlay of 525 nm (black squares) and 715 nm (red circles) in H_2O (open) and H_2O/MeOH/TEA (closed) for P8s (a), showing the rapid quenching of a PIA exciton to form a long-lived species at 715 nm in the presence of electron donors. Spectral signatures of P8s (b) at 0.70 ps (black), 1.74 ps (red) and 1.23 ps (blue), showing the rate at which charge separation occurs in a H_2O/MeOH/TEA system under an argon atmosphere..

Notably an increase in the $t_{50\%}$ to 58 ps at 715 nm is recorded, and a further *ca.* 10% of the intensity of the PIA at 715 nm persists beyond the longest time delay that can be studied by the instrument (3 ns), Figure 3.13. It is therefore apparent that the feature at 715 nm decays *via* multiple pathways. Such long lifetimes for the 715 nm band in the presence of a sacrificial electron donor mix, which would be expected to reductively quench the exciton, are indicative of the formation of an electron polaron state.[82] It is striking that no further evolution in the shape of the TA spectrum occurs after *ca.* 2 to 3 ps in H_2O alone indicating by this time only a minimal PIA remains, leading to the conclusion that exciton quenching occurs within *ca.* 2 to 3 ps (Figure 3.10). The similarity between the proposed UV-Visible absorption maxima of the exciton state (seen in the absence of the electron donor mix) and the electron polaron is in-line with other reports of carbazole polymers for OPV applications.[82] It is also feasible in H_2O that a small amount of the original exciton population evolves to form only a low level of the electron polaron state at *ca.* 715 nm. However, it is notable that in the absence of TEA/MeOH the 715 nm species is short-lived and rapidly decays within the first 100 ps, Figure 3.10b.

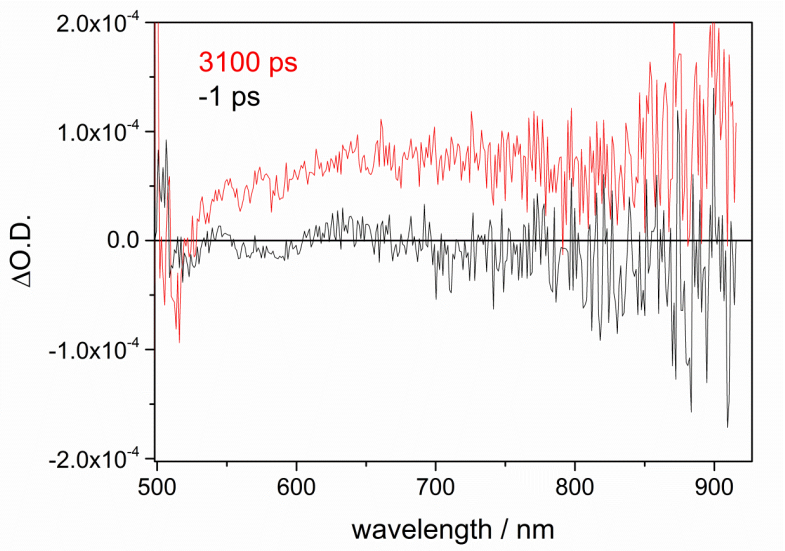

Figure 3.13 TA spectra of P8s at -1 and 3100 ps following 365 nm excitation in a H_2O/MeOH/TEA (1:1:1) solvent under an argon atmosphere. The spectrum at 3.1 ns shows the presence of long-lived species that persists beyond the timescale of this experiment.

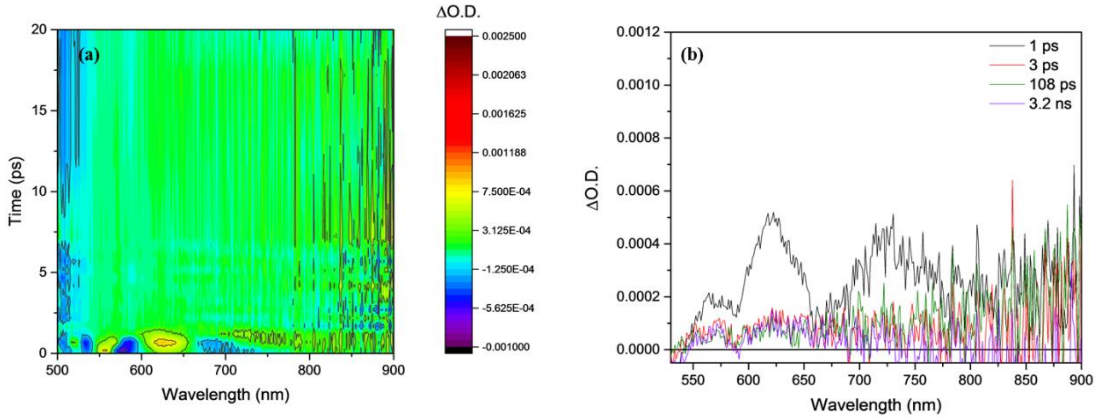

Figure 3.14 Contour plot of P8s in H_2O/MeOH (a) and time slices at 1 ps (black), 3 ps (red), 108 ps(green) and 3.2 ns (purple) (b) under an argon atmosphere upon 365 nm excitation.

To understand if TEA was the acting sacrificial electron donor, analysis of P8s was carried out in H_2O/MeOH (1:1 volume ratio), Figure 3.14. Very similar TA spectra were recorded in H_2O/MeOH to H_2O alone. A short-lived PIA is present at *ca.* 620 nm, with only a small change in $t_{50\%}$ of the PIA being observed from 2 to 4 ps upon the addition of MeOH, leading to the conclusion that MeOH is not acting as a sacrificial donor, Figure 3.14. Comparison of the TA kinetic traces at 715 nm for all 3 systems are shown in Figure 3.15. The long-lived electron polaron state is only formed in the presence of TEA with a sustained $t_{50\%}$ = 58 ps confirming its role as the active sacrificial donor (Figure 3.15), in H_2O alone $t_{50\%}$ ~ 2 ps, in H_2O/MeOH $t_{50\%}$ = 4 ps.

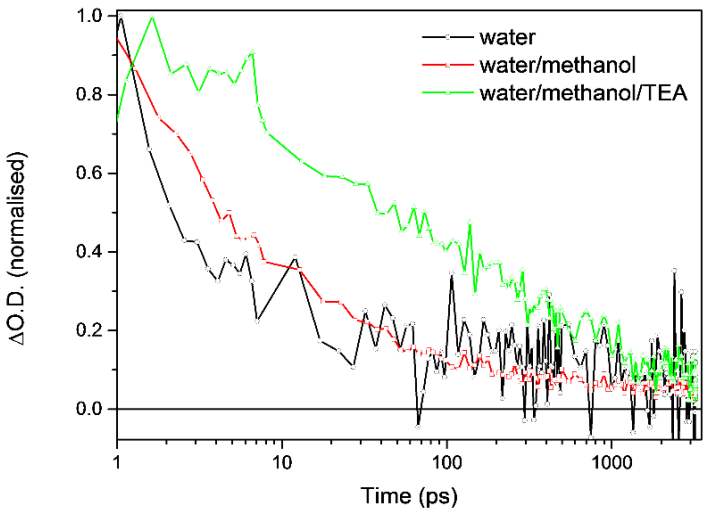

Figure 3.15 Kinetic trace of P8s in H_2O (black), H_2O/MeOH (red) and H_2O/MeOH/TEA (green) recorded at 715 nm following 365 nm excitation under an atmosphere of argon.

The TA conclusions, that the TEA is acting as the electron donor, agree with the photocatalyst measurements that were carried out as part of the collaborative project by D. Woods (Cooper group, Liverpool), Figure 3.16. Although MeOH is a well-known sacrificial donor,[83,84] here it

is suggested that its primary role is the wetting of the hydrophobic polymer in aqueous solution,[47] and the wetting behaviour of P8s samples will be discussed in more detail later in the chapter.

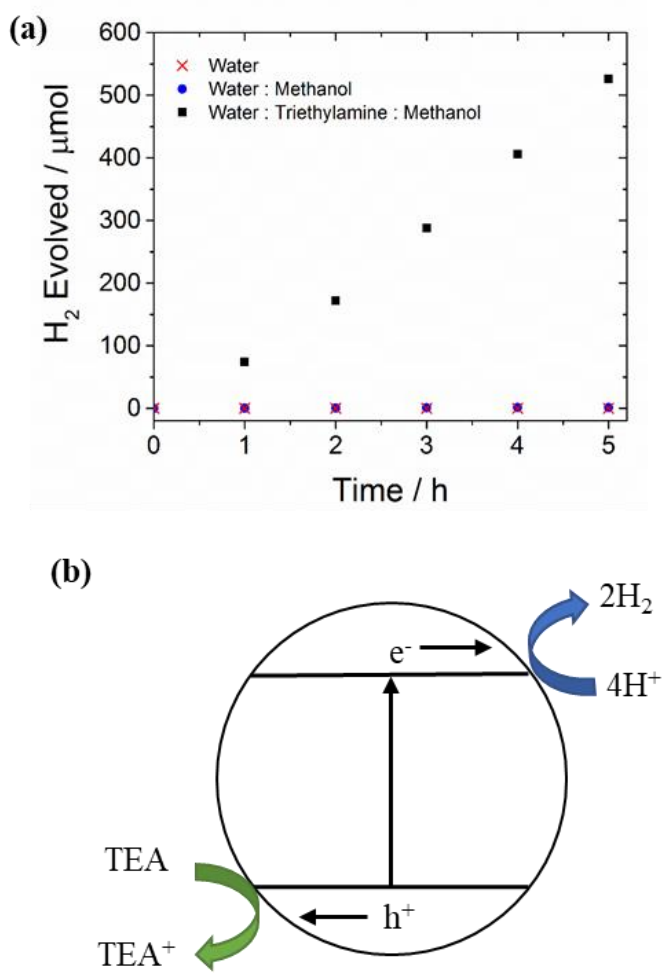

Figure 3.16 Hydrogen evolution of P8 (25 mg) in solutions of H_2O, H_2O/MeOH (2:1) and H_2O/MeOH/TEA (1:1:1) under $\lambda > 295$ nm irradiation (a) reaction scheme of P8s when illuminated showing the role of TEA as a sacrificial electron donor to reduce electron – hole pair recombination (b).

3.2.2 Photocatalytic excited state dynamics of P56

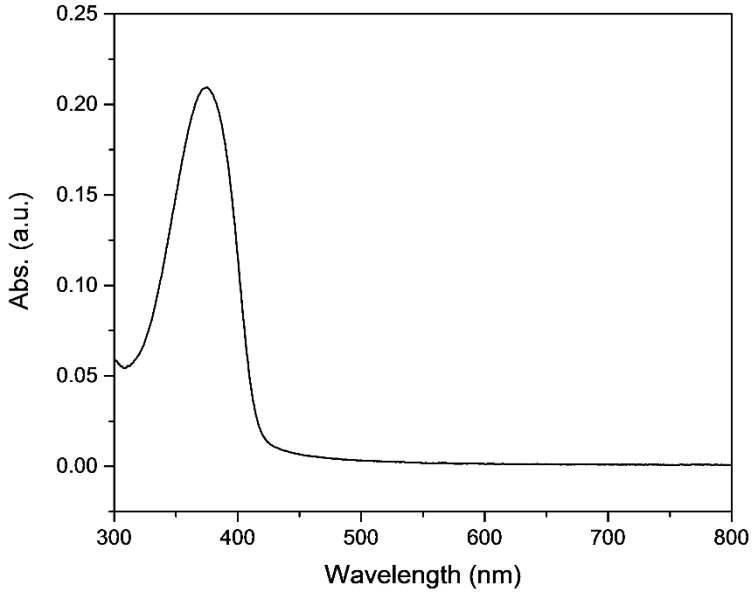

Figure 3.17 UV-Visible absorption spectrum of P56 on a glass substrate.

To understand if the photocatalytic mechanism described above is exhibited for other linear polymers under the same experimental conditions, experiments to investigate the mechanism of P56 film on a glass substrate in H_2O, MeOH and TEA solvent systems with TA spectroscopy were also carried out. Although the increased scattering of suspended photocatalysts can lower the signal to noise of the data it is shown below that insights can still be obtained. The UV-Visible absorption spectrum of P56 in water is shown in Figure 3.17. In the TA experiments P56 was excited at 365 nm (600 μW, 5 kHz repetition rate). In a suspension of H_2O/MeOH/TEA at times > 3 ps P56 exhibited a broad PIA that extended across the visible region, with a maxima at ~775 nm at 3 ps, which by 3 ns has resolved into PIA with maxima at 535, 653 (sh.) and 710 (br.) nm, Figure 3.18. Similarly, to P8s, the broad feature at 710 nm was long-lived where *ca.* 10% of the excited state feature persisted beyond 3.2 ns. Analysis of the earliest spectra in Figure 3.18b shows the PIA at ~500 and ~600 nm which decay within 1 ps.

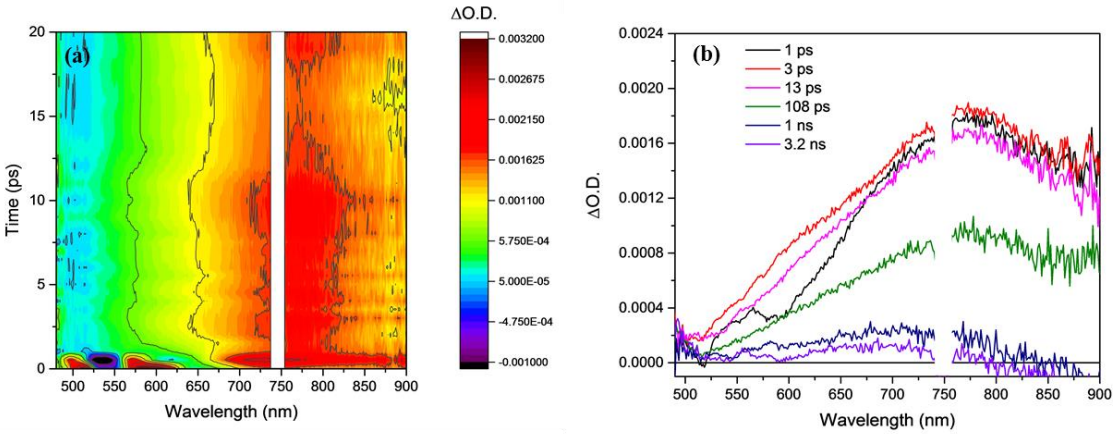

Figure 3.18 Contour plot of P56 in H_2O/MeOH/TEA (a) and time slices at 1 ps (black), 3 ps (red), 13 ps (pink), 108 ps(green), 1 ns (blue) and 3.2 ns (purple) (b) under an argon atmosphere upon 365 nm excitation. Data that has been blocked out by a white bar is due to the presence of a negative feature as a result of half-harmonic generation, where a photon splits into two photons of the half the original energy and so that of half the frequency and double the wavelength of the initial photon.

Attempts to identify if the broad long-lived feature at ~775 to 710 nm grows in as the initially formed PIA decay are shown in Figure 3.19. Although it is clear that the PIA at 715 nm is significantly longer-lived than the initially formed bands (probed here at 500 nm), the kinetic resolution of the data obtained is insufficient to confirm if one species is formed from the other.

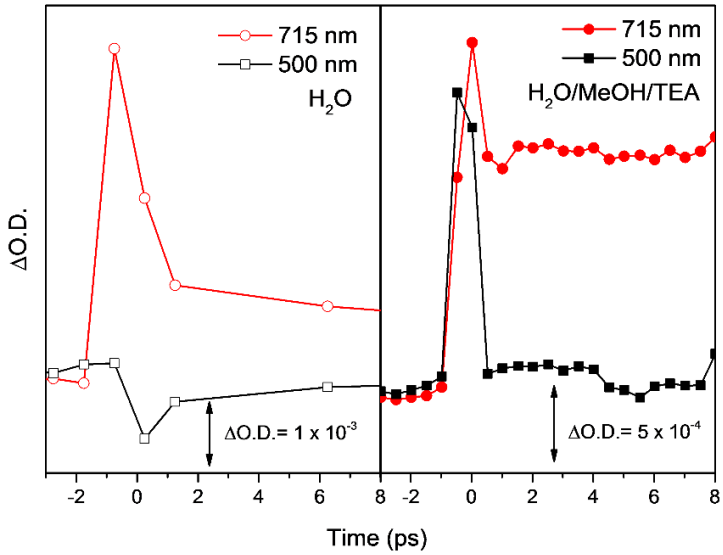

Figure 3.19 Kinetic overlay of 500 nm (black squares) and 715 nm (red circles) in H_2O (open) and H_2O/MeOH/TEA (closed) for P56 (a), showing the rapid quenching of a PIA exciton to form a long-lived species at 715 nm in the presence of electron donors.

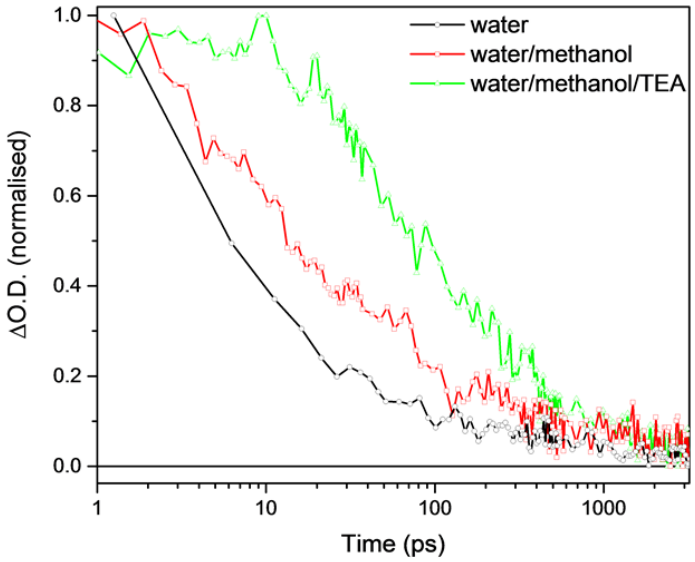

Figure 3.20 Kinetic trace of P8s in H_2O (black), H_2O/MeOH (red) and H_2O/MeOH/TEA (green) recorded at 715 nm following 365 nm excitation under an atmosphere of argon (b).

Although the mechanism of formation of the long-lived PIA at ~775 to 710 nm could not be resolved it is assigned to an electron polaron state, similar to that seen for P8s, on the basis of the long-lifetime of the PIA in the presence of the sacrificial electron donor mix of (H_2O/MeOH/TEA). Both H_2O and H_2O/MeOH solvent systems were also analysed to confirm this assignment and to demonstrate that TEA was acting as the sacrificial electron donor with P56. The TA spectra for P56 in H_2O and H_2O/MeOH are shown in Figure 3.21. In H_2O 365 nm excitation gives rise to weak very short-lived PIAs at ~510 and 560 nm which decay within the first 2 ps. A stronger broad PIA at ~750 nm is also present, but this also decays rapidly with only a small signal remaining beyond 10 ps. In H_2O/MeOH P56 has similar TA spectra after 365 nm excitation with a strong broad PIA at ~750 nm dominating, however the initially formed species being observed at slightly different wavelengths (~525 and 600 nm). The addition of methanol does increase the lifetime of the ~750 nm PIA, and it persists for longer than in H_2O. However, at the longest time-scale recorded (3.2 ns) all of the PIA had decayed down to the ground state, Figure 3.21. It is clear that in the absence of TEA, P56 showed significantly shorter $t_{50\%}$ at 715 nm (6 and 13 ps for the H_2O and H_2O/MeOH solvent systems respectively), in contrast H_2O/MeOH/TEA had a $t_{50\%}$ of 72 ps, Figure 3.20. Therefore, it is proposed that in a manner similar to that seen with P8s the amine (TEA) acts as the main sacrificial electron donor, quenching the exciton and giving rise to a long-lived electron polaron state. In the presence of MeOH/H_2O the increase in lifetime of the ~750 nm band, compared to H_2O alone, also suggests that with P56 MeOH may be able to act as a sacrificial

electron donor, however it appears to be less effective than TEA as indicated by the shorter $t_{50\%}$ of the PIA due to a larger percentage of the exciton population recombining.

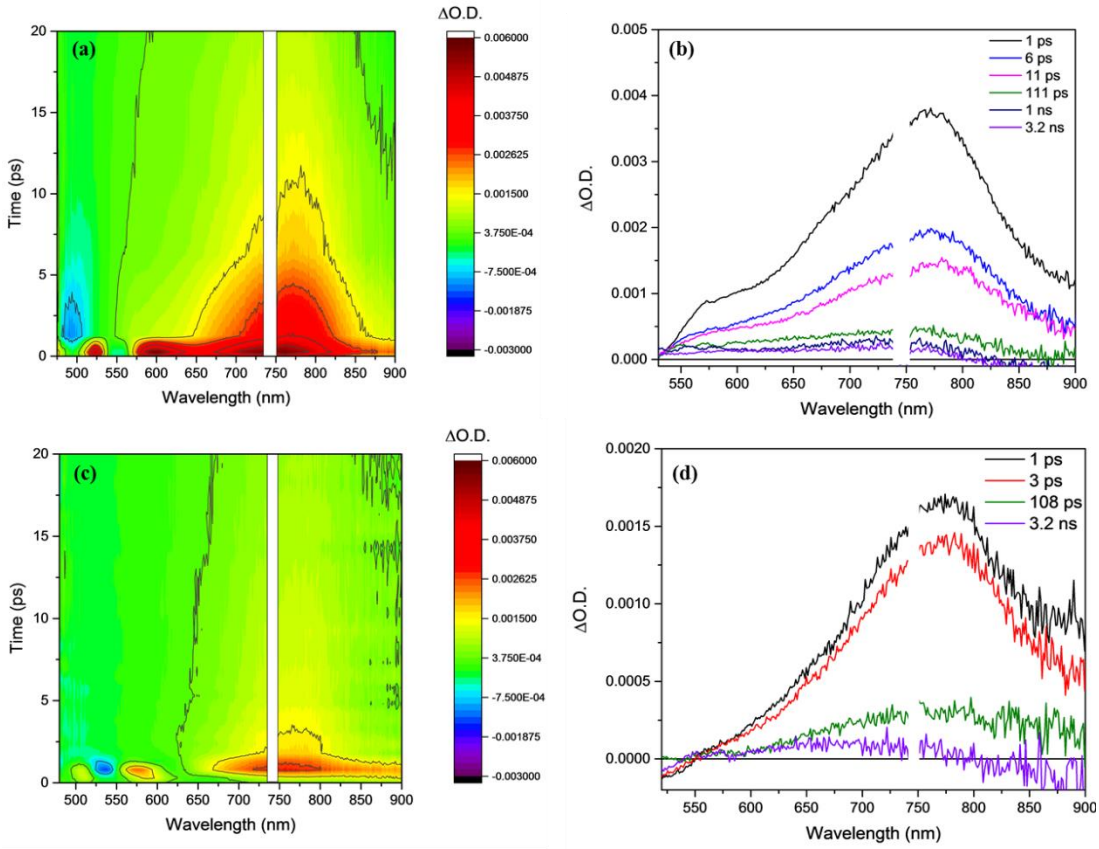

Figure 3.21 TA spectra of P56 in H_2O shown as a 3D contour plot (a) and time slices (b) and for P56 in H_2O/MeOH (1:1 volume ration) respectively (c and d). Spectra were recorded on the fs-ns timescale with an excitation wavelength of 365 nm and a pump energy of 150 µW. Data that has been blocked out by a white bar is due to the presence of a negative feature as a result of half-harmonic generation, where a photon splits into two photons of the half the original energy and so that of half the frequency and double the wavelength of the initial photon.

In conclusion, we rationalised for the first time the mechanism of hydrogen evolution for a class of linear polymers when in a H_2O/MeOH/TEA solvent mixture which is often used with linear polymer photocatalysts.[28,29] We find the photo-generation of a short-lived PIA for both P8s and P56 in H_2O alone. Although MeOH can act as a sacrificial electron donor, here we show that with P8s its primary role is not as an electron donor, instead it is believed to act as a co-solvent to enhance miscibility of the linear polymers and H_2O.[29,47] Instead we find that TEA is the main sacrificial electron donor, indicated by a significant enhancement in the $t_{50\%}$ for the transient absorption spectra of both polymers.

3.2.3 Developing and optimising a soluble processable polymer photoanode

P8s has been shown to be a good hydrogen evolution photocatalyst. However, hydrogen evolution requires the use of a sacrificial electron donor which is unsustainable. The fabrication of photoelectrodes provides a way to remove the need for a sacrificial donor from photocatalytic systems as the polymer can be used either as a photocathode, with the electrons coming from water oxidation at the anode, or as a photoanode which provides electrons for the cathode to carry out the HER.[85,86] P8s and P56 are promising materials for their use as photoelectrodes as both exhibit good HER rates for this class of photocatalysts,[7,29,46,87] and the solution processability of P8s from organic solvents offer a facile route for the fabrication of photoelectrodes. In addition, P8s is studied here due its superior HER rates (72 ± 1 *vs* 6 ± 1 μmol $g^{-1}h^{-1}$). P8s is a carbazole polymer, materials which have been shown to be good electron donors in organic photovoltaics,[88] and so it is therefore possible that P8s may be able to inject an electron into a supporting electrode material (e.g. FTO, TiO_2), leaving the P8s hole to carry out water oxidation. To determine if P8s is capable of carrying out water oxidation, determination of the band gap and HOMO and LUMO energies was carried out.

Table 3.2 Summary of the optical properties and $E_{HOMO/LUMO}$ positions for P8s as a film, powder and solution, where a change in the optical properties show a change in the packing of the polymer. Solution UV-Visible absorption and photoluminescence spectra were recorded in chloroform, and films were cast from a chloroform solution. $P8s_{pow}$ $E_{HOMO/LUMO}$ positions were determined from XPS measurements. All potentials are reported vs NHE at pH = 0.

	λ_{abs} (nm)	λ_{em} (nm)[1]	λ_{onset} (nm)[2]	Eg_{opt} (eV)[3]	E_{LUMO} (V)	E_{HOMO} (V)
$P8s_{film}$	400	430	444	2.79	-	-
$P8s_{pow}$	-	455	457	2.71	-0.91	+1.80
$P8s_{sol}$	358	407	400	3.10		

[1] Excitation wavelength was 360 nm. [2] Calculated from the onset of the absorption spectrum. [3]Calculated by $Eg_{opt} = 1240/\lambda_{onset}$.

Dai *et al.* have previously investigated the use of fluorene-dibenzothiophene-S,S-dioxide-based conjugated polymers, C6-i (insoluble polymer), C6-s (soluble polymer) and C12, for photoelectrochemical water oxidation.[70] X-ray diffraction (XRD) was used to gain insight into the difference between packing of the polymers upon spin coating on FTO, showing an amorphous structure of C6-i and C12 and a semi-crystalline structure of C6-s.[70] We have previously shown using powder XRD that P8s is semi-crystalline,[46] which is expected to give rise to good conduction pathways, allowing efficient charge separation and transfer for the oxidisation of water.[70] UV-Visible absorption and photoluminescence spectroscopy give insight into the optical properties of a material. Analysis of P8s as a powder ($P8s_{pow}$), as a film

($P8s_{film}$) or as a solution ($P8s_{sol}$) showed significant changes in optical properties, and an increase in bandgap of $2.71 \leq 2.79 < 3.10$ eV respectively.

A significant blue shift in the UV-Visible absorption maxima for $P8s_{sol}$ in comparison to $P8s_{film}$ or $P8s_{pow}$ indicates a change in π-π stacking of the polymer as a result of increased degrees of freedom, Figure 3.9.[46,89] When in solid form, powder and film, P8s has fewer degrees of freedom compared to the solution resulting in more planar structures.[46,89] As a result of such a change in band gap, a shift in the HOMO/LUMO energies are likely. X-ray photoelectron spectroscopy (XPS) is a technique commonly used in photovoltaics and catalysis to gain insight into chemical environments, and the occupied and unoccupied electronic states of inorganic and organic materials, more so the former.[90–93] Therefore, XPS was used to determine the valence band position of $P8s_{pow}$ which is expected to be closer in energy to that of $P8s_{film}$. A valence band energy of +1.80 V_{NHE} (pH = 0), and conduction band potential of -0.91 V_{NHE} (pH = 0) was also determined from XPS and the $P8s_{pow}$ bandgap, showing sufficient driving force for water oxidation (570 mV overpotential at pH 0 and 460 mV at pH 13). Determination of the valence band and band gap of P8s indicated that it is a suitable material for water oxidation, Figure 3.22.

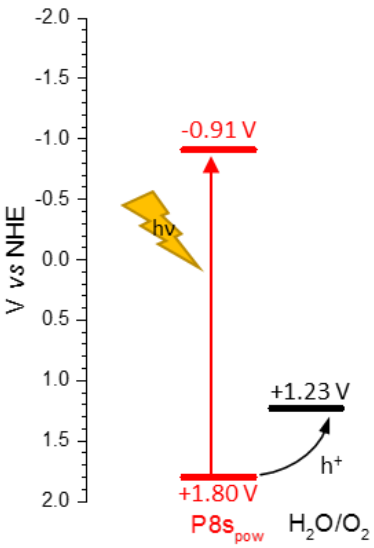

Figure 3.22 Energy band diagram for $P8s_{pow}$ determined from XPS where pH = 0 vs NHE.

To test the application of P8s as a water oxidation catalyst, immobilisation of the polymer onto a conductive support was carried out *via* spin coating 30 layers of a P8s (3 mg/mL) solution in chloroform on FTO, resulting in an optically thin film. For the remainder of this chapter we will focus on the study of P8s films, therefore the term P8s will be used

instead of $P8s_{film}$. Activity of P8s was initially tested in two different electrolytes 60 mM phosphate buffer (pH 7) to mimic the natural pH of water, and 0.1 M KOH (pH 13) as basic working conditions usually result in better photoanode performance.[74,75,94,95] All PEC measurements were carried out under an argon atmosphere using Ag/AgCl (3.5 M KCl) reference electrode, Pt counter electrode and a 300 W Xe lamp (315-795 nm) with a typical light intensity of 63 mW cm^{-2}. Although both electrolyte systems showed photoanodic behaviour from as early as 0 $V_{Ag/AgCl}$ from chopped linear sweep voltammogram (LSV) measurements (Figure 3.23), charge separation was significantly different for the different working conditions.

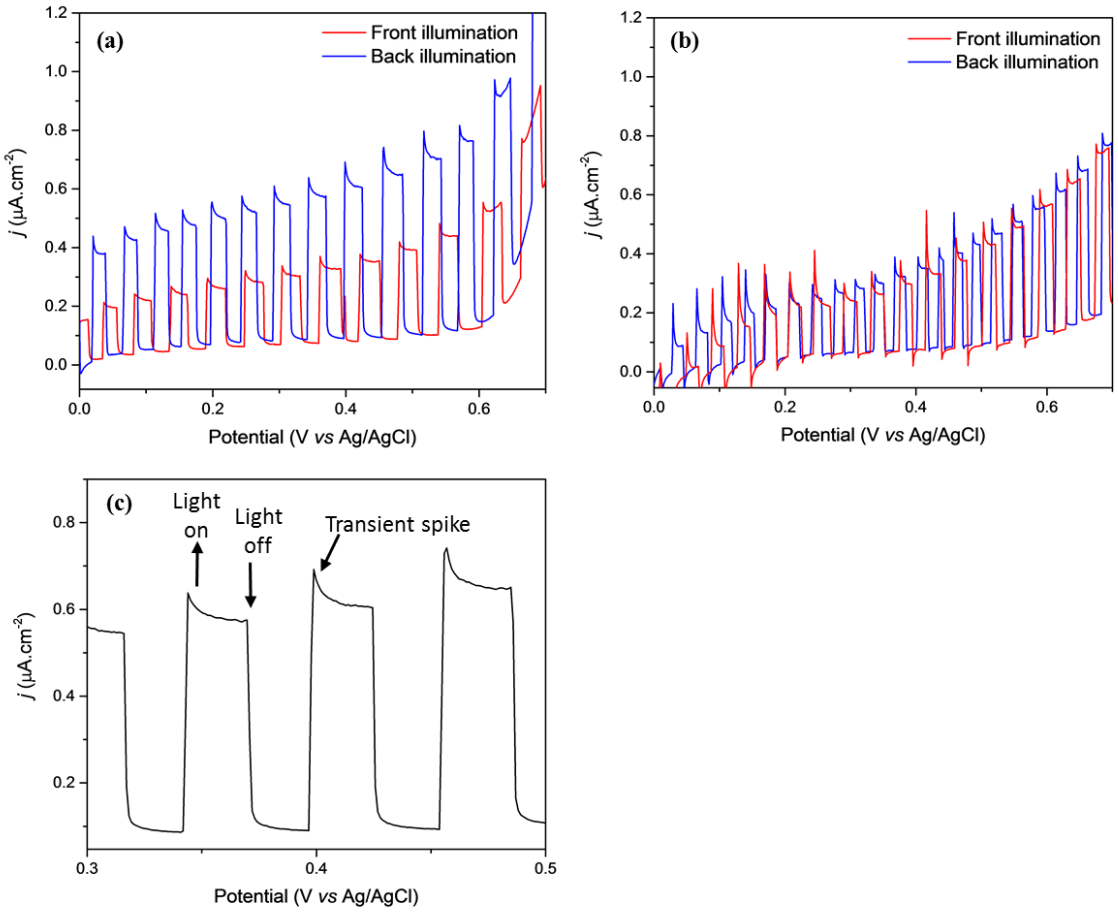

Figure 3.23 Photoelectrochemistry of P8s/FTO in 0.1 M KOH, pH13 (a) and 60 mM phosphate buffer, pH 7 (b) where front illumination (directly on P8s, red) and back illumination (through FTO, blue) are shown. The presence of a photocurrent upon irradiation and of transient spikes are indicated by arrows for P8s/FTO in 0.1 M KOH illuminated from the back face (c). All measurements were carried out under 300 W Xe white light irradiation 300 W Xe lamp (315-795nm, 63 mW.cm^{-2}), under an argon atmosphere using a 10 mVs^{-1} scan rate.

When illuminated through the FTO (back illumination) in pH 7 electrolyte, P8s showed little increase in photocurrent compared to front illumination, leading to a value of 0.31 μA cm^{-2} (Figure 3.23b). In contrast, the films showed a more significant difference between front and back illumination (61%) in a pH 13 electrolyte, from 0.25 to 0.64 μA cm^{-2} at 0.4 $V_{Ag/AgCl}$ (Figure 3.23a). Such behaviour is indicative of electron transport through the polymer being hindered by charge recombination before the electron/exciton reaches the FTO/polymer interface, and is also evidenced by the presence of transient spikes in the PEC for both working environments. The transient spikes can be used to investigate electron-hole pair kinetics in the material, Figure 3.23c. The rate of decay of the transient spike can give insight into recombination rates of photoexcited electron-hole pairs, and how well electrons can move through the material to reach the FTO. Here, fast electron hole pair recombination rates of 0.139 ± 0.00713 seconds and 0.437 ± 0.0185 seconds were observed, and stable photocurrents were achieved after 1.2 and 1.96 seconds for pH 7 and 13 working conditions respectively. Due to superior photocurrents and slower recombination rates of photo-generated electrons and holes, 0.1 M KOH (pH 13) was used for further PEC studies.

Photocurrents obtained for P8s on FTO were significantly lower than literature precedents, where photocurrents ranging from <10 μA cm^{-2} up to 0.23 mA cm^{-2} have been reported for π-conjugated organic photoanodes on a conducting glass substrate.[53,70,75,96] The overall efficiency of such systems is dependent on the efficiency of charge separation (η_{sep}), light harvesting (η_{LH}) and hole injection (η_{inj}).[97] The efficiency of charge separation can be improved by the incorporation of a heterojunction consisting of a suitable semiconductor, which has a LUMO more positive than that of the catalyst material to allow a flow of electrons to the semiconductor and prevent electron-hole pair recombination.[98,99] From the energy band diagrams determined for $P8s_{pow}$ earlier in the chapter, TiO_2 (anatase) was selected as a suitable semiconductor. TiO_2 has a large band gap (3.2 eV),[100] and so requires high energy photons from the UV region to photoexcite an electron from the valence to conduction band, and so it is largely inactive in the visible region. The valence and conduction bands of TiO_2 reside lower than the HOMO and LUMO for P8s respectively, allowing holes to be used to oxidise water, and electrons to move from the conduction band of P8s to TiO_2. Thin layer TiO_2 heterojunctions were prepared on FTO *via* a spray coating method, then 30 layers of P8s were spin coated onto the surface of the TiO_2 electrode, yielding a pale-yellow electrode. The properties of the photoanode were studied by carrying out linear sweep voltammetry from -0.9 V to +1.2 $V_{Ag/AgCl}$ whilst simultaneously chopping the light, where the photocurrent onset potential was ~ -0.8 $V_{Ag/AgCl}$ with photoactivity increasing at more positive potentials. The incorporation of a thin layer TiO_2 heterojunction significantly increases the photocurrent by a factor of 30 (96% increase), from 0.64 μA cm^{-2} to 18.69 μA cm^{-2} at +0.4 $V_{Ag/AgCl}$ when the

photoelectrodes are back illuminated, due to an increase in electron-hole pair separation, Figure 3.24 a and c. A reduction of transient spikes present in the PEC response indicates a significant decrease in electron-hole pair recombination, with only a small number of photo-generated electrons and holes quickly recombining within the first 0.33 seconds of irradiation at a rate of 0.127 ± 0.098 seconds, Figure 3.24 b. In the presence of a heterojunction, charge transport through the material was increased, as the difference in photocurrent between front and back illumination was reduced by 25% in comparison to P8s/FTO.[98,100] As TiO_2 is photoactive in the UV region, it was important to confirm that the increase in photoactivity was owed to improved charge separation in P8s, and not TiO_2 photoactivity. PEC measurements of TiO_2 irradiated on the front and back face showed *ca.* 50% lower photocurrents, confirming the improved photoactivity is due to increased electron-hole pair separation in P8s, Figure 3.24 c and d.

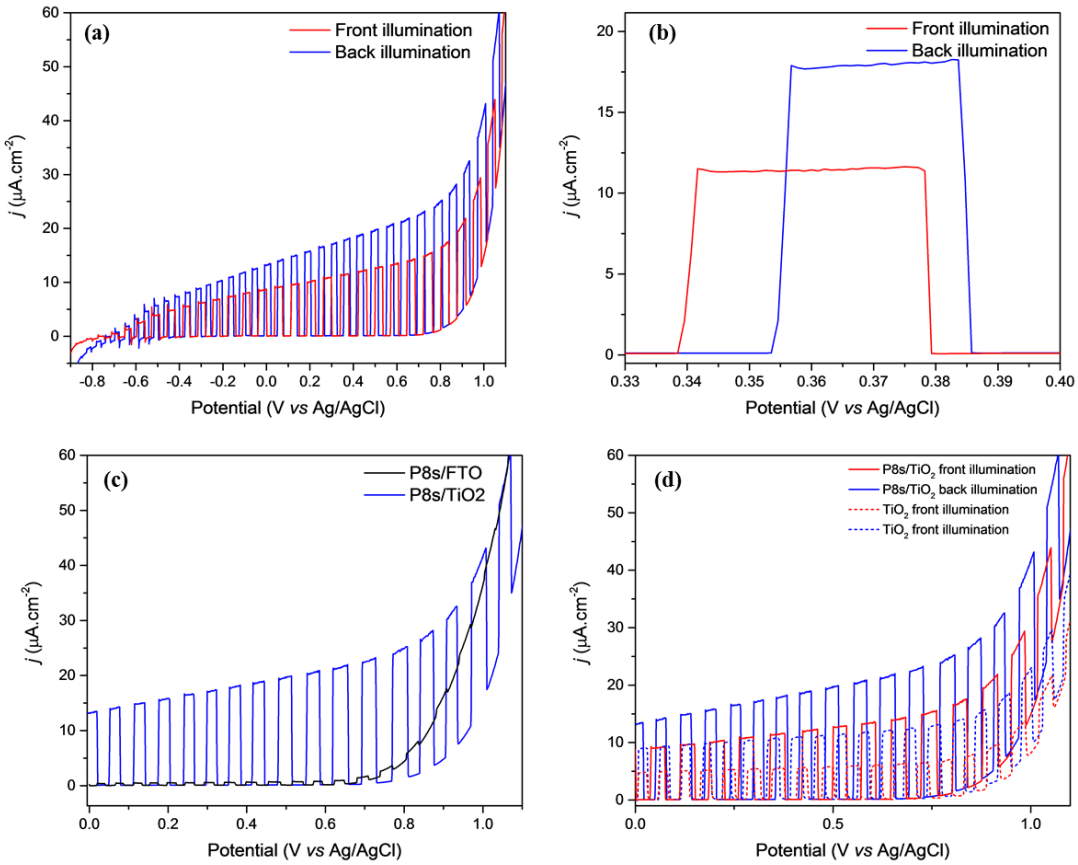

Figure 3.24 P8s/TiO_2 PEC from -0.9 to 1.2 $V_{Ag/AgCl}$ showing front (red) and back (blue) illumination (a), and a zoomed in region on the voltammogram between +0.33 and +0.44 $V_{Ag/AgCl}$ (b). Overlay of P8s on FTO (black) and on a thin layer of TiO_2 (blue) (c). Overlay of front (red) and back (blue) illumination of P8s /TiO_2 (solid) and blank TiO_2 (dashed) (d). Linear sweep voltamograms were carried out at 10 mVs^{-1} under chopped illumination with 300 W Xe lamp (315-795nm, 63 mW cm^{-2}), in 0.1 M KOH electrolyte under an argon atmosphere. 30 layers of P8s were spin coated onto TiO_2 from a solution of P8s (3 mg/mL) in chloroform.

To obtain an efficient photoanode, the rapid utilisation of photo-generated holes is essential. We probed the ability of P8s to carry out oxidation by the addition of a hole scavenger to the electrolyte. 10% MeOH was added to the aqueous electrolyte leading to only a small (2.71 µA cm^{-2}) increase in photocurrent, Figure 3.25. As previously discussed within this chapter, TA spectroscopy has shown MeOH to be a good solvent to increase the wettability of P8s. Therefore, to ensure MeOH was not acting solely as a wetting agent, TEA (also a hole scavenger) was added to the system in the same concentration. This resulted in an identical photocurrent response, indicating that MeOH was acting as the hole scavenger. A further increase in the concentration of MeOH/TEA to a 1:1 ratio with water saw a 6.35 µA cm^{-2} photocurrent increase in comparison to 0.1 M KOH, Figure 3.25, which could partially be due to an increased wetting of the polymer. Although a hole scavenger is thermodynamically easier to oxidise than water, the lack of a large increase in photocurrent indicates that hole transfer from the polymer to the electrolyte is not limiting activity. Instead it is likely that either light absorption, charge separation or transport remains limiting.

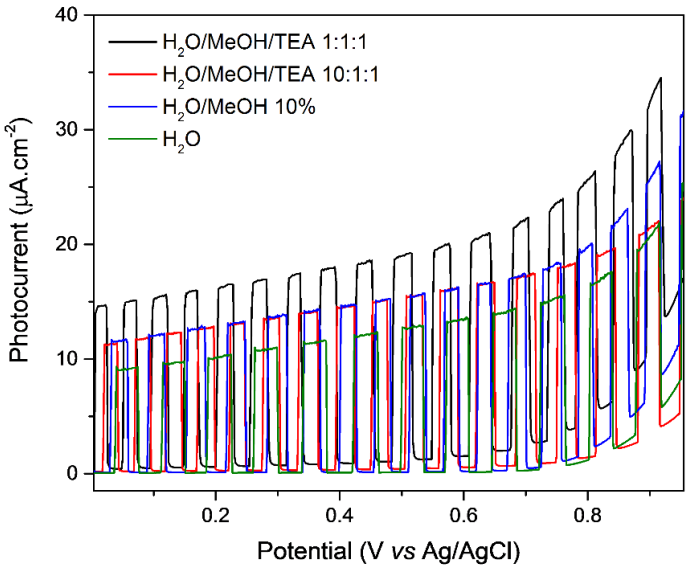

Figure 3.25 LSV under chopped illumination of white light with a KG1 filter in H_2O (green), H_2O and 10% MeOH (blue), H_2O and 10% MeOH/TEA (red) and H_2O/MeOH/TEA in a 1:1:1 ratio under an argon atmosphere, showing an increase in photocurrent upon the incorporation of a hole scavenger which is indicative of the ability for P8s to carry out oxidation and utilise its photo generated holes. Irradiated with 300 W Xe lamp (315-795nm, 63 mW cm^{-2}).

Although significantly improved photocurrents of 12.14 µA cm^{-2} were achieved by the incorporation of a thin layer of a TiO_2 heterojunction, the photocurrents are not comparable to literature precedents which report photocurrents as high as 32.50 µA cm^{-2} for a system of solution processable linear polymers.[70,75] As the addition of a hole scavenger did not indicate that hole transfer was limiting, efforts to further enhance the photoactivity were explored. The

P8s/TiO_2 photoelectrodes used are optically thin, and UV-Visible absorption spectra of P8s/TiO_2 showed only 46% of light being absorbed between 350-500 nm, Figure 3.26. Changing the morphology of TiO_2 from planar to nanoporous TiO_2 (n-TiO_2) was hypothesised to increase the light harvesting properties of the material due to a large increase in the surface area of the film. n-TiO_2 films on FTO were made by doctor blading titanium (IV) oxide paste on FTO, and annealing at 450˚C for 1 hour to obtain TiO_2 anatase. A standard n-TiO_2 paste used in the dye sensitized solar cell community consisting of 15 nm diameter TiO_2 nanoparticles which upon annealing form an interconnected network. n-TiO_2 films were prepared with a thickness of 4 µm. Full details can be found in section 3.4. P8s was then loaded onto n-TiO_2 by soaking in a solution of P8s (3 mg/mL) in chloroform for 48 hours. The UV-Visible absorption spectra of n-TiO_2/P8s films showed an increased photon absorption (> 95% between 360 and 800 nm), compared to the planar films, Figure 3.26.

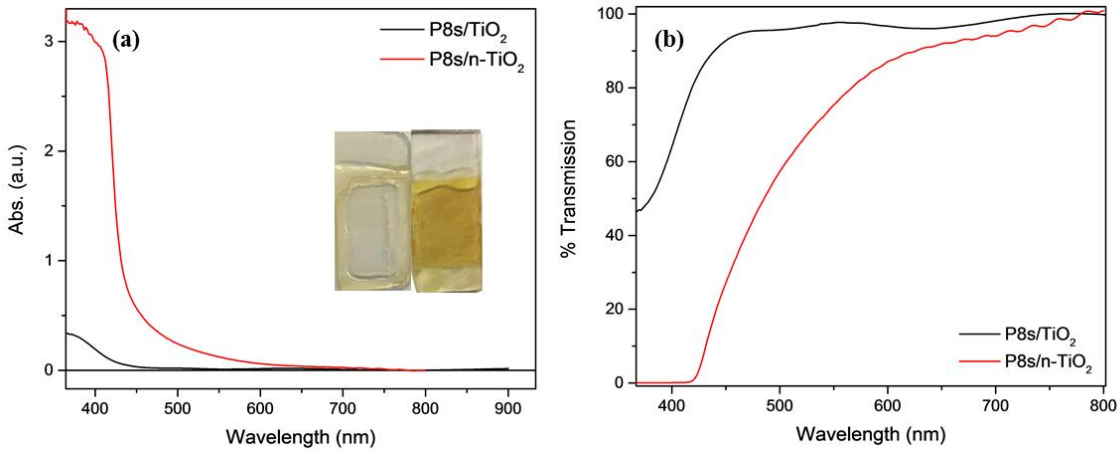

Figure 3.26 UV-Visible absorbance (a) and transmission (b) spectra of P8s on TiO_2 (blue) and n-TiO_2 (red), with an inset of photographs of P8s/TiO_2 (left) and P8s/n-TiO_2 (right) showing an increase in P8s loading upon the fabrication of a high surface area nonporous TiO_2 electrode.

PEC measurements of P8s/n-TiO_2 showed a further 10% increase in photocurrent compared to the planar electrode, achieving photocurrents up to 20.97 µA cm^{-2}. Similarly, to P8s on FTO and TiO_2, back illumination gave rise to superior photocurrents. In fact, charge transport for P8s/n-TiO_2 was even more hindered in comparison to P8s/TiO_2, with a 51% decrease in photocurrent for front illumination, as opposed to 36% for P8s/TiO_2 suggesting that the increased path length of the photoelectrons through the nanostructured TiO_2 leads to recombination. Charge transport limitations were also evident from the shape of the chopped LSVs. Unlike our previous results, no transient spikes are present in the chopped LSV, instead a slow rise in photocurrent during the first 2 seconds of irradiation before reaching a steady state was observed, showing that charge cannot be extracted from P8s and is instead accumulating within the structure, Figure 3.27. From PEC measurements under the full

spectrum of a Xe lamp it was evident that P8s was covering the surface of n-TiO_2 as the photocurrent of bare n-TiO_2 was 5 times larger than that of P8s/n-TiO_2, indicating that P8s is absorbing the light as opposed to n-TiO_2, Figure 3.27 a and b. However, as is shown below the n-TiO_2 activity only arises from the UV part of the solar spectrum, Figure 3.28.

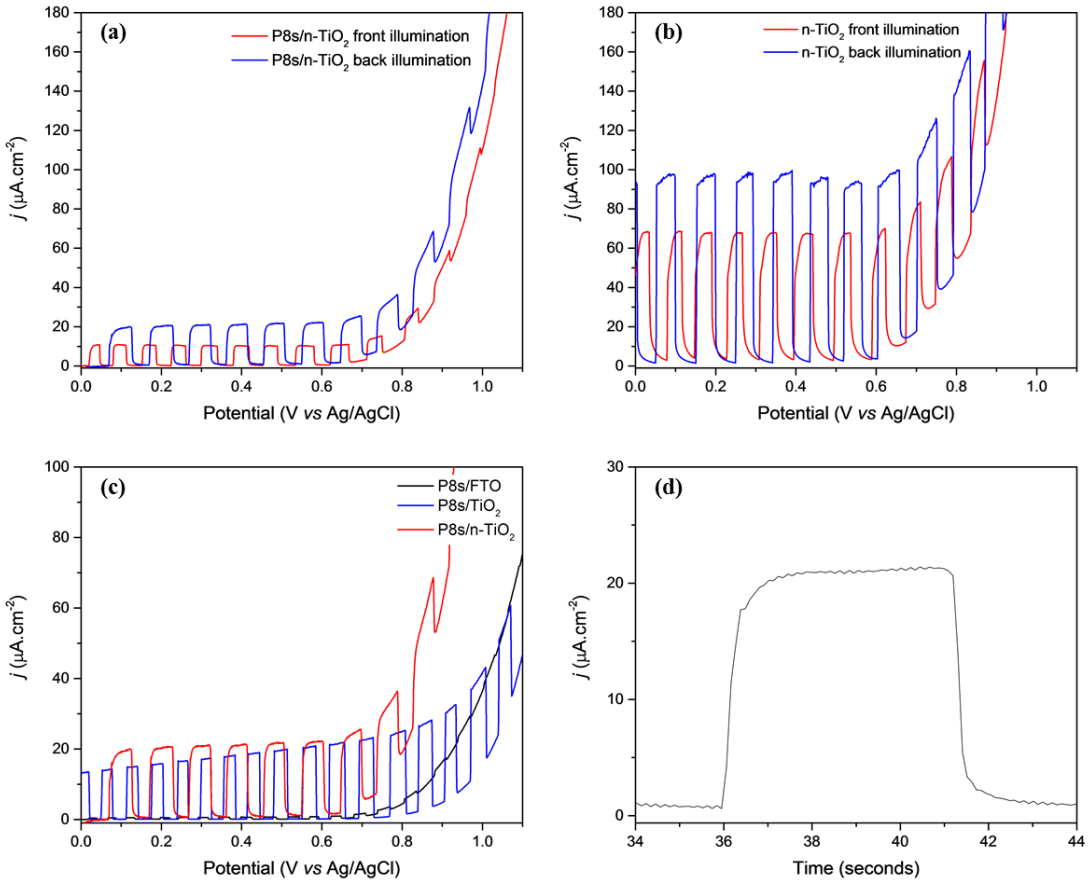

Figure 3.27 P8s/n-TiO_2 (a) and n-TiO_2 (b) PEC in 0.1 M KOH illuminated on the front (P8s) face (red) and back (FTO) face (blue). Overlay of P8s on FTO (black), TiO_2 thin layer (blue) and n-TiO_2 (red) PEC (c). P8s/n-TiO_2 photo-response to the light being switched on and off, where the x-axis is time, showing poor charge transport (d) Irradiated with 300 W Xe lamp (315-79 5nm, 63 mW cm^{-2}).

The activity of the photoanode was probed using monochromatic light as this should allow the monitoring of the photoactivity of n-TiO_2 (365 nm) and P8s (420 nm) separately, as these wavelengths correspond to the maximum absorbance of either TiO_2 or P8s, therefore ensuring activity is not correlated to P8s acting as a photosensitizer for TiO_2. At 365 nm P8s/n-TiO_2 showed lower photocurrents in comparison to n-TiO_2 alone *via* back illumination (3.61 *vs.* 27.48 µA cm^{-2} TiO_2 alone), due to superior photoactivity of n-TiO_2 under UV irradiation, Figure 3.28a. Whereas, when P8s/n-TiO_2 was irradiated with 420 nm wavelength P8s/TiO_2

showed superior photocurrents (7.49 *vs*. 0.16 µA cm^{-2} TiO_2 alone), indicating the photoactivity under visible light is largely due to the presence of P8s, and not to that of TiO_2, Figure 3.28b.

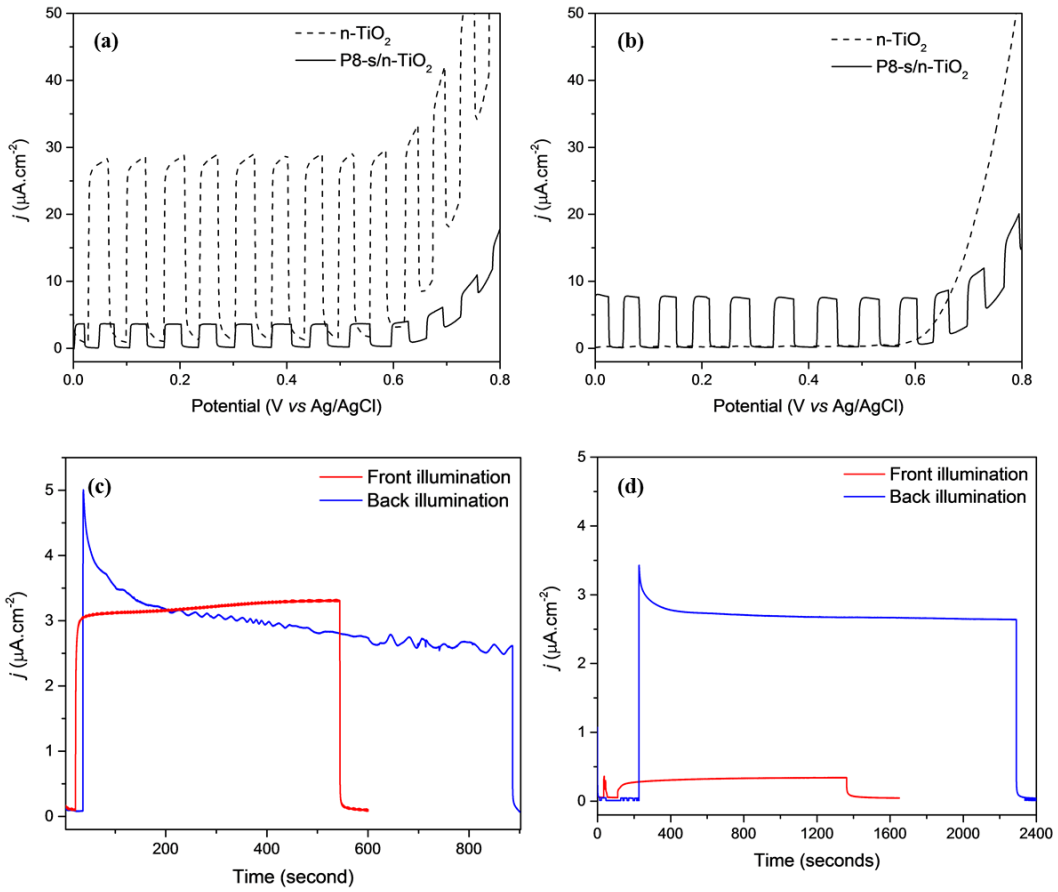

Figure 3.28 PEC measurements of P8s/n-TiO_2 (solid) and n-TiO_2 (dash) under 365 nm (a) and 420 nm (b) LED illumination with a light intensity of 1.18 and 1.3 mW.cm^{-2} respectively. The photocurrent response for P8s/TiO_2 under 420 nm (c) and 365 nm (d) illumination was monitored over the duration of ≥ 600 seconds via front (red) and back (black) illumination. All measurements were carried out in 0.1 M KOH electrolyte under an argon atmosphere, Ag/AgCl reference electrode and a Pt counter electrode.

As discussed previously within this chapter, charge transport is limited through the material, and was also evident from steady state illumination measurements of the material. In these experiments the photoelectrode was irradiated with 420 or 365 nm LEDs on the front or back face for > 600 seconds, Figure 3.28c and d. Back illumination shows a 47.50% and 22.40% decrease from its initial maximum value over 600 s for 420 and 365 nm illumination respectively. In contrast front illumination shows a 23% and 50% rise under 420 nm and 365 nm illumination respectively over 540 seconds, indicating that charge is accumulating within the structure and only being slowly transported to the FTO/TiO_2 interface. It is notable that these studies also show that as the photoactivity does not decay to 0 µA.cm^{-2}, the samples show reasonable stability and complete photo-degradation over the timescales of PEC measurements does not occur.

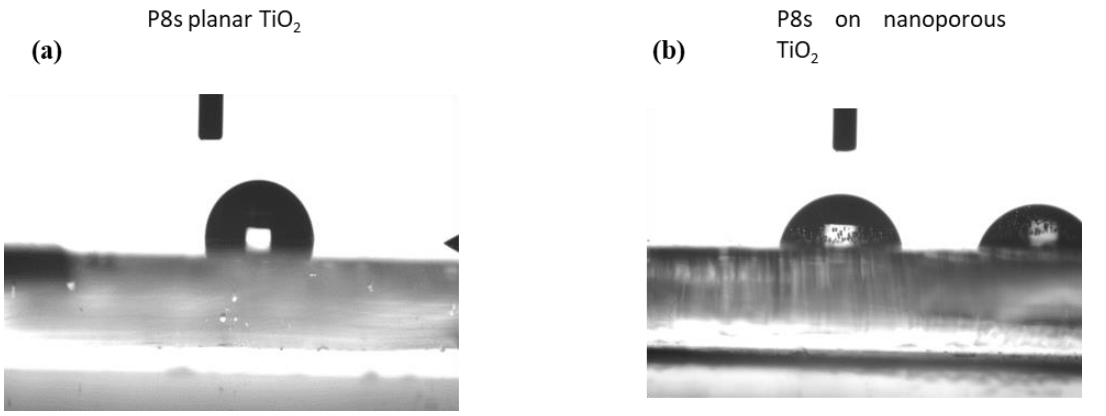

Figure 3.29 Contact angle measurements of a 3 µL droplet of water of P8s on a planar (a) and nanoporous (b) TiO_2 electrode, where a 3 µL droplet of water was deposited.

Contact angle measurements are used to determine the hydrophobicity of a material.[46] Here, we used it to gain understanding of the wetting of the electrode by the electrolyte, to ensure that the low level of activity was not due to poor electrolyte permeation through the nonporous structure of the electrode. Deposition of a 3 µL water droplet onto the electrode surface showed P8s/TiO_2 (107 ± 1.35˚) had a larger contact angle in comparison to P8s/n-TiO_2 (76.93 ± 0.68˚), showing electrolyte is able to penetrate through the pores of the n-TiO_2 electrode, Figure 3.29. However, large contact angles suggest that the hydrophobicity of P8s prevents the electrolyte penetrating all the way through the P8s/n-TiO_2 electrode, resulting in only a small portion of the photoelectrode being active. As a result of this, only a fraction of photons absorbed will contribute to the PEC response, therefore resulting in a less than expected photocurrent.

It is known that organic photoanodes suffer from stability issues in the harsh working conditions such as the ones used here,[74] and analysis of the post experimental electrolyte after *ca.* 7 hours of use showed delamination of P8s. To determine whether this was due to instability of P8s in pH 13 electrolyte, which is not uncommon for organic photoelectrodes, or as a result of applying a potential bias to the electrode, P8s/n-TiO_2 was soaked in 0.1 M KOH for 6 hours. After this time period it was evident that a small amount of material had delaminated off the electrode. As the delamination by soaking was smaller than after extensive use, it was concluded that P8s/n-TiO_2 instability arises from both the electrolyte pH and potentially PEC instability, Figure 3.30.

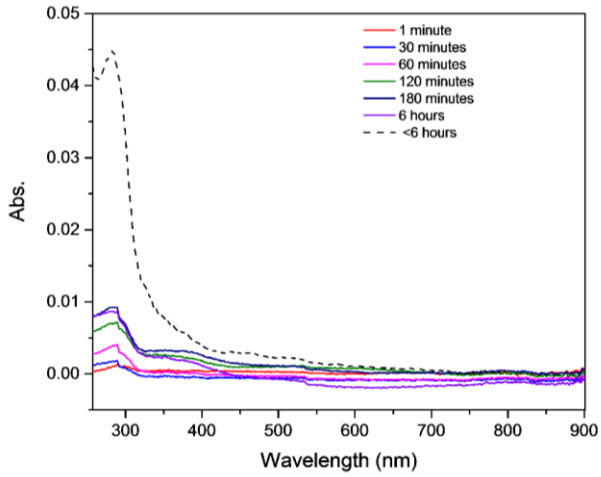

Figure 3.30 UV-Visible absorption spectra of P8s/n-TiO_2 electrode soaking in 0.1 M KOH pH 13 electrolyte for 1 minute (red), 30 minutes (blue), 60 minutes (pink), 120 minutes (green) and 180 minutes (navy blue) and 6 hours (purple). Data from the soaking experiment is overlaid with the UV-Visible spectra of the post experimental electrolyte after photoelectrochemical use for up to 6 hours. It is worth noting that the surface area for the electrode used for the soaking experiment was smaller than that for photoelectrochemical experiments, meaning delamination may also be occurring due to photoelectrochemcial instability.

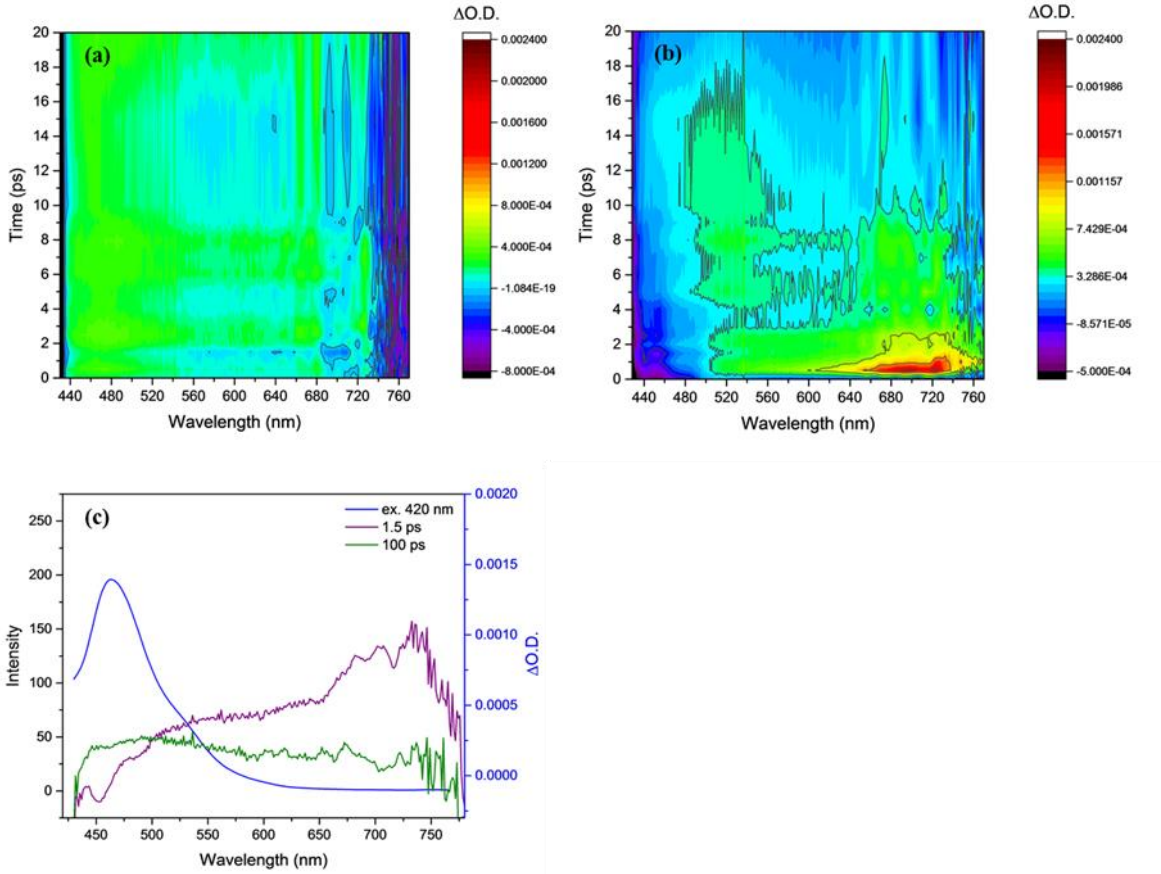

Figure 3.31 Contour plot of n-TiO_2 (a) and P8s/n-TiO_2 (b) on FTO where samples were probed from the back face (through FTO). Data was collected as an average of 6 cycles in a random order of time delays to reduce noise using, a 30 nJ/pulse with a spot diameter of 200 µm. The excitation wavelength was 420 nm, and spectra were measured under an atmosphere of air. Overlay of P8s on n-TiO_2 emission spectra with an excitation wavelength of 420 nm (blue), and TA spectra at 1.5 ps (purple) and 100 ps (green) (c.)

To gain insight into the mechanism by which P8s operates on n-TiO_2, TA spectroscopy was used. Upon 420 nm excitation of P8s/n-TiO_2 positive features at *ca.* 700 nm and 520 nm, and negative features at 450 and 490 nm are present in the TA spectra, Figure 3.31b. The excitation wavelength chosen selectively excites the P8s, and TA spectra of TiO_2 alone show minimal PIA. The negative features are ascribed to loss of ground state and stimulated emission respectively, where the latter was determined by the emission spectra of P8s/n-TiO_2, Figure 3.31c. For P8s in the previous section it was shown that excitation led to the formation of a PIA at 525, 625 and ~715 nm, with the broad 715 nm band at long times (> 10 ps) being assigned to the formation of an electron polaron state, and similar bands at < 10 ps being proposed to be either from the excitonic state or a small population of the polaron. Here, we find that the broad spectral absorbance at *ca.* 700 nm is short-lived (< 10 ps), and as it decays it forms a longer-lived species at *ca.* 520 nm (Figure 3.31b). As the species *ca.* 700 nm is formed within 1 ps of excitation of P8s/n-TiO_2, it is again assigned to the excitonic state, although the presence of a population of the electron polaron can also not be ruled out. The longer-lived species *ca.* 520 nm may be assignable to the generation of a hole polaron, which is formed when charge injection from P8s to n-TiO_2 occurs. The PIA at 520 nm is in-line for the reported wavelength of cations of similar organic donor acceptor polymer materials in the literature.[101–103] Based on the results obtained from TA spectroscopy, visible light excitation of P8s on n-TiO_2 initially leads to a short-lived excitonic state, at *ca.* 710 nm, which is able to inject an electron into the TiO_2 leaving a long-lived (>1 ns) hole polaron state that absorbs at *ca.* 510 nm (Figure 3.32).

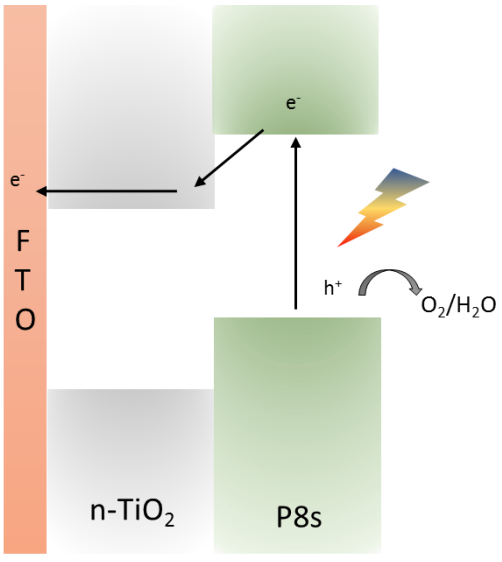

Figure 3.32 Schematic diagram showing the proposed mechanism of the formation of photo-generated holes in P8s upon photoexcitation with visible light (420 nm), where the photo-generated electron injects into n-TiO_2 and so leaving the residing hole to potentially be used in water oxidation reactions.

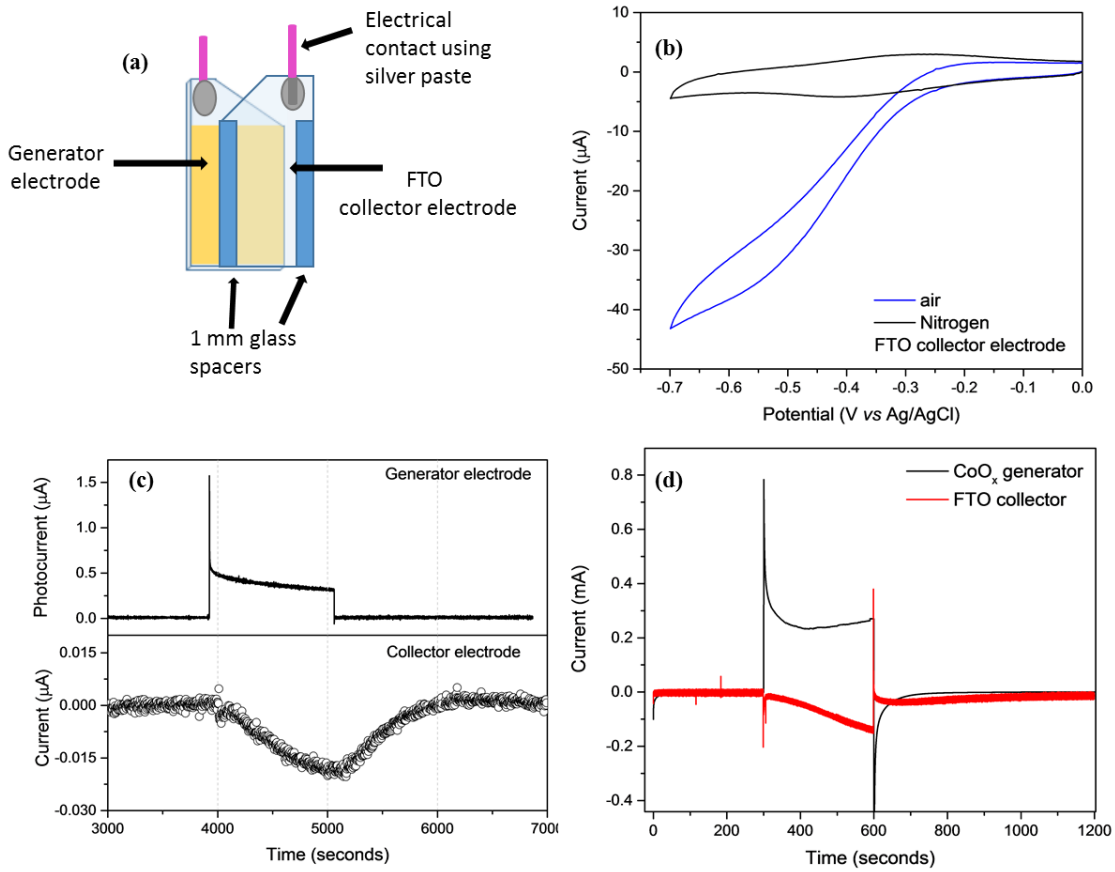

Figure 3.33 Schematic diagram of the generator-collector electrode set up for oxygen evolution measurements, where FTO and P8s/n-TiO_2 are the collector and generator electrodes respectively, and are separated by 1 mm glass spacer (a). CV of FTO collector electrode under an atmosphere of air (blue) and nitrogen (black) at 100 mVs^{-1}, showing removal of oxygen from the cell (b). Oxygen measurement for P8s/n-TiO_2, where the FTO collector electrode was held at –0.6 V and the P8s/n-TiO_2 generator at +0.2 V for the duration of the experiment and illuminated with a 420 nm LED on the back face (c). Calibation oxygen measurements using CoO_x generator electrode that is known to produce O_2 with 100% Faradaic efficiency and FTO collector electrode, where the generator was held at +0.6 V and switched to +1.6 V for electrochemical oxygen production (d) in 0.1 M phosphate buffer pH 7.

In this chapter we have aimed to develop a photoanode for water oxidation using a soluble processable polymer. The ability of the photoanodes to generate oxygen was examined using a generator-collector electrode method which is described in detail in section 3.4. Oxygen detection could not be carried out using conventional approaches (GC-MS) as the photocurrents are small. Therefore, electrochemical O_2 detection is employed *via* a dual working electrode system developed elsewhere.[76,104,105] Briefly, the experimental set up reported by Kirner *et al.* consisted of an adapted set up to that reported by the Mallouk group.[76] It is comprised of two working electrodes, an oxygen producing photoanode as the generator electrode, and an FTO collector electrode which is held at a potential sufficiently negative enough (-0.6 $V_{Ag/AgCl}$) to selectively reduce oxygen. Both generator and collector electrode are positioned at a defined distance from each other, in this case 1 mm, with the use of glass

spacers. The top of both generator and collector electrodes were cut at a 45˚ angle to ensure that the electrical contacts, connected with silver paste and epoxy resin, were completely isolated from each other, and to also ensure a uniform distance between both electrodes. Both generator and collector electrodes were fixed together using parafilm, with the working sides facing towards each other, Figure 3.33a. Initial CV analysis recorded under an air atmosphere of both collector and generator electrodes, ensured both electrode were functioning correctly. Once purged under nitrogen loss of a reduction feature at ~ -0.6 $V_{Ag/AgCl}$ owed to the presence of oxygen, indicates all oxygen has been removed from the cell, Figure 3.33b. For the remainder of the experiment a nitrogen blanket was used to prevent oxygen leaking into the cell. Oxygen measurements using a P8s/n-TiO_2 generator electrode in 0.1 M KOH, were carried out using a 420 nm LED irradiating the back face of the electrode. Experiments were carried out in 0.1 M KOH electrolyte under a nitrogen atmosphere. During oxygen measurements the P8s/n-TiO_2 generator electrode was held at +0.2 $V_{Ag/AgCl}$, whilst the FTO collector electrode was held at -0.6 $V_{Ag/AgCl}$. Once the current for both generator and collector electrodes had stabilised, the generator electrode was illuminated from the back face using a 420 nm LED, corresponding to the absorption peak maxima of P8s. Although this measurement does show that O_2 can be produced by the P8s/n-TiO_2 photoelectrode the FE is very low (*ca.* 2 %).

The low yield of oxygen can be due to inefficient hole transfer to water preventing the oxygen evolution reaction from occurring, with holes instead oxidising either a contaminant or the polymer itself. This can be overcome by the incorporation of a water oxidation co-catalyct (WOC) to increase the rate of extraction of photo-generated holes in P8s and use them to oxidised water. CoO_x is a suitable WOC for such electrolyte systems,[106] and was incorporated into P8s/n-TiO_2 electrodes *via* photoelectrochemical deposition to ensure CoO_x was optimally localised at sites where P8s photo-generated hole are generated.[53] A full description of the method of deposition of CoOx on the photoelectrode is given in section 3.4. Briefly, P8s/n-TiO_2 in 0.5 mM cobalt nitrate solution under an argon atmosphere was held at +0.2 $V_{Ag/AgCl}$ for 5 minutes whilst illuminating the sample with a 300 W Xe lamp, followed by a further 12 minutes at +0.1 $V_{Ag/AgCl}$. A change in the CV after deposition, consisting of an earlier onset potential, and *ca.* 6-fold photocurrent enhancement both indicate incorporation of the CoO_x WOC, Figure 3.34 a and b.

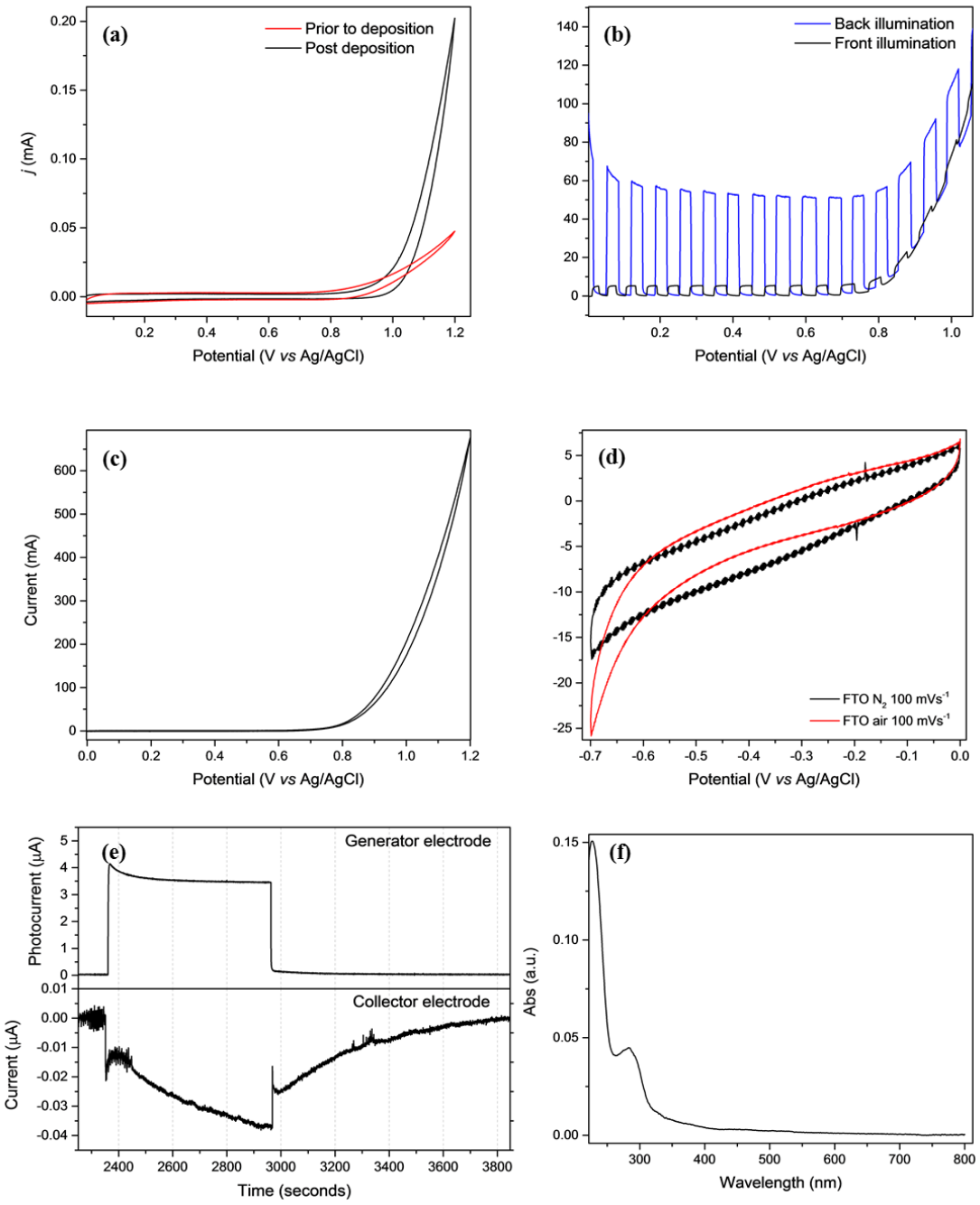

Figure 3.34 CV of P8s/n-TiO_2 photoelectrode at a scan rate of 100 mVs^{-1} before (red) and after (black) CoO_x photoelectrochemical deposition (a). PEC of P8s/n-TiO_2/CoO_x via back (blue) and front (black) illumination under white light chopped illumination (b). CV of P8s/n-TiO_2/CoO_x prior to oxygen measurements at a scan rate of 100 mVs^{-1} (c). CV of FTO generator electrode under an atmosphere of air (red) and nitrogen (black) (d). Oxygen detection measurement for P8s/n-TiO_2/CoO_x showing the generator electrode (top) and collector electrode (bottom) response upon irradiation with 420 nm LED with a light intensity of 6.39 mW cm^{-2} (e). UV-Visible absorption spectra of the post experimental electrolyte (0.1 M, KOH) (f). All experiments were carried out under and inert atmosphere unless stated otherwise, using 0.1 M KOH electrolyte and a Ag/AgCl reference electrode and a Pt counter electrode.

PEC was carried out on both the front (through P8s/n-TiO_2) and back (through FTO) face, where back illumination showed superior photoactivity indicating that CoO_x is localised at the P8s/FTO interface. As per all oxygen measurements, CVs of both generator (P8s) and collector (FTO) electrodes are recorded to ensure normal behaviour of the electrodes and the removal of any oxygen within the cell prior to the experiment, Figure 3.34 c and d. After incorporation of CoO_x WOC, no enhancement in the FE for oxygen evolution was observed when irradiated with a 420 nm LED, with a value of *ca.* 2% being recorded again, Figure 3.34e. The FEs can be rationalised by oxidation of the polymer due to slow kinetics of hole transfer from P8s to the WOC, and so optimisation of the catalyst/polymer interface is expected to be key in the optimisation of oxygen evolution.

3.3 Conclusions

Photocatalytic water splitting using organic materials is a clean route to producing hydrogen and oxygen using non-toxic and earth abundant materials. To date organic materials have been extensively studied for their application in photocatalytic hydrogen evolution, with little insight into the mechanistic route by which hydrogen is produced for this class of polymers. Here, we rationalise the mechanism of hydrogen evolution for two linear polymers and the role of solvents in the mixture using TA spectroscopy. Both polymers exhibited similar excited state dynamics upon photoexcitation in the UV region, where the polymers display dominant activity. Typically, hydrogen evolution is optimal in a H_2O/MeOH/TEA mixture. In the absence of MeOH/TEA, a short lived excimer state was present at *ca.* 530 nm, with no significant changes in lifetime kinetics upon the addition of MeOH, indicating its role as a wetting agent. Upon the addition of TEA, assignment of an electron polaron state at *ca.* 710 nm was made due to quenching of the excimer state upon its formation. Charge separation was seen to occur > 2 ps, whereby the electron polaron persisted for >3.2 ns, allowing for effective electron extraction for hydrogen evolution.

We then proceeded to develop a water oxidation photoanode using P8s, due its ease of solution processability and previous development in photocatalytically active thin films, for the production of an overall water splitting device. Photocurrents were significantly improved from 0.64 µA cm^{-2} to 20 97 µA.cm^{-2} by the incorporation of a n-TiO_2 heterojunction, improving both charge separation and increased light absorption (> 95%), due to a higher surface area and loading of P8s. The use of TA spectroscopy has shown the formation of a short-lived hole polaron when irradiated with visible light in water. Although the use of a hole scavenger showed utilisation of holes, oxygen measurements yielded negligible oxygen FEs, even in the presence of a WOC. This is likely to be due to a lack of ability to utilise photo-

generated holes, due either (i) self-trapping of holes and/or (ii) short-lived lifetimes for electron-hole pairs, preventing sufficient time for hole migration to water for water oxidation.

3.4 Materials and Methods

3.4.1 Materials

Milli-Q water (18.2 MΩ) was used throughout (Millipore Corp). All chemicals were purchased from sigma Aldrich, except for P8s and P56 which were synthesised by D. Woods[46] and Dr. R. S. Sprick. Argon and nitrogen were purchased from BOC at pureshield grade N6.

3.4.2 Methods

Cleaning of FTO: Fluorine-doped tin oxide (FTO, TEC-15, Pilkington, 14 x 20 mm^2) glass substrates were cleaned *via* sonication for 20 minutes in three different solutions: 1% helmanex solution, ethanol and water, and rinsed with water between each sonication. It is important that FTO pieces are not stacked on top of each other to ensure the FTO is covered in solution for efficient cleaning. After drying of the FTO glass substrates with compressed air, they were heated in an oven to 400˚C (ramped at 20 ˚C/min) and held for 20 minutes before cooling.

Preparation of planar TiO_2 *via* spray coating: As soon as FTO had been cleaned in the furnace it was placed conducing side up on a hot plate which was set to 500˚C. 30 layers of a 0.2 M solution of titanium diisoropoxide bis(acetylacetonate) in ethanol was sprayed from left to right in one motion on the FTO surface to ensure an even coverage. The electrode was placed back into the furnace at 450˚C for 1 hour to obtain the anatase phase of TiO_2.

Preparation of nanoporous TiO_2 (n-TiO_2): Following cleaning of FTO as described above, scotch tape was placed at the top and bottom of the conducting face of the electrode, to leave only the working area of the electrode exposed. Titanium (IV) oxide paste was placed along one of the outer edges of the FTO between both scotch tapes. Using the side of a glass pipette the TiO_2 paste was doctor bladed across the FTO surface, resulting in a uniform layer. The TiO_2 was left to dry in air for no more than 5 minutes, and the scotch tape carefully removed, and the electrode placed in the furnace for 1 hour at 450˚C.

Preparation of P8s/n-TiO_2 electrodes: n-TiO_2 was left to soak in a solution of P8s (3 mg/mL in chloroform) for 48 hours.

Spin-coating: 30 layers of 3 mg/mL of P8s in chloroform was spin-coated at 3000 rpm for 30 seconds using a Laurell WS-650 series spin processor.

UV-Visible absorption spectroscopy: Spectra were obtained using a Shimadzu 2550 UV/VisNIR spectrophotometer in absorbance mode. To obtain UV-Visible absorption spectra of electrodes, an air background was taken and the electrodes were then placed in the beam path of the spectrophotometer. For post experimental solutions a 1 x 1 cm^2 quartz cuvette was used following a background of 0.1 M KOH electrolyte.

Contact angle measurements: A Krüss DSA100 instrument was used to perform contact angle measurements at room temperature, using a sessile drop to deposit 3 µL droplet of water across various positions of the surface of a P8s/TiO_2 electrode. The Laplace-Young method was used to calculate the contact angles of the water droplet on the surface of the electrode.

X-ray photoelectron spectroscopy (XPS): XPS measurements were carried out on $P8s_{pow}$ (powder form) in an ultrahigh vacuum surface science chamber, with hydrogen as the residual gas. A PSP vacuum technology electron energy analyser, with an angle integrating ± 10˚, and a dual anode Mg Kα (1253.6 eV) X-ray source. The base pressure of the system was 2×10^{-10} mbar, and the spectrometer was calibrated using Au $4f_{7/2}$ at 83.9 eV. Spectra were fitted using Voigt functions after Shirley background removal with a resolution of 0.2 eV. XPS measurements were carried out and fitted by J. A. Coca Clemente.

Photoelectrochemical experiments: Photoelectrochemical measurements were carried out in a custom-designed 3 electrode cell. The working electrode was the P8s on an FTO(/TiO_2) glass substrate connected *via* a crocodile clip and nickel wire. The reference electrode was Ag/AgCl (3.5 M KCl), a counter electrode of Pt wire, and KOH electrolyte (0.1 M, pH 13) were used in all experiments. A palmsens potentiostat was used to carry out electrochemical methods. Prior to all experiments the cell was degassed under a stream of argon. Photoelectrochemical measurements were carried out *via* front and back illumination of the working electrode using a 300 W Xe lamp with a KG1 filter. The light intensity of the lamp was recorded each time using a Thor labs diode in the same position as the sample. Photocurrent measurements were recorded *via* linear sweep voltammetry at 100 mVs^{-1} and 10 mVs^{-1}, with the light being manually chopped for 1 second and 3 seconds respectively.

Femtosecond transient absorption spectroscopy: Determination of the excited state kinetics for photocatalytic hydrogen evolution of P8s spin-coated on a glass substrate. TA spectroscopy was carried out using a HELIOS spectrometer (Ultrafast systems) PHAROS laser (Light Conversion Ltd) operating at 10 kHz coupled to an ORPHEUS optical parametric amplifier (Light Conversion Ltd) in tandem with a LYRA harmonic generator (Light Conversion Ltd). For photocatalytic hydrogen evolution studies the pump wavelength was 365 nm (150 µW for P8s and 600 µW for P56). For transient spectroelectrochemistry the pump wavelength was 375 nm (600 µW). The spot size of the probe beam was ~100 µm diameter

which overlapped with the pump beam, with an optical time delay of 1 s. Samples were recorded in a 2 x 1 cm^2 quartz cuvette in the required solvent and purged for 30 minutes under argon. Data was chirp corrected using Surface Xplorer software.

For P8s/n-TiO_2 a time-resolved multiple-probe spectrometer was used at the Central Laser Facility in Rutherford Appleton Labs. TA spectroscopy was carried out using a dual fs and ps Thales Laser and fs or ps Spectra Physics Spittfire XP titanium sapphire amplifiers, synchronised using a 68 MHz oscillator laser (Femtolasters Synergy), 1 kHz and 10 kHz ultrafast lasers were used to measure on the sub-ps to 100 μs and 100 μs to ms timescales respectively. Data was collected as an average of 6 cycles in a random order of time delays to reduce noise using, a 30 nJ/pulse with a spot size of 200 μm. The excitation wavelength was 420 nm, and was measured under an atmosphere of air. Data was collected by Dr. A. Gardner, K. Saeed and Dr. I. Sazanovich.

Spectroelectrochemistry (SEC): Measurements were carried out in a 2 x 1 cm^2 quartz cell containing P8s spin coated on an FTO working electrode, a Ag/AgCl reference electrode and a Pt counter electrode in 60 mM phosphate buffer, pH 7, electrolyte under and argon atmosphere. TA spectrelectrochemistry was carried out using a HELIOS spectrometer as described above and a palmsens potentiostat, with an excitation wavelength of 375 nm and a pump energy of 600 μW. UV-Visible spectroelectrochemistry was carried out using a Shimadzu 2550 UV/VisNIR spectrophotometer in absorbance mode, and a palmsens potentiostat. Spectra were recorded once steady state was achieved at the given potential.

CoO_x photoelectrochemical deposition: P8s/n-TiO_2 in 0.5 mM cobalt nitrate solution under an argon atmosphere was held at +0.2 $V_{Ag/AgCl}$ for 5 minutes whilst sequentially illuminating the sample with a 300 W Xe lamp, followed by a further 12 minutes at +0.1 $V_{Ag/AgCl}$. Photodeposition was carried out using a light intensity of 62 $mW.cm^{-2}$ across 315-795 nm.

Oxygen measurements: Oxygen measurements were carried out using a generator -collector electrode method as developed by other groups previously.[76,104,105] On either side of the collector electrode 1 mm spacers were used, to prevent electrical contact between both generator and collector electrodes, and to allow space for electrolyte. FTO used for the collector electrode was not pre-treated. A wire was connected to the top left corner of the electrodes using conductive silver paste, and once dry covered in epoxy resin. Electrodes were then cut in the top right corner to isolate the connections when sandwiched together. Electrodes were pressed together with the conducting sides facing each other, and parafilm was wrapped around the top and the bottom of the sandwiched electrodes to hold them together.

Prior to purging the electrolyte (0.1 M KOH) a CV at 100 mVs^{-1} was obtained for the electrodes. The cell was then purged for 30 minutes with nitrogen, after which a nitrogen blanket was kept over the cell for the remainder of the experiment. CV of the collector electrode was taken to ensure no oxygen was present within the cell. Here, P8s is the generator electrode. It was held at +0.2 or +0.4 $V_{Ag/AgCl}$ throughout the experiment. FTO is the collector electrode, and was held at -0.6 $V_{Ag/AgCl}$, a potential selective to oxygen reduction. Once steady state had been reached by both electrodes, the back face of the generator electrode was illuminated with a 420 nm LED, after which the LED was switched off and the current allowed to plateau. Faradaic efficiencies were calculated using the equation below, where $-Q_C$ and Q_G are the areas for the collector and generator electrode respectively. $\%_{col}$ is the collection efficiency (54 ± 10 %) which was determined by taking the average of 5 oxygen measurements using a Co-Pi electrode as the generator electrode. Co-Pi is used as a calibration material as it is known to show ~ 100% Faradic efficiency for water oxidation. For these measurements Co-Pi was prepared *via* electrochemical deposition in 0.5 mM cobalt nitrate, in 0.1 M phosphate buffer at pH 7. The FTO electrode was held at +1.2 $V_{Ag/AgCl}$ for 25 minutes, after which the FTO electrode had a brown colouring owed to the presence of Co-Pi on the surface. Calibration measurements were carried out with the Co-Pi held at +0.6 $V_{Ag/AgCl}$ initially, and oxygen production was triggered by a potential switch to +1.6 $V_{Ag/AgCl}$.

$$FE_{O2} = (-Q_C / Q_G)\ (1/\%_{col})$$

$$\%_{col} = -Q_C/Q_G$$

References

1 S. Yanagida, A. Kabumoto, K. Mizumoto, C. Pac and K. Yoshino, *J. Chem. Soc. Chem. Commun.*, 1985, 474.

2 X. Wang, K. Maeda, A. Thomas, K. Takanabe, G. Xin, J. M. Carlsson, K. Domen and M. Antonietti, *Nat. Mater.*, 2009, **8**, 76–80.

3 Y. Wang, X. Wang and M. Antonietti, *Angew. Chemie - Int. Ed.*, 2012, **51**, 68–89.

4 G. Liu, T. Wang, H. Zhang, X. Meng, D. Hao, K. Chang, P. Li, T. Kako and J. Ye, *Angew. Chemie - Int. Ed.*, 2015, **54**, 13561–13565.

5 D. J. Martin, P. J. T. Reardon, S. J. A. Moniz and J. Tang, *J. Am. Chem. Soc.*, 2014, **136**, 12568–12571.

6 L. Lin, H. Ou, Y. Zhang and X. Wang, *ACS Catal.*, 2016, **6**, 3921–3931.

7 G. Zhang, Z.-A. Lan and X. Wang, *Angew. Chemie Int. Ed.*, 2016, **55**, 15712–15727.

8 H. Zhang, G. Liu, L. Shi, H. Liu, T. Wang and J. Ye, *Nano Energy*, 2016, **22**, 149–168.

9 K. R. Reddy, C. V. Reddy, M. N. Nadagouda, N. P. Shetti, S. Jaesool and T. M. Aminabhavi, *J. Environ. Manage.*, 2019, **238**, 25–40.

10 A. Kudo and Y. Miseki, *Chem. Soc. Rev.*, 2009, **38**, 253–278.

11 X. Chen, S. Shen, L. Guo and S. S. Mao, *Chem. Rev.*, 2010, **110**, 6503–6570.

12 J. Xing, W. Q. Fang, H. J. Zhao and H. G. Yang, *Chem. - An Asian J.*, 2012, **7**, 642–657.

13 D. Praveen Kumar, M. V. Shankar, M. Mamatha Kumari, G. Sadanandam, B. Srinivas and V. Durgakumari, *Chem. Commun.*, 2013, **49**, 9443–9445.

14 H. V. Babu, M. G. M. Bai and M. Rajeswara Rao, *ACS Appl. Mater. Interfaces*, 2019, **11**, 11029–11060.

15 L. Stegbauer, K. Schwinghammer and B. V. Lotsch, *Chem. Sci.*, 2014, **5**, 2789–2793.

16 T. Banerjee, K. Gottschling, G. Savasci, C. Ochsenfeld and B. V. Lotsch, *ACS Energy Lett.*, 2018, **3**, 400–409.

17 S. He, B. Yin, H. Niu and Y. Cai, *Appl. Catal. B Environ.*, 2018, **239**, 147–153.

18 N. Keller, M. Calik, D. Sharapa, H. R. Soni, P. M. Zehetmaier, S. Rager, F. Auras, A.

C. Jakowetz, A. Görling, T. Clark and T. Bein, *J. Am. Chem. Soc.*, 2018, **140**, 16544–16552.

19 V. S. Vyas, F. Haase, L. Stegbauer, G. Savasci, F. Podjaski, C. Ochsenfeld and B. V. Lotsch, *Nat. Commun.*, 2015, **6**, 1–9.

20 P. Kuhn, M. Antonietti and A. Thomas, *Angew. Chemie - Int. Ed.*, 2008, **47**, 3450–3453.

21 J. Bi, W. Fang, L. Li, J. Wang, S. Liang, Y. He, M. Liu and L. Wu, *Macromol. Rapid Commun.*, 2015, **36**, 1799–1805.

22 A. Bhunia, D. Esquivel, S. Dey, R. Fernández-Terán, Y. Goto, S. Inagaki, P. Van Der Voort and C. Janiak, *J. Mater. Chem. A*, 2016, **4**, 13450–13457.

23 D. Nepak, V. K. Tomer and K. Kailasam, The Royal Society of Chemistry, 2018, pp. 67–102.

24 C. S. Diercks and O. M. Yaghi, *Science*, 2017, 355.

25 M. Liu, L. Guo, S. Jin and B. Tan, *J. Mater. Chem. A*, 2019, **7**, 5153–5172.

26 L. Guo, Y. Niu, H. Xu, Q. Li, S. Razzaque, Q. Huang, S. Jin and B. Tan, *J. Mater. Chem. A*, 2018, **6**, 19775–19781.

27 R. S. Sprick, J.-X. Jiang, B. Bonillo, S. Ren, T. Ratvijitvech, P. Guiglion, M. A. Zwijnenburg, D. J. Adams and A. I. Cooper, *J. Am. Chem. Soc.*, 2015, **137**, 3265–3270.

28 R. S. Sprick, B. Bonillo, M. Sachs, R. Clowes, J. R. Durrant, D. J. Adams and A. I. Cooper, *Chem. Commun.*, 2016, **52**, 10008–10011.

29 R. S. Sprick, B. Bonillo, R. Clowes, P. Guiglion, N. J. Brownbill, B. J. Slater, F. Blanc, M. A. Zwijnenburg, D. J. Adams and A. I. Cooper, *Angew. Chemie - Int. Ed.*, 2016, **55**, 1792–1796.

30 Y. Xu, N. Mao, S. Feng, C. Zhang, F. Wang, Y. Chen, J. Zeng and J. X. Jiang, *Macromol. Chem. Phys.*, 2017, **218**, 1–9.

31 Y. Xu, N. Mao, C. Zhang, X. Wang, J. Zeng, Y. Chen, F. Wang and J. X. Jiang, *Appl. Catal. B Environ.*, 2018, **228**, 1–9.

32 Y. Liu, Z. Liao, X. Ma and Z. Xiang, *ACS Appl. Mater. Interfaces*, 2018, **10**, 30698–30705.

33 V. S. Mothika, P. Sutar, P. Verma, S. Das, S. K. Pati and T. K. Maji, *Chem. - A Eur. J.*, 2019, **25**, 3867–3874.

34 D. Schwarz, A. Acharja, A. Ichangi, P. Lyu, M. V. Opanasenko, F. R. Goßler, T. A. F. König, J. Čejka, P. Nachtigall, A. Thomas and M. J. Bojdys, *Chem. - A Eur. J.*, 2018, **24**, 11916–11921.

35 G. Zhang, W. Ou, J. Wang, Y. Xu, D. Xu, T. Sun, S. Xiao, M. Wang, H. Li, W. Chen and C. Su, *Appl. Catal. B Environ.*, 2019, **245**, 114–121.

36 L. Li, W. Lo, Z. Cai, N. Zhang and L. Yu, *Macromolecules*, 2016, **49**, 6903–6909.

37 Z. Wang, N. Mao, Y. Zhao, T. Yang, F. Wang and J. X. Jiang, *Polym. Bull.*, 2019, **76**, 3195–3206.

38 Z. Hu, X. Zhang, Q. Yin, X. Liu, X. fang Jiang, Z. Chen, X. Yang, F. Huang and Y. Cao, *Nano Energy*, 2019, **60**, 775–783.

39 R. Sebastian Sprick, Y. Bai, A. A. Y Guilbert, M. Zbiri, C. M. Aitchison, L. Wilbraham, Y. Yan, D. J. Woods, M. A. Zwijnenburg and A. I. Cooper, *Chem. Mater.*, 2018, **31**, 305–313.

40 Y. Xiang, X. Wang, L. Rao, P. Wang, D. Huang, X. Ding, X. Zhang, S. Wang, H. Chen and Y. Zhu, *ACS Energy Lett.*, 2018, **3**, 2544–2549.

41 J. Kosco, M. Sachs, R. Godin, M. Kirkus, L. Francas, M. Bidwell, M. Qureshi, D. Anjum, J. R. Durrant and I. McCulloch, *Adv. Energy Mater.*, 2018, **8**, 1802181.

42 J. Kosco and I. McCulloch, *ACS Energy Lett.*, 2018, **3**, 2846–2850.

43 M. Schwarze, D. Stellmach, M. Schröder, K. Kailasam, R. Reske, A. Thomas and R. Schomäcker, *Phys. Chem. Chem. Phys.*, 2013, **15**, 3466.

44 M. Schröder, K. Kailasam, J. Borgmeyer, M. Neumann, A. Thomas, R. Schomäcker and M. Schwarze, *Energy Technol.*, 2015, **3**, 1014–1017.

45 J. Mei and Z. Bao, *Chem. Mater.*, 2014, **26**, 604–615.

46 D. J. Woods, R. S. Sprick, C. L. Smith, A. J. Cowan and A. I. Cooper, *Adv. Energy Mater.*, 2017, **7**, 1700479.

47 M. Sachs, R. S. Sprick, D. Pearce, S. J. Hillman, A. Monti, A. A. Y. Guilbert, N. J. Brownbill, S. Dimitrov, F. Blanc, M. A. Zwijnenburg, J. Nelson, J. R. Durrant and A. I. Cooper, *Nat. Commun.*, 2018, 1–11.

48 R. S. Sprick, C. M. Aitchison, E. Berardo, L. Turcani, L. Wilbraham, B. M. Alston, K. E. Jelfs, M. A. Zwijnenburg and A. I. Cooper, *J. Mater. Chem. A*, 2018, **6**, 11994–12003.

49 A. Fujishima and K. Honda, *Nature*, 1972, **238**, 37–38.

50 S. Licht, B. Wang, S. Mukerji, T. Soga, M. Umeno and H. Tributsch, *Int. J. Hydrogen Energy*, 2001, **26**, 653–659.

51 A. J. Bard and M. A. Fox, *Acc. Chem. Res.*, 1995, **28**, 141–145.

52 C. Jiang, S. J. A. Moniz, A. Wang, T. Zhang and J. Tang, *Chem. Soc. Rev.*, 2017, **46**, 4645–4660.

53 J. T. Kirner, J. J. Stracke, B. A. Gregg and R. G. Finke, *ACS Appl. Mater. Interfaces*, 2014, **6**, 13367–13377.

54 K. Sivula, F. Le Formal and M. Grätzel, *ChemSusChem*, 2011, **4**, 432–449.

55 G. Wang, H. Wang, Y. Ling, Y. Tang, X. Yang, R. C. Fitzmorris, C. Wang, J. Z. Zhang and Y. Li, *Nano Lett.*, 2011, **11**, 3026–3033.

56 E. A. Mohamed, Z. N. Zahran and Y. Naruta, *J. Mater. Chem. A*, 2017, **5**, 6825–6831.

57 X. Liu, F. Wang and Q. Wang, *Phys. Chem. Chem. Phys.*, 2012, **14**, 7894–7911.

58 Y. W. Chen, J. D. Prange, S. Dühnen, Y. Park, M. Gunji, C. E. D. Chidsey and P. C. McIntyre, *Nat. Mater.*, 2011, **10**, 539–544.

59 F. Le Formal, N. Tétreault, M. Cornuz, T. Moehl, M. Grätzel and K. Sivula, *Chem. Sci.*, 2011, **2**, 737–743.

60 M. Bledowski, L. Wang, A. Ramakrishnan, O. V. Khavryuchenko, V. D. Khavryuchenko, P. C. Ricci, J. Strunk, T. Cremer, C. Kolbeck and R. Beranek, *Phys. Chem. Chem. Phys.*, 2011, **13**, 21511–21519.

61 L. Wang, M. Bledowski, A. Ramakrishnan, D. König, A. Ludwig and R. Beranek, *J. Electrochem. Soc.*, 2012, **159**, H616–H622.

62 B. Mei, H. Byford, M. Bledowski, L. Wang, J. Strunk, M. Muhler and R. Beranek, *Sol. Energy Mater. Sol. Cells*, 2013, **117**, 48–53.

63 M. Bledowski, L. Wang, A. Ramakrishnan and R. Beranek, *J. Mater. Res.*, 2013, **28**, 411–417.

64 M. Bledowski, L. Wang, A. Ramakrishnan, A. Bétard, O. V. Khavryuchenko and R. Beranek, *ChemPhysChem*, 2012, **13**, 3018–3024.

65 M. Bledowski, L. Wang, S. Neubert, D. Mitoraj and R. Beranek, *J. Phys. Chem. C*, 2014, **118**, 18951–18961.

66 M. Faraji, M. Yousefi, S. Yousefzadeh, M. Zirak, N. Naseri, T. H. Jeon, W. Choi and A. Z. Moshfegh, *Energy Environ. Sci.*, 2019, **12**, 59–95.

67 S. Samanta, S. Martha and K. Parida, *ChemCatChem*, 2014, **6**, 1453–1462.

68 X. Sun, Q. Li, J. Jiang and Y. Mao, *Nanoscale*, 2014, **6**, 8769–8780.

69 Gratzel Michael, *Nature*, 2001, **414**, 338–344.

70 C. Dai, X. Gong, X. Zhu, C. Xue and B. Liu, *Mater. Chem. Front.*, 2018, **2**, 2021–2025.

71 Z. Wang, P. Xiao, L. Qiao, X. Meng, Y. Zhang, X. Li and F. Yang, *Phys. B Condens. Matter*, 2013, **419**, 51–56.

72 K. Wippermann, J. W. Schultze, R. Kessel and J. Penninger, *Corros. Sci.*, 1991, **32**, 205–230.

73 H. Gerischer, *J. Electroanal. Chem. Interfacial Electrochem.*, 1977, **82**, 133–143.

74 L. Yao, A. Rahmanudin, N. Guijarro and K. Sivula, *Adv. Energy Mater.*, 2018, **8**, 1802585.

75 P. Bornoz, M. S. Prévot, X. Yu, N. Guijarro and K. Sivula, *J. Am. Chem. Soc.*, 2015, **137**, 15338–15341.

76 J. T. Kirner and R. G. Finke, *ACS Appl. Mater. Interfaces*, 2017, **9**, 27625–27637.

77 M. Salomäki, O. Jaakkola, S. P. Hirvonen, H. Tenhu and C. Kvarnström, *Synth. Met.*, 2018, **245**, 144–150.

78 L. Wang, D. Yan, D. W. Shaffer, X. Ye, B. H. Layne, J. J. Concepcion, M. Liu and C. Y. Nam, *Chem. Mater.*, 2018, **30**, 324–335.

79 K. J. Laidler, *Pure Appl. Chem.*, 1996, **68**, 167.

80 N. Zarrabi, D. M. Stoltzfus, P. L. Burn and P. E. Shaw, *J. Phys. Chem. C*, 2017, **121**, 18412–18422.

81 A. De Sio, F. Troiani, M. Maiuri, J. Réhault, E. Sommer, J. Lim, S. F. Huelga, M. B.

Plenio, C. A. Rozzi, G. Cerullo, E. Molinari and C. Lienau, *Nat. Commun.*, 2016, **7**, 1–8.

82 C. Huang, M. M. Sartin, M. Cozzuol, N. Siegel, S. Barlow, J. W. Perry and S. R. Marder, *J. Phys. Chem. A*, 2012, **116**, 4305–4317.

83 F. Guzman, S. S. C. Chuang and C. Yang, *Ind. Eng. Chem. Res.*, 2013, **52**, 61–65.

84 P. Guiglion, C. Butchosa and M. A. Zwijnenburg, *J. Mater. Chem. A*, 2014, **2**, 11996–12004.

85 B. Y. Alfaifi, H. Ullah, S. Alfaifi, A. A. Tahir and T. K. Mallick, *Veruscript Funct. Nanomater.*, 2018, **2**, BDJOC3.

86 J. Schneider and D. W. Bahnemann, *J. Phys. Chem. Lett.*, 2013, **4**, 3479–3483.

87 L. Wang, Y. Zhang, L. Chen, H. Xu and Y. Xiong, *Adv. Mater.*, 2018, **1801955**, 1–12.

88 J. Li and A. C. Grimsdale, *Chem. Soc. Rev.*, 2010, **39**, 2399.

89 A. B. Koren, M. D. Curtis, A. H. Francis and J. W. Kampf, *J. Am. Chem. Soc.*, 2003, **125**, 5040–5050.

90 P. F. Zhang, X. L. Liu, R. Q. Zhang, H. B. Fan, A. L. Yang, H. Y. Wei, P. Jin, S. Y. Yang, Q. S. Zhu and Z. G. Wang, *Appl. Phys. Lett.*, 2008, **92**, 012104.

91 P. J. Schmitz, J. W. Holubka and S. Srinivasan, *Surf. Interface Anal.*, 1997, **25**, 643–649.

92 T. V. M. Sreekanth, P. C. Nagajyothi, G. R. Dillip and Y. R. Lee, *J. Phys. Chem. C*, 2017, **121**, 25229–25242.

93 K. Akaike, K. Aoyama, S. Dekubo, A. Onishi and K. Kanai, *Chem. Mater.*, 2018, **30**, 2341–2352.

94 S. Crawford, E. Thimsen and P. Biswas, *J. Electrochem. Soc.*, 2009, **156**, H346.

95 B. Zhang, X. Zheng, O. Voznyy, R. Comin, M. Bajdich, M. Garcia-Melchor, L. Han, J. Xu, M. Liu, L. Zheng, F. P. Garcia de Arquer, C. T. Dinh, F. Fan, M. Yuan, E. Yassitepe, N. Chen, T. Regier, P. Liu, Y. Li, P. De Luna, A. Janmohamed, H. L. Xin, H. Yang, A. Vojvodic and E. H. Sargent, *Science*, 2016, 352, 333–337.

96 J. T. Kirner and R. G. Finke, *J. Mater. Chem. A*, 2017, **5**, 19560–19592.

97 A. J. Cowan, W. Leng, P. R. F. Barnes, D. R. Klug and J. R. Durrant, *Phys. Chem.*

Chem. Phys., 2013, **15**, 8772.

98 A. Hagfeldt and M. Grätzel, *Acc. Chem. Res.*, 2000, **33**, 269–277.

99 F. Pichot and B. A. Gregg, *J. Phys. Chem. B*, 2002, **104**, 6–10.

100 M. Grätzel, *Nature*, 2001, **414**, 338–344.

101 J. Jiang, A. Alsam, S. Wang, S. M. Aly, Z. Pan, O. F. Mohammed and K. S. Schanze, *J. Phys. Chem. A*, 2017, **121**, 4891–4901.

102 R. Wang, Y. Yao, C. Zhang, Y. Zhang, H. Bin, L. Xue, Z.-G. Zhang, X. Xie, H. Ma, X. Wang, Y. Li and M. Xiao, *Nat. Commun.*, 2019, **10**, 398.

103 B. S. Veldkamp, W.-S. Han, S. M. Dyar, S. W. Eaton, M. A. Ratner and M. R. Wasielewski, *Energy Environ. Sci.*, 2013, **6**, 1917.

104 D. L. Ashford, B. D. Sherman, R. A. Binstead, J. L. Templeton and T. J. Meyer, *Angew. Chemie - Int. Ed.*, 2015, **54**, 4778–4781.

105 S. A. Lee, Y. Zhao, E. A. Hernandez-pagan, L. Blasdel, W. Justin and T. E. Mallouk, 2012, 165–176.

106 M. W. Kanan and D. G. Nocera, *ChemInform*, 2008, **39**, 1072–1076.

"It matters not what someone is born,
but what they grow to be"

– Harry Potter and the Goblet of Fire

Chapter 4

Self-Assembled Hydrogel Photoelectrodes For Water Oxidation: Investigating Visible Light Induced Charge Separation Efficiency

Part of this work is submitted for publication: "Gelation enabled charge separation following visible light excitation using self-assembled perylene bisimides" C. L. Smith, L. L. E. Mears, B. J. Greeves, E. R. Draper, J. Doutch, D. J. Adams, A. J. Cowan, 2019, Physical Chemistry Chemical Physics.

4.1 Introduction

As discussed in chapter 3, there are relatively few reports of organic photoelectrodes for overall water splitting. In this thesis we have explored the use of a linear soluble conjugated polymer for the fabrication of a photoelectrode. However, in line with other reports for organic photoelectrodes, the electrode was unstable under the working conditions required and very little oxygen was detected. In this chapter we explore a different class of organic materials, PBI, which can self-assemble to form long-range self-supporting structures that promote charge transport making them interesting materials to study for PEC water splitting.

4.1.1 Perylene bisimide

Perylene bisimides (PBIs) also known as perylene diimides (PDIs) are polycyclic aromatic hydrocarbons (Figure 4.1), and have been extensively explored as a dye, and more recently a gelator.[1–4] First synthesised in 1934 by Morgan *et al.*,[5] PBI has been extensively studied for applications in organic light emitting diodes, solar cells, dyes, field effect transistors, pigments, catalysis and fluorescence sensors.[6] Their popularity arises from their strong visible light absorption, chemical and thermal stability, high quantum yields and synthetic tunability.[7,8] Of particular interest is PBIs ability to form large aggregated structures which are widely used as low molecular weight gelators (LMWGs).

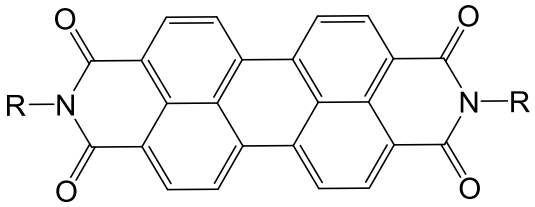

Figure 4.1 General structure of perylene bisimide.

4.1.1.1 PBI Aggregates

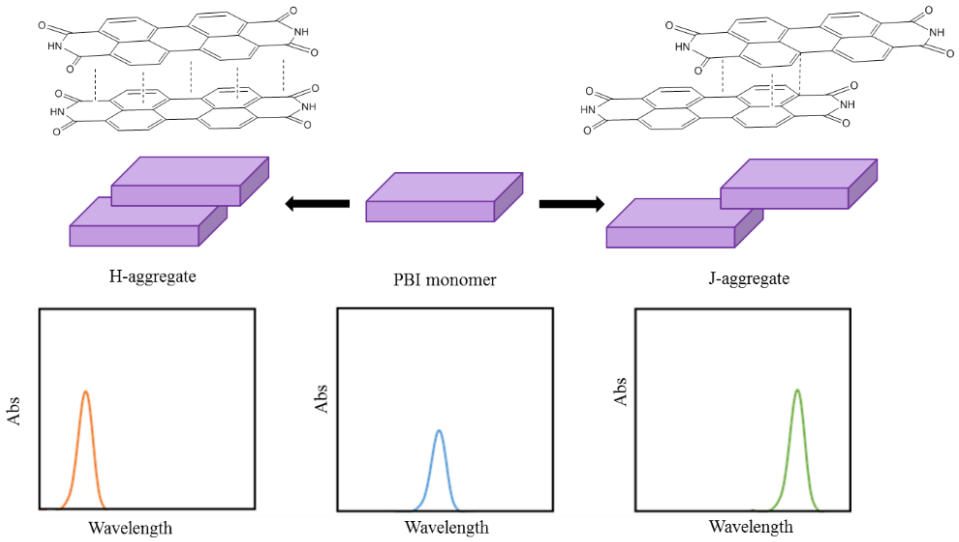

*Figure 4.2 The purple blocks represent a PBI monomer unit and show the arrangement of H- and J- aggregates, where H-aggregates arrange in a face to face arrangement, and J-aggregates in a head to tail arrangement. The π-π interaction between PBI units is shown above, which forms an electron conductive pathway. Figure reproduced from Chem. Soc. Rev., 2014, **43**, 5211–5233.*[10]

PBI monomers readily aggregate, stacking in either a face to face or head to tail arrangement to form H- or J- aggregates respectively (Figure 4.2).[9] The formation of H- and J- type aggregates is typically determined by studying the electronic properties of the gel with techniques such as electronic circular dichroism, or more simply UV-Visible absorption spectroscopy.[10] A blue shift in absorbance maxima is seen for H-aggregates, and a red shift for J-aggregates relative to the monomer (Figure 4.2). The exciton model developed by Kasha and co-workers rationalise why such a difference in absorbance maxima is observed between H- and J- aggregates.[11,12] This model assumes weak intermolecular forces between molecules within aggregates, and so small electron overlap.[11,13] It is therefore assumed that the interaction of transition dipoles are the same for the aggregates as they are for the monomer, with a perturbation of the spectra due to electron cloud overlap of monomers within an aggregate.[11] Excitation of a PBI monomer gives a transition from the ground state to an excited state, but when PBI monomers aggregate, the excited state splits into two exciton states represented by E′ and E″ in Figure 4.3. As the transition dipole moment from the ground state to E″ has an overall zero transition moment, it is an allowed transition, as opposed to E′ which is forbidden.[14] For H-aggregates the allowed transition is higher in energy due to repulsion between the overlapping in-phase dipoles, giving rise to a blue shift in comparison to the monomer. Whereas for J-aggregates a red shift in the UV-Visible absorption spectra is observed, due to the in-phase transition dipoles being attractive due to the geometric alignment of the dipoles lowering the energy. Figure 4.3 shows an angle greater than or less than 54.7˚

(i.e. between the polarization axes of molecular centres (slipping angle, θ)), which gives rise to H- and J- aggregates respectively.[15] It demonstrates how this affects the repulsion between dipoles, and therefore the energy of the allowed (solid line) and forbidden (dotted line) transitions.

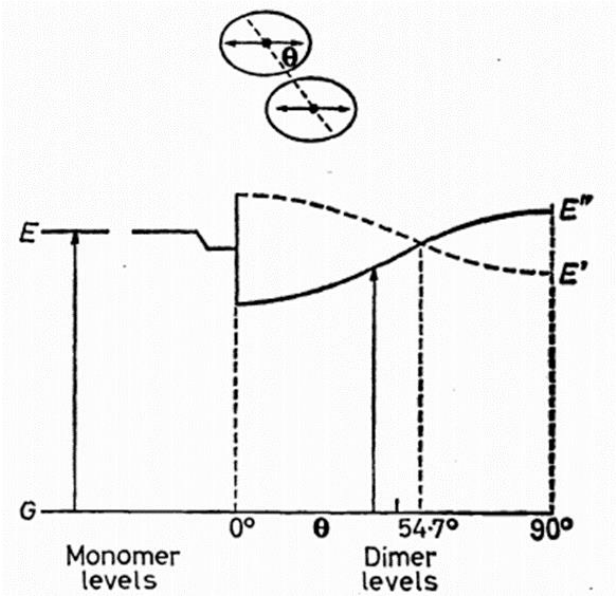

Figure 4.3 Exciton energy band diagram for a monomer and dimer with co-planar transition dipoles which are interconnected by angle θ. Allowed transition dipoles (solid line) are highest in energy when θ > 54.7 ˚, whereas forbidden transitions (dashed line) are highest in energy when θ < 54.7 ˚, showing θ changes from 0 ˚ to 90 ˚ the energies of exciton states interchanges. Figure taken from Pure Appl. Chem., 1965, ***11****, 371–392.*[15]

Typically, three vibronic transitions can be seen within the S_0-S_1 electronic transition due to the 0-0′, 0-1′ and 0-2′ vibronic transitions. The oscillator strength of each vibronic mode is dependent on the degree of overlap between the vibrational ground state and excited state in accordance to the Franck-Condon principle (Figure 4.4). Typically PBIs form H-aggregates, due to the favourable interactions between the closely stacked aromatic groups, making a high degree of overlap giving a larger increase in enthalpy upon formation.[16] To date there are few reported PBIs forming J-aggregates, but many studies have achieved the formation of the H-aggregated structure.[17–20] Modification of the PBI core unit is a popular route to controlling structure. In some cases PBIs have been reported to form both H- and J- type aggregates, by careful consideration of the solvent and hydrogen bonding sites, and modifications of the substituent with bulky groups to supress π-π stacking.[30,32,33] Yan *et al.* have altered the PBI core with either a butadiynylene (PBP) or ethynylene (PEP) linking PBIs together in a series of oligomer lengths from 1 PBI unit up to 3 PBI units.[16] PBP was seen to give H-aggregates, whereas PEP gave rise to J-aggregates in the monomer and oligomer forms. The drastic differences in stacking was attributed to the slipping angle, θ, for both types of oligomer being close to that of the critical angle 54.7˚, demonstrating how a small variation in θ for PEP and

PBP oligomers, can alter the type of aggregate formed.[16] The high degree of π-π stacking and orbital overlap between PBI molecules within both H- and J- type aggregates, gives rise to the presence of a conductive pathway which makes PBI aggregates ideal materials for applications as photoelectrodes, OPV devices and field effect transistors.

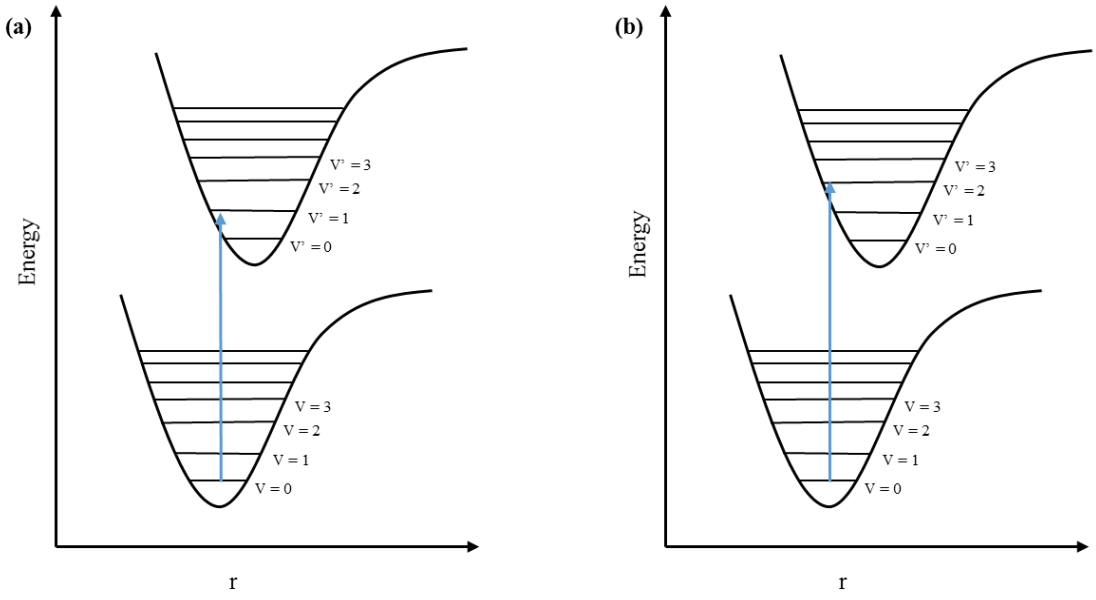

Figure 4.4 Franck Condon energy principle diagrams for an anharmonic oscillator with a bond length of r for vertical vibrational transitions from the ground state v = 0 to v' = 1 (a) and v' = 2 (b), showing the favoured transitions are those with the strongest overlap of wavefunctions from ground state to excited state.

4.1.1.2 Low molecular weight gelators

Low molecular weight gelators (LMWG) are small molecules that can self-assemble to form solvent rich gels when triggered.[23] Self-assembly results in the formation of a conductive pathway, and as a result PBI-gelled materials have potential applications in solar energy.

Typically, LMWG are suspended or dissolved in a solvent, and upon the application of a trigger the monomeric LMWG self-assembles to form less soluble fibres *via* hydrogen bonding, π-π stacking and ion paring. The fibres continue to aggregate to reduce unfavourable interactions with the surrounding solvent, and go on to form an entangled cross linked self-supported gel network, with the ability to trap large amounts of solvent through surface tension and capillary force, resulting in solid like properties (Figure 4.5).[24] A hydrogel or organogel is formed when the liquid phase used in the gelation process is water or an organic solvent respectively.[23] If left to dry, typically ~5% of solvent is retained within the supramolecular structure, and a xerogel is formed.[8] For gelation to successfully occur it is important that 1D growth of the fibres is favoured, as this ensures the formation of aggregates that can go on to

form a cross linked matrix.[24] The use of PBI gelled materials therefore allows for the formation of polymer materials with different solvent and interface environments.

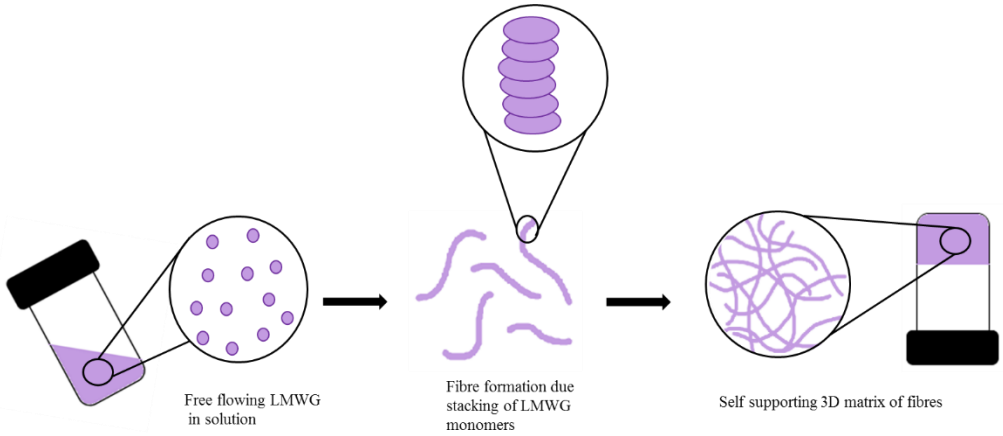

*Figure 4.5 Cartoon demonstrating the "bottom up" gelation process of LMWGs in a free flowing solution to a self-supporting matrix of cross linked fibres upon the application of a trigger. Figure adapted from Chem. Soc. Rev., 2013, **42**, 5143.*[3]

The application of a trigger which reduces the solubility of the LMWG, results in self-assembled aggregates, and there are many factors which can affect gel properties from the molecular scale through to the bulk meaning the fabrication of gels is not trivial. The preparation method of LMWG greatly influences the properties, therefore experimental accuracy is critical to ensure reproducibility of gelation on a molecular scale. There are five commonly employed gelation trigger methods, and these are briefly described below:

1. **pH switch:** This utilises the change in solubility of the gelator upon protonation/deprotonation of basic or acidic groups present in the LMWGs resulting in gelation, and this common trigger for hydrogels is used throughout this chapter. There are different methods by which a pH switch can be applied, such as the use of HCl vapour to lower the pH of the local surrounding environment. This approach often results in less reproducible gels as the rate of gelation is controlled by the diffusion of HCl which is hard to keep constant. The top solution/air interface gels first, as the HCl vapour is in direct contact with the LMWG solution, whereas below the solution/air interface gelation occurs more slowly due to HCl needing to diffuse through the top layers. One approach in which gelation homogeneity can be achieved, is by hydrolysis of sugars and anhydrides such as glucono-δ-lactone (GdL) whereby a slow and uniform pH lowering is achieved, resulting in gelation at the same rate to

yield reproducible molecular stacking and aggregates.[2325] However this leaves residual GdL within the structure.

2. **Temperature switch:** A decrease in temperature below the solution-gel transition temperature stabilises weak non-covalent interactions formed between monomers giving rise to the 1D growth of fibres.[23] If the gel is reheated, annihilation of the gel occurs resulting in the starting LMWG monomer solution.
3. **Solvent switch:** Concentrated solutions of the gelator are prepared in an organic solvent which can dissolve the gelator. A second anti-solvent is then added triggering gelation,[26] and due to the promotion of repulsive interactions a decrease in solubility with surrounding solvent causes aggregation and hence the growth of a 1D fibre.[27]
4. **Enzyme switch:** This is typically used with small hydrophobic aromatic gelators.[28] The use of an enzyme can be used to promote gelation in two ways (i) to produce a peptide bond, or (ii) to cleave a bond rendering the gelator more hydrophobic.[29,30]
5. **Salt switch:** Metal-ion gelation occurs upon the binding of peptides to a heavy metal ion such as zinc, mercury and lead. [31] Metal-salt formation causes a conformational change from the unfolded to the folded states prompting self-assembly.[32] Control of the gel structure (e.g. the degree and type of folding) is possible by the use of metals having different co-ordination sites and geometries.[32]

4.1.1.3 Studying supramolecular structures

SANS is a particularly useful technique for gels, as unlike other structural analytical methods it allows for analysis in the wet state, and has been used as a technique for probing primary fibres within gels. Mears *et al.* carried out an extensive study on how the structure of a gel changes upon drying using a variety of imaging techniques, in order to address whether or not it is acceptable to assume drying has little effect upon the structure.[33] Xerogels were prepared by air drying or freeze drying a hydrogel, and showed a collapse in the network for air dried xerogels. Freeze drying resulted in an aerogel type material, where the liquid phase of a gel is removed and replaced with a gas, resulting in no or little shrinkage/collapsing of the gel network. Xerogels prepared *via* freeze drying resembled an aerogel network, which is more open and more clearly defined as opposed to the collapsed network obtained by air drying. Data obtained from freeze dried xerogels concurred with a decrease in cylinder dimensions as for the air dried xerogels.[33] Mears *et al.* clearly demonstrated that a change in fibre dimensions occurs upon drying, and showed that SANS is a technique that has the ability to probe the primary fibre network. In contrast, other spectroscopic techniques, such as atomic force microscopy and scanning electron microscopy (SEM), are more suited to the study of larger aggregated structures.[33]

Draper *et al.* have also used SANS to study how different methods of pH gelation affect the mechanical properties of a hydrogel on the macro- and micro- scale, and how the chosen gelation method affects the homogeneity of the gel produced.[25] Various pH triggers were studied, HCl, GdL, acetic anhydride, glutaric anhydride, diglycolic anhydride and maleic anhydride. Gelation was triggered by mixing the acid into a basic solution of LMWG. SANS was used to understand the difference in primary fibres formed. For gels formed with HCl, maleic anhydride and diglycolic anhydride, rapid gelation resulted in densely clustered regions of network fibres, whereas GdL, acetic anhydride and glutaric anhydride, led to slow gelation resulting in evenly distributed cross links within the fibre network.[25] Indicating that the rate of which gelation occurs has a profound effect upon fibre formation. It is therefore important to ensure the preparation conditions of a gel are consistent, as parameters such as rate of mixing, concentration, gelation trigger, temperature and solvents used can all affect the gel network obtained.[24]

4.1.1.4 PBIs for solar energy conversion

The ability of PBIs to π-stack results in the formation of extended structures. Coupled to their strong light harvesting abilities, they have been extensively studied for their use in solar energy conversion technologies. Direct excitation of the PBI often leads to initial excited state generation, and a suitable electron donor (hole acceptor) site needs to be present to enable charge separation, and allow electron transport through the PBI structure. However, efficient charge separation has proven to be problematic due to the tendency for PBIs and its derivatives to aggregate, resulting in fast excimer formation as opposed to charge separation.[34] Once a donor-acceptor system has been developed, PBIs have been shown to have efficient carrier migration.[46–49] In the absence of such a donor acceptor structure, excimer states are short lived (ps-ns).

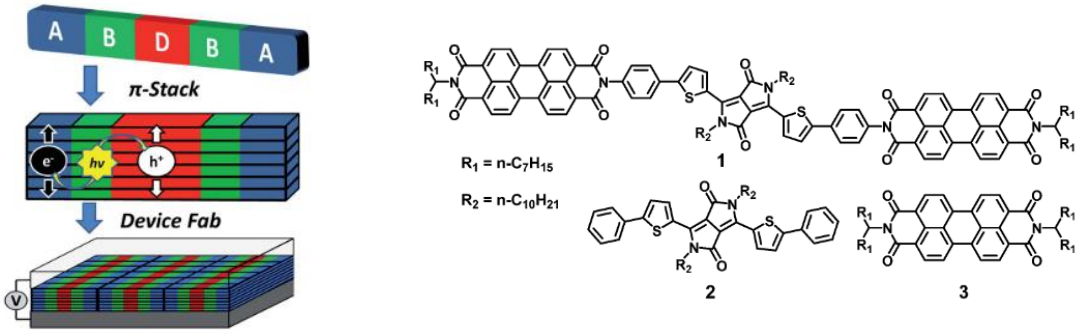

*Figure 4.6 Cartoon showing self-assembly of a donor-acceptor system, allowing control over charge separation due to the formation of electron and hole conducting pathways. Donor (2) and acceptor (3) groups are often used to make donor-acceptor (1) molecules, which aid the synthesis of ordered structures and give increased charge separation. Figure taken from Chem. Sci., 2015, **6**, 402–411.*[37]

Hartnett *et al.* have studied the charge carrier kinetics of donor-acceptor molecules, where diketopyrrolopyrrole (DPP, donor) was attached to two perylenediimides (PBI, acceptor) to give PBI-DPP-PBI, using TA spectroscopy (Figure 4.6).[37] The photophysics and charge separation of PBI-DPP-PBI were followed both in solution and as a solid film. In a thin film, charge separation occurred under 250 fs to form $PBI^{\bullet-}$-$DPP^{\bullet+}$,[37] whereby charge recombination occurred *via* multiple pathways due to the presence of various different stacking environments. The different recombination rates are attributed to inter- and intra- molecular charge recombination pathways occurring on the 50 - 340 ps timescale, where 10% of excited population persists for ~ 6 ns.[37] By annealing the films with solvent vapour to obtain films which had a higher degree of order, the formation of long lived free charge carriers with lifetimes > 6 ns was achieved.[37] The high degree of ordering in donor-acceptor systems for the generation of free charge carriers has been shown to be highly important. Wu *et al.* have developed a Guanine (G) -quadruplex based organic framework, consisting of an electron donating G-quartet which is made up of guanine capped naphthalene or perylene based electron accepting groups, Figure 4.7.[35] The 2D sheets π stack in such a way that mixed stacking of donor and acceptor segments are minimised, to prevent fast charge recombination, and so charge separation should be improved. TA spectroscopy showed the presence of long lived charge carriers, which were seen to be mobile over many sites in the organic framework. Upon visible light excitation of a G-PBI, a broad species was present at 700 nm, owed to the formation of $PBI^{\bullet-}$ which is well reported in the literature.[35] The lifetime of the decay for the charge separated state species is consistent of a fast and slow recombination pathway, owed to recombination of $G^{\bullet+}$- $PBI^{\bullet-}$ and the presence of free charge carriers, which had a lifetime on the microsecond timescale. Due to a high degree of ordering within the organic framework, ~ 30% of the charge separated state formed long-lived free charge carriers.[35]

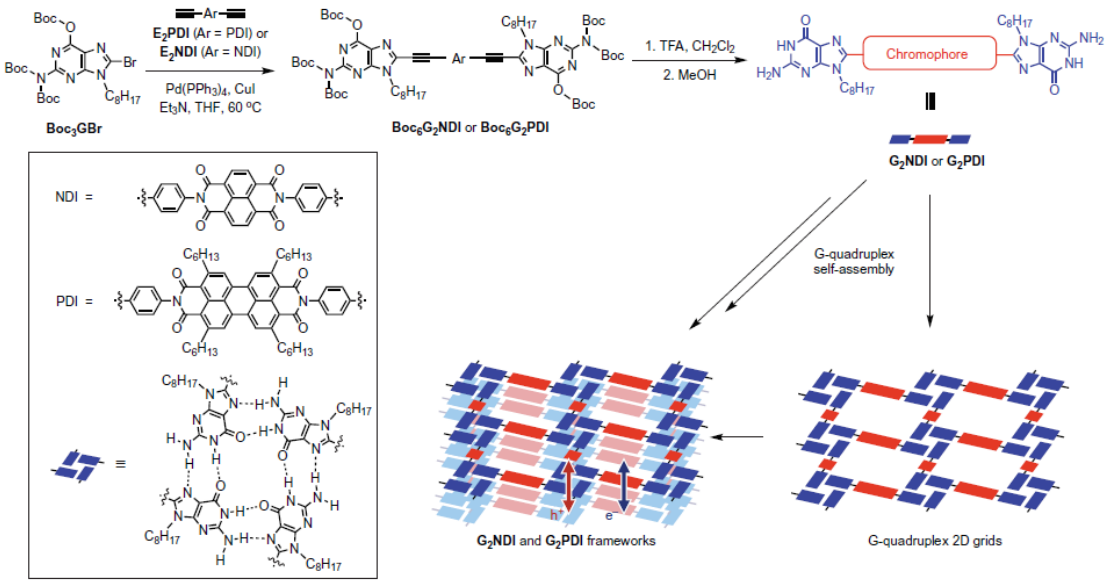

*Figure 4.7 Synthetic preparation of G-quadruplex organic framework with naphthalene or perylene bisimides. The framework π-stacks in such a way that stacking of donating and acceptor segments are segregated allowing for a very ordered framework aiding charge separation for the generation of free charge carriers. Figure taken from Nat. Chem., 2017, **9**, 466–472.*[35]

To further reduce recombination of charge carriers, the generation of triplet excited states prior to charge separation *via* singlet fission is of interest, as the long lifetime of triplet states may increase the probability of charge separation.[39–41] The generation of triplet states have been reported for slip stacked co-facial arrangement of PBIs with transient features at ~510 and ~530 nm.[39] It has been shown that an x-axis offset of 3.0-4.5 Å between co-facially stacked PBIs results in > 100% triplet yield, as singlet fission occurs by the conversion of one single excited state into two triplet states,[41] in comparison to < 1% in monomeric PBI due to slow spin orbit induced intersystem crossing.[39,42,43] Wasielewski and co-workers have shown that triplet state generation can be induced by simply restricting the distance and orientation of PBI dimers and trimers with the use of a rigid bridging unit, xanthene.[44] Other ways in which triplet states have been formed are by the addition of heavy metal atoms, and bromination to promote intersystem crossing.[45–47]

There are relatively few reported self-assembled hydrogelators reported in the literature that exhibit photoconductive properties. Therefore, it was an important step for the community when Roy *et al.* reported a water soluble LMWG in 2012.[4] PBI was functionalised with L-tyrosine, and the hydrogelator formed *via* a temperature switch between pH's 5-9. Photoconductive studies with $PBI^{\bullet-}$ formation focused on the xerogel, where a photoconductive response was seen under both visible and white light illumination, indicating that light induced charge separation had occured.[4] Following on from Roy *et al.* many different amino acid functionalised PBIs have been synthesised.[48,49] When PBI amino acids are gelled long range supramolecular conductive pathways are formed, and upon gelation of amino acid PBIs the supramolecular structure is stable in aqueous conditions (Figure 4.8a). PBI functionalised with amino acids potentially provides a way to use PBIs as photoanodes, without the need for a metal oxide support which have been used in past studies.[50] The acceptor-donor-acceptor nature of this class of PBI hydrogels can aid charge separation as electrons will localise on the PBI core and holes on the amino acid side groups.[51] This chapter reports some of the first studies of a self-assembled organised photoanode for water oxidation that uses an internal donor-acceptor structure.

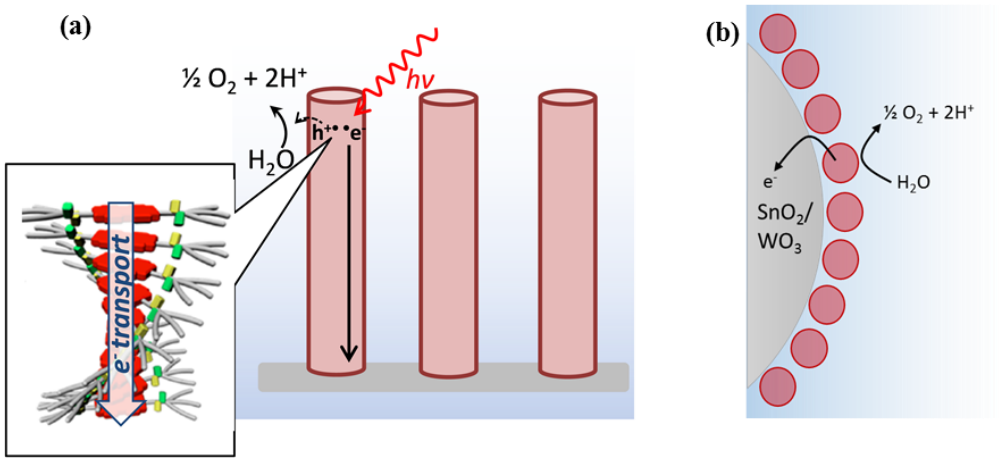

Figure 4.8 Schematic representation of the proposed amino acid functionalised PBI photoanode to be explored here, demonstrating the extended electron transport through the network upon generation of an electron-hole pair (a) and the conventional use of PBI as a dye molecule bound to the metal oxide surface, SnO_2 or WO_3, which does not make use of PBIs abilities to self-assemble into large conductive structures (b).

4.1.1.5 PBI-amino acid materials

Since their discovery a large amount of work has been invested into understanding the synthetic design, photoconductivity and charge transfer pathways of PBI amino acid materials, predominantly in the form of a xerogel.[8,52,53] Draper *et al.* have recently reported a series of amino acid functionalised PBIs (Figure 4.9), where although a difference in photoconductivity was reported for dried films of different amino acids, dominant photoactivity occurred when illuminated with UV light (365 nm).[49] The dried films are prepared from solutions of PBI-amino acids at high pH. Although in this study the PBIs have not been gelled, they still contain large supramolecular structures due to concentration induced aggregation. They determined the concentration of the radical anion using electron paramagnetic resonance (EPR), which showed that quenching of the PBIs could occur depending upon the morphology of the network. EPR measurements also showed that the PBIs with the lowest concentration of radical anion had the lowest photoconductivity, and the PBIs which had the largest concentration had the highest photoconductivity. This is thought to be due to a change in the length of fibres and differences between the aggregates formed.[49] Previously, the same behaviour had been reported for PBI xerogels functionalised with alanine, histidine, phenylalanine and valine.[8] In all cases dried films of the PBIs showed photoconductive behaviour, and formation of $PBI^{\bullet-}$ under UV light only.[49]

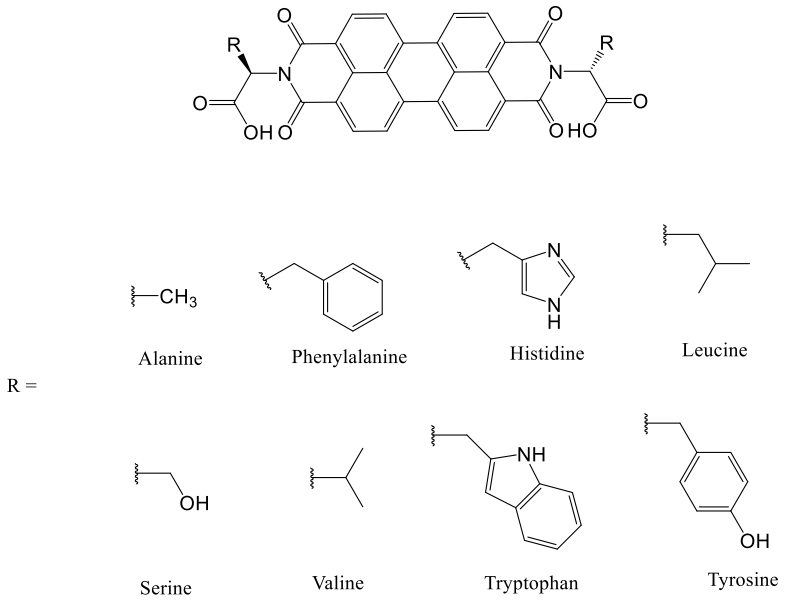

*Figure 4.9 Amino acid functionalised PBI with various amino acid R groups studied by Draper et al. Figure reproduced from Chem. - A Eur. J., 2018, **24**, 4006–4010.*[49]

Recently Castilla *et al.* explored how the self-assembly of two oligo(*p*-phenylenevinylene)s (OPV3)-based hydrogelators with a PBI based hydrogelator effects the semiconductor properties upon a pH trigger using GdL.[54] Photoconductive studies of the OPV3 PBI based xerogels showed greatest activity at 400 nm excitation, demonstrating that

visible region activity is accessible unlike previous reports showing dominant UV activity.[8,54] An interpenetrating network of donors and acceptors is expected to aid charge transport through the network, hence increasing the device performance due to the formation of long lived charge separated states. The excited state dynamics of a dried film of PBI functionalised with alanine (PBI-A) under UV (365 nm) and visible (490 nm) excitation was reported by Walsh *et al.*, demonstrating how charge carrier kinetics can be modified by the solvent environment of the LMWG.[7] UV excitation saw the generation of a $PBI^{\bullet-}$-A charge separated state, as opposed to a short lived excited state when under visible excitation with dried films.[7] The Adams group have also demonstrated that the presence of the PBI radical anion is linked to photoconductivity,[8,49,53,55] and it is therefore the reason why visible region activity is hindered. It was found that changing the local environment from air to that of a more polar one such as methanol, the photoconductivity for PBI-A under visible light irradiation increased due the formation of a charge separated $PBI^{\bullet-}$-A state.[7] Therefore, a change in dielectric environment is expected to aid efficient electron hole pair separation, due to a higher dielectric environment stabilising photo-generated charges within the aggregated structures.[7]

To date, the majority of studies have explored the photoconductive behaviour of supramolecular structures within dried solutions and xerogels of PBIs, as the presence of water limits the electrochemical potential window. However, it is proposed that a water rich environment may promote visible light induced charge separation, making PBI-amino acid hydrated gel materials interesting water splitting photoanodes.

4.1.1.6 PBIs for water splitting

In addition to being promising OPV materials, PBIs are beginning to receive attention as potential solar fuel materials.[56] In particular they are being used for water oxidation, including the fabrication of heterojunctions, and incorporation of well-known WOCs.[57,58]

Ronconi *et al.* have shown facile transfer of electrons from [(N,N′-bis(2-(trimethylammonium)ethylene) perylene 3,4,9,10-tetracarboxylic acid bisimide) $(PF_6)_2$] dye to WO_3 which acted as an electron acceptor, Figure 4.8b, with charge separation only occurring at the WO_3-PBI interface.[57] To utilise the photo-generated holes in the PBI dye, IrO_x nanoparticles were added to the system in various ways, such as drop casting, spin coating and soaking. They found that spin coating and drying in warm air gave the highest photocurrent, which resulted in a factor of 6 increase in photocurrent to 70 μA/cm^2 in pH 3 buffer under 1 sun illumination, demonstrating that efficient hole transfer to IrO_x occurred using this synthesis method.[57] Kirner *et al.* have also explored a similar route and shown that anchoring of a perylene diimide dye, N,N′-bis(phosphonomethyl)-3,4,9,10-perylenediimide (PMPDI), on TiO_2 as opposed to on WO_3 enabled higher dye loading, due to more favourable surface

interactions with the more basic TiO_2 surface. Although TiO_2 had shown to give optimal loading, PBI/TiO_2 materials gave the lowest photocurrent and SnO_2 the highest (~55 and 270 μA cm^{-2} respectively in pH 7 buffer with a hydroquinone electron donor), this was proposed to be due to a low yield of charge injection from the dye into TiO_2.[59] CoO_x was deposited into the SnO_2/PBI structure which although led to a decrease in photocurrent saw improved oxygen efficiencies of 31%. The decrease in photocurrent is thought to be due to increased recombination, due to CoO_x being absorbed on the surface of SnO_2, as opposed to its deposition at suitable sites, promoting unfavourable back reactions.[59]

Although PBI gel photoanodes had not been largely explored prior to the start of this work, perylene gels have been used for both photocatalytic water oxidation and hydrogen evolution in the presence of sacrificial donors. In 2014 Weingarten *et al.* first reported perylene monoimide (PMI) gels for photocatalytic hydrogen evolution, where they synthesised a PMI chromophore amphiphile (CA).[60] A Ni co-catalyst was used for H_2 evolution experiments, whereby the Ni catalyst was added into a solution of PMI-CA, resulting in the formation of a hydrogel which exhibited higher hydrogen evolution activity in comparison to a xerogel and powder.[60] The same group have subsequently demonstrated how a change in packing affects the photocatalytic activity of this class of materials by altering the length of the CA unit.[61,62] Recently, the Adams and Cowan groups have developed an alternative way in which self-assembly can be controlled, by fine tuning the pH of LMWG in solution. At high pHs low concentration solutions of PBIs functionalised at the imide position with L-phenylalanine (F) existed primarily as free PBI-F molecules in solution, whereas at low pHs self-assembly and gelation was favoured, giving rise to long ranged self-assembled networks and superior hydrogen evolution rates under UV irradiation.[63]

To the best of our knowledge there is only one past report where a PBI gel was used as a water oxidation photoanode. In 2014 Kirner *et al.* reported a system where PBI supramolecular structures were both the light absorber and charge (exciton) transporting medium. They used a functionalised PBI gel, which self-assembled *via* π stacking, in conjunction with a co-catalyst for water oxidation, Figure 4.10.[50] The photoelectrode was prepared by spin coating the dye onto an ITO substrate from a basic solution; once dry it was then dipped into an acidic solution. By doing so the phosphonate groups on the dye were protonated, resulting in the dye being insoluble when placed into water. CoO_x was used as a co-catalyst, and was photoelectrochemically deposited. A Faradaic Efficiency of 80 ± 15% and a photocurrent of 150 μA cm^{-2} at positive bias was reported, although the stability of the photoanode was poor. This is a remarkable result. However, the photocurrent was limited by the use of the ITO/PBI interface as the site for charge separation, meaning only very thin films could be studied. Furthermore, a high positive bias of +1.1 $V_{Ag/AgCl}$ (pH 7) was required to

achieve water oxidation. However, these findings are of particular significance as they were the first report of a photochemically driven system for water oxidation using a single layer organic semiconductor with a co-catalyst.[50]

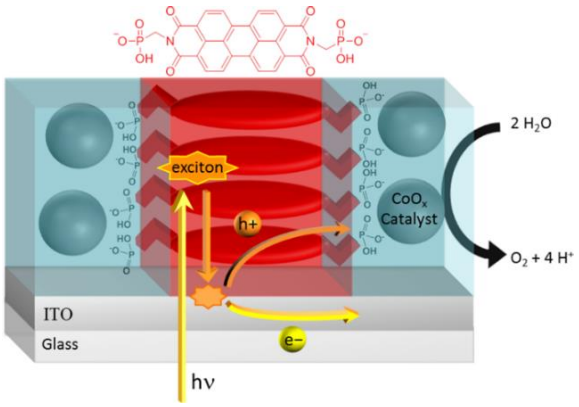

*Figure 4.10 Diagram showing the self-assembly of N,N′-bis(phosphonomethyl)-3,4,9,10-perylenediimide on ITO with the addition of a CoO_x co-catalyst for water oxidation. Figure taken from ACS Appl. Mater. Interfaces, 2014, **6**, 13367–1337.*[50]

4.1.3 Scope of this chapter

This chapter explores the viability of PBI-A (alanine) gels for use as water splitting photoanodes, Figure 4.11. The aim is to assess: (i) If the high dielectric environment of the hydrogel will enable visible light driven charge separation, potentially with the amino acid acting as the electron donor. (ii) To test the efficiency of electron (e^-) transport through the PBI materials. This will provide validation (or otherwise) of the use of the large (micron scale) fibres as a low cost photoanode. (iii) To test if coupling of a water oxidation electrocatalyst evolves light driven water splitting.

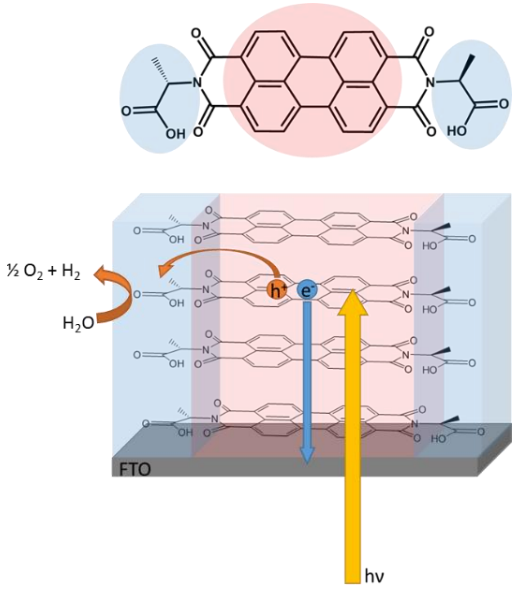

Figure 4.11 Cartoon representation showing electron transport through the PBI core units and hole migration onto an amino acid donor to carry out water oxidation.

4.2. Results and Discussion

All samples were prepared using the following procedure, unless stated otherwise. PBI-A was gelled directly onto cleaned FTO, which had quick drying epoxy resin on the outer perimeter of the FTO to form a well for the PBI-A solution. The area of the well was 150 mm^2. The FTO substrates were placed in a petri dish containing 8 layers of blue roll dampened with water, and 20 µL of 7.5 mg/mL PBI-A solution was evenly deposited into each well. 40 drops of concentrated HCl were placed around both the outer corners of the petri dish and near to the PBI-A electrode. The petri dish was sealed with parafilm, allowing for an acidic atmosphere to form. Sample preparation is discussed in further detail in section 4.4.2 of this chapter. Xerogels are hydrogels dried in air for ≥ 20 hours. Throughout this chapter a rehydrated xerogel is defined as a xerogel that has rehydrated in 0.1 M KCl (pH 4) for 1-4 hours, with the exception of SANS experiments due to longer measurement times required (50 hours).

4.2.1 Gel formation, structure determination and water content

UV-Visible absorption spectroscopy reports on the electronic structure of materials, and is an excellent probe to follow the gelation process, where the self-assembled structures form. Time resolved in-situ gelation of a PBI-A solution *via* a HCl pH trigger shows a blue shift in the UV-Visible peak maxima. In both the high concentration solution and the gel the low intensity of the 0-0′ vibronic transition compared to the 0-1′ and 0-2′ is indicative of the presence of aggregated structures, and the lack of a blue shift demonstrates they are H-aggregates (Figure 4.12a).[64] This is characteristic of the formation of H type aggregates stacked in a cofacial arrangement.[48] The formation of aggregates is also indicated by the broadening of features in the UV-Visible absorption spectra due to molecules being stacked closely together.[48] The formation of aggregates is favoured as they give rise to conductive pathways making them ideal candidates for their use as photoanodes. [37] Hydrogel films are water rich, and drying in air for ≥ 20 hours results in a 95% water loss to form a xerogel structure as measured by TGA. Heating of the PBI-A xerogel under an argon atmosphere up to 200˚C shows approximately a 5% mass loss between 0 – 120˚C, establishing approximately 5% water is retained upon drying (Figure 4.12b).

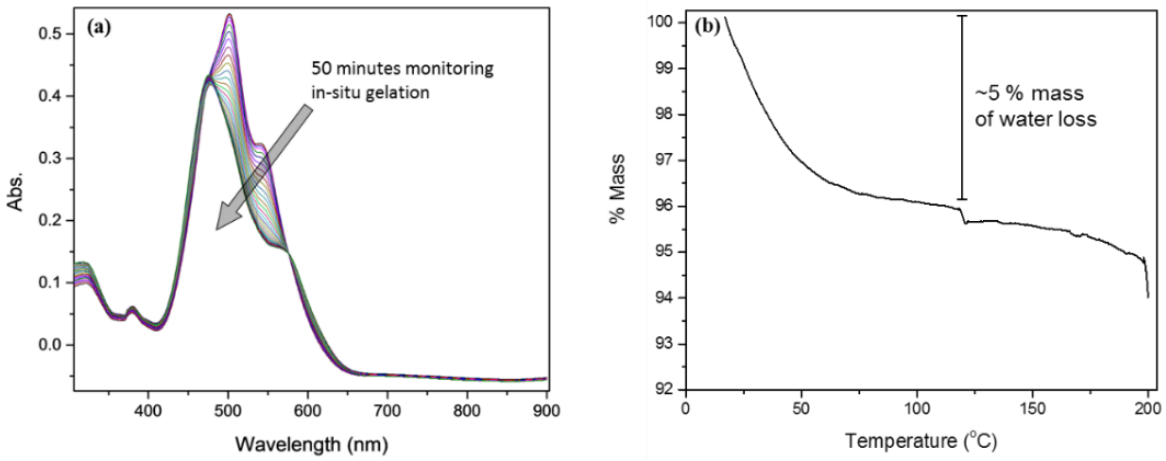

Figure 4.12 In-situ gelation of PBI-A with the application of a pH trigger. The experiment was carried out in a 2 x 1cm² quartz cell, with wetted blue roll at the bottom of the cell, and wetted blue roll with small amount of HCl on at the top to seal the cell in order to create an acidic atmosphere to trigger the gelation process (a). TGA analysis of a hydrogel left to dry in air for 20 hours to form a xerogel, showing a mass loss of water from the xerogel upon heating to 120˚C (b).

A change in the molecular stacking within PBI-A fibres was seen for a hydrogel and xerogel *via* UV-Visible absorption spectroscopy (Figure 4.13a). Although there is a change in packing upon drying of a hydrogel, the peak maxima for both hydrogel and xerogel are similar, within 10 nm of each other. For a hydrogel (and xerogel) three transitions are observed at 579 (581) nm, 499 (507) nm, 467 (469) nm respectively, due to the 0-0′, 0-1′ and 0-2′ vibronic states (Figure 4.13).[7,8] Therefore the electronic properties of the perylene cores in both films are expected to be similar. The peak maxima for each vibronic state in the visible region was determined from Lorentzian fitting of the UV-Visible absorption spectra (Figure 4.13b and c), which also permitted the determination of the relative area contributions for each vibronic state for the gels, Figure 4.13d. The dominant band for both gels is from the 0-1′ vibronic state transition within S_1. For a xerogel the second largest band is from the 0-0′ vibronic state, with the smallest contribution from the 0-2′ state, whereas for a hydrogel there are similar contributions of 0-0′ and 0-2′ vibronic states. The difference in vibronic ratios between gels confirms a difference in H-aggregated structures of PBIs upon drying, likely due to the hydrated aggregated network collapsing and altering the stacking within the fibres,[33] and is discussed in detail later in the chapter. A slight red shift in peak maxima upon drying of a hydrogel indicates an increase in slipped stacking between perylene units within fibres, which represents a smaller degree of face to face stacking in a xerogel than the hydrogel.[65]

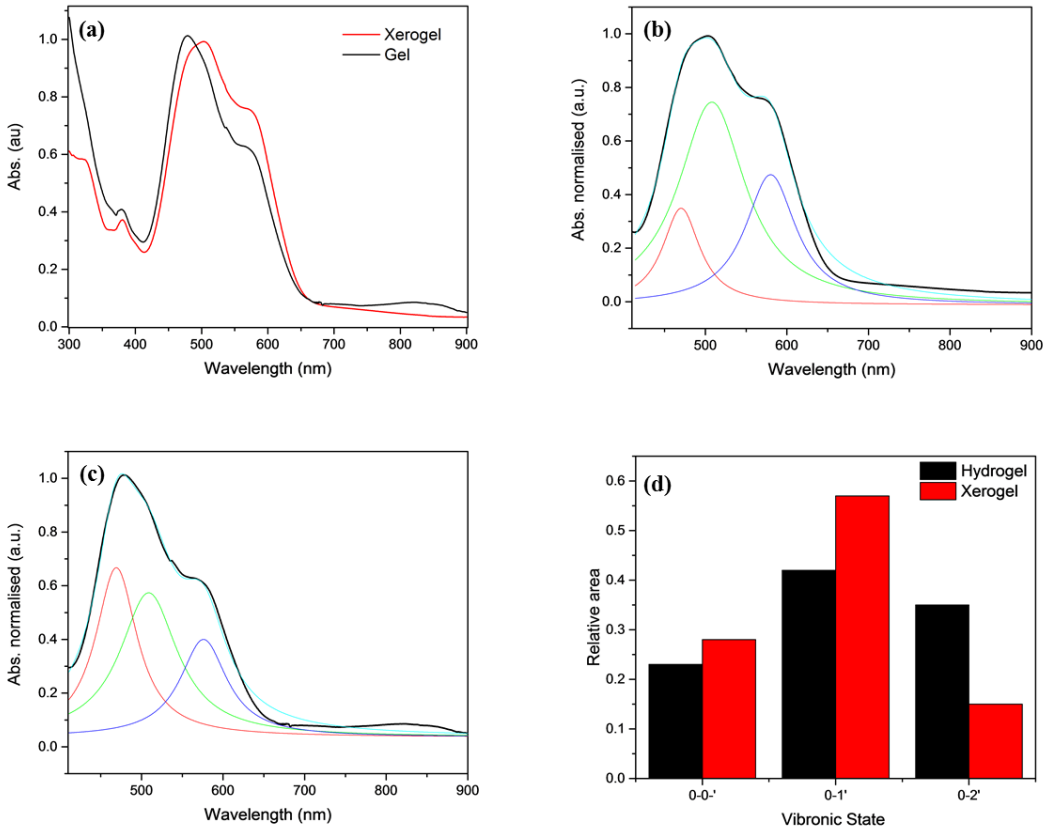

Figure 4.13 UV-Visible absorption spectra of a 20 µL 7.5 mg/mL film of a xerogel (red) in air and hydrogel (black) in pH 4 KCl (a). Lorentzian spectral fitting of a xerogel (b) and hydrogel (c); raw data is shown in black, and individual Lorentzian peaks (red, green, blue) and overall fit line (cyan) are shown. The difference in relative area of each vibronic state contributes to the UV-Visible absorption spectra of a xerogel (red) and hydrogel (black) (d).

When a PBI-A xerogel is placed into pH 4 electrolyte rehydration occurs (as high as *ca.*70 - 80% wt. water[66–68]). However, it is evident that the structural difference between a hydrogel and xerogel is not reversible (Figure 4.14a). A small but distinct change in the UV-Visible absorption spectrum occurs within the first 10 minutes of rehydration, indicating a change in local structure of the PBI-A aggregates, due to the partial rehydration of the xerogel. Soaking of a xerogel for prolonged periods of time in 0.1 M KCl electrolyte (pH 4) for >50 hours, showed further small structural changes in the UV-Visible absorption spectra (Figure 4.14a). It is therefore clear that the collapsed gel network is not fully restored by rehydration.

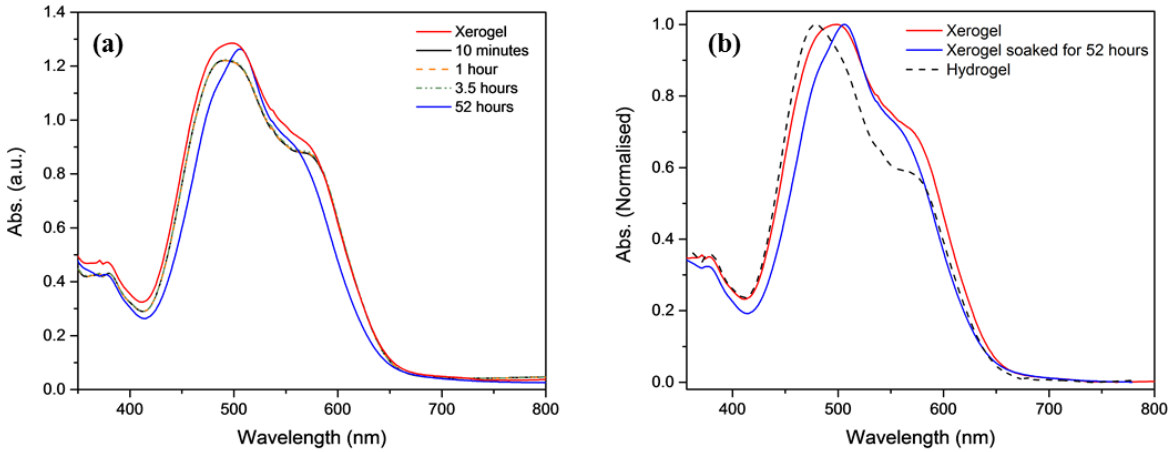

Figure 4.14 UV-Visible absorption spectra of a 20 µL 7.5 mg/mL xerogel (black) rehydrated in water pH 4, at various time intervals over a 3.5 hour period and after 52 hours of soaking (red) (a). UV-Vis absorption spectra overlay of xerogel prior to soaking (red), after soaking for 52 hours (blue) and of a 7.5 mg/mL 20 µL hydrogel (black dashed line) (b).

UV-Visible absorption spectroscopy allows for insight into the stacking of PBIs within aggregates, indicating a small change in the aggregated structure of the gels on the molecular scale, but it is not possible to determine the fibre properties directly from these measurements. Scanning electron microscopy (SEM) has shown fibre bundles on the micron scale (Figure 4.15), but SEM does not allow for studies of the hydrated gel. SANS on the other hand, allows for insight into the structure on a larger scale ranging from a couple of nanometres to hundreds of nanometres, providing information into the primary fibre structure and size. Similarly to UV-Visible absorption spectroscopy, SANS can be applied to both hydrated and dry samples, and is therefore an ideal structural probe into the difference of the primary fibres of PBI-A gels in different hydrated states.[33] A customised flexible cylinder and power law model in SasView was used in the fitting of SANS data collected by myself and was fitted by Dr. L. Mears.

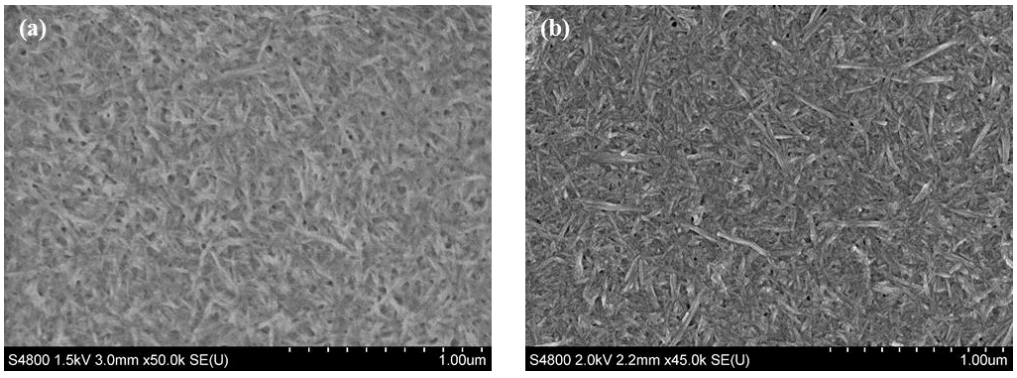

Figure 4.15 SEM images of a PBI-A xerogel on FTO (a) and with a 10 nm thick layer of chromium (b) to reduce a build-up of charge on the surface resulting in clearer images. Fibre bundles smaller than 1 µm are present within the gel network. The scale bar on both images represents 1 µm.

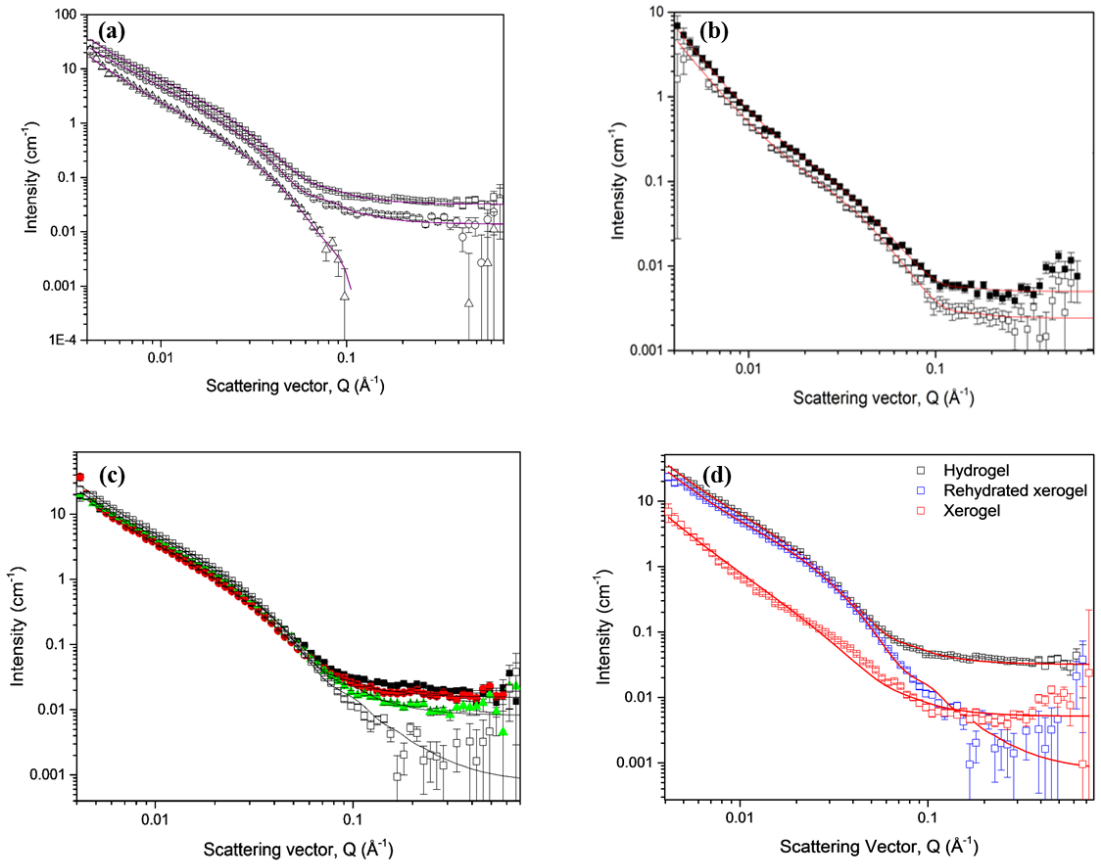

Figure 4.16 SANS data for hydrogels of 1.0 mm (square), 0.5 mm (circle) and 0.25 mm (triangle) thickness (a). Xerogels with starting thickness of 1.0 mm (filled square) and 0.5 mm (open squares) (b). 1.0 mm xerogel (black squares) rehydrated with electrolyte (0.1 M KCl, pD 4 in D_2O) for 7 (red diamonds), 23 (green triangles) and 50 (open squares) hours (c). Overlay of a 1.0 mm hydrogel (black), rehydrated xerogel after 50 hour rehydration period (blue) and xerogel with a 1.0 mm starting thickness (red), raw data is shown by open squares and fits are shown as red solid lines (d). For hydrogels and rehydrated xerogels the remainder of the 1 mm demountable cell thickness was filled with 0.1 M KCl electrolyte, pD 4, in D_2O. Data was fitted to a custom flexible cylinder and power law model within the SasView package. The fits for each data set are given as solid lines.

SANS data plots for a hydrogel, xerogel and rehydrated xerogel are shown in Figure 4.16. Even from the raw data it is apparent that differences in the scattering patterns exist. Raw data is shown as scatter plots, and solid lines are the fits of the data to a customised flexible cylinder model, which are tabulated in Table 4.1-Table 4.3. The flexible cylinder model has been successfully used to model SANS data for similar hydrogel materials,[24,33,69,70] and also dried films containing supramolecular structures of PBI-A. Full details of the fitting model are included in the introduction to SANS (chapter 1.4.2).

Table 4.1 SANS fitting parameters for a hydrogel, xerogel and rehydrated xerogel each of 1.0 mm thickness. Both the hydrogel and rehydrated xerogel the cell was filled with 0.1 M KCl electrolyte, pD 4, in D_2O. The rehydrated xerogel data was obtained after 50 hours of rehydration. A custom flexible cylinder combined with a power law model within SasView package was used for the fitting of the data.[71]

	Hydrogel	Xerogel	Rehydrated Xerogel
Power law scale ($/10^{-5}$)	8.0 ± 1.0	0.3 ± 1.0	5.1 ± 1.0
Power law value, N	2.3 ± 0.2	2.6 ± 0.2	2.4 ± 0.1
Cylinder scale ($/10^{-5}$)	0.7 ± 0.2	0.1 ± 0.03	0.5 ± 0.01
Radius, R (nm)	5.9 ± 0.2	3.1 ± 0.3	5.0 ± 0.5
Kuhn length (nm)	14.3 ± 5.0	7.6 ± 5.0	5.2 ± 3.0
Apparent contour length, L (nm)	57.4 ± 5.0	31.0 ± 11.0	76.0 ± 7.0
Background (cm^{-1})	0.0320 ± 0.001	0.0050 ± 0.0002	0.00078 ± 0.0004
χ^2	3.8	1.5	2.1

Parameters associated with Porod's power law show distinct changes in fibre dimensions upon the drying of a hydrogel, Table 4.1. The radii of segments within the fibres decreased (*ca.* 50%) upon drying, and the apparent contour lengths are shortened by a similar amount. Although contour length is typically described as the length of a polymer chain when fully extended,[72] in a cross-linked fibre network the apparent contour length modelled within the SANS data gives a measure of the polymer length between crossover points, Figure 4.17. Therefore the shrinking of the previously hydrated fibre leads to a more compact, rigid network, due to the loss of water and an increase in the rigidity of the fibre network and a greater level of overlap between fibres in the xerogel.

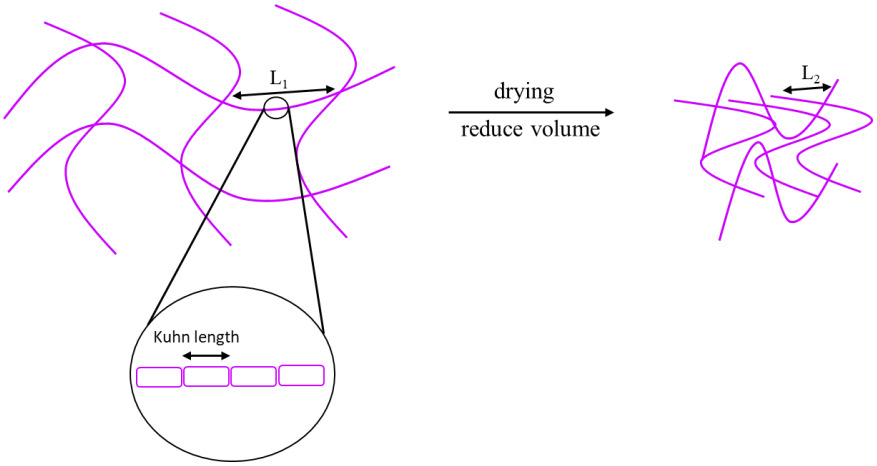

Figure 4.17 The apparent contour length of a PBI-A hydrogel, L_1, decreases due to the collapse and shrinking of the PBI-A network upon drying, L_2. The apparent contour length is defined as the distance between two entanglement points, in contrast the Kuhn length is less sensitive to drying.

Analysis of changes in the Kuhn length upon drying are more challenging as the magnitude of the error on the fitted value is greater than the change in each case. The Kuhn length, a measure of the length of sub-units within a fibre, may be expected to be less sensitive to hydration than the apparent contour length, given the reasonable level of similarity between the UV-Visible absorption spectra upon drying which indicated no large change (e.g. from H- to J- aggregation) in the local structure of segments. The Kuhn length appears less sensitive to drying as the values reported here are within error for a hydrogel and xerogel, indicating the length of sub-units within the fibre are unaffected by the presence of water within the fibre network. In principle the degree of crossover and overlap between fibres in the samples can also be evaluated using the power law value, N. A power law value of 2-3 indicates a clustered, cross-linked network and all samples are within these limits.[73] Values closer to 3 indicate a more dense compact network, with higher levels of cross linking.[25] However, again the relatively large errors associated with the fitted value of N prevent its interpretation. It is also not possible to compare scaling factors, because an assumed thickness was used in the flexible cylinder power law model for data fitting of a xerogel due to thickness changes upon drying. Nonetheless, the clear decrease in fibre radius and apparent contour length and minimal change in Kuhn length provide strong evidence that water removal leads to the formation of a more compact, cross-linked (and hence rigid) network, made up of similar sub-units.[33]

Table 4.2 SANS fitting parameters for a rehydrated xerogel at different time points. A reservoir of with electrolyte (0.1 KCl, pD 4 in D_2O) filled the free space of the cell containing the gel. Data was fitted using a customized flexible cylinder model.

Rehydration time (hours)	0.5	7	23	50
Power law scale ($/10^{-5}$)	6.6 ± 0.6	5.0 ± 1.0	6.1 ± 0.4	5.1 ± 1.0
Power law value, N	2.3 ± 0.2	2.3 ± 0.2	2.3 ± 0.1	2.4 ± 0.1
Cylinder scale ($/10^{-3}$)	0.59 ± 0.2	0.47 ± 0.01	0.61 ± 0.04	0.54 ± 0.01
Radius, R (nm)	4.9 ± 0.2	4.9 ± 0.4	4.9 ± 0.5	5.0 ± 0.5
Kuhn length (nm)	9.3 ± 5.0	9.6 ± 5	7.6 ± 3.0	5.2 ± 3.0
Apparent contour length, L (nm)	46 ± 5.0	65 ± 30	76 ± 6.0	76 ± 7.0
Background (cm^{-1})	0.019 ± 0.001	0.016 ± 0.01	0.0082 ± 0.0003	0.00078 ± 0.0004
χ^2	1.8	1.3	2.3	2.1

As previously shown from monitoring the rehydration of a PBI-A xerogel *via* UV-Visible absorption spectroscopy, the structure of the PBI-A network does not revert back to that of the pristine hydrogel after 50 hours of rehydration. This was also evident from the SANS data, Table 4.1-4.2. Rehydration of a xerogel was tracked using 0.1 M KCl in D_2O electrolyte (pD 4). The radii for the rehydrated xerogel was 5.0 ± 0.5 nm, which lies between that of the xerogel and hydrogel radii (3.1 ± 0.3 nm and 5.9 ± 0.2 nm respectively). It is also interesting that rehydration leads to a large increase in apparent contour length, in agreement with the xerogel expanding in volume upon rehydration, increasing the distances between cross over points. However, the apparent contour length actually reaches a final value that is greater than that of the starting hydrogel, further reinforcing the conclusion that although rehydration leads to an expansion of volume the original hydrogel network structure is not regenerated.

A study of hydrogels of different thickness was also carried out as it was important to ensure there was no change in primary fibre structure for different thicknesses. In all studies we have used a HCl trigger as it provides hydrogels without trapped organic acid residues that may modify the photoelectrochemical behaviour. However gelling PBI-A with a HCl pH trigger results in an inhomogeneous film. No changes were seen with respect to Porod's power law parameters upon alteration of the thickness of the gel from 0.25 mm - 1.0 mm (Table 4.3). This indicates that there is no change in the primary fibre structure across different thicknesses, ensuring that the gel network is consistent across the entirety of the gel electrodes.

Table 4.3 SANS fitting parameters for a 0.50 and 0.25 mm hydrogel thickness, and a 0.50 mm xerogel. For hydrogel samples, a reservoir of with electrolyte (0.1 KCl, pD 4 in D_2O) filled the free space of the cell. Data was fitted using a customized flexible cylinder model.

	1.00 mm hydrogel	0.50 mm hydrogel	0.25 mm hydrogel
Power law scale ($/10^{-5}$)	8.0 ± 1.0	5.60 ± 1.0	2.3 ± 0.3
Power law value, N	2.3 ± 0.2	2.31 ± 0.2	2.3 ± 0.1
Cylinder scale ($/10^{-3}$)	0.7 ± 0.2	0.37 ± 0.2	0.19 ± 0.04
Radius, R (nm)	5.9 ± 0.2	6.2 ± 0.4	5.8 ± 0.6
Kuhn length (nm)	14.3 ± 5.0	25.2 ± 5.0	25.8 ± 5.0
Contour length, L (nm)	57.4 ± 5.0	81.3 ± 30.0	80 ± 20.0
Background (cm^{-1})	0.0320 ± 0.001	0.0138 ± 0.01	-0.0057 ± 0.0004
χ^2	3.8	1.71	0.83

4.2.2 Electrochemical characterisation

To predict if PBI-A materials can make suitable photoanodes, the following section presents a series of experiments to calculate the donor and acceptor sites, and the driving force for charge separation in the hydrogel, xerogel and rehydrated xerogel. Initially, we measured the reduction potentials of the PBI-A hydrogel and rehydrated xerogel.[59] In an aqueous pH 4 KCl solution, CV analysis at 100 mV s^{-1} showed changes in the electrochemistry upon the alteration of the hydrated state (Figure 4.18). The CV of a hydrogel shows two reductions (-0.56 V, -0.68 $V_{Ag/AgCl}$, Figure 4.18a). Due to the broadness of the reductions, and literature precedent for other perylene, terrylene and quaterrylene diimides,[74–76] the reductions may be occurring across multiple PBI environments within the aggregated networks.[77,78]

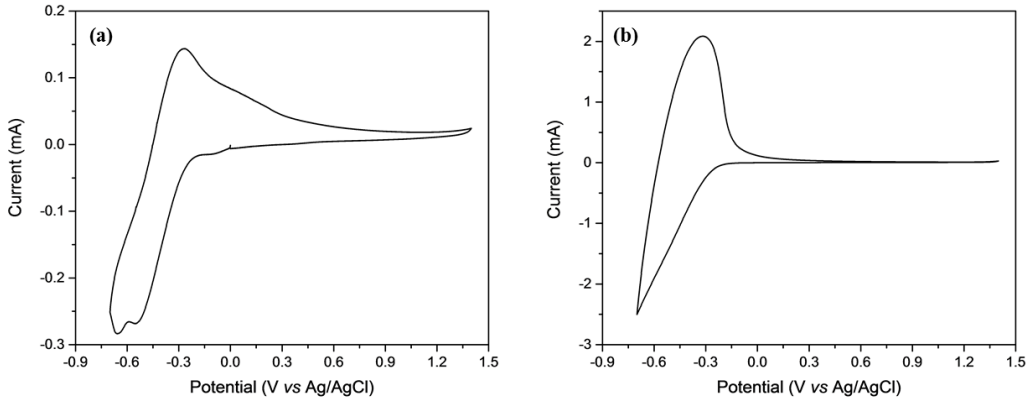

Figure 4.18 Cyclic voltammogram of a hydrogel (a) and rehydrated xerogel (b) under an inert atmosphere at 100 mVs^{-1} in 0.1 M KCl electrolyte (pH 4). A Pt counter electrode and 3.5 M KCl Ag/AgCl reference electrode were used.

To enable assignment of the reduced states, spectroelectrochemistry (SEC) was carried out. The electrode potential was held at single potentials between 0 V and -0.7 $V_{Ag/AgCl}$, and UV-Visible absorption spectra were recorded once the current reached a steady state. SEC studies permit assignment of the hydrogel reductions to $PBI^{\bullet-}$-A (λ_{max} = *ca.* 510 nm, *ca.* 556 nm, *ca.* 649 nm, *ca.* 736 nm, *ca.* 820 nm) and PBI^{2-}-A (λ_{max} = *ca.* 524 nm, *ca.* 548 nm, *ca.* 620 nm, *ca.* 732 nm) by comparison to the previously reported UV-Visible absorption spectra of reduced PBI-A (Figure 4.19a and Table 4.4).[7,8,53,79] Although it is likely that a rehydrated xerogel can form both $PBI^{\bullet-}$-A and PBI^{2-}-A, the CV measurement did not show two well-defined reductions (Figure 4.18b). SEC of the rehydrated sample does show two distinct reductions though. Comparing the UV-Visible absorption SEC data for a hydrogel with that of the rehydrated xerogel, we see that that behaviour of the rehydrated xerogel is quite similar (Figure 4.19b). Similarly for the rehydrated xerogel, formation of $PBI^{\bullet-}$-A (λ_{max} = *ca.* 524 nm, *ca.* 552 nm, *ca.* 644 nm, *ca.* 736 nm, *ca.* 820 nm) and PBI^{2-}-A (λ_{max} = *ca.* 540 nm, *ca.* 607 nm, *ca.* 720 nm, *ca.* 809 nm) were observed, Table 4.4. In a rehydrated xerogel $PBI^{\bullet-}$-A formation occurs at slightly earlier potentials of -0.2 $V_{Ag/AgCl}$, and yields higher concentrations of $PBI^{\bullet-}$-A than the hydrogel at -0.3 $V_{Ag/AgCl}$, suggesting less facile formation of a $PBI^{\bullet-}$-A in a hydrogel. Significant amounts of PBI^{2-}-A formation at *ca.* 610 nm, occurred 300 mV earlier in a rehydrated xerogel at -0.4 $V_{Ag/AgCl}$ in comparison to the hydrogel (-0.7 $V_{Ag/AgCl}$). For a rehydrated xerogel, as the concentration of $PBI^{\bullet-}$-A decreased the formation of PBI^{2-}-A increased, resulting in almost complete conversion of $PBI^{\bullet-}$-A to PBI^{2-}-A.

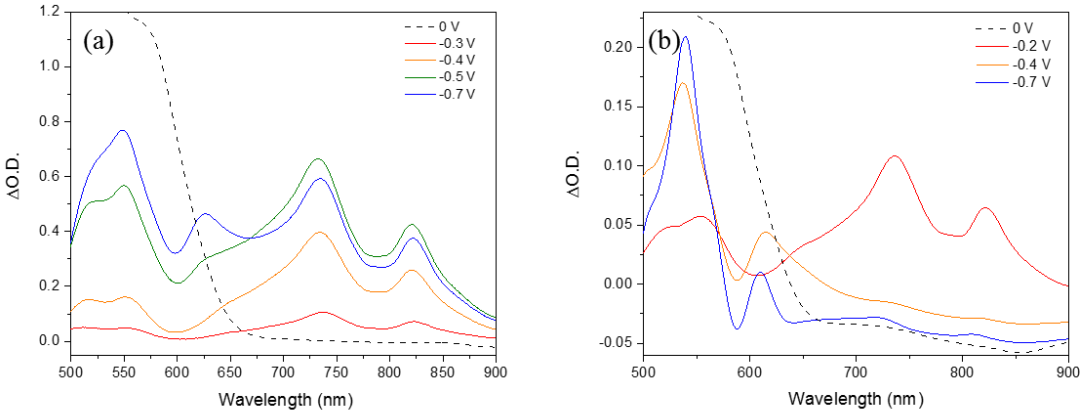

Figure 4.19 SEC of a 20 µL 7.5 mg/mL PBI-A (a) hydrogel and (b) rehydrated xerogel at various potentials for the electrochemical formation of $PBI^{\bullet-}$-A and PBI^{2-}-A under an inert atmosphere in 0.1 M KCl (pH 4) electrolyte. All data has been subtracted with UV-Visible absorption spectra recorded at 0V. The presence of $PBI^{\bullet-}$-A was evident at ca. 736 nm and 820 nm, PBI^{2-}-A at ca. 620 nm for a hydrogel and ca. 610 nm for a partially rehydrated xerogel.

Table 4.4 Summary of $\lambda_{max.}$ for the electrochemical generation of $PBI^{\bullet-}$-A and PBI^{2-}-A.

	Hydrogel λ_{max} (nm)	Rehydrated xerogel λ_{max} (nm)
$PBI^{\bullet-}$	512, 556, 649, 736, 823	523, 552, 644, 736, 821
PBI^{2-}	524, 548, 625, 732	540, 607, 720, 809

As distinct electrochemical reduction features were not identified in a rehydrated xergoel CV, (Figure 4.18b), differential cyclic voltabsorptometry (DCVA) was used to obtain an accurate measurement of the reduction potentials of the xerogel.[80] Although other studies within this chapter have focused on a 20 µL (5 µL of a 7.5 mg/mL film was chosen here to ensure a suitable level of transmission of UV-Visible light. DCVA measurements consist of recording the change in UV-Visible absorbance at a specific wavelength, whilst a CV measurement is acquired. In this way it was possible to identify the potential of electrochemically generated species formed by comparing the first derivative of the UV-Visble absorption data to the corresponding CV, both of which were plotted against time. Electrochemically-generated species appear as positive features, with maxima at the potential where the maximum current for the same electrochemical process would be measured in the CV. As the optical response obtained is free from background capacitance, and if there is

minimal spectral overlap between electrochemically generated species, reduction potentials can be obtained.

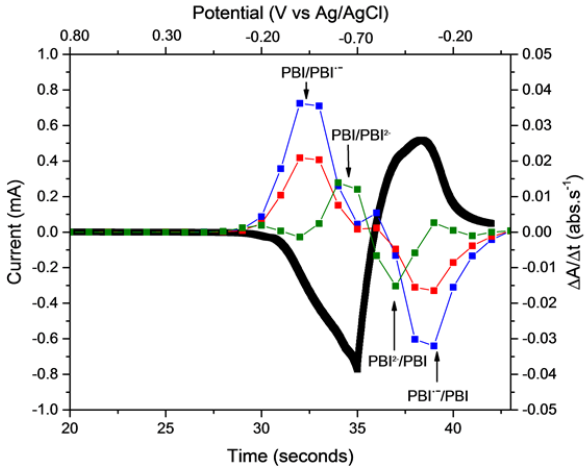

Figure 4.20 DCVA of a rehydrated xerogel under an inert atmosphere in 0.1 M KCl (pH 4) electrolyte. The formation of the $PBI^{\bullet-}$-A and PB^{2-}-A are seen. The CV obtained at 100 mVs^{-1} is shown in black, and differential absorbance at 729 nm (blue), 820 nm (red) and 608 nm (green) are shown.

In Figure 4.20, the DCVA spectra of a PBI-A rehydrated xerogel recorded at wavelengths corresponding to $PBI^{\bullet-}$-A (730 nm and 820 nm) and PBI^{2-}-A (608 nm) are shown. From this reduction potentials for $PBI^{0/-}$-A and $PBI^{\bullet-/2-}$-A were obtained at -0.46 $V_{Ag/AgCl}$ and -0.66 $V_{Ag/AgCl}$, and their corresponding PBI^{-} (-0.34 $V_{Ag/AgCl}$) and PBI^{2-} (-0.46 $V_{Ag/AgCl}$) oxidations. To assess the PBI HOMO position and the possibility of the alanine group acting as an electron donor, CV and square wave voltammetry (SWV) measurements of the PBI in water have been carried out (Figure 4.18 and Figure 4.21).

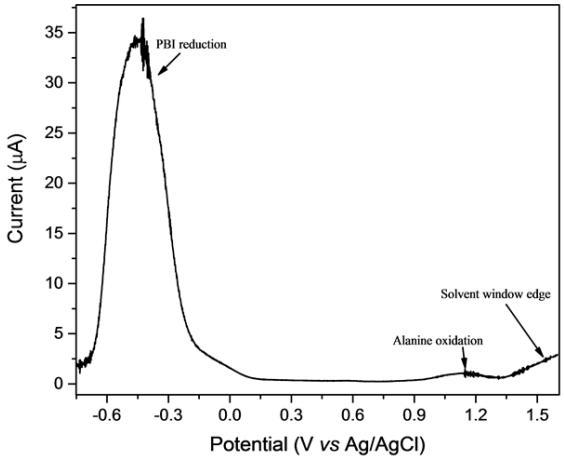

Figure 4.21 SWV of a PBI-A rehydrated xerogel under a nitrogen atmosphere, scanning from -0.75 V to + 1.55 V at a frequency of 25 Hz with a 90 second equilibration time, in 0.1 M KCl pH 4 electrolyte, using a Ag/AgCl reference electrode and Pt counter electrode.

In the SWV an oxidation at +1.15 $V_{Ag/AgCl}$ is assigned to the oxidation of the alanine side group on the basis of past electrochemical and computational studies.[7] The oxidation of the perylene core is expected to be beyond the electrochemical window in water. Instead we use a method for the determination of the HOMO reported elsewhere.[46,75] The HOMO position is calculated using the energy of the transition between the lowest vibrational levels of the electronic ground and first excited states ($E_{0\text{-}0}$), with $E_{0\text{-}0}$ being readily obtained from the average of the 0-0′ vibronic transition absorption maximum at *ca.* 580 nm and its corresponding emission maximum (Figure 4.22) respectively.

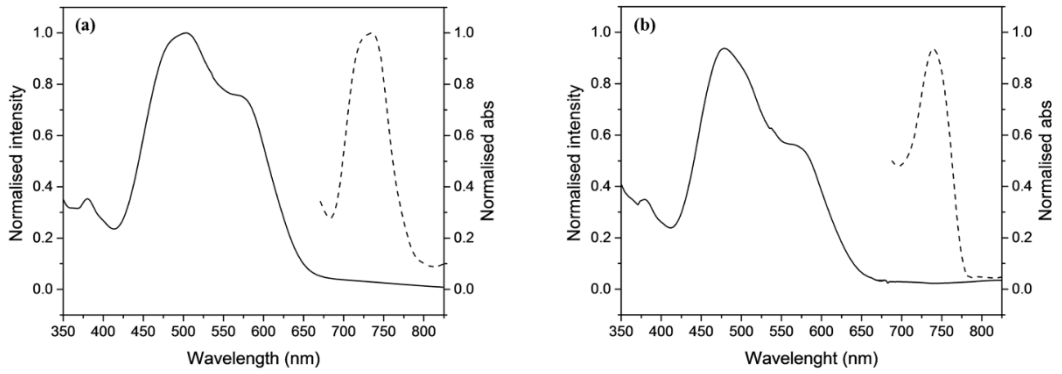

Figure 4.22 UV-Visible absorption (solid) and emission spectra (dashed line, $\lambda_{exc.}$ 580 nm) of a PBI-A xerogel (a) hydrogel (b). The average of the absorption and emission maxima for the 0-0′ vibronic state is used to determine the band gap of the material, $E_{0\text{-}0}$.

On the basis of all measurements, we can construct the energy band diagrams for both a hydrogel and rehydrated xerogel shown in Figure 4.23. The HOMO positions were estimated to be +1.69 and +1.61 $V_{Ag/AgCl}$ for a rehydrated xerogel and hydrogel respectively.

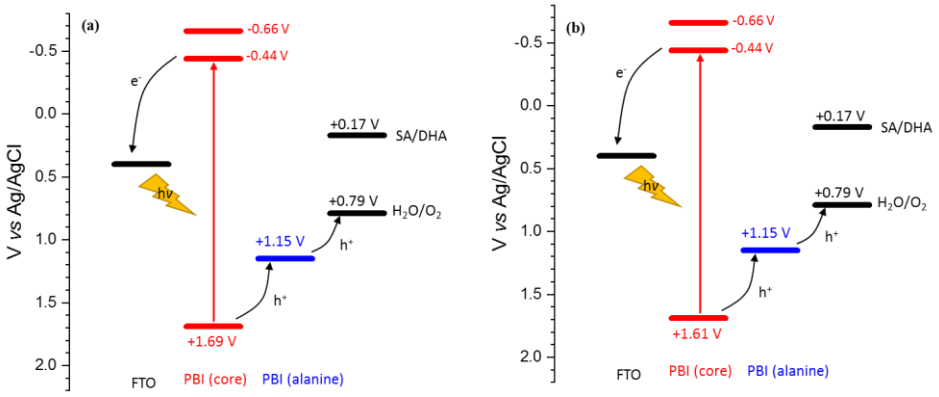

Figure 4.23 Energy level diagrams for a rehydrated PBI-A xerogel (a) and hydrogel (b) are shown, and based on electrochemical measurements described above. All potentials shown are given vs Ag/AgCl at pH 4. The potential used for incident photon conversion efficiency (IPCE) measurements was +0.4 V, was used for FTO. SA= sodium ascorbate, DHA = dehydroascorbic acid.

Figure 4.23 indicates that alanine may be able to act as an electron donor enabling internal charge separation with electrons accumulating in the PBI core. Furthermore, as the alanine oxidation resides more positive than that of water oxidation, it is possible that it may act as a hole relay to water. The Gibbs free energy for the photo-induced electron transfer pathway can be estimated from the Rehm-Weller equation (Equation 4.1, 4.2), and are shown in Table 4.5.[81] Where E_{ox} and E_{red} refer to the oxidation and reduction potentials of the donor (alanine group) and acceptor (PBI) units respectively, and are measured by SWV and CV respectively. As all electrochemical and transient data were recorded in the same electrolyte, there is no change in the solvation energy for an electrochemically or photochemially generated states yielding a solvation term (S) of zero. E^* is the excited state energy, and is calculated in the same manner as $E_{0\text{-}0}$. Coulombic interactions (C) are present within the donor-acceptor ions. The donor acceptor distance r_{DA} is the distance between the chiral carbon on the alanine and the centre of the PBI core. This has been calculated to be *ca.* 7 Å elsewhere for a PBI-A monomer.[7]

$$\Delta G_{ET} = E_{OX} - E_{RED} - E^* - \frac{e^2}{4\pi r_{DA}\varepsilon_0\varepsilon_s} + \frac{e^2}{8\pi\varepsilon_0}\left(\frac{1}{r_D}+\frac{1}{r_A}\right)\left(\frac{1}{\varepsilon_s}-\frac{1}{\varepsilon_p}\right) \quad \text{(Eq. 4.1)}$$

$$\Delta G_{ET} = E_{OX} - E_{RED} - E^* - C + S \quad \text{(Eq. 4.2)}$$

Visible light induced charge separation within a dried PBI-A film was not previously observed,[7] due to a minimal driving force for photo-induced charge transfer (ΔG_{ET}) from the PBI core to the alanine side group.[7] This was rationalised by the low dielectric environment (air, ~3) in dried solutions, which destabilised the oxidised and reduced forms of the donor/acceptor.[7] In contrast, Table 4.5 shows that the higher dielectric environment (water, ~80) means that the PBI-A hydrgel electrodes are expected to exhibit a large driving force for charge transfer from the initially excited state calculated from $E_{0\text{-}0}$ (ΔG_{ET} ~ -0.6 eV (rehydrated xerogel) and ~-0.5 eV (hydrogel)).

Table 4.5 Calculated Gibbs energy of photoinduced electron transfer from the intramolecular alanine donor functionality to the PBI core.

	$E_{OX\ ALANINE}$ ($V_{Ag/AgCl}$)	$E_{RED\ PBI}$ ($V_{Ag/AgCl}$)	E^* (eV)	C (eV)	ΔG_{ET} (eV)
Rehydrated xerogel	1.15	-0.44	2.13	0.03	-0.57
Hydrogel	1.15	-0.56	2.17	0.03	-0.49

To experimentally determine if visible light induced charge separation can occur in our gel structures, we have measured the TA spectra of a PBI-A hydrogel (Figure 4.24a and c) and PBI-A xerogel (Figure 4.24b and d) following visible light excitation (490 nm, 275 μW). 3 ns after excitation of the PBI-A hydrogel, new positive absorptions are present at 546, 650 (sh) 730 and 819 nm, and these are overlapped with a broad negative feature due to the ground state absorption at wavelengths below *ca.* 580 nm. The positive absorption bands can be assigned to a $PBI^{\bullet-}$ through the excellent agreement with the spectrum of $PBI^{\bullet-}$-A that was electrochemically generated in the SEC studies described above (Table 4.4). We label the photochemically generated state as $PBI^{\bullet-}$-A', where the A' indicates that the oxidation state of the alanine side-group is not experimentally determined. Our electrochemical study indicates that electron transfer from the alanine group is favourable. Although electrochemical studies indicate that the alanine group becomes oxidised its spectral features are expected. However, we are unable to detect a spectral fingerprint for the oxidised alanine group in-line with past reports, which suggest that it would occur at shorter wavelengths than those studied here preventing us from studying how the oxidised alanine site evolves with time.[7] Careful inspection of the TA spectra of the PBI-A hydrogel (Figure 4.24a) indicates that at the earliest timescales studied (*ca.* 0.3 ps), well-defined TA bands for $PBI^{\bullet-}$-A' at 813 and 719 nm are not discernible. Instead, a broad feature is present at 650 nm which partially decays as the spectral features of the $PBI^{\bullet-}$-A' grow in (within 1 ps). The temporal resolution of our instrumentation prevents accurate determination of the rate of charge separation from the initially generated excited state in PBI-A hydrogels. However, it is clear that the $PBI^{\bullet-}$-A' formation occurs very rapidly (~1 ps or faster), and a significant population of the charge separated state persists for longer than the maximum time addressable in our experiment (Figure 4.24b and c).

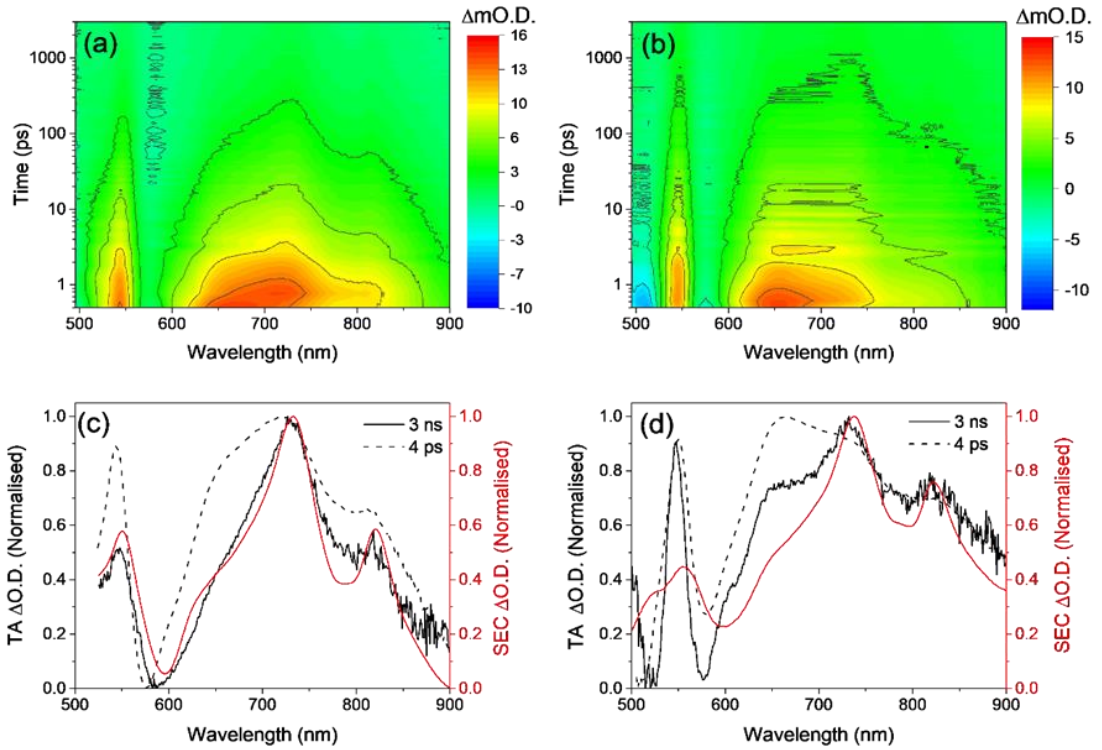

Figure 4.24 TA spectra of a PBI-A hydrogel (a) and rehydrated xerogel (b) in pH 4 electrolyte following visible light (490 nm) excitation. The TA spectra at 3 ns and 4 ps are compared to the UV Visible absorption spectrum of the electrochemically generated (SEC data) PBI$^{\bullet-}$-A for the hydrogel (c) and rehydrated xerogel (d).

The TA spectra of the rehydrated xerogel at 3 ns (Figure 4.24d) also shows transient bands at 547, 646, 732 and 820 nm, which can also be assigned to PBI$^{\bullet-}$-A' by comparison to the spectroelectrochemical data, Figure 4.25.

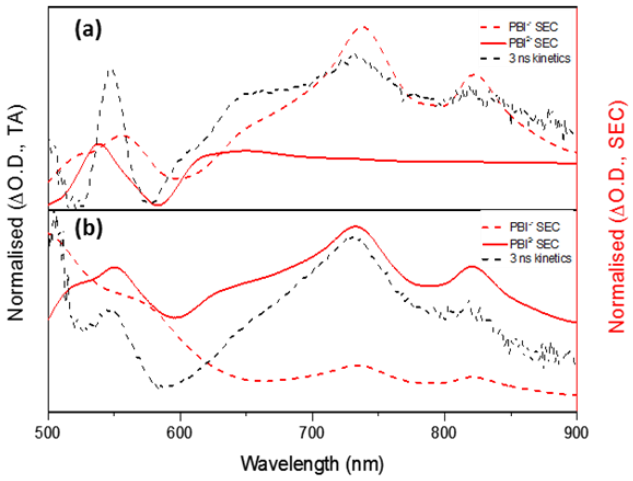

Figure 4.25 At longer time scales, both the hydrogel and rehydrated xerogel are seen to have similar charge separated states. UV Visible absorption spectrum SEC (red) aids assignment of the TA spectral features at 3 ns (black) to a charge separated state and the generation of both a singly and doubly reduced PBI species for a partially rehydrated xerogel (a) and hydrogel (b). The presence of PBI$^{\bullet-}$-A' (red, dashed) is seen at 546, 730 and 820 nm, and PBI^{2-}-A' (red, solid) at 545 and 610 nm. All TA spectra were excited with 490 nm and a pump energy of 275 μW.

It is therefore apparent that visible light induced charge separation does occur within both the rehydrated xerogel and hydrogel samples in contrast to past studies on dried solutions of PBI-A where the initially formed excited state decayed rapidly, within 200 ps.[7] The yield of long-lived charge separated state is very similar for both the rehydrated xerogel and hydrogel samples, with the intensity of the *ca*. 730 nm TA band of PBI$^{\bullet-}$-A' being ~16 % of its peak value by 3.2 ns, Figure 4.26 and Table 4.6.

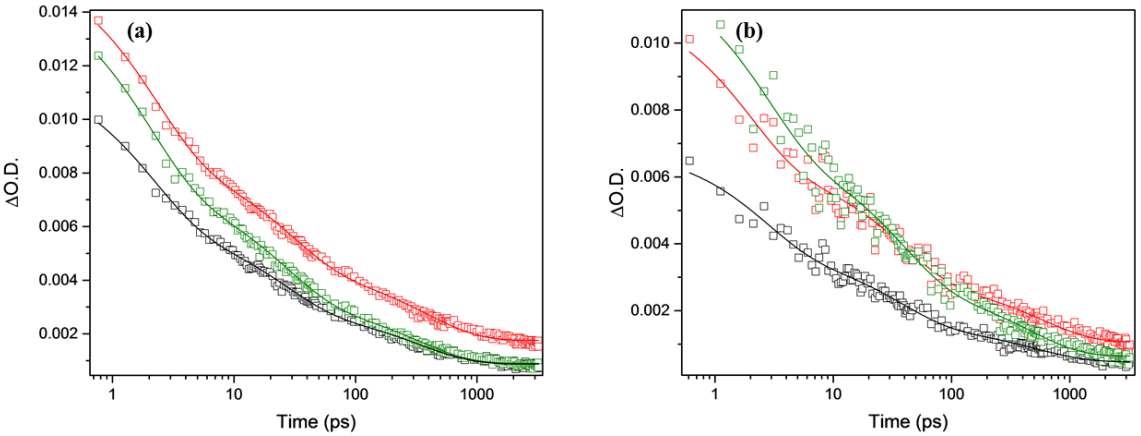

Figure 4.26 Kinetic lifetime traces of a PBI-A hydrogel (a) and rehydrated xerogel (b) at 662 (green), 730 (red) and 820 (black) nm. Hydrogel and rehydrated xerogel measurements were carried out in 0.1 M KCl aqueous solution, with an excitation wavelength of 490 nm with a pump power of 275 µW.

Table 4.6 Lifetimes for PBI$^{\bullet-}$ for a hydrogel, rehydrated xerogel and xerogel under 490 nm excitation with the corresponding amplitudes. Kinetic traces were fitted to a triexponential, where it is seen that the longest lived species of the PBI$^{\bullet-}$ is at 730 nm with a xerogel having the longest lived PBI$^{\bullet-}$owed to its increase in conductivity. Amplitude weighted averages (AWA) were calculated taking into consideration both the lifetime of the species and its amplitude.

	665 nm (ps)	**730 nm (ps)**	**820 nm (ps)**	**% of PBI$^{\bullet-}$ remaining after 3.2 ns at 730 nm**
Hydrogel	τ_1 = 1.91 (± 0.09), τ_2 = 25.09 (± 1.25), τ_3 = 328.75 (± 17.41)	τ_1 = 2.13 (± 0.10), τ_2 = 27.81 (± 1.42), τ_3 = 387.65 (± 18.32),	τ_1 = 2.05 (± 0.11), τ_2 = 24.63 (± 1.40), τ_3 = 339.38 (± 17.46),	16
	A_1= 0.0075 (± 2.23x10^{-4}), A_2= 0.0043 (± 9.27x10^{-5}), A_3= 0.0023 (± 8.13x10^{-5})	A_1 = 0.0072 (± 2.12 x10^{-5}), A_2= 0.0041 (± 9.36 x10^{-5}), A_3= 0.0027 (± 7.9 x10^{-5})	A_1 = 0.0057 (± 1.76x10^{-4}), A_2 = 0.0032 (± 8.13x10^{-5}), A_3 = 0.0020 (± 6.62x10^{-5})	
	AWA = 71.73 (± 4.21)	AWA = 84.00 (± 4.33)	AWA = 70.57 (± 3.98)	
Rehydrated xerogel	τ_1 = 2.59 (± 0.42), τ_2 = 36.52 (± 4.75), τ_3 = 461.47 (± 78.90),	τ_1 = 1.84 (± 0.21), τ_2 = 36.33 (± 3.16), τ_3 = 582.37 (± 77.75),	τ_1 = 2.55 (± 0.29), τ_2 = 35.41 (± 3.94), τ_3 = 517.13 (± 82.21),	
	A_1 = 0.0054 (± 5.83x10^{-4}), A_2 = 0.0041 (± 2.39x10^{-4}), A_3 = 0.0021 (± 2.11x10^{-4})	A_1 = 0.0048 (± 4.29x10^{-4}), A_2 = 0.0034 (± 1.72x10^{-4}), A_3 = 0.0018 (± 1.45x10^{-4})	A_1 = 0.0031 (± 1.89x10^{-4}), A_2 = 0.0022 (± 1.10x10^{-4}), A_3 = 0.0011 (± 8.95x10^{-5})	16
	AWA = 97.66 (± 6.97)	AWA = 116.91 (± 17.52)	AWA = 102.29 (± 13.01)	

The kinetics of the hydrogel and rehydrated xerogel have been further studied (Figure 4.26). The kinetic traces recorded at the UV-Visible absorption maximum of PBI$^{\bullet-}$-A' require fitting to at least three exponential functions indicating that multiple PBI$^{\bullet-}$-A' pathways exist (Figure 4.26). Amplitude weighted averages (AWA) were calculated as shown in Equation 4.3 for each wavelength assigned to the formation of the photo generated PBI$^{\bullet-}$-A, it accounts for the average lifetime at a given wavelength by taking into account both the lifetime (τ) and corresponding amplitude (A) generated from the triexponential fitting for the kinetic traces in Table 4.6.

$$AWA = \frac{\sum_i (A_i \tau_i)}{\sum_i A_i} \qquad \text{(Eq. 4.3)}$$

Walsh *et al.* have reported that for a PBI-A dried solution at 830 nm under 490 nm excitation, a short lived PBI singlet excited state is formed with lifetimes of $\tau_1 < 1$ ps, $\tau_2 = 7.1$ (± 0.2) ps

and τ_3 = 107 (± 5.4) ps.[7] The increased lifetimes observed with the hydrated samples here, further reinforce the assignment to a charge separated state. AWAs of 116.91 (± 17.52) ps and 84.00 (± 4.33) ps for a rehydrated xerogel and a hydrogel respectively.

4.2.3 Photoelectrochemistry

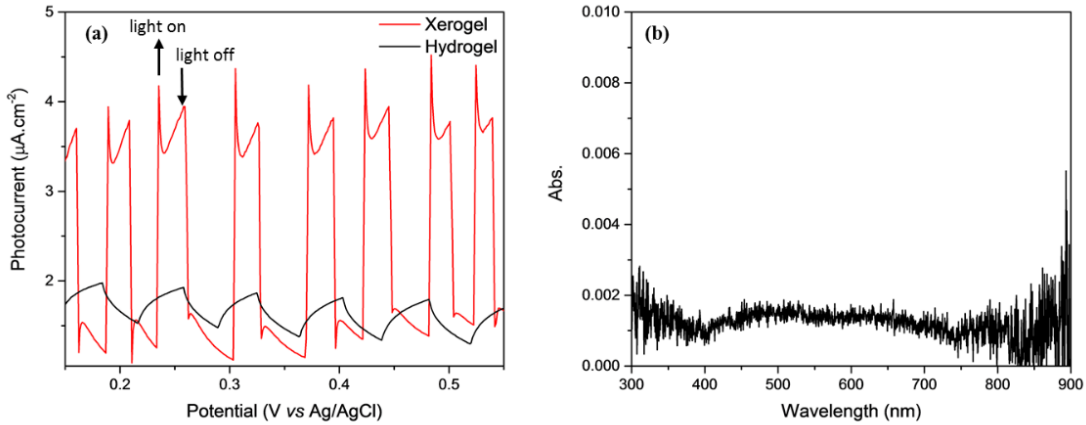

Figure 4.27 Photoelectrochemical response of a 20 µL 7.5 mg/mL PBI-A xerogel (red) and a hydrogel (black) irradiated on the back face of the electrode (a). PBI-A photoanodes had good stability in pH 4 KCl electrolyte over the timescale of experiments as shown by a UV-Visible spectra of post experimental electrolyte (> 2 hours) (b). Electrochemical measurements were carried out under an inert atmosphere, in 0.1 M KCl pH 4 electrolyte using Ag/AgCl reference electrode and Pt counter electrode.

As the transient spectroscopic studies indicate both PBI-A hydro- and rehydrated gels can undergo visible light induced charge separation, likely with electron transfer from the PBI core to the alanine group, we have tested them as photoanodes. PEC measurements were carried out under chopped visible and UV light illumination from a Xe lamp (315 – 795 nm). Both the hydrogel and rehydrated xerogel photoelectrodes operated as photoanodes at potentials positive of 0 $V_{Ag/AgCl}$, Figure 4.27a. In all cases experiments were carried out in 0.1 M KCl electrolyte at pH 4, and photoelectrodes displayed a good stability and minimal dissolution on the timescales of experiments (< 2 hours, Figure 4.27b). Although both electrodes displayed photoelectrochemcial activity, the rehydrated xerogel photoelectrodes exhibited approximately four times greater photocurrent than an equivalent hydrogel photoelectrode (Figure 4.27a). From these photoelectrochemical measurements, it appears that the structural changes are hydration induced, and so hydration appears to effect the activity. UV-Visible absorption spectroscopy and SANS has given insight into how the structure of the xerogel changes upon rehydration, and that the change in structure is not reversible. The marked difference between the samples is explained further below.

Incident photon to current efficiencies (IPCE) measurements for electrodes held at +0.2 $V_{Ag/AgCl}$ in KCl are shown in Figure 4.28. It is striking that the IPCE (wavelength) relationship mirrors the UV Visible absorption spectra of the samples, and light induced current occurs predominantly following visible light excitation with hydrated samples.

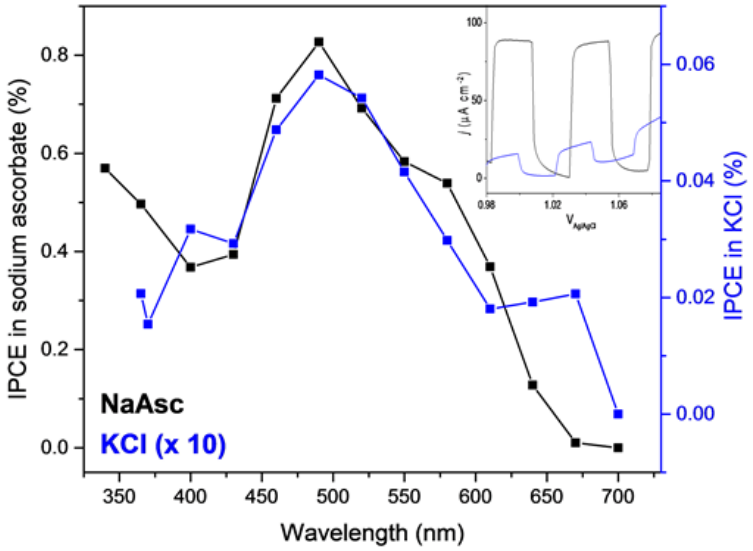

Figure 4.28 IPCE measurements of a rehydrated PBI-A xerogel in pH 4 KCl (blue) electrolyte and in the presence of a hole scavenger, sodium ascorbate, at pH 4 (black). The inset shows a large increase in photocurrent in the presence of a hole scavenger. Experiments were carried out with 20 µL PBI-A over a 150 mm² area.

The photoelectrochemical response therefore confirms the TA results, and shows that by using gel-based electrodes in an aqueous electrolyte, for the first time we have managed to develop a self-assembled PBI photoanode, that undergoes internal charge separation to generate long-lived charge separated states that can be used in solar fuels applications. The photocurrent densities achieved (~4 µA cm^{-2}) using the rehydrated xerogel in KCl electrolyte are on the order of those often seen with other state-of-the-art organic photoelectrodes in water, where values of 1-10 µA cm^{-2} are commonly reported using similar light intensities.[50,57,82,83] Nonetheless, the achieved IPCE values for the electrodes in KCl are low (<0.1%) (Figure 4.28). The IPCE values (η_{IPCE}) for inorganic photoanodes have been described elsewhere to be the product of the efficiency of light harvesting by the photoanode (η_{LH}), the efficiency of generation of separated charges (η_{sep}), which is often described as the population of holes that reach the site where the desired oxidation reaction can take place, and the efficiency of hole injection (η_{inj}), i.e. the fraction of holes which reach the correct site and then go onto proceed *via* the desired reaction (Equation 4.4).[84,85]

$$\eta_{IPCE} = \eta_{LH} \times \eta_{sep} \times \eta_{inj} \qquad \text{Eq. 4.4.}$$

In Equation 4.4, recombination losses occurring during electron transport through the structure are not considered as a separate term, and instead are contained within the efficiency of injection and separation terms. In contrast to many inorganic photoanodes, where electron transport efficiencies can be relatively high, it is feasible that electron transport to the FTO interface through the self-assembled PBI-A structures, which form disordered fibrous bundles (Figure 4.15), may be a significant loss mechanism. Therefore, here we also include an explicit charge collection efficiency (η_{col}) in Equation 4.5.

$$\eta_{IPCE} = \eta_{LH} \times \eta_{sep} \times \eta_{col} \times \eta_{inj} \quad \text{Eq. 4.5.}$$

Our TA studies show high-yields of the PBI$^{\bullet-}$-A' charge separated state following visible light excitation. The ability to undergo internal charge separation is of significant benefit, and appears to contrast the one previous study on the related PMDI photoanodes, where exciton separation only occurred at the ITO/PMDI interface.[50] Although significant recombination does occur in our system, *ca.* 84% of the initially generated PBI$^{\bullet-}$-A' is lost 3.2 ns after excitation, it is clear that a long-lived population of photoelectrons/holes can be formed. UV-Visible absorption spectra of the electrodes also indicate that light harvesting is not the major limiting factor, as between 450 to 580 nm > 90% of light is absorbed in a typical hydrogel and rehydrated xerogel electrode (Figure 4.29).

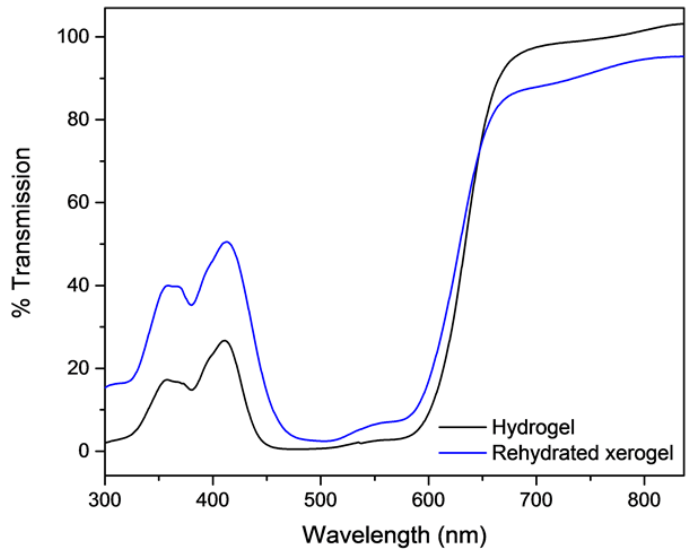

Figure 4.29 Transmission spectra of a 20 µL 7.5 mg/mL PBI-A rehydrated xerogel (blue) and hydrogel (black) show that the electrodes are highly light harvesting with typical absorbance's > 1. The difference in absorbance between each sample is due to inhomogeneity across samples, as a result of the HCl vapour gelation method.

As the samples are optically thick the ratio of photocurrent achieved when under illumination from the front (directly onto the PBI-A gel) and the back (illuminated through the FTO substrate) gives a measure of the charge transport efficiency, Figure 4.30.

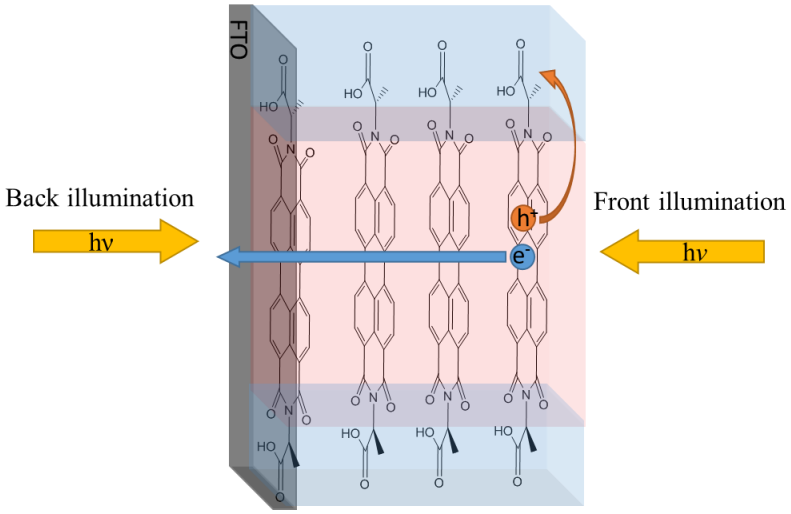

Figure 4.30 Schematic diagram showing front and back illumination of a PBI-A photoanode where front illumination irradiates directly onto the PBI-A gel and back illumination through the FTO substrate.

For rehydrated xerogels, we measure (at 1.0 V) a slight (35%) decrease in the photocurrent when the sample is front illuminated (η_{col}~0.65). Using a hydrogel we find front illumination gives a large decrease with an 80% lower photocurrent when compared to the same sample back illuminated (η_{col}~0.20), Figure 4.31a. These results indicate that for rehydrated xerogels, charge transport appears to be remarkably efficient, with >65% of photogenerated electrons able to reach the FTO collector regardless of where in the PBI-A anode they are generated, confirming the potential of self-assembled PBI materials to enable long-range electron transport. The shape of the chopped photocurrent response also indicates charge transport limitations in the hydrogel sample, Figure 4.31a. Even during back illumination, we find that the photocurrent continues to rise for ~4 seconds after the light is switched on, indicating that photo-generated electrons cannot be extracted, and are accumulating within the PBI-A structure. In contrast with the rehydrated xerogel electrode, following a sharp initial current spike as the light is switched on we obtain relatively stable photocurrents within 1 s during back illumination, and only a small rise in photocurrent during front illumination, Figure 4.31b. It is interesting to note the correlation between the improved collection efficiency in the rehydrated xerogel derived photoelectrodes, and the changes in structure that are identified in the SANS measurements previously outlined. The decrease in radii and shrinking of fibres to a more rigid network upon drying of the hydrogel, and a more rigid structure may be expected to aid electron transport through the PBI fibres.

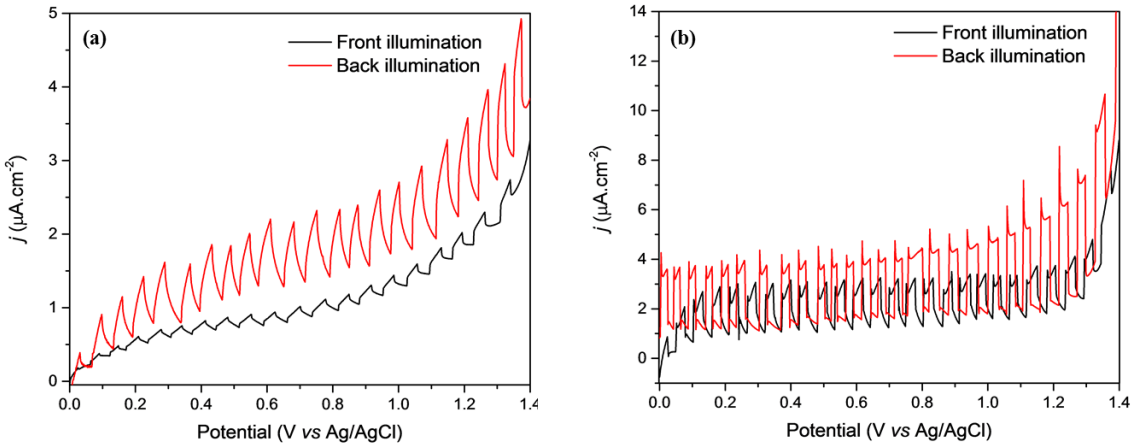

Figure 4.31 Linear sweep voltammogram for a hydrogel (a) and rehydrated xerogel (b) photoelectrode with light incident on the PBI-A (front, black) and FTO (back, red) in pH 4 0.1 M KCl at 10 mVs^{-1}, Xe lamp (315-795 nm, 80 mW cm^{-2}).

Finally, we examine the fate of the photo-generated holes in the PBI-A photoanodes. We have carried out experiments in the presence of a hole scavenger that is thermodynamically easier to oxidise than water. The addition of sodium ascorbate results in a ~13-fold increase in IPCE peak value for the PBI rehydrated xerogel, and current densities up to 80 μA cm^{-2} were achieved. This indicates that inefficient hole transfer from the PBI-A into water is one of the major factors limiting the efficiency of the rehydrated xerogel photoelectrode, Figure 4.28. Oxygen measurements were carried out as described in chapter 3 and experimental details can be found in section 4.4.2 of this chapter. Oxygen measurements using a PBI-A rehydrated xerogel in 0.1 M KCl adjusted to pH 4, were carried out using a 490 nm LED irradiating from the back face of the electrode. The PBI-A rehydrated xerogel generator electrode was held at +0.2 $V_{Ag/AgCl}$ in the dark until a stable baseline was acquired, then illuminated with a 490 nm LED prompting the generation of a photocurrent, Figure 4.32. During the period that the PBI-A photoelectrode was illuminated, we measured a slight increase in current at the collector electrode assigned to O_2 evolution from the PBI-A sample, and when the light was turned off (5000 s) as expected the concentration of O_2 at the collector electrode began to decrease. Therefore, we are able to demonstrate that PBI-A rehydrated xerogel photoanodes do evolve O_2 in pH 4 KCl electrolyte, but with very low Faradic Efficiencies (*ca.* 7 ± 4.24 %, Figure 4.32).

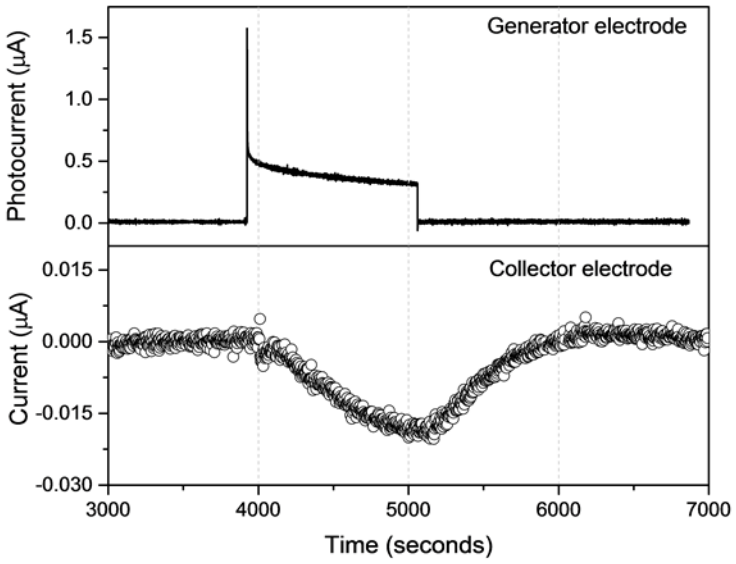

Figure 4.32 Oxygen measurement for PBI rehydrated xerogel, where the FTO collector electrode was held at –0.6 V and the PBI generator at +0.2 V for the duration of the experiment, and illuminated with a 490 nm LED on the back face

As hole transfer into water is inefficient and limiting behaviour, we examined the use of an inorganic WOC, in the hope that it would facilitate hole transfer from alanine to water. Past studies using a PMPDI material showed a large increase in photocurrent and Faradaic Efficiency when a cobalt co-catalyst was selectively deposited at the sites of hole accumulation.[50] IrO_x is a well-known WOC, and IrO_x nanoparticles were synthesised and incorporated into the gel *via* in-situ acid condensation prompted by the gelation of PBI-A, which did not destabilise the PBI-A electrode. 1% wt. IrO_x was achieved by the addition of K_2IrCl_6 to 7.5 mg/mL PBI-A solution, upon the application of the gelation trigger, the pH of the PBI-A/ K_2IrCl_6 mixture is lowered from basic (*ca.* pH 10) to acidic (*ca.* pH 1) resulting in gelation and IrO_x formation. The incorporation of IrO_x was seen from cyclic voltammetry, where $E_{1/2}$ = +0.85 $V_{Ag/AgCl}$ for the redox couple (Figure 4.33a).[86,87] A slight change in UV-Visible absorption spectra due to the presence of IrO_x ($\lambda_{max.}$ of IrO_x is *ca.* 550 nm) is challenging to interpret given the overlap of the PBI and IrO_x spectral features (Figure 4.33b).[88] Initial studies using an IrO_x nanoparticle co-catalyst added into the gel show a large improvement in Faradic Efficiency (*ca*. 30%, Figure 4.33c). However, the electrode is expected to be limited by the lack of control of localisation of WOC, preventing efficient hole migration, likely from the alanine, onto the WOC. This was also evident from PEC measurements of PBI-A/IrO_x under while light irradiation, where little change in photocurrent in comparison to PBI-A without a WOC was observed, in-line with other PBI/WOC systems. Nonetheless this

promising first attempt to use a WOC to enhance the efficiency of water oxidation does suggest such an approach is viable.

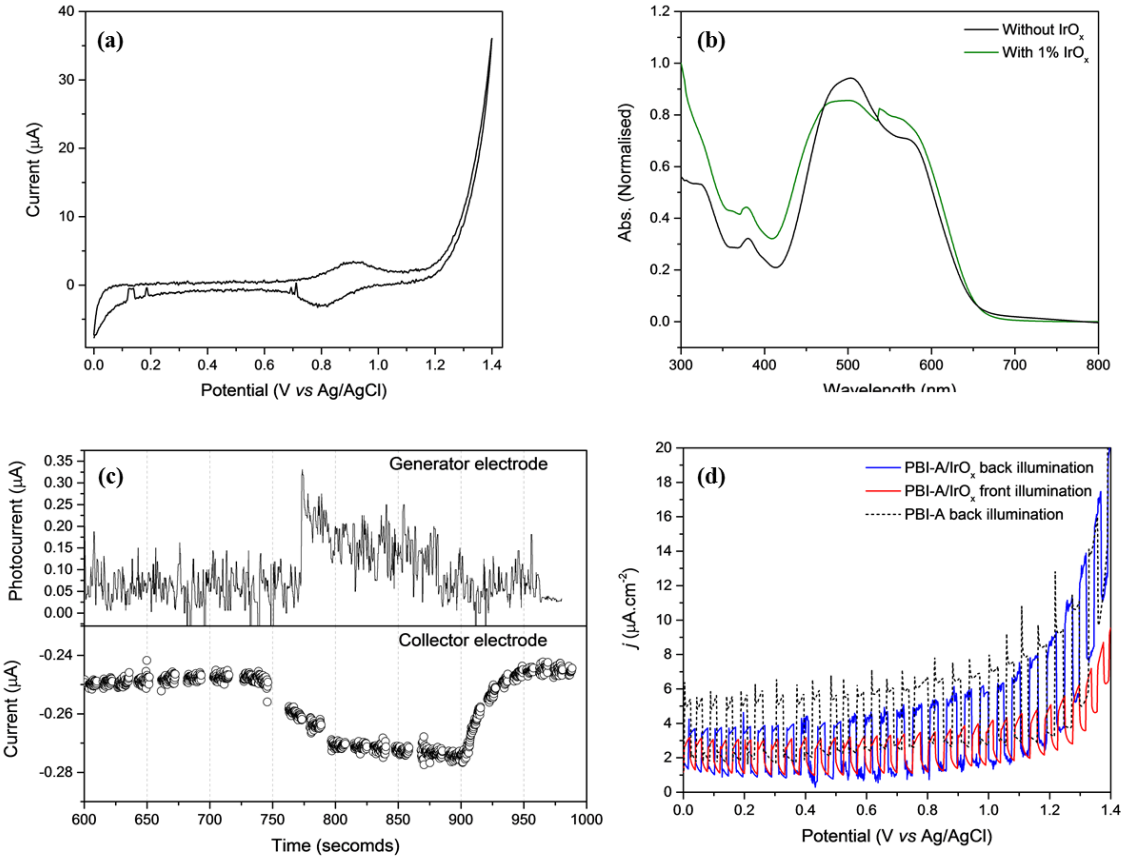

Figure 4.33 Cyclic voltammetry of a rehydrated xerogel containing 1% IrO_x with a scan rate of 100 mVs^{-1} under a nitrogen atmosphere demonstrating successful addition of IrO_x (a). UV-Visible spectra of a PBI-A xerogel with (green) ad without (black) 1% IrO_x co-catalyst, showing some change to the aggregated network upon its incorporation (b). Oxygen measurements for a rehydrated xerogel containing 1% IrO_x nanoparticles as a water oxidation co-catalyst. Throughout the experiment the FTO collector electrode was held at -0.6 V, and the PBI-A/IrO_x generator electrode at +0.2 V with illumination with a 490 nm LED from the back face to promote oxygen evolution (c). PEC measurements of a PBI-A rehydrated xerogel (black, dashed) irradiated from the back face, and a rehydrated PBI-A/IrO_x front (red, solid) and back (blue, solid) illumination, irradiated with a 300 W Xe lmap (315-795 nm, 80 $mWcm^{-2}$) at a scn rate of 10 mVs^{-1} in pH 4 0.1 M KCl (d).

4.3 Conclusions

The use of organic self-assembled structures are highly attractive materials for their applications in solar fuel generation, due to their low cost and facile synthetic routes to the formation of a supramolecular network, consisting of both a donor and acceptor groups. Although the maximum absorption of such materials are in the visible region of the spectrum, previous studies of PBI-A dried solutions only become photoactive under UV light. Here we have shown that by simply gelling the sample to enable the formation of hydrated PBI-A structures, activity can be shifted to the visible region. The use of TA spectroscopy has shown that long lived charge separation can occur when irradiated with visible light in the presence of water. Although both a hydrogel and rehydrated xerogel show such behaviour, the photoresponse for a rehydrated xerogel was significantly higher than that of a hydrogel. The higher photocurrent of a rehydrated xerogel photoanodes is assigned to the superior conductive behaviour of these materials, owed to more efficient charge transport through the rigid rehydrated xerogel network. Both SANS and UV-Visible spectroscopic analysis showed a change in structure upon drying of a hydrogel to form a more compact network, and the rehydration of a xerogel. A collapse of the network upon drying gave rise to shorter and more rigid fibres, which did not revert back to the pristine hydrogel network upon rehydration, yielding an irreversible change in the supramolecular network. Although low Faradic Efficiencies for oxygen evolution were improved by the addition of a WOC, the work presented in this chapter show a rare example of an organic based photoanode for water oxidation.

4.4 Materials and Methods

4.4.1 Materials

Milli-Q water (18.2 MΩ) was used throughout (Millipore Corp). All chemicals were obtained from Sigma-Aldrich and used as received, except for PBI-A which was synthesised according to literature precedent by Dr. E. Draper.[8] Argon was purchased from BOC at pureshield grade.

4.4.2 Methods

Cleaning of FTO: Fluorine-doped tin oxide (FTO, TEC-15, Pilkington, 14 x 20 mm^2) glass substrates were cleaned *via* sonication for 20 minutes in three different solutions; 1% helmanex solution, ethanol and water, and rinsed with water between each sonication. It is important that the FTO are not stacked on top of each other to ensure the FTO is covered in solution for efficient cleaning. After drying of the FTO glass substrates with compressed air, they were heated in an oven to 400˚C (ramped at 20˚C min^{-1}) and held for 20 minutes before cooling. Quick drying epoxy resin was used to mask out a surface area of 150 mm^2 (10 x 15 mm^2) on the conducting face of the FTO and left to dry.

Preparation of electrodes: Gelation was carried out in a petri dish within a glove bag in order to ensure PBI-A gel electrodes did not dry out. FTO glass substrates, prepared as above, were placed in a petri dish containing 8 layers of blue roll dampened with water, and 20 µL of PBI-A (7.5 mg/mL dissolved with 1 molar equivalence of 0.1 M NaOH with the remainder made up with Milli-Q water) was deposited onto each FTO conductive surface. 40 drops of concentrated HCl were evenly dropped around both the outer corners of the petri dish and near to the PBI-A FTO electrode. The lid was placed on the petri dish and sealed with parafilm, allowing for an acidic atmosphere to build up within the petri dish. Typically a gel was formed after *ca.* 1 hour, and if necessary a little more HCl was added. Once gelled the PBI-A electrode was transferred out of the petri dish into a vial containing KCl electrolyte (0.1 M, pH 4 adjusted by HCl) in the glove bag to prevent drying. In the case of PBI-A xerogel electrodes the electrode was removed from the glove bag, and allowed to dry in air overnight.

Addition of IrO_x to PBI-A: Co-catalyst deposition was carried out in situ. Gelation was carried out with K_2IrCl_6 added to the 7.5 mg/mL PBI-A solution to achieve 1% wt. IrO_x. Upon the application of the pH trigger to prompt the gelation of PBI-A, IrO_x was formed *via* an acid condensation reaction.[88]

UV-Visible Absorption Spectroscopy: UV-Visible absorption data were obtained using Shimadzu 2550 UV/VisNIR spectrophotometer in absorbance mode, either by direct absorbance through a PBI-A electrode or a 1 cm^2 quartz cell or spectroelectrochemical cell.

Fluorescence Spectroscopy: PerkinElmer Fluorescence Spectrometer LS55 was used. Samples were excited at 580 nm in air, with a slit width of 5 nm and a scan speed of 200 nm/min.

Thermogravimetric Analysis (TGA): TGA was carried out on a PBI-A gel at different drying times. PBI-A gel was prepared *via* the same method described above, but on a larger scale to allow for enough material to be obtained for analysis. TGA was performed on an EXSTAR6000 with aluminium pans using a constant air flow of 100 mL/min and 10 mL/min nitrogen air flow. A heating rate of 10˚C/min was used to reach 120˚C and held for 10 minutes, before continuing to ramp to 200˚C, where the temperature was held for 10 minutes followed by cooling to 30˚C.

Scanning Electron Microscopy (SEM): Hitachi S-4800 FE-SEM was used. As sample preparation involves the of epoxy resin to create a well which is an insulating material and organic materials are not highly conducting, the epoxy resin was cut away after gelation to help prevent a large build-up of charge on the surface during the measurement. Silver conducting paste was used to adhere the electrode to the surface of an SEM stub, and silver paste was coated around the top and outer edges of the electrode to create a connection to the

SEM stub, and leave a section of PBI-A exposed. Samples were measured in deceleration mode with an acceleration voltage of 1.5 kV, using an upper electron detector, and a working distance of 3 mm. Due to a large build-up of charge the SEM had to be taken immediately after focusing, or focusing and moving to a nearby area and quickly taking the image, to prevent destruction of the sample. To overcome this, 10 nm of chromium was sputtered onto the surface to dissipate charge build-up. Chromium takes the morphology of the surface it is coated onto, and has a small grain size making it difficult to see in the SEM image. Images taken with a 10 nm chromium layer were done so using an acceleration voltage of 2 kV and a working distance of 2.2 mm in deceleration mode using an upper electron detector. SEM measurements were carried out with assistance from Dr. M. Forster and Dr. K. Arnold.

Photoelectrochemical Experiments: Photoelectrochemical measurements were carried out in a custom-designed 3 electrode cell. The working electrode was the PBI-A (xero)gel on an FTO glass substrate connected *via* a crocodile clip and nickel wire. The reference electrode was Ag/AgCl (3.5 M KCl), a counter electrode of Pt wire, and KCl electrolyte (0.1 M, pH 4 adjusted by HCl) were used in all experiments. Palmsens[3] was used to carry out electrochemical methods. Prior to all experiments the cell was degassed under a stream of argon. Photoelectrochemical measurements were carried out *via* back illumination of the working electrode using a 300 W Xe lamp with a KG1 filter. The light intensity of the lamp was recorded each time using a Thor labs diode in the same position as the sample. Photocurrent measurements were recorded *via* linear sweep voltammetry at 100 mVs^{-1} and 10 mVs^{-1}, with the light being manually chopped for 1 second and 3 seconds respectively.

Incident Photon Conversion Efficiency (IPCE): IPCE measurements were carried out using Xe lamp with a monochromator, inside a 2 x 1 cm^2 quartz cell. Electrodes were made by gelling 20 µL of 7.5 mg/mL PBI-A as desciribed above. For the wavelengths selected with the monochromator greater than 420 nm, a 420 nm long pass filter was used to block out UV wavelengths of λ/2. This is because high order diffraction gratings are generated by the monochromator, meaning if a wavelength (λ) of 600 nm is used, diffraction peaks of 300 nm will be produced also.[89] Therefore when irradiating with a λ in the visible region, it is important to avoid λ/2 to prevent UV λ excitation also. Upon back illumination of the PBI-A FTO electrode the current was allowed to stabilise at +0.4 $V_{Ag/AgCl}$. Once stabilised the light was chopped to obtain a photocurrent.

Spectroelectrochemistry: UV-Visible absorption spectroscopy was carried out using a Shimadzu UV-2600 spectrophotometer using a slit width of 5 nm on all electrodes. For the spectroelectrochemistry a 2 x 1 cm^2 quartz cell was used containing a 5 µL 7.5 mg/mL PBI-A gel or xerogel on an FTO electrode, a Ag/AgCl reference and Pt counter electrodes were used along with KCl electrolyte (0.1 M, pH 4 adjusted with HCl). The cell was purged for 10

minutes under argon, and then aligned in the beam path of the UV-Visible spectrometer. The potential was held using amperometric detection until a steady current was obtained, and a UV-Visible absorption spectra recorded.

Differential Cyclic Voltabsorptometric (DCVA): A custom made spectroelectrochemical cell was used, with a 3.5 M Ag/AgCl reference electrode and a platinum wire counter electrode. The working electrode was either that of a 20 µL 7.5 mg/mL PBI-A gel or a xerogel on FTO prepared as described above. 0.1 M KCl electrolyte at pH 4 adjusted by the addition on HCl was also used. UV-Visible absorption spectrometer as described in 4.4.3 was used, and the kinetics program in the software used to carry out DCVA measurements. The cell was purged with an inert gas, either argon or nitrogen, for 10-15 minutes. Initially before any DCVA measurements were ran a UV-Visible spectra was recorded of the working electrode (backgrounded against blank FTO), and a cyclic voltammogram at 100 mVs^{-1} to ensure that the working electrode was responding as expected. Single wavelength measurements were carried out at 487 nm, 608 nm, 729 nm and 820 nm. A typical experimental measurement would consist of simultaneously running a cyclic voltammogram at either 10 mVs^{-1} or 100 mVs^{-1} between +1.4 V to -0.8 $V_{Ag/AgCl}$ with a single wavelength kinetic absorption spectra.

Femtosecond Transient Absorption Spectroscopy: TA spectroscopy was carried out using a HELIOS spectrometer (Ultrafast systems) PHAROS laser (Light Conversion Ltd) operating at 10 kHz coupled to an ORPHEUS optical parametric amplifier (Light Conversion Ltd) in tandem with a LYRA harmonic generator (Light Conversion Ltd). The pump wavelength was 490 nm (275 µW). The spot size of the probe beam was ~100 µm diameter which overlapped with the pump beam, with an optical time delay of 1 s. Thin film PBI-A gel samples were recorded in a 2 x 1 cm^2 quartz cuvette containing KCl electrolyte (0.1 M KCl, pH 4 adjusted by HCl), and thin film xerogel samples were recorded solely on the FTO glass substrate under air and argon. The thin films consisted of 20 µL PBI-A (7.5 mg/mL) deposited on an FTO substrate prepared as described in 1.2. Data was chirp corrected using Surface Xplorer software.

Small Angle Neutron Scattering (SANS): The PBI-A solution was prepared at 7.5 mg/mL as above but with D_2O and NaOD. Gels were prepared on quartz discs with a 1 mm PTFE spacer creating a well for the gel. Here, the gels were thicker compared to that used for previous experiments (240 µL over 113 mm^2 with one at half that thickness) in order to fill the cell and obtain a suitable signal from the scattering and were gelled as above using DCl vapour. Hydrated gels were covered with a second quartz disc before loading into aluminum cells, as were the xerogels once dried and the rehydrated xerogels were loaded into the same cells with the 1 mm space filled with KCl electrolyte (0.1 M, pD 4) made in D_2O or water contrast matched to air, H_2O_{ACM}. All cells were housed in a temperature controlled sample

rack at 25˚C during the measurements. SANS measurements were performed using the SANS2D instrument (ISIS pulsed neutron source, Oxfordshire, UK). A neutron beam allowed measurements over a large range in Q [$Q = 4\pi\sin(\theta/2)/\lambda$] of 0.005 to 0.7 $Å^{-1}$ using incident wavelengths (λ) from 1.75 to 16.5 Å and employing a sample-to-detector distance of 4 m, with the 1 m^2 detector offset vertically 60 mm and sideways 100 mm. The measuring time was typically 1 hour.

Each raw scattering data set was corrected for the detector efficiencies, sample transmission and background scattering and converted to scattering cross-section data ($\partial\Sigma/\partial\Omega$ vs. Q) using the instrument-specific software.[90] These data were placed on an absolute scale (cm^{-1}) using the scattering from a standard sample (a solid blend of hydrogenous and perdeuterated polystyrene) in accordance with established procedures.[91] The scattering from the electrolyte was also measured and subtracted from the wet and rehydrated data sets. For data from dried samples, the empty beam was subtracted.

The instrument-independent data were then fitted to customized models in the SasView software package;[71] these combined an absolute power law with a (Kratky-Porod) flexible cylinder, as described previously.[92] The Q-dependent power law (Q^{-N}) accounts for the mass fractal contribution to the scattering intensity, which is superimposed on that from the cylindrical structures i.e. the fibers. The fibers of the gel are represented as a flexible worm-like chain of cylindrical Kuhn segments. SANS data fitting was carried out by Dr. L. Mears.

CoO_x photoelectrochemical deposition: FTO in 0.5 mM cobalt nitrate solution under an argon atmosphere was held at +0.2 $V_{Ag/AgCl}$ for 5 minutes whilst sequentially illuminating the sample with a 300 W Xe lamp, followed by a further 12 minutes at +0.1 $V_{Ag/AgCl}$. Photodeposition was carried out using a light intensity of 62 $mW.cm^{-2}$ across 315-795 nm.

Oxygen measurements: Oxygen measurements were carried out using a generator -collector electrode method as developed by other groups previously.[59,93,94] On either side of the collector electrode 1 mm spacers were used, to prevent electrical contact between both generator and collector electrodes, and to allow space for electrolyte. FTO used for the collector electrode was not pre-treated. A wire was connected to the top left corner of the electrodes using conductive silver paste, and once dry covered in epoxy resin. Electrodes were then cut in the top right corner to isolate the connections when sandwiched together. Electrodes were pressed together with the conducting sides facing each other, and parafilm was wrapped around the top and the bottom of the sandwiched electrodes to hold them together.

Prior to purging the electrolyte (0.1 M KOH) a CV at 100 mVs^{-1} was obtained for the electrodes. The cell was then purged for 30 minutes with nitrogen, after which, a nitrogen blanket was kept over the cell for the remainder of the experiment. CV of the collector

electrode was taken to ensure no oxygen was present within the cell. Here, PBI-A is the generator electrode. It was held at +0.2 or +0.4 $V_{Ag/AgCl}$ throughout the experiment. FTO is the collector electrode and was held at -0.6 $V_{Ag/AgCl}$, a potential selective to oxygen reduction. Once steady state had been reached by both electrodes, the back face of the generator electrode was illuminated with a 420 nm LED, after which the LED was switched off and the current allowed to plateau. Faradic efficiencies were calculated using the equation below, where $-Q_C$ and Q_G are the areas for the collector and generator electrode respectively. $\%_{col}$ is the collection Efficiency (54 ± 10 %) which was determined by taking the average of 5 oxygen measurements using a Co-Pi electrode as the generator electrode. Co-Pi is used as a calibration material as it is known to show ~ 100% Faradic Efficiency for water oxidation. For these measurements Co-Pi was prepared *via* electrochemical deposition in 0.5 mM cobalt nitrate, in 0.1 M phosphate buffer at pH 7. The FTO electrode was held at +1.2 $V_{Ag/AgCl}$ for 25 minutes, after which the FTO electrode had a brown colouring owed to the presence of Co-Pi on the surface. Calibration measurements were carried out with the Co-Pi held at +0.6 $V_{Ag/AgCl}$ initially, and oxygen production was triggered by a potential switch to +1.6$V_{Ag/AgCl}$.

$$FE_{O2} = (-Q_C / Q_G)\ (1/\%_{col}),\ \%_{col} = -Q_C/Q_G$$

References

1 S. S. Babu, V. K. Praveen and A. Ajayaghosh, *Chem. Rev.*, 2014, **114**, 1973–2129.

2 J. T. Kirner and R. G. Finke, *J. Mater. Chem. A*, 2017, **5**, 19560–19592.

3 J. Raeburn, A. Zamith Cardoso and D. J. Adams, *Chem. Soc. Rev.*, 2013, **42**, 5143.

4 S. Roy, D. Kumar Maiti, S. Panigrahi, D. Basak and A. Banerjee, *RSC Adv.*, 2012, **2**, 11053–11060.

5 Gilbert T. Morgan and James G. Mitchell, *J. Chem. Soc.*, 1934, 536.

6 D. Görl, X. Zhang and F. Würthner, *Angew. Chemie Int. Ed.*, 2012, **51**, 6328–6348.

7 J. J. Walsh, J. R. Lee, E. R. Draper, S. M. King, F. Jackel, M. A. Zwijnenburg, D. J. Adams and A. J. Cowan, *J. Phys. Chem. C*, 2016, **120**, 18479–18486.

8 E. R. Draper, J. J. Walsh, T. O. McDonald, M. A. Zwijnenburg, P. J. Cameron, A. J. Cowan and D. J. Adams, *J. Mater. Chem. C*, 2014, **2**, 5570–5575.

9 M. Más-Montoya and R. A. J. Janssen, *Adv. Funct. Mater.*, 2017, **27**, 1605779.

10 G. Pescitelli, L. Di Bari and N. Berova, *Chem. Soc. Rev.*, 2014, **43**, 5211–5233.

11 R. M. Hochstrasser and M. Kasha, *Photochem. Photobiol.*, 1964, **3**, 317–331.

12 E. G. McRae and M. Kasha, *J. Chem. Phys.*, 1958, **28**, 721–722.

13 W. T. Simpson and D. L. Peterson, *J. Chem. Phys.*, 1957, **26**, 588–593.

14 A. E. Clark, C. Qin and A. D. Q. Li, *J. Am. Chem. Soc.*, 2007, **129**, 7586–7595.

15 M. Kasha, H. R. Rawls and M. Ashraf El-Bayoumi, *Pure Appl. Chem.*, 1965, **11**, 371–392.

16 Q. Yan, K. Cai and D. Zhao, *Phys. Chem. Chem. Phys.*, 2016, **18**, 1905–1910.

17 H. Marciniak, X.-Q. Li, F. Würthner and S. Lochbrunner, *J. Phys. Chem. A*, 2011, **115**, 648–654.

18 S. Herbst, B. Soberats, P. Leowanawat, M. Stolte, M. Lehmann and F. Würthner, *Nat. Commun.*, 2018, **9**, 1–9.

19 Z. Xie, B. Xiao, Z. He, W. Zhang, X. Wu, H. Wu, F. Würthner, C. Wang, F. Xie, L. Liu, Y. Ma, W. Y. Wong and Y. Cao, *Mater. Horizons*, 2015, **2**, 514–518.

20 T. E. Kaiser, V. Stepanenko and F. Würthner, *J. Am. Chem. Soc.*, 2009, **131**, 6719–6732.

21 Y. Tian, V. Stepanenko, T. E. Kaiser, F. Würthner and I. G. Scheblykin, *Nanoscale*,

2012, **4**, 218–223.

22 S. Ghosh, X. Q. Li, V. Stepanenko and F. Würthner, *Chem. - A Eur. J.*, 2008, **14**, 11343–11357.

23 X. Du, J. Zhou, J. Shi and B. Xu, *Chem. Rev.*, 2015, **115**, 13165–13307.

24 E. R. Draper and D. J. Adams, *Chem*, 2017, **3**, 390–410.

25 E. R. Draper, L. L. E. Mears, A. M. Castilla, S. M. King, T. O. McDonald, R. Akhtar and D. J. Adams, *RSC Adv.*, 2015, **5**, 95369–95378.

26 P. A. Korevaar, C. J. Newcomb, E. W. Meijer and S. I. Stupp, *J. Am. Chem. Soc.*, 2014, **136**, 8540–8543.

27 J. Raeburn, C. Mendoza-Cuenca, B. N. Cattoz, M. A. Little, A. E. Terry, A. Zamith Cardoso, P. C. Griffiths and D. J. Adams, *Soft Matter*, 2015, **11**, 927–935.

28 M. J. Webber, C. J. Newcomb, R. Bitton and S. I. Stupp, *Soft Matter*, 2011, **7**, 9665–9672.

29 S. Toledano, R. J. Williams, V. Jayawarna and R. V. Ulijn, *J. Am. Chem. Soc.*, 2006, **128**, 1070–1071.

30 T. Koga, K. I. Kitamura and N. Higashi, *Chem. Commun.*, 2006, 4897–4899.

31 P. J. Knerr, M. C. Branco, R. Nagarkar, D. J. Pochan and J. P. Schneider, *J. Mater. Chem.*, 2012, **22**, 1352–1357.

32 S. N. Dublin and V. P. Conticello, *J. Am. Chem. Soc.*, 2008, **130**, 49–51.

33 L. L. E. Mears, E. R. Draper, A. M. Castilla, H. Su, Zhuola, B. Dietrich, M. C. Nolan, G. N. Smith, J. Doutch, S. Rogers, R. Akhtar, H. Cui and D. J. Adams, *Biomacromolecules*, 2017, **18**, 3531–3540.

34 P. E. Hartnett, E. A. Margulies, H. S. S. R. Matte, M. C. Hersam, T. J. Marks and M. R. Wasielewski, *Chem. Mater.*, 2016, **28**, 3928–3936.

35 Y. L. Wu, N. E. Horwitz, K. S. Chen, D. A. Gomez-Gualdron, N. S. Luu, L. Ma, T. C. Wang, M. C. Hersam, J. T. Hupp, O. K. Farha, R. Q. Snurr and M. R. Wasielewski, *Nat. Chem.*, 2017, **9**, 466–472.

36 L. Zhao, H. Sun, X. Liu, C. Liu, H. Shan, J. Xia, Z. Xu, F. Chen, Z. K. Chen and W. Huang, *Chem. - An Asian J.*, 2017, **12**, 2052–2056.

37 P. E. Hartnett, S. M. Dyar, E. A. Margulies, L. E. Shoer, A. W. Cook, S. W. Eaton, T. J. Marks and M. R. Wasielewski, *Chem. Sci.*, 2015, **6**, 402–411.

38 J. E. Bullock, R. Carmieli, S. M. Mickley, J. Vura-Weis and M. R. Wasielewski, *J. Am. Chem. Soc.*, 2009, **131**, 11919–11929.

39 K. M. Lefler, K. E. Brown, W. A. Salamant, S. M. Dyar, K. E. Knowles and M. R. Wasielewski, *J. Phys. Chem. A*, 2013, **117**, 10333–10345.

40 I. Paci, J. C. Johnson, X. Chen, G. Rana, D. Popović, D. E. David, A. J. Nozik, M. A. Ratner and J. Michl, *J. Am. Chem. Soc.*, 2006, **128**, 16546–16553.

41 C. A. Nelson, N. R. Monahan and X. Y. Zhu, *Energy Environ. Sci.*, 2013, **6**, 3508–3519.

42 S. Millicent B and M. Josef, *Chem. Rev.*, 2010, **110**, 6891–936.

43 D. Veldman, S. M. A. Chopin, S. C. J. Meskers, M. M. Groeneveld, R. M. Williams and R. A. J. Janssen, *J. Phys. Chem. A*, 2008, **112**, 5846–5857.

44 J. M. Giaimo, J. V Lockard, L. E. Sinks, A. M. Scott, T. M. Wilson and M. R. Wasielewski, *J. Phys. Chem. A*, 2008, **112**, 2322–2330.

45 K. Nagarajan, A. R. Mallia, V. S. Reddy and M. Hariharan, *J. Phys. Chem. C*, 2016, **120**, 8443–8450.

46 R. J. Lindquist, B. T. Phelan, A. Reynal, E. A. Margulies, L. E. Shoer, J. R. Durrant and M. R. Wasielewski, *J. Mater. Chem. A*, 2016, **4**, 2880–2893.

47 E. O. Danilov, A. A. Rachford and F. N. Castellano, 2009, 5763–5768.

48 M. C. Nolan, J. J. Walsh, L. L. E. Mears, E. R. Draper, M. Wallace, M. Barrow, B. Dietrich, S. M. King, A. J. Cowan and D. J. Adams, *J. Mater. Chem. A*, 2017, **5**, 7555–7563.

49 E. R. Draper, L. J. Archibald, M. C. Nolan, R. Schweins, M. A. Zwijnenburg, S. Sproules and D. J. Adams, *Chem. - A Eur. J.*, 2018, **24**, 4006–4010.

50 J. T. Kirner, J. J. Stracke, B. A. Gregg and R. G. Finke, *ACS Appl. Mater. Interfaces*, 2014, **6**, 13367–13377.

51 L. Yang, M. Wang, P. M. Slattum, B. R. Bunes, Y. Wang, C. Wang and L. Zang, *ACS Appl. Mater. Interfaces*, 2018, **10**, 19764–19772.

52 M. Burian, F. Rigodanza, N. Demitri, L. Dordević, S. Marchesan, T. Steinhartova, I. Letofsky-Papst, I. Khalakhan, E. Mourad, S. A. Freunberger, H. Amenitsch, M. Prato and Z. Syrgiannis, *ACS Nano*, 2018, **12**, 5800–5806.

53 E. R. Draper, J. R. Lee, M. Wallace, F. Jäckel, A. J. Cowan and D. J. Adams, *Chem. Sci.*, 2016, **7**, 6499–6505.

54 A. M. Castilla, E. R. Draper, M. C. Nolan, C. Brasnett, A. Seddon, L. L. E. Mears, N. Cowieson and D. J. Adams, *Sci. Rep.*, 2017, **7**, 1–10.

55 E. R. Draper, O. O. Mykhaylyk and D. J. Adams, *Chem. Commun.*, 2016, **52**, 6934–6937.

56 W. Chen and Q. Zhang, *J. Mater. Chem. C*, 2017, **5**, 1275–1302.

57 F. Ronconi, Z. Syrgiannis, A. Bonasera, M. Prato, R. Argazzi, S. Caramori, V. Cristino and C. A. Bignozzi, *J. Am. Chem. Soc.*, 2015, **137**, 4630–4633.

58 S. Berardi, V. Cristino, M. Canton, R. Boaretto, R. Argazzi, E. Benazzi, L. Ganzer, R. Borrego Varillas, G. Cerullo, Z. Syrgiannis, F. Rigodanza, M. Prato, C. A. Bignozzi and S. Caramori, *J. Phys. Chem. C*, 2017, **121**, 17737–17745.

59 J. T. Kirner and R. G. Finke, *ACS Appl. Mater. Interfaces*, 2017, **9**, 27625–27637.

60 A. S. Weingarten, R. V. Kazantsev, L. C. Palmer, M. McClendon, A. R. Koltonow, A. P. S. Samuel, D. J. Kiebala, M. R. Wasielewski and S. I. Stupp, *Nat. Chem.*, 2014, **6**, 964–970.

61 A. S. Weingarten, R. V. Kazantsev, L. C. Palmer, D. J. Fairfield, A. R. Koltonow and S. I. Stupp, *J. Am. Chem. Soc.*, 2015, **137**, 15241–15246.

62 N. J. Hestand, R. V. Kazantsev, A. S. Weingarten, L. C. Palmer, S. I. Stupp and F. C. Spano, *J. Am. Chem. Soc.*, 2016, **138**, 11762–11774.

63 M. C. Nolan, J. J. Walsh, L. L. E. Mears, E. R. Draper, M. Wallace, M. Barrow, B. Dietrich, S. M. King, A. J. Cowan and D. J. Adams, *J. Mater. Chem. A*, 2017, **5**, 7555–7563.

64 K. Wang, Z. Yang and X. Li, *Chem. - A Eur. J.*, 2015, **21**, 5680–5684.

65 D. Bialas, C. Brüning, F. Schlosser, B. Fimmel, J. Thein, V. Engel and F. Würthner, *Chem. - A Eur. J.*, 2016, **22**, 15011–15018.

66 H. Emoto, H. Kambic, J. Chen and Y. Nose, *Artif. Organs*, 1991, **15**, 29–34.

67 B. Lu, H. Yuk, S. Lin, N. Jian, K. Qu, J. Xu and X. Zhao, *Nat. Commun.*, 2019, **10**, 1043.

68 W. S. Chang and H. H. Chen, *Food Hydrocoll.*, 2016, **53**, 75–83.

69 A. Z. Cardoso, L. L. E. Mears, B. N. Cattoz, P. C. Griffiths, R. Schweins and D. J. Adams, *Soft Matter*, 2016, **12**, 3612–3621.

70 E. R. Draper, R. Schweins, R. Akhtar, P. Groves, V. Chechik, M. A. Zwijnenburg and D. J. Adams, *Chem. Mater.*, 2016, **28**, 6336–6341.

71 www.sasview.org.

72 A. D. McNaught and A. Wilkinson., in *IUPAC Compendium of Chemical Terminology*, eds. M. Nič, J. Jirát, B. Košata, A. Jenkins and A. McNaught, IUPAC, Research Triagle Park, NC, 2009.

73 J. Teixeira, *J. Appl. Crystallogr.*, 1988, **21**, 781–785.

74 M. J. Ahrens, M. J. Tauber and M. R. Wasielewski, *J. Org. Chem.*, 2006, **71**, 2107–2114.

75 S. K. Lee, Y. Zu, A. Herrmann, Y. Geerts, K. Müllen and A. J. Bard, *J. Am. Chem. Soc.*, 1999, **121**, 3513–3520.

76 G. Goretzki, E. S. Davies, S. P. Argent, W. Z. Alsindi, A. J. Blake, J. E. Warren, J. McMaster and N. R. Champness, *J. Org. Chem.*, 2008, **73**, 8808–8814.

77 E. R. Draper, B. J. Greeves, M. Barrow, R. Schweins, M. A. Zwijnenburg and D. J. Adams, *Chem*, 2017, **2**, 716–731.

78 F. Schlosser, M. Moos, C. Lambert and F. Würthner, *Adv. Mater.*, 2013, **25**, 410–414.

79 R. O. Marcon and S. Brochsztain, *Langmuir*, 2007, **23**, 11972–11976.

80 J. J. Walsh, M. Forster, C. L. Smith, G. Neri, R. J. Potter and A. J. Cowan, *Phys. Chem. Chem. Phys.*, 2018, **20**, 6811–6816.

81 Y. Wu, R. M. Young, M. Frasconi, S. T. Schneebeli, P. Spenst, D. M. Gardner, K. E. Brown, F. Würthner, J. F. Stoddart and M. R. Wasielewski, *J. Am. Chem. Soc.*, 2015, **137**, 13236–13239.

82 L. Yao, A. Rahmanudin, N. Guijarro and K. Sivula, *Adv. Energy Mater.*, 2018, **8**, 1802585.

83 J. T. Kirner and R. G. Finke, *J. Mater. Chem. A*, 2017, **5**, 19560–19592.

84 H. Dotan, K. Sivula, M. Grätzel, A. Rothschild and S. C. Warren, *Energy Environ. Sci.*, 2011, **4**, 958–964.

85 A. J. Cowan, W. Leng, P. R. F. Barnes, D. R. Klug and J. R. Durrant, *Phys. Chem. Chem. Phys.*, 2013, **15**, 8772–8778.

86 P. Steegstra, M. Busch, I. Panas and E. Ahlberg, *J. Phys. Chem. C*, 2013, **117**, 20975–20981.

87 J. Juodkazyte, B. Šebeka, I. Valsiunas and K. Juodkazis, *Electroanalysis*, 2005, **17**, 947–952.

88 Y. Zhao, E. A. Hernandez-Pagan, N. M. Vargas-Barbosa, J. L. Dysart and T. E. Mallouk, *J. Phys. Chem. Lett.*, 2011, **2**, 402–406.

89 Z. Chen, H. N. Dinh and E. Miller, *Photoelectrochemical Water Splitting*, Springer New York, New York, NY, 2013.

90 O. Arnold, J. C. Bilheux, J. M. Borreguero, A. Buts, S. I. Campbell, L. Chapon, M. Doucet, N. Draper, R. Ferraz Leal, M. a. Gigg, V. E. Lynch, A. Markvardsen, D. J. Mikkelson, R. L. Mikkelson, R. Miller, K. Palmen, P. Parker, G. Passos, T. G. Perring, P. F. Peterson, S. Ren, M. a. Reuter, A. T. Savici, J. W. Taylor, R. J. Taylor, R. Tolchenov, W. Zhou and J. Zikovsky, *Nucl. Instruments Methods Phys. Res. Sect. A Accel. Spectrometers, Detect. Assoc. Equip.*, 2014, **764**, 156–166.

91 G. D. Wignall and F. S. Bates, *J. Appl. Crystallogr.*, 1987, **20**, 28–40.

92 A. Z. Cardoso, L. L. E. Mears, B. N. Cattoz, P. C. Griffiths, R. Schweins and D. J. Adams, *Soft Matter*, 2016, **12**, 3612–3621.

93 D. L. Ashford, B. D. Sherman, R. A. Binstead, J. L. Templeton and T. J. Meyer, *Angew. Chemie - Int. Ed.*, 2015, **54**, 4778–4781.

94 S. A. Lee, Y. Zhao, E. A. Hernandez-pagan, L. Blasdel, W. Justin and T. E. Mallouk, 2012, 165–176.

“Scatenate la samba…”

Chapter 5

Conclusions and Future Work

In this thesis we explored the engineering and activity of (i) photoanodes for photoelectrochemical water splitting using PBI-A gels and organic semiconducting polymers and (ii) electrocatalytic CO_2 reduction using [Mn(bpy)$(CO)_3$Br] electrocatalyst incorporated into a CMP.

In chapter 2 we synthesised a known porous polymer, CMP-$(bpy)_{20}$, and immobilised a CO_2 reduction molecular catalyst, [Mn(bpy)$(CO)_3$Br], into the polymer backbone to prevent dimerisation of the molecular catalyst in an attempt to reduce the overpotential required for CO_2 reduction. Various different synthetic routes were explored to gain a high BET surface area of the polymer material whilst possessing high catalyst loadings. Post metalation of CMP-$(bpy)_{20}$ at lower synthetic temperatures of 45˚C resulted in both high surface area and catalyst loading. Immobilisation of CMP-$(bpy)_{20}$-Mn was achieved using Nafion as a supporting polymer by drop casting a suspension of CMP-$(bpy)_{20}$-Mn in a Nafion solution onto the surface of a GCE. It was found that using 0.5% wt Nafion resulted in good stability as well as optimal current densities as high as *ca.* 40 mA cm^{-2} with addition of NTs. The use of a conducting polymer such as PANI as a supporting polymer showed improved current densities in comparison to Nafion prepared electrodes. Both Nafion and PANI electrodes showed low Faradaic efficiencies for carbon based products, <1%, and low electroactive catalyst content. It was found that soaking the electrode prior to use resulted in a current increase, demonstrating diffusion limitations across the electrode. Low electroactive content of Mn centres also demonstrated the lack of extended conjugation as a result of structural defects within CMP-$(bpy)_{20}$ framework. Therefore, it was expected that only CMP-$(bpy)_{20}$-Mn particles very close to the GCE electrode surface were electroactive. To overcome this and increase conjugation and diffusion across the electrode, CMP-$(bpy)_{20}$-Mn was templated onto the surface of a GCE by exploiting π-π interactions. Although, selectivity and electroactive content was not improved, this study is a first example of the immobilisation of [Mn(bpy)CO_3Br] into a CMP for electrochemical analysis and is an important step for the development of such electrodes for CO_2 reduction. Future studies will be carried out using a gas diffusion electrode to aid diffusion of gases in and out of the porous structure.

In chapter 3 we begin by rationalising the electron transfer process of two linear polymers, P8s and P56, for photocatalytic hydrogen evolution in a H_2O/MeOH/TEA mixture using TA spectroscopy. Both polymers showed similar excited state dynamics upon photoexcitation in the UV region (365 nm). Photoexcitation of a suspension of polymer in H_2O/MeOH/TEA showed the formation of a long-lived excited state, with an absorption maxima *ca.* 700 nm, of which *ca.* 10% persists beyond 3.2 ns. The long-lived excited state was assigned to the formation of an electron polaron state. In contrast, when in H_2O only a short-lived PIA is observed, indicating MeOH and/or TEA was acting as a sacrificial electron

donor. TA spectroscopy in H_2O/MeOH showed only a small increase in $t_{50\%}$ in comparison to H_2O, showing the role of MeOH in this case to be a wetting agent of the polymer, and therefore confirming TEA as the acting sacrificial electron donor. Due to their solubility in organic solvent, we went on to explore the fabrication of photoanodes for water oxidation, primarily focusing our study on P8s due to its superior HER for water oxidation. Initial testing of P8s on FTO exhibited small photocurrents of 0.64 μA cm^{-2}. Systematic engineering of the photoanode by the incorporation of a bulk heterojunction, n-TiO_2, improved photon absorption to >95%, and resulted in photocurrents as high as *ca.* 21 μA cm^{-2} in-line with those reported in the literature for other organic photoanodes. Although TA spectroscopy showed the photo-generation of a hole polaron, and PEC measurements using a hole scavenger showed increased photocurrents, only negligible oxygen Faradaic efficiencies were obtained in the presence of a WOC. Lack of oxygen generation is thought to be due either (i) self-trapping of holes and/or (ii) short-lived lifetimes for electron-hole pairs, preventing sufficient time for hole migration to water for water oxidation. Future work will focus on the mechanistic insight into the charge separation when in the presence of a WOC to gain insight into the lack of oxygen evolution. The addition of protecting layers to the surface of the photoanode is also of interest, as this has been reported to aid stability of organic photoanodes in such harsh working conditions. Furthermore, the testing of other processable hydrogen evolution polymers, such as P56, will be carried out for their applications as photoelectrodes for water splitting.

In chapter 4 we show that by hydrating a PBI-A self-assembled network *via* gelation, a shift in activity from the UV to the visible region is observed corresponding to the maximum absorption of the material, in contrast to previous reports PBI-A dried solutions. Investigations into the structure and excited state dynamics of various hydrated states of a PBI-A gel was carried out using SANS, UV-Visible absorption spectroscopy and TA spectroscopy. Upon drying of a hydrogel, the formation of a compact and more rigid network was observed and was reflected in the apparent shortening of fibres. UV-Visible absorption spectroscopy showed that overall the aggregated networks between a dried and hydrated gel were similar, as only a small change in the stacking of PBIs within aggregates occurred. However, rehydration of a dried gel showed the changes upon drying were irreversible. In all gels long-lived charge separation was achieved under visible light illumination (490 nm) when in water (pH 4), where it is likely electron transfer from the PBI core to the alanine group occurs. We therefore tested the gels as photoanodes for water oxidation. Optimal photocurrents of ~4 μA cm^{-2} were observed for a rehydrated xerogel, in-line with those reported for the state-of-the-art organic photoelectrodes in water (1-10 μA cm^{-2}). Low oxygen Faradaic efficiencies of 7 ± 4.24% were improved by the addition of 1% wt. IrO_x WOC to *ca.* 30% at +0.2 $V_{Ag/AgCl}$. Although the Faradaic efficiency was improved, the low yield of oxygen is thought to be due

to poor localisation of the WOC hindering efficient hole transfer into the electrolyte. Alternative methods such as photoelectrochemical deposition present promise for optimal positioning of WOC. To improve photoactivity of amino acid functionalised PBIs, the screening of various different amino acid groups would provide insight into which donor groups work most effectively for water oxidation applications.